technische universität
dortmund

Electron and Nuclear Spin Dynamics in Fluorine-doped ZnSe Epilayers

Dissertation

submitted in partial fulfillment of
the requirements for the degree of

Dr. rer. nat.

to the Faculty of Physics
TU Dortmund University, Germany

by

Fabian Heisterkamp

Dortmund, March 2017

Accepted by the Faculty of Physics, TU Dortmund University, Germany.

Day of the oral examination: 28th April 2017

Examination board:
Prof. Dr. Manfred Bayer
Prof. Dr. Joachim Stolze
Prof. Dr. Heinz Hövel
Dr. Bärbel Siegmann

Contents

> Quantum information is a radical departure in information technology, more fundamentally different from current technology than the digital computer is from the abacus.
>
> W. D. Phillips, Nobel laureate [Cal17]

1 Introduction

Although the scientific community is in agreement that quantum information processing will offer advantages for certain applications [Lad10], such as Shor's quantum algorithm for integer factorization [Sho94] and simulating quantum systems [Fey82; Llo96; Bul09; Cir12], it is not clear yet which technology (physical system or material) can be used to ultimately build a quantum computer [Lad10].

Furthermore, quantum simulators based on quantum computers might also become important for conventional semiconductor technology, as it is approaching the limits of Moore's law [Moo98; Moo75], which states that the number of transistors on a chip will double every two years [Wal16]: Following this law, the elements on microchips become successively smaller so that an end of this process might either be given by fundamental physical limits, if the elements become so small that quantum mechanical effects need to be considered, or will even make the transistors unreliable, or by economic limits, if the cost for a transistor will no longer decrease but increase due to downscaling [Wal16]. Quantum simulators might also be used for developing emerging artificial nanotechnology or for understanding the nanomachinery of biological molecules [Lad10].

A quantum computer is based on the quantum analog to a classical bit: the so-called qubit. It maintains the properties, which distinguish it from a classical bit, such as entanglement and quantum interference, during the coherence time T_2.

There are several ways to realize a quantum computer, i. e., candidates for physical representations of qubits: The implementation of quantum algorithms with photons (flying qubits) [Pol09] was demonstrated and even multi-photon entanglement and interferometry [Pan12] were achieved. The Knill-Laflamme-Milburn (KLM) scheme allows for scalable quantum computing, which is solely based on single-photon sources, single-photon detectors, and linear optics [Kni01]. While photon-based quantum computing is less challenged by decoherence compared to other quantum systems, the loss of photons remains a problem [Lad10].

Another candidate is a superconducting qubit, consisting of a superconducting circuit with a defined inductance and capacitance. However, this circuit is interrupted by a thin insulating layer, a so-called *Josephson junction*, to induce anharmonicity to the otherwise harmonic LC-resonator. Recently, quantum error correction was demonstrated on a superconducting circuit with nine qubits [Kel15]. However, according to Ref. [Lad10] understanding and eliminating decoherence remains a huge challenge, which might require material engineering on the microscopic level.

The nuclear spins, on the other hand, represent the physical system with the most preliminary technological development [Lad10], as the nuclear spins have been studied in nuclear magnetic resonance (NMR) experiments [Blo46; Pur46] since 1946 and for magnetic resonance imaging (MRI) [Dam71; McR07; Dam77] since 1971. While a set of 12 nuclear spin qubits was successfully manipulated using liquid-state NMR techniques [Neg06] and

Shor's algorithms was realized using seven qubits in a molecule [Van01], the suitability of this physical system for quantum computers remains limited, since the coherence times of the nuclear spin qubits are rather short compared to the timescales for their initialization and measurement [Lad10].

Qubits in the form of trapped ions, in turn, exhibit coherence times that are much longer than the necessary operations for computations (initialization, multi-qubit control, and readout). They show long T_1 and T_2 times (cf. Section 2.4.2), high homogeneity and can be entangled by laser-induced coupling of the spins [Lad10]. Furthermore, entanglement of more than 10 qubits was demonstrated [Mon11]. However, scaling this system and simultaneously maintaining the high-fidelity control is a critical challenge [Lad10; Lei03].

While the scalability of trapped ions is limited by the requirement to cool and trap them, semiconductor based qubits, e. g., quantum dots (QDs) and impurities, are integrated into a solid-state host, which could allow for a better scalability and easier cooling of systems with many qubits [Lad10]. The localization of one or more electrons or holes due to the potential of the semiconductor nanostructure, impurity or impurity complex leads to discrete energy levels, forming a so-called *artificial atom* [Lad10], and reduces the decoherence of the qubit due to environmental influences. *Artificial atoms* in the form of QDs have been realized in two different ways: Electrostatically defined QDs, where the confinement is accomplished by voltages on lithographically defined metallic gates (cf., e. g., Ref. [Han07]), and self-assembled QDs, where the confinement results from the difference of the bandgaps of the dot and host material. While a long coherence time $T_2 = (3.0 \pm 0.3)\,\mu s$ was demonstrated [Gre06b] for electron spins in self-assembled QDs, they exhibit a bigger inhomogeneity compared to impurities in semiconductors and the nuclear spins of the mainly used III-V materials limit the coherence time [Cla09].

Many different kinds of impurities in semiconductors are considered as possible candidates for qubits: The ^{31}P impurity in silicon, where the donor-bound electron [Tyr03], as well as the nuclear spin [Pla13; Ste12; Sae13; Muh14] are considered as a candidate for a qubit. Here, a coherence time $T_2 = 60\,ms$ of the donor-bound electron spin in a silicon host with natural abundances of isotopes at a temperature of about 7 K [Tyr03], and a T_2 time of up to 39 min of the nuclear spin of the ionized ^{31}P donor using dynamic decoupling at room-temperature [Sae13] were demonstrated. Other candidates for qubits are electron spins bound to defects in silicon carbide (SiC) [Chr15] that is already used for high power semiconductors and optoelectronics. For this material system, a coherence time of about 1 ms at cryogenic temperatures [Chr15; Seo16] and coherent control of the electron spin [Wid15] were demonstrated. The silicon-based candidates would offer technological advantages due to the techniques, developed for manufacturing conventional semiconductors. However, despite the long coherence times and technological possibilities, efficient methods to couple these qubits have yet to be developed.

An electron spin bound to the negatively charged nitrogen-vacancy center in diamond exhibits a coherence time of about 0.6 s at liquid nitrogen temperature [Bar13] and the coherence time of the nuclear spin of the ^{13}C isotope in the vicinity of a nitrogen-vacancy exceeded 1 s [Mau12]. However, the photoluminescence from nitrogen-vacancies is weaker than for typical quantum dot transitions [Lad10], so connecting them to each other via flying qubits should prove more difficult.

In contrast to this, the fluorine donor impurity in the wide-bandgap group II-VI semi-

conductor ZnSe (ZnSe:F), studied in this work, shows strong optical characteristics [San09; Lad10]. The transition of the exciton bound to a donor that was isolated in a ZnSe/ZnMgSe nanostructure exhibits a small inhomogeneous linewidth and bright photoluminescence (recombination time of about 210 ps [Gre12]). Quantum interference between photons of this transition has been demonstrated [San09]. Similar to phosphor-doped silicon, the single donor-bound electron spin in its ground state can be used as a spin qubit. Greilich *et al.* studied the spin coherence of an ensemble of donor-bound electron spins in homogeneously fluorine-doped ZnSe epilayers with different dopant concentrations and demonstrated an inhomogeneous dephasing time T_2^* of up to 33 ns, which remained stable at temperatures of up to 40 K. The longitudinal spin relaxation time T_1 of up to 1.6 µs, demonstrated in this thesis (cf. Chapter 4 and Ref. [Hei15b]), hints at a coherence time T_2 in the microsecond range by far exceeding the inhomogeneous dephasing time T_2^*. Further steps towards the application of this material system for quantum information include indistinguishable single photon emission [San09], fluorine ion implantation to ensure a controlled location of single donor impurities [Kim12], entangled photon pairs from independently tuned and remote semiconductor emitters [San12], photon antibunching [De 10], and optical control of the electron spin qubit [Kim12; Sle13].

This work provides a better understanding of the ZnSe:F material system. We gain further insight by extending the time-resolved Kerr rotation (TRKR) technique with helicity modulation with variable frequency as well as additional radio frequency (RF) excitation. Furthermore, we develop the spin inertia method (cf. Chapter 4 and Ref. [Hei15b]) that allows us to determine the longitudinal electron spin relaxation time T_1 in a broad range of longitudinal magnetic fields B_F and at different temperatures. The method is especially suitable to study the dynamics of strongly localized electron spins, where a measurement of the Hanle curve would not yield the correct spin relaxation time.

Moreover, this work demonstrates that despite the low natural abundance of isotopes with nonzero nuclear spin in ZnSe strong nuclear effects can be observed (cf. Chapter 5 and Ref. [Hei15a]) so that the possibility to grow samples from isotopically purified constituents (zinc and selenium) with zero nuclear spin is promising. Such samples will be nuclear spin free except for the spin of the fluorine donor and thus should exhibit increased electron spin coherence times.

The inhomogeneously polarized nuclei, in turn, are controlled coherently (cf. Chapter 6 and Ref. [Hei16]) by additional RF excitation, where we use the advantages of optical dynamic nuclear polarization and optical detection, such as high sensitivity and selectivity [San06]. This allows us to measure the nuclear inhomogeneous dephasing time $T_2^{*,\mathrm{N}}$ as well as the nuclear spin coherence time T_2^N. Moreover, modifying the standard TRKR technique, it is possible to estimate the longitudinal nuclear spin relaxation time T_1^N under the conditions of the TRKR experiment (cf. also Chapter 6).

If I have seen further, it is by standing on ye shoulders of giants.

Sir Isaac Newton, 1675 [Wes94]

2 Theoretical Background

This chapter introduces the basic physical concepts, which are necessary to understand and analyze the experiments, presented in this thesis.

2.1 Fluorine-doped Zinc Selenide

The spins of electrons and nuclei in the II-VI semiconductor zinc selenide (ZnSe) are the subject of the research in this work. Here, the Roman numbers refer to the 2nd and the 6th group of the periodic table. In this section, the main properties of this material are discussed.

2.1.1 Crystal Structure

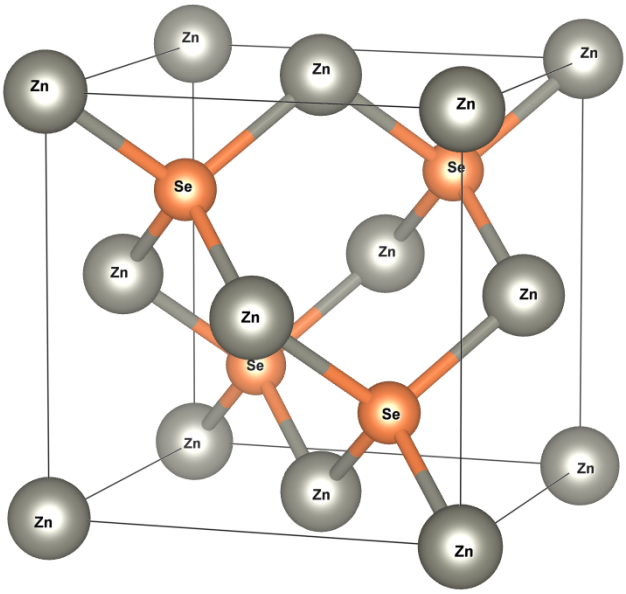

Figure 2.1 Schematic of the unit cell of ZnSe (stick and ball model), drawn with VESTA [Mom11] in analogy to Ref. [Gru16b]. It contains four zinc (gray spheres) and four selenium (orange spheres) atoms (stoichiometric ratio 1 : 1). Each atom of both constituents binds to four atoms of the other constituent (tetrahedral coordination).

The compound ZnSe crystallizes in the so-called zincblende structure. However, the term zincblende actually refers to the compound ZnS only, which can be found in two different phases: the sphalerite and wurtzite structure [Gru16b]. The correct, though hardly used term, is sphalerite structure. A diatomic base of a zinc atom at $(0, 0, 0)$ and a selenium

atom at $(1/4, 1/4, 1/4)$ is arranged in a face-centered cubic (fcc) lattice. Thus, it can also be described by two fcc sublattices, which are shifted with respect to each other by a quarter of the body diagonal. Figure 2.1 shows the unit cell of this crystal as a stick and ball model. The coordination number of both zinc and selenium is four so that each atom is bonded to four atoms of the other element. The stacking order along the body diagonal is given by aAbBcCaAbBcC..., so this crystal exhibits no inversion symmetry (point group T_d) [Gru16b]. It is important to note that the III-V semiconductor GaAs also crystallizes in the sphalerite structure. Please refer to Refs. [Yak01; Ast02; Paw11] for details on the optical properties of ZnSe structures.

In this thesis, ZnSe epilayers (cf. Section 3.3) modulation doped with fluorine (F) during molecular beam epitaxy (MBE) are studied. The fluorine dopant replaces the selenium atom, and each fluorine atom provides one additional electron, which is bound to the donor at low temperatures. Due to the large binding energy $E_\mathrm{a} = (29.3 \pm 0.6)\,\mathrm{meV}$ [Mer72], the electron bound to the fluorine impurity in ZnSe represents a promising candidate for a spin qubit [Gre12]. Its electron spin with a g factor $g_\mathrm{e} = 1.1 \pm 0.1$ exhibits a long spin dephasing time T_2^* (cf. Section 2.4.2) of up to 33 ns, which was shown to remain stable at temperatures of up to 40 K [Gre12]. Indistinguishable single photons were obtained from single donors isolated in ZnSe micropillars [San09]. By means of these nanostructures photon entanglement with photons from two emitters [San12], separated by macroscopic distances, and optical interference of a single electron spin [De 10; Kim12; Sle13] were demonstrated.

Moreover, this material system offers a high homogeneity, in the past restricted to atomic systems, and combines it with the controlled location in a semiconductor [Gre12]: Although in this thesis only modulation doped samples are studied, ion implantation of the fluorine donors, which allows for an exact control of the location, was demonstrated as well [Kim12].

A further advantage is the low natural concentration of isotopes with nonzero nuclear spin in the ZnSe host crystal, since the interaction of the electron spins with the fluctuating nuclear fields is seen as a main factor leading to electron spin decoherence [Mer02; Gre12]. Table 2.1 lists the different isotopes with nonzero nuclear spin I. Despite their relatively low concentrations strong signatures of electron-nuclear interaction were demonstrated for the ^{67}Zn and especially for the ^{77}Se isotope in this thesis. Furthermore, low threshold

Table 2.1 Parameters of the isotopes with nonzero nuclear spin ($I \neq 0$) according to Ref. [Gre12].

	Abundance χ	Nuclear spin I	Hyperfine constant A
^{67}Zn	4.11 %	5/2	3.7 µeV
^{77}Se	7.58 %	1/2	33.6 µeV
^{19}F	100 %	1/2	200 µeV

microdisk lasers, based on the donor-bound exciton transitions, were demonstrated for this material system. [Paw08; Paw09].

2.1.2 Band Structure

The band structure depicts the energy levels of the electrons as a function of the modulus of the wave vector k in a crystal and therefore is of great importance for optical studies of

the electron spin coherence. Due to the principle of the conservation of momentum, only nearly vertical optical transitions from one band to another (interband transitions) are possible, since the length of the light $\boldsymbol{k}$ vector, $k = 2\pi/\lambda$, is very small compared to the size of the Brillouin zone $k \leq \pi/a_0$ [Gru16a]. Here, a_0 is the lattice constant of the crystal.

Figure 2.2 shows a schematic of the ZnSe band structure near the Γ point ($\boldsymbol{k} = 0$) at the center of the Brillouin zone. The minimum of the conduction band (CB, $j = 1/2$, $m_j = \pm 1$, black line) and the maxima of the valence bands (heavy hole (HH, $j = 3/2$, $m_j = \pm 3/2$): green line; light hole (LH, $j = 3/2$, $m_j = \pm 1/2$): orange line; split-off hole (SH, $j = 1/2\, m_j = \pm 1/2$): blue line) are located at the Γ point (direct semiconductor) [Dya84]. Here, j denotes the total angular momentum quantum number and m_j its projection. E_g is the so-called band gap, denoting the energy difference between the energy maximum of the valence band and the energy minimum of the conduction band. Note the degeneracy

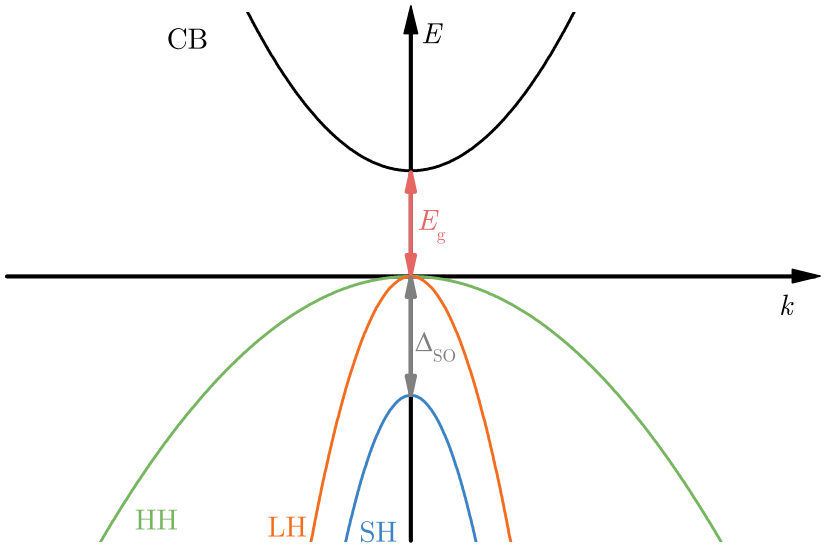

Figure 2.2 Bandstructure of ZnSe near the Γ point. HH (green line) denotes the heavy hole band, LH (orange line) the light hole band, SH (blue line) the split-off hole and CB the conduction band band. E_g is the band gap separating the CB from the valence bands (HH and LH), where the third valence band, the SH band is split-off from the other two due to spin-orbit interaction with the LH band (energy difference Δ_SO, marked by the gray arrow). In analogy to Ref. [Dya84].

of the HH and LH band at the Γ point. The schematic in Fig. 2.2 is based on the spherical approximation [Dya84]. It is valid for sufficiently small k, at which the warping of the energy surfaces of the HH and LH band, exhibiting actually cubic symmetry, can be neglected. In this approximation, the energies of the different bands are given by the following equations for the conduction band

$$E_\mathrm{CB} = E_\mathrm{g} + \frac{\hbar^2 k^2}{2m_\mathrm{e}^*}, \tag{2.1}$$

the HH band

$$E_{\mathrm{HH}} = \frac{\hbar^2 k^2}{2m^*_{\mathrm{HH}}}, \tag{2.2}$$

and the LH band

$$E_{\mathrm{LH}} = \frac{\hbar^2 k^2}{2m^*_{\mathrm{LH}}}. \tag{2.3}$$

Here, $E_{\mathrm{g}} = 2.82\,\mathrm{eV}$ [Paw11] denotes the band gap at a temperature $T = 2\,\mathrm{K}$, k the modulus of the $\boldsymbol{k}$ vector, $m^*_{\mathrm{e}} = 0.145 m_{\mathrm{e}}$ [Gre12] the effective electron mass (CB), $m^*_{\mathrm{HH}} = 0.96 m_{\mathrm{e}}$ [Paw11] the effective HH mass and $m^*_{\mathrm{LH}} = 0.27 m_{\mathrm{e}}$ [Paw11] the effective LH mass. Note that the energy difference (gray arrow) between the HH or LH band and the SH band at the Γ point is denoted

$$\Delta_{\mathrm{SO}} = E_{\mathrm{HH}} - E_{\mathrm{SH}} = E_{\mathrm{LH}} - E_{\mathrm{SH}} \tag{2.4}$$

and caused by the spin-orbit interaction with the LH band. The energy of the SH cannot be described properly in the spherical approximation so that no effective mass is given for this band. The schematic, shown in Fig. 2.2, is sufficient to understand the experiments, presented in this work, but represents a very rough approximation.

A more accurate description of the band structure can be given using $\boldsymbol{k} \cdot \boldsymbol{p}$ perturbation theory ($\boldsymbol{p}$: momentum operator) [Yu96; Gru16a]: According to the Bloch theorem [Blo29] the stationary Schrödinger equation (cf. Eq. (G.1) in Ref. [Gru16a])

$$H\psi_{n\boldsymbol{k}} = \left(-\frac{\hbar^2}{2m_{\mathrm{e}}}\nabla^2 + U(\boldsymbol{r})\right)\psi_{n\boldsymbol{k}} = E_n(\boldsymbol{k})\psi_{n\boldsymbol{k}} \tag{2.5}$$

for electrons in a periodic potential $U(\boldsymbol{r}) = U(\boldsymbol{r} + \boldsymbol{R})$ has a solution of the following form

$$\psi_{n\boldsymbol{k}}(\boldsymbol{r}) = \exp(i\boldsymbol{k}\boldsymbol{r}) u_{n,\boldsymbol{k}}(\boldsymbol{r}),\ u_{n,\boldsymbol{k}}(\boldsymbol{r}) = u_{n,\boldsymbol{k}}(\boldsymbol{r} + \boldsymbol{R}). \tag{2.6}$$

Here, $\boldsymbol{R}$ denotes direct lattice vectors and n labels the eigenstate of the electron with the corresponding energy $E_n(\boldsymbol{k})$. Inserting Eq. (2.6) into Eq. (2.5) we obtain the following equation for the periodic Bloch function $u_{n,\boldsymbol{k}}(\boldsymbol{r})$

$$\left(-\frac{\hbar^2}{2m_{\mathrm{e}}}\nabla^2 + U(\boldsymbol{r}) + \frac{\hbar}{m_{\mathrm{e}}}\boldsymbol{k}\cdot\boldsymbol{p}\right) u_{n,\boldsymbol{k}}(\boldsymbol{r}) = \left(E_n(\boldsymbol{k}) - \frac{\hbar^2 k^2}{2m_{\mathrm{e}}}\right) u_{n,\boldsymbol{k}}(\boldsymbol{r}) \tag{2.7}$$

Near the Γ point, the $\boldsymbol{k} \cdot \boldsymbol{p}$ term represents only a small perturbation [Gru16a] so that we obtain the following equation for a nondegenerate (besides spin degeneracy) band up to second order in k

$$E_n(\boldsymbol{k}) = E_n(0) + \sum_{i,j=1}^{3}\left(\frac{\hbar^2}{2m_{\mathrm{e}}}\delta_{ij} + \frac{\hbar^2}{m_{\mathrm{e}}}\sum_{l\neq n}\frac{p^i_{nl}p^j_{ln}}{E_n(0) - E_j(0)}\right)k_i k_j, \tag{2.8}$$

where l runs over so-called *remote* bands and $p^i_{nl} = \langle u_{n0}|p_i|u_{l0}\rangle$ denotes the momentum matrix element.

2.1.3 Lattice Mismatch

Studying heterostructures, we must take into account that at boundaries between different compounds mechanical stress can occur due to the different lattice constants and crystal structures. The samples under study in this work are ZnSe epilayers grown on GaAs substrate (cf. Section 3.3 for details), so it is important to consider how this II-VI on III-V heteroepitaxy alters the ZnSe crystal structure and thereby changes its band structure.

The lattice mismatch between two crystals is given by the following equation [Tra97]

$$\varepsilon = \frac{a_{\mathrm{sub}} - a_{\mathrm{epi}}}{a_{\mathrm{sub}}}, \tag{2.9}$$

and with the lattice constants of GaAs $a_{\mathrm{sub}} = 5.6533\mathrm{nm}$ and ZnSe $a_{\mathrm{epi}} = 5.6686\mathrm{nm}$ [Paw11] we obtain

$$\varepsilon \approx -0.27\%.$$

The negative sign indicates that the ZnSe crystal experiences compressive strain. However, this lattice mismatch is quite small. For example, a wurtzite AlN layer (buffer layer for GaN epitaxy) grown on (001)-oriented hexagonal sapphire (α-Al_2O_3) has a lattice mismatch of $\varepsilon = 13.29\,\%$ [Yos83; Tra97]). It is possible to grow ZnSe structures, which exhibit only a small amount of compressive strain by molecular beam epitaxy on GaAs substrates. Nevertheless, this small lattice mismatch is sufficient to lift the LH and HH degeneracy at the Γ point (cf. Section 2.1.2 and Fig. 2.3(b)) in the samples under study [Gre12].

Note that the strain depends on the temperature [Tho95], i. e., it increases with increasing temperature due to the different thermal expansion coefficients of GaAs and ZnSe, which becomes important for nanostructures, e. g., micropillars: Their structural quality can decrease with the number of cooling cycles (to cryogenic temperatures) that might be necessary for the measurements.

2.2 Optical Selection Rules

Optical selection rules are important to understand how and which kind of spin polarization is induced in the studied samples. They represent the key concept necessary to understand the process of optical orientation (cf. Section 2.4). Direct transitions between different bands in a semiconductor can be described using the correspondence principle [Dya84]: A quantum transition from the initial state i to the final state f, e. g., the transition from a subband of the valence band to the conduction band at $\boldsymbol{k} = 0$, can be described by a classical dipole with the frequency $\omega_{\mathrm{if}} = (E_{\mathrm{f}} - E_{\mathrm{i}})/\hbar$. Here, E_{i} and E_{f} are the energies of the initial and final states, respectively. The amplitude of the optical transition is given by the corresponding dipole matrix element

$$M_{\mathrm{if}} = \langle \mathrm{i}|er|\mathrm{f}\rangle\,, \tag{2.10}$$

where r is the modulus of the position vector, e is the elementary charge, and er forms the dipole moment operator. Taking into account only $M_{\mathrm{if}} \neq 0$, we find that only transitions fulfilling

$$\Delta l = 1 \tag{2.11}$$

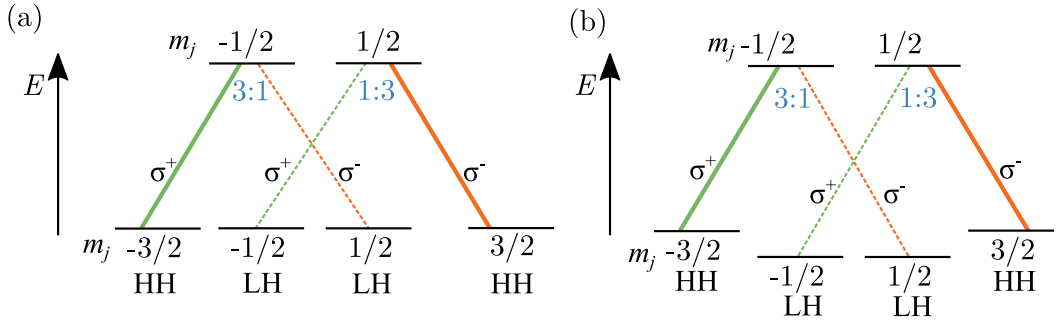

Figure 2.3 (a) Scheme of the optical selection rules of a bulk crystal with sphalerite structure. HH and LH denote the heavy hole and the light hole, respectively. The relation 3:1 (blue) state the relative intensity of the HH (thick lines) and the LH (thin, dashed lines) transitions, where right circularly polarized light (σ^+) is denoted by green lines and left circularly polarized light (σ^-) by orange lines. In analogy to Refs. [Gru16e; Dya84]). (b) Scheme of the optical selection rules of a strained crystal with sphalerite structure or a quantum well. The strain on the crystal or the confinement in the quantum well lifts the LH and HH degeneracy, so that the LH states have a lower energy than the HH states at the Γ point. In analogy to Ref. [Gru16d]).

are possible. Here, l is the quantum number of the square of the angular momentum operator $\boldsymbol{L}^2$ (azimuthal quantum number). Furthermore, according to the energy conservation principle only photons with an energy

$$E_\gamma = \hbar\omega_{\mathrm{if}} \tag{2.12}$$

can excite the corresponding single-photon transition in the semiconductor. Here, ω_{if} is the frequency of the corresponding dipole and $\hbar$ is the reduced Planck constant. A photon, as a massless particle with spin $S = 1$ (Boson, cf. Section 2.3.1), can only have a spin angular momentum $S_z = \pm\hbar = \pm\hbar m_z$, $m_z = \pm 1$ (m_z : magnetic quantum number). Combining this with the principle of angular momentum conservation, one finds that all single-photon transitions must obey

$$\Delta m_j = \pm 1, \tag{2.13}$$

where Δm_j is the difference of the projection of the total angular momentum m_j of the initial and the final state [Gru16e; Dya08]. Following these considerations and taking into account the band structure of a sphalerite crystal, one can determine the scheme of optical selection rules, presented in Fig. 2.3.

Figure 2.3(a) illustrates the selection rules for a strain-free bulk crystal, while Fig. 2.3(b) depicts the rules for a strained crystal or a quantum well. Thus, it displays the situation for the samples under study, which are strained as a result of the II-VI (ZnSe) on III-V (GaAs) heteroepitaxy. The strain on the ZnSe layer lifts the HH and LH degeneracy at the Γ point [Gre12] and thus only the scheme in Fig. 2.3(b) will be considered in the following. Figure 2.4 shows the two basic complexes of quasiparticles as they occur in experiments on coherent spin dynamics [Yak08], where only undoped and n-doped samples are considered here. These complexes can be excited optically (resonant excitation) following the rules discussed before. The generation of a spin-oriented exciton (X, see Fig. 2.4(a)) results in an electron spin coherence, which can be studied during the exciton lifetime (typically

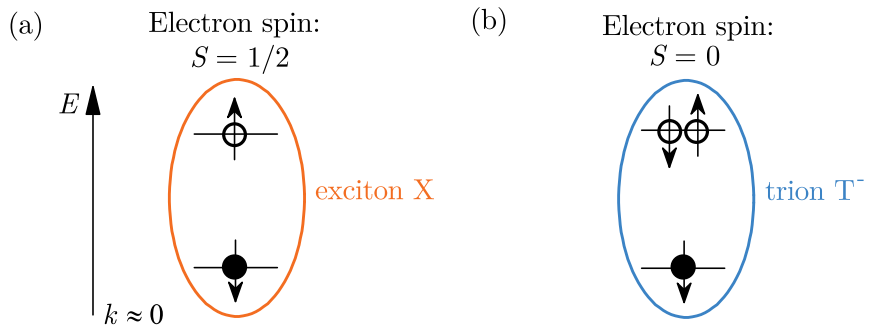

Figure 2.4 Scheme of optically excited complexes. (a) Undoped semiconductor: The optical excitation results in the formation of a bound electron-hole pair, a so-called exciton (X). (b) n-doped semiconductor: Formation of a negatively charged exciton trion (T^-) with a singlet electron spin ground state ($S = 0$). It can be described as an exciton bound to a resident electron, e. g., donor-bound electron, in the semiconductor. The open circles symbolize electrons, and the full circles symbolize holes. In analogy to Ref. [Yak08].

30 ps to 1 ns) [Yak08]. In contrast to this, the generation of a negatively charged exciton (trion (T^-), see Fig. 2.4(b)) does not result in any obvious electron spin polarization or electron spin coherence, since the state with the lowest energy (T^-) is formed by two antiparallel electron spins (singlet, $S = 0$) and one hole [Ast02; Yak08]. However, there are two ways to explain how an optical excitation, as it is illustrated in Fig. 2.4(b), can result in the generation of electron spin coherence. Furthermore, it was already demonstrated experimentally (cf. Ref. [Gre06a]). (i) In a transverse external magnetic field (Voigt geometry, B_V) a circularly polarized laser pulse creates a coherent superposition of the electron and the trion state [Gre06a; Ken06; Sha03; Yak08]. (ii) Considering the whole ensemble of initially randomly oriented resident (donor-bound) electron spins, which precess about the external field B_V one can also explain the generation of electron spin coherence: The optical excitation of trions with a finite lifetime removes a specific spin orientation from this ensemble so that, in turn, the ensemble becomes spin polarized in the opposite direction (polarization with the opposite sign) [Yak08].

2.3 Spin

Considering the electron as a charged, moving particle, one can explain the occurrence of its magnetic moment using only classical physics. However, in this way one will not obtain the correct result. Furthermore, there remain experimental observations [Ger22b; Ger22a], which can be only explained taking into account the essentially quantum mechanical nature of the electron spin, the fact that the electron has a half-integral spin $S = 1/2$ and that this is an intrinsic property of the electron.

In this section, the main interactions related to the electron spins in semiconductors are described.

2.3.1 Pauli Exclusion Principle

According to the spin-statistics theorem [Fie39; Pau40] the spin of a particle determines whether multiple particles of the same kind have a Fermi-Dirac statistic [Fer26; Dir26] or a Bose-Einstein statistic [Bos24]. The behavior of particles with integral spin is determined by the Bose-Einstein statistic, while the Fermi-Dirac statistic describes the behavior of particles with half-integral spin. The electron has a half-integral spin (see discussion before). Thus, it is a so-called "fermion," and its behavior is determined by the Fermi-Dirac statistic. The Pauli exclusion principle, in turn, restricts the number of fermions per quantum state to one [Pau25]. This restriction on the number of electrons per quantum state is of huge importance for the structure of atoms, their chemical properties and condensed matter physics in general [Dya08].

2.3.2 Exchange Interaction

Another consequence of the spin-statistics theorem is that the Coulomb interaction between electrons becomes spin-dependent: The electron wave function must be antisymmetric with respect to an interchange of the quantum-mechanically indistinguishable electrons. Thus, either the spin or the coordinate part of the wave function must be antisymmetric. If two electrons have parallel spins, the spin part is symmetric so that the coordinate part of the wave function must be antisymmetric [Dya08]. As a result, the Coulomb energy of electrons with parallel spins is reduced due to the increased spatial separation of the electrons with an antisymmetric coordinate part of the wave function. The exchange interaction explains, e. g., the occurrence of ferromagnetism.

2.3.3 Zeeman Energy

In 1896 Pieter Zeeman discovered that the spectral lines of atoms shift in an external magnetic field [Zee97]. The magnetic momenta of the electrons couple to the magnetic field $\boldsymbol{B}$. The strength of this interaction for the electron spin is given by the following equation [Kal08]

$$H_{\mathrm{Ze,e}} = \mu_{\mathrm{B}} g_{\mathrm{e}} \boldsymbol{B} \boldsymbol{S}, \tag{2.14}$$

where $\mu_{\mathrm{B}} = 5.7884 \times 10^{-5}\,\mathrm{eV\,T^{-1}} = 9.274 \times 10^{-24}\mathrm{J/T}$ is the Bohr magneton [Moh15], g_{e} is the electron g-factor (in vacuum: $g_{\mathrm{e}}/2 = 1.00115965218085$ [Odo06; Gab07]) and $\boldsymbol{B}$ is the magnetic field. Note that the value of g_{e} and its sign strongly depend on the composition of the sample and its structure.

2.3.4 Larmor Precession

In 1897 Sir Joseph Larmor [FRS97] provided an explanation for the Zeeman effect based on the rotation of ions in an external magnetic field around a center. Based on this assumption, he could explain the splitting and the polarization of spectral lines in an external magnetic field. Hence, the precession of an electron spin or a nuclear spin about the axis defined by the external magnetic field, the so-called quantization axis, has been named "Larmor precession". For these considerations, without loss of generality the magnetic field shall be aligned along the x axis. One can derive the frequency of this precession, the so-called

"Larmor frequency," from classical physics in analogy to a spinning top precessing about an axis defined by the gravitational force. However, the correct Larmor frequency for the electron can only be obtained by taking into account the inherently quantum mechanical, intrinsic angular momentum of the electron - the electron spin (cf. Sec. 2.3). It is given by [Gri12]

$$\omega_{\mathrm{L}} = \frac{\mu_{\mathrm{B}} g_{\mathrm{e}} B}{\hbar}, \tag{2.15}$$

In analogy to the electron spin, the Larmor precession frequency of the nuclear spins is given by the following equation

$$\omega_{\mathrm{N}} = \frac{\mu_{\mathrm{N}} g_{\mathrm{N}} B}{\hbar}, \tag{2.16}$$

where $\mu_{\mathrm{N}} = 3.1525 \times 10^{-8}\mathrm{eV/T} = 5.051 \times 10^{-27}\mathrm{J/T}$ is the nuclear magneton [Dya08; Moh15] and g_{N} the g factor of the nucleus [Kal08]. It is related to the gyromagnetic ratio γ, commonly used for NMR experiments, via $\gamma = \frac{\mu_{\mathrm{N}} g_{\mathrm{N}}}{\hbar}$.

2.3.5 Spin-Orbit Interaction

The spin-orbit interaction is of most importance to this thesis, since without this interaction no "optical orientation" (cf. Section 2.4) of the electron spins would be possible [Dya08]. Only the spin-orbit interaction provides a coupling between the angular momentum $\boldsymbol{L}$ and the electron spin $\boldsymbol{S}$ and thereby provides a means to change the electron spin by illumination with circularly polarized light. The spin-orbit interaction for an atom is given by the following expression [Ger10]

$$H_{\mathrm{so}} = \frac{\hbar^2}{2 m_{\mathrm{e}} c^2} \cdot \frac{1}{r} \frac{d\Phi}{dr} \boldsymbol{S} \cdot \boldsymbol{L}, \tag{2.17}$$

where $\hbar$ is the reduced Planck constant, m_{e} the free electron mass, c the speed of light in vacuum, Φ the potential of the electric field of the nucleus, and $\boldsymbol{L}$ the angular momentum of the electron. Note that the eigenstates of H_{so} and therefore of the whole system are eigenstates of the total angular momentum operator $\boldsymbol{J} = \boldsymbol{L} + \boldsymbol{S}$, but not of the angular momentum operator $\boldsymbol{L}$ or the spin angular momentum operator $\boldsymbol{S}$.

One should also stress that the form H_{so} for a semiconductor depends on its structure and the model used to describe it. In the case of a sphalerite crystal, it leads to a coupling of the crystal momentum $\boldsymbol{k}$ to the total angular momentum $\boldsymbol{J}$ of the corresponding quasiparticle (electron or hole). In $\boldsymbol{k} \cdot \boldsymbol{p}$ perturbation theory it has the following form [Yu96; Gru16a]

$$H_{\mathrm{so}} = \frac{\hbar}{4 m_{\mathrm{e}}^2 c^2} \left(\boldsymbol{\sigma} \times \nabla U \right) \boldsymbol{p}, \tag{2.18}$$

where $\boldsymbol{\sigma}$ is the vector of the Pauli matrices [Yu96]:

$$\boldsymbol{\sigma} = \begin{pmatrix} \sigma_x \\ \sigma_y \\ \sigma_z \end{pmatrix}; \; \sigma_x = \begin{pmatrix} 0 & 1 \\ 1 & 0 \end{pmatrix}; \; \sigma_y = \begin{pmatrix} 0 & -i \\ i & 0 \end{pmatrix}; \; \sigma_z = \begin{pmatrix} 1 & 0 \\ 0 & -1 \end{pmatrix} \tag{2.19}$$

Due to the spin-orbit interaction the term H_{so}, given by Eq. (2.18), must be added to Eq. (2.5) and Eq. (2.7). Furthermore, the momentum operator $\boldsymbol{p}$ in the $\boldsymbol{k} \cdot \boldsymbol{p}$ term in Eq. (2.7) is replaced by

$$\boldsymbol{\pi} = \boldsymbol{p} + \frac{\hbar}{4m_{\mathrm{e}}^2 c^2} (\boldsymbol{\sigma} \times \nabla U)\, \boldsymbol{p}. \tag{2.20}$$

2.3.6 Hyperfine Interaction

The interaction of electron spins and nuclear spins is of great importance for the spin dynamics of electrons in semiconductors. In most semiconductors the coupling of the spin systems is mediated by the Fermi contact interaction [Kal08], which is described by the following equation.

$$H_{\mathrm{hf}} = \sum_n c_n \left(\boldsymbol{S}\boldsymbol{I}_n\right). \tag{2.21}$$

Here, $\boldsymbol{S}$ is the electron spin, $\boldsymbol{I}_n$ is the nuclear spin of the nth nucleus, and the coefficient c_n is given by the following equation

$$c_n = v_0 A_n |\Psi(\boldsymbol{r}_n)|^2, \tag{2.22}$$

where v_0 is the unit cell volume, A_n the hyperfine constant of the nth nucleus, and $\Psi(\boldsymbol{r}_n)$ the envelope wave function of the electron at this nucleus. Note that the hyperfine interaction of holes is not caused by the Fermi contact interaction, since their Bloch wave function is p-type and, as a consequence, their probability density at the position of the nucleus is zero. Thus, the hyperfine interaction of nuclei and holes is $4-5$ orders of magnitude weaker than the interaction of nuclei and electrons in the conduction band [Kal08; Grn77], since the nuclear spins and the hole spins are coupled by the much weaker dipole-dipole interaction [Dya08].

2.3.7 Knight Field

An effect of the hyperfine interaction between electrons and nuclei was discovered by W. D. Knight [Kni49] in 1949. He found a shift of the nuclear magnetic resonance (NMR) frequency in metals in comparison with the NMR frequencies of the same isotopes in corresponding salts, using radio frequency (RF) techniques. This shift can be explained by the effective hyperfine field of the conduction electrons acting on the nuclei. This field results from the spin polarization (magnetization) of these electrons, which is caused by the external magnetic field used for the NMR measurement. However, exciting the sample with circularly polarized light provides another way to polarize the electron spins (see also Section 2.4) and occurs in the experiments, which are the subject of this thesis. Here, in contrast to Ref. [Kni49], a spin polarization of localized, donor-bound electrons is created [Kal08; Hei15a], whose so-called Knight field (effective hyperfine field) at the n-th nucleus is given by

$$\boldsymbol{B}_{\mathrm{K}} = -\frac{v_0 A_n}{\mu_{\mathrm{N}} g_{\mathrm{N},n}} |\Psi(\boldsymbol{r}_n)|^2 \boldsymbol{S}. \tag{2.23}$$

Here, $g_{\mathrm{N},n}$ is the g factor of the n-th nucleus. Considering only a single nucleus at a distance r from a donor site the magnitude of the Knight field is given by

$$B_{\mathrm{K}}(r) = b_{\mathrm{e}} S \exp\left(-2r/a_{\mathrm{loc}}\right), \tag{2.24}$$

where a_{loc} is the localization radius of the donor-bound electron, and the maximal Knight field amplitude b_{e} is given by the following equation

$$b_{\mathrm{e}} = -\frac{Av_0}{\gamma_{\mathrm{Se}}\hbar\pi a_{\mathrm{loc}}^3}. \tag{2.25}$$

2.3.8 Overhauser Field

An average polarization of the nuclear spins of the nuclei of the lattice, in turn, results in a magnetic (hyperfine) field acting on the electron spins, which does not depend on the degree of localization of the electrons [Kal08]. Its effect on the electron Zeeman splitting, the so-called Overhauser shift [Ber78], was discovered by A. W. Overhauser [Ove53] in 1953. Its strength is given by

$$\boldsymbol{B}_{\mathrm{N}} = \frac{v_0 \sum_n A_n \langle \boldsymbol{I}_n \rangle}{\mu_{\mathrm{B}} g_{\mathrm{e}}}. \tag{2.26}$$

2.3.9 Nuclear Spin Temperature

In 1951 R. V. Pound demonstrated that the low entropy of the nuclear spin system (NSS) can be conserved for long times under certain conditions [Pou51; Fle84]. This observation, in turn, led to the concept of a spin temperature: The state of a system in thermodynamic equilibrium can be described by its temperature. The NSS has the peculiarity that it is effectively decoupled from the lattice of the crystal: An energy transfer between the latter and the NSS occurs on the timescale given by the nuclear spin relaxation time T_1^{N}, while the NSS is driven towards thermodynamic equilibrium by spin-spin relaxation processes, whose timescale is given by the nuclear spin coherence time T_2^{N} [Fle84]. Thus, providing the relation

$$T_1^{\mathrm{N}} \gg T_2^{\mathrm{N}} \tag{2.27}$$

holds the NSS can be treated as a system in thermodynamic equilibrium and can be described by the nuclear spin temperature θ_{nuc}. For a system with nuclear spin $I = \frac{1}{2}$, as the selenium ^{77}Se spins studied in this thesis, it is given by the following equation [Fle84]

$$\frac{1}{\theta_{\mathrm{nuc}}} = \frac{2}{\mu_{\mathrm{N}}} \frac{\boldsymbol{B}\cdot\boldsymbol{S} + b_{\mathrm{e}} S^2}{\left(\boldsymbol{B} + b_{\mathrm{e}}\boldsymbol{S}\right)^2 + \xi B_{\mathrm{L}}^2}, \tag{2.28}$$

where B_{L} is the root mean square local field due to nuclear dipole-dipole interactions and $\xi \approx 2$ to 3 is a dimensionless parameter, characterizing the spin-spin interaction. Note that the terms $\propto b_{\mathrm{e}}$ allow for a cooling of the NSS even in a transverse magnetic field $\boldsymbol{B} \perp \boldsymbol{S}$ and describe the cooling in the Knight field $\boldsymbol{B}_{\mathrm{K}}$ (cf. Section 2.3.7) of the electrons [Fle84].

2.3.10 Interaction of Electron and Nuclear Spin Systems

Figure 2.5 schematically illustrates the complex interaction of the electron and nuclear spin systems under the conditions of optical orientation of the electron spin system. The electron and nuclear spin systems are coupled via the hyperfine interaction (black arrows). The excitation with circularly polarized light (blue arrow) creates an average electron spin

polarization. The Knight field $\boldsymbol{B}_\mathrm{K}$ of the spin-polarized electrons leads to a polarization of the nuclear spin system. The nuclear spins, in turn, act back on the electron spins system via the Overhauser field $\boldsymbol{B}_\mathrm{N}$. The electron spin polarization or the electron Zeeman splitting resulting from the mutual feedback of electrons and nuclei can be detected optically (light blue arrow).

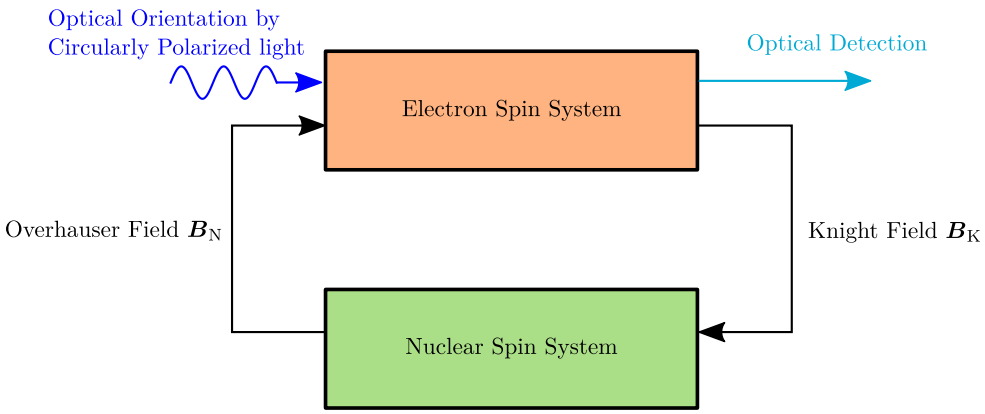

Figure 2.5 Schematic of the "internal feedback" [Fle84] in the system of electron and nuclear spins. The black arrows illustrate the coupling of these systems, which is mediated by the effective hyperfine fields, resulting from the electron ($\boldsymbol{B}_\mathrm{K}$) and nuclear spin polarization ($\boldsymbol{B}_\mathrm{N}$), respectively. The electron spin polarization is created by excitation with circularly polarized light (blue arrow), influenced by the nuclear Overhauser field $\boldsymbol{B}_\mathrm{N}$, and can be measured with different optical techniques (light blue arrow). In analogy to Ref. [Fle84].

2.4 Optical Orientation

Although all spins, including the nuclear spins, in a sample, which is exposed to a magnetic field, exhibit Larmor precession, a well-defined, spin-polarized state of the ensemble of carriers allows one to measure this Larmor precession more easily and to gain better insight into the spin dynamics of the system under study. The so-called "optical orientation" of carriers is achieved through circularly polarized optical excitation of the semiconductor [Dya84] and is the key concept for all experiments, performed for this work. Due to optical selection rules (cf. Section 2.2), the absorption of circularly polarized photons results in the creation of spin-polarized carriers. The spin of these carriers may relax with the characteristic time τ_S during the lifetime τ of these carriers [Dya84; Hei15b]. However, in n-type semiconductors the spin polarization is achieved by replacing unoriented, resident electrons with optically generated, spin-oriented electrons. Thus, the spin polarization prevails after the recombination of the photoexcited carriers. The spin relaxation time τ_S of the spin-oriented, resident electrons can exceed by far the lifetime of the photo-generated carriers, which is the case in the material system studied in this thesis (see Chap. 4 and Ref. [Hei15b]).

2.4.1 Spin Lifetime

As discussed above, the following processes determine the electron spin relaxation in n-type semiconductors: the recombination of spin-oriented, photogenerated carriers, the spin relaxation, which may occur during their lifetime, as well as the spin relaxation of spin-oriented resident electrons. Depending on the excitation density, more or less spin-oriented resident electrons and photogenerated carriers, which are spin-oriented as well, are present in the sample at the same time. Thus, the spin lifetime T_S

$$\frac{1}{T_S} = \frac{1}{\tau_S} + \frac{1}{\tau} \tag{2.29}$$

also depends on the excitation density [Dya84] via the recombination time τ of the photogenerated carriers. It is given by (see Ref. [Hei15b])

$$\tau = \frac{n_0}{G}, \tag{2.30}$$

here n_0 is the resident electron concentration and G is the rate of electron-hole generation, which influences the macroscopic spin polarization due to the recombination of electrons with photogenerated holes. Hence, one usually aims to extrapolate to zero excitation density ($G \to 0$, $1/\tau \to 0$) and in this way obtains the spin relaxation time τ_S (see Chapter 4).

2.4.2 Spin Relaxation and Spin Coherence

Longitudinal Spin Relaxation

The application of an external magnetic field $\boldsymbol{B}$ can change the spin relaxation time τ_S, and usually a different terminology in analogy to the studies on nuclear spins, preceding similar experiments on electron spins, is used. The magnetic field leads to a certain alignment of the electron and nuclear spins due to their respective Zeeman energies (cf. Section 2.3.3). This alignment occurs in the direction parallel or antiparallel to $\boldsymbol{B}$, depends on the temperature for a system in thermodynamic equilibrium, and results in a net magnetization $M \neq 0$. As a result of the electron and the nuclear Zeeman splitting, spin-flips are accompanied by an energy transfer. After a sufficiently long time the system reaches its thermodynamic equilibrium, corresponding to an equilibrium magnetization M_{eq}. The time scale, on which the system reaches the thermodynamic equilibrium, is defined as the longitudinal spin relaxation time or spin-lattice relaxation time. It will be denoted T_1 for the electron spins and T_1^{N} for the nuclear spins in the following. For nuclei, this process is approximately exponential and two cases, illustrated in Fig. 2.6(a) and (b), can be distinguished [Lev01]. Please refer to Chapter 4 for a measurement of T_1 and Chapter 6 for a measurement of T_1^{N}.

Transverse Spin Relaxation: Homogeneous Dephasing

It is important to note that the timescale given by the T_1 time is not the only important timescale for the spin dynamics. Especially regarding quantum information applications, the transverse spin relaxation time or spin coherence time, denoted T_2 (electron spins) and

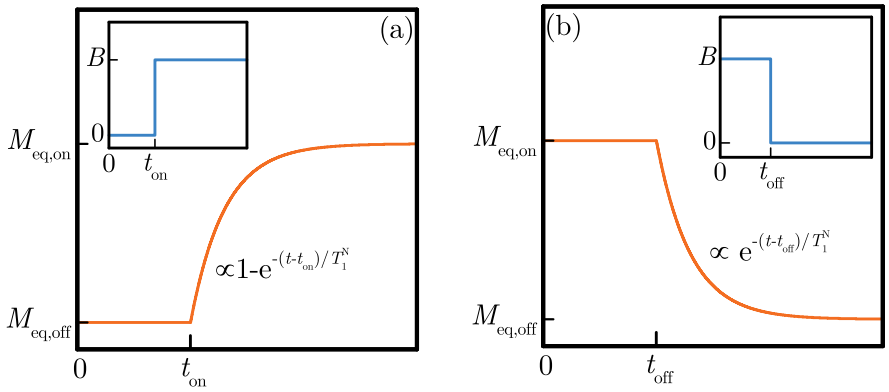

Figure 2.6 (a) Build-up of a net magnetization M_{eq} of the nuclear spins upon "switching on" the external field $\boldsymbol{B}$. (b) Decay of this magnetization M_{eq} to zero after "switching off" the external field $\boldsymbol{B}$. Both processes are characterized by the longitudinal nuclear spin relaxation time T_1^N. In analogy to [Lev01].

T_2^N (nuclear spins), is of great importance, since it limits the time a spin qubit exhibits "true" quantum behavior, e. g., superposition or entanglement, and allows one to perform operations based on quantum computing models [DiV00].

In the case of the electron spins, the transverse relaxation can be observed in experiments using the Voigt geometry, where the magnetic field $\boldsymbol{B}_V$ is applied perpendicular to the $\boldsymbol{k}$ vector of the light wave ($\boldsymbol{B}_V \perp \boldsymbol{k}$). The optical orientation (see the previous discussion) then results in a superposition of the two eigenstates spin-up $|\uparrow\rangle$ and spin-down $|\downarrow\rangle$ defined with respect to the field $\boldsymbol{B}_V$. In other words, the process of optical orientation results in a net magnetization, which is transverse to the external magnetic field $\boldsymbol{B}_V$. Thus, the spins exhibit Larmor precession (cf. Section 2.3.4) about the axis given by $\boldsymbol{B}_V$ (in the plane $\perp \boldsymbol{B}_V$). The transverse spin relaxation time or spin coherence time T_2 determines the timescale, on which the phase of the precession of the transverse spin components is lost [Yak08]. Irreversible processes of different physical origin lead to the dephasing or decoherence of a single spin or an ensemble of spins for which an average T_2 time can be defined. It is important to note that in contrast to the longitudinal relaxation the transverse relaxation is not accompanied by an energy transfer so that any scattering event can cause spin decoherence [Yak08].

The T_2 time is difficult to obtain from measurements on an ensemble of electron spins due to the contributions of inhomogeneous dephasing to the dephasing of the polarization of the ensemble (cf. the following discussion). One can use an optical realization of the Hahn echo sequence [Hah50] or rely on the phenomenon of spin mode-locking [Gre06b]. Furthermore, one could obtain it from measurements on a single spin.

In the case of the nuclear spins the definition of the spin coherence time T_2^N is the same as of the electron spin coherence time T_2. It can be obtained from measurements on an ensemble of nuclear spins using the Hahn echo sequence, but it is not feasible to measure the T_2^N time of a single nuclear spin using RF techniques. Please refer also to Section 2.3.9 for the implications of T_2^N and T_1^N for the spin temperature approach. The decay with

T_2^{N} can be explained by microscopic, fluctuating magnetic fields acting on the nuclear spins [Lev01].

Transverse Spin Relaxation: Inhomogeneous Spin Dephasing

As stated before, the measurement of T_2 on an ensemble electron of spins requires special experimental techniques or conditions [Hah50; Gre06b]. The macroscopic coherence, studied in this case, does not decrease with T_2, but with the considerably shorter inhomogeneous spin dephasing time T_2^* [Yak08]. It is given by the following equation

$$\frac{1}{T_2^*} = \frac{1}{T_2} + \frac{1}{T_2^{\mathrm{inh}}}. \tag{2.31}$$

In addition to the irreversible processes, leading to a decay of the transverse spin components with T_2, the decay of the macroscopic coherence is accelerated by a reversible phase shift between different spins of the ensemble due to a dispersion of precession frequencies [Yak08]. This phase shift occurs with the inhomogeneous spin relaxation time T_2^{inh}. Two different mechanisms, causing the phase shift, can be distinguished: (i) At zero and very weak magnetic fields T_2^{inh} is determined by fluctuating nuclear fields $\boldsymbol{B}_{\mathrm{N}}$, which lead to Larmor precession about $\boldsymbol{B}_{\mathrm{N}}$ and thereby to a frequency dispersion of the electron spins. (ii) At strong magnetic fields, in turn, properties intrinsic to the sample, e. g., differences between donor sites in bulk semiconductors, monolayer fluctuations in semiconductor quantum wells (QWs) and size and shape dispersion of quantum dots (QDs) lead to a spread of g factors and thus to a dispersion of precession frequencies. The g factor spread leads to a $1/B$ dependence of T_2^{inh} and therefore to a decrease of T_2^* with increasing magnetic field [Sch11].

Similar to T_2^* of the electron spins one can define the inhomogeneous nuclear spin dephasing time $T_2^{*,\mathrm{N}}$, which is given by the following equation

$$\frac{1}{T_2^{*,\mathrm{N}}} = \frac{1}{T_2^{\mathrm{N}}} + \frac{1}{T_2^{\mathrm{N,inh}}}. \tag{2.32}$$

Here, the Larmor frequency dispersion, leading to a phase difference between different spins in the ensemble, is caused by the variation of the magnetic field, either due to the variation of the macroscopic magnetic field over the sample volume [Lev01] or effective, static fields in the sample, e. g., the Knight field B_{K} of the electrons. This phase difference occurs with the time $T_2^{\mathrm{N,inh}}$.

2.4.3 Hanle Effect

The Hanle effect denotes the depolarization of the electron spin by a transverse magnetic field [Dya08]. It is important, since it can be used to measure the electron spin lifetime T_S as an alternative to the spin inertia effect, presented in Chapter 4 of this work. The Hanle effect was first observed by Wood and Ellett in 1924 [Woo24; Dya08] as a dependence of the degree of polarization of mercury vapor fluorescence on the orientation of the direction of observation with respect to the magnetic field of the earth. W. Hanle studied it in more detail and provided the theoretical model to describe the underlying physics [Han24]: The

excitation with circularly polarized light polarizes the spins of the carriers along the light wave $\boldsymbol{k}$ vector, while a transverse, external magnetic field $\boldsymbol{B}_\mathrm{V}$ leads to Larmor precession of the spins about the axis defined by this field. The stronger the field, the more rotations the spins perform during their lifetime T_S. Thus, in a strong magnetic field $T_S \gg \frac{1}{\omega_\mathrm{L}}$ the average spin polarization along the $\boldsymbol{k}$ is reduced due to these rotations. The so-called Hanle curve describes this behavior [Dya84; Hei15b]

$$S_z(B_\mathrm{V}) = \frac{S_z(0)}{1 + (B_\mathrm{V}/B_{1/2})^2}. \tag{2.33}$$

The half width of this Lorentz curve is given by

$$B_{1/2} = \frac{\hbar}{g_\mathrm{e}\mu_\mathrm{B}T_S}. \tag{2.34}$$

One can obtain the Hanle curve by measuring the degree of circular polarization ρ_c of the photoluminescence (PL, cf. also Section 3.2.1) as a function of the magnetic field B_V [Dya84]. Alternatively, it can be determined from a measurement of the Kerr rotation (KR) angle θ_KR (cf. Section 2.4.4), e. g., from a time-resolved Kerr rotation experiment (cf. Section 3.2.2), in dependence on B_V. Commonly, a continuous-wave (CW) excitation is used to excite the PL or measure the Kerr rotation, resulting from the CW excitation. However, Astakhov *et al.* determined similar spin relaxation times τ_S of resident electrons in CdTe/CdMgTe QWs from a KR measurement using a pulsed excitation and one using a CW excitation [Ast08b].

2.4.4 Kerr Rotation

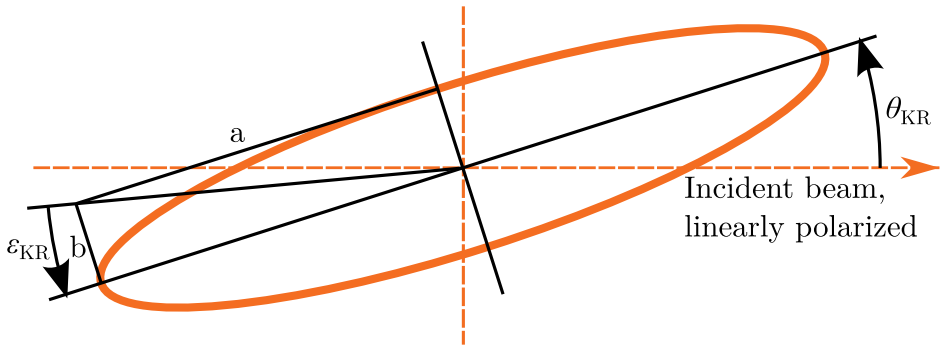

Figure 2.7 Rotation of the polarization axis of a linearly polarized beam (dashed orange arrow) about the angle θ_KR. The complex Kerr rotation also leads to an elliptic shape (ellipticity ε_KR) of the polarization (orange ellipsis). Here, a and b denote the semiaxes of the polarization ellipsis. Modified from Ref. [Mur11].

All measurements of the electron spin dynamics presented in this thesis rely on the magneto-optical Kerr effect [Jah00], which allows one to measure the magnetization $\boldsymbol{M}$of a medium by the rotation of the polarization plane of light reflected from the surface of

this medium. The complex magneto-optical rotation $\tilde{\theta}$ of the reflected light can be defined as a superposition of the Kerr rotation θ_{KR} and the Kerr ellipticity $\varepsilon_{\mathrm{KR}}$

$$\tilde{\theta} = \theta_{\mathrm{KR}} + i\varepsilon_{\mathrm{KR}} \tag{2.35}$$

and we find the following relation to the magnetization $\boldsymbol{M}$

$$\tilde{\theta} = \tilde{F}M, \tag{2.36}$$

where $\tilde{F}$ is the generalized Fourier coefficient determined by the sample properties and the experimental setup [Koo03; Koo07].

Figure 2.7 illustrates the complex Kerr rotation of an initially linearly polarized beam (dashed orange arrow). As a result of the optical Kerr effect, the polarization has now an elliptic shape (orange ellipsis), and its axis is rotated about the angle θ_{KR}.

The magnetization, causing the complex Kerr rotation, can result from the application of external magnetic field $\boldsymbol{B}$, a non-vanishing spin polarization $\boldsymbol{S} \neq 0$ or both. Thus, we can determine changes of the average spin polarization by measuring, e. g., the Kerr rotation angle θ_{KR}.

3 Experimental Details

This chapter provides an overview of the basic principles of the experimental setup, the function and interplay of the equipment, the experimental methods and the samples under study.

3.1 Equipment and Setup

3.1.1 Optical Cryostat

Since all measurements required cryogenic sample temperatures ($T < 45\,\mathrm{K}$) and most of them also an external magnetic field, they were conducted with the sample placed in an optical cryostat - the `Oxford Instruments 3D Vector Magnet`.

To achieve cryogenic temperatures a sufficient insulation from the environment at a temperature of $T \approx 293\,\mathrm{K}$ is necessary. To that end, the sample compartment, called variable temperature insert (VTI) and consisting mainly of a long cylindrical tube with a diameter of about 25 mm and four windows near the bottom, is "suspended" (mounted with as less mechanical contact as possible) in a vacuum chamber. This chamber is evacuated to pressures on the order of $1 \times 10^{-6}\,\mathrm{mbar}$. As a result, the thermal conductivity by convection is reduced to a minimum, and the remaining coupling to the environment would occur mainly by thermal radiation. The power P of the thermal radiation of a black body is given by the Stefan–Boltzmann law [Ste79; Bol84]

$$P = \sigma A T^4, \tag{3.1}$$

where A is the area of the black body and $\sigma = 5.670\,367 \times 10^{-8}\,\mathrm{Wm^{-2}K^{-4}}$ [Moh15] is the Stefan-Boltzmann constant. Thus, the contribution of thermal radiation to the heat exchange between two "black bodies" strongly depends on the temperature difference between them. Therefore, the cryostat employs two coolants stored in different compartments "suspended" in the vacuum volume. The one closest to the enclosure of the cryostat, containing the outer, so-called room-temperature windows, is filled with liquid nitrogen (boiling temperature: 77 K) and shields the inner compartment, as well as the VTI by a metal tube, which is in thermal contact with the nitrogen volume. This construction drastically reduces the evaporation of the liquid helium stored in the inner volume, since liquid helium has a boiling temperature of 4.2 K and a much lower heat capacity than liquid nitrogen. The helium volume surrounds the VTI so that the metal tube at liquid nitrogen temperature around the VTI serves mainly as a shield for the helium volume. This further reduces the evaporation of helium, since the VTI can be heated up to temperatures of up to 300 K and has a relatively large thermal contact to the environment due to the sample holder and the thermal radiation through the windows. A metal enclosure, the so-called nitrogen shield, is mounted to the bottom of the nitrogen volume and surrounds

the bottom part of the helium volume, containing the split coil magnets (cf. discussion in the following), and the bottom part of the VTI. As the VTI, the nitrogen shield has four windows, facing the VTI and room-temperature windows. Due to thermal contact to the nitrogen shield, these so-called nitrogen windows are at a temperature close to the boiling point of liquid nitrogen and therefore provide an additional shield of the VTI and the helium volume against thermal radiation.

A thin capillary tube connects the VTI to the helium volume. The flow of liquid helium through this capillary tube can be regulated by an electrically controlled needle valve to cool the sample either by a controlled gas flow or by immersion in liquid helium. A second means to regulate the sample and VTI temperature is provided by an electrical heating with an ohmic resistor, located in the bottom part of the VTI, which is formed by a massive copper cylinder. Furthermore, this cylinder contains a calibrated semiconductor resistor, which allows for a measurement of the temperature of this cylinder.

The motor of the needle valve, the electric heating and the semiconductor resistor at the bottom of the VTI, as well as the optional semiconductor resistor at the sample holder, are connected to an electronic temperature controller. The device features a controller circuit that is able to stabilize the temperature at the semiconductor resistor at the bottom of the VTI. The available temperatures range from about 5 K to 300 K without pumping on the VTI. Setting temperatures below 5 K can lead to a flooding of the VTI with boiling helium, which hinders the optical access to the sample due to significantly increased scattering. However, pumping on the liquid helium induces a phase transition to the superfluid phase (Helium II, cf. Refs. [Kap38; All38]) and one can reach a temperature of about 1.8 K. The biggest advantage of the superfluid phase is its very low viscosity and, in turn, very high thermal conductivity, which prevents the formation of bubbles.

It is not recommended to heat up the VTI to temperatures exceeding 285 K and one should cool down from elevated temperatures > 200 K at reduced speed (needle valve not completely opened), since the windows of the VTI are mounted and sealed using two-component adhesive and leaks of this sealing can be caused by thermal stress. Note that the temperature in the vicinity of the sample (sensor at the sample holder) and at the bottom of the VTI can deviate by about 8 K to 10 K.

The helium volume not only provides the coolant for the VTI, but contains three superconducting split coil solenoids that are made from niobium-titanium. They allow us to apply magnetic fields of up to $B = 3$ T in any direction of space and are maintained in a superconducting state by immersion in liquid helium. Each coil is operated by a separate power supply labeled according to the alignment of the respective pair of split coils: “X” (perpendicular to the optical axis, but parallel to the surface of the optical table, Voigt geometry, field B_V, cf. orange ellipses in Fig. 3.5), “Y” (parallel to the optical axis and to the surface of the table, Faraday geometry, field B_F, cf. blue ellipses in Fig. 3.5) and “Z” (perpendicular to the optical axis and the surface of the table). Note that it was necessary to compensate residual fields along the directions defined by the other, not magnetized split coils. Especially, if we performed measurements at relatively low magnetic fields on the order of a few tens of mT. We observe that ramping up the field along a coil to more than 200 mT magnetizes parts of the cryostat and causes hysteresis effects. To compensate these fields, we performed either an RSA measurement (“X” or “Z” axis) or a polarization recovery measurement (“Y” axis) along the axis, which should be compensated.

The measurement yielded the zero position, which we installed on the power supply to compensate the residual field along the corresponding axis.

3.1.2 Sample Holder

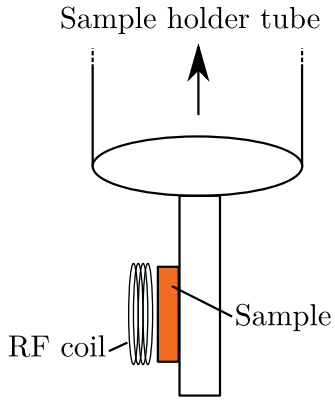

Figure 3.1 Schematic of the bottom part of the sample holder to illustrate the mounting of the sample and the position and alignment of the RF coil.

The sample holder consists of a long tube that is inserted into the VTI. It allows us to adjust the vertical position of the sample in the VTI and its angle with respect to the optical axis. The sample holder without a radio frequency (RF) coil was equipped with two hall sensors (first: Faraday geometry ("Y" axis); second: Voigt geometry ("X" axis)) to measure the respective components of the magnetic field and one semiconductor resistor to measure the temperature in the vicinity of the samples. The sample holder with an RF coil was equipped with one hall sensor (Voigt geometry ("X" axis)).

Figure 3.1 shows a schematic of the bottom part of the sample holder, illustrating the mounting of the sample and the position of the RF coil. Here, it is important that the RF coil was placed directly at the sample surface and the RF signal from the arbitrary function generator (AFG, `Tektronix AFG 3022`) was amplified by a class AB RF amplifier with complementary transistor output stages (cf. Fig. 3.2) for all RF measurements presented in Chapter 6. Otherwise, the coil used for these measurements could not provide the necessary RF power for the experiments. In contrast to this, the measurements, presented in Chapter 5, were performed without additional amplification of the RF signals from the AFG.

3.1.3 Electro-Optical Modulators

The linear electro-optic effect or *Pockels effect* [Pas17], discovered by Pockels [Poc94] in 1894, is the change of the refractive index by an externally applied, static electric field. This effect creates an additional birefringence in an optically uniaxial nonlinear crystal, e. g., a potassium dihydrogen phosphate (KDP) crystal [Dem11]. This birefringence depends on the orientation of the external, static electric field $\boldsymbol{E}_{\text{stat}}$ with respect to the optical axis so that one distinguishes the transverse ($\boldsymbol{k} \perp \boldsymbol{E}_{\text{stat}}$) and the longitudinal electro-optic effect

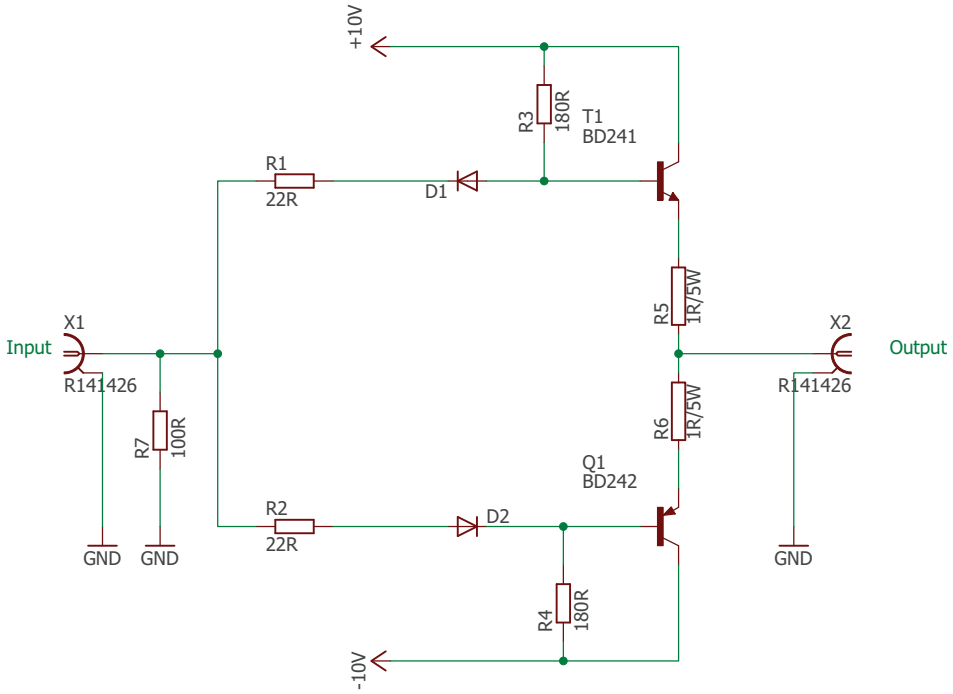

Figure 3.2 Circuit diagram of the Class AB RF amplifier, used for the RF measurements presented in Chapter 6. Depending on the power supplies used for the transistors the maximum power is $P \leq 40\,\mathrm{W}$. Modified from Ref. [Stö17].

($\boldsymbol{k} \parallel \boldsymbol{E}_{\mathrm{stat}}$) [Bil49; Zwi44]. These effects are used in so-called *Pockels cells* in electro-optical modulators (EOMs) to modulate the phase, the polarization or the intensity of laser beams. Furthermore, EOMs can be used as intensity modulators in actively mode-locked lasers.

An EOM provided the modulation of the helicity of the pump beam for the experiments in this work, where two different EOMs were used. These required slightly different setups.

(i) The `LINOS LM 0202 5W P` acts as a switching half-wave plate, which can rotate the polarization plane of the linearly polarized (Glan-Taylor prism (Glan)) pump pulses up to 90° depending on the voltage applied to its crystal by the digital high voltage amplifier (`LINOS DIV-20`). The digital high voltage amplifier, in turn, is controlled by the AFG (`Tektronix AFG 3022`) connected to its transistor-transistor logic (TTL) input. When a "1" (about 4 V to 5 V) is applied to this input, the voltage adjusted at the "high" setting of the amplifier is applied to the EOM and leads to a rotation of the polarization plane of 90°, while the "offset" voltage is applied for a "0" (0 V to 1 V) at this input and the polarization plane is not rotated. Thus, the EOM switches the pump polarization between two perpendicular linear polarizations. In combination with the quarter-wave plate this results in a switching between a left- (σ^-) and a right-circularly (σ^+) polarized laser beam.

(ii) The `Polytec 350-105 Laser Modulator`, in turn, acts as a switching quarter-wave plate, which can "convert" the linearly polarized laser beam into a circularly polarized one. It is also provided with a dedicated high voltage amplifier (`Modell 25D controller`) and can be controlled with a TTL signal from the AFG. It features a "bias voltage adjustment"

to set the optical operating point of the system, e. g., set one circular polarization at a logical "0"(0 V to 1 V) at the TTL input, and a "drive voltage adjustment" to set the additional voltage applied at a logical "1" (about 4 V to 5 V). The "drive voltage" is adjusted so that the EOM provides the circular polarization with the opposite sign, compared to the circular polarization at the "bias voltage".

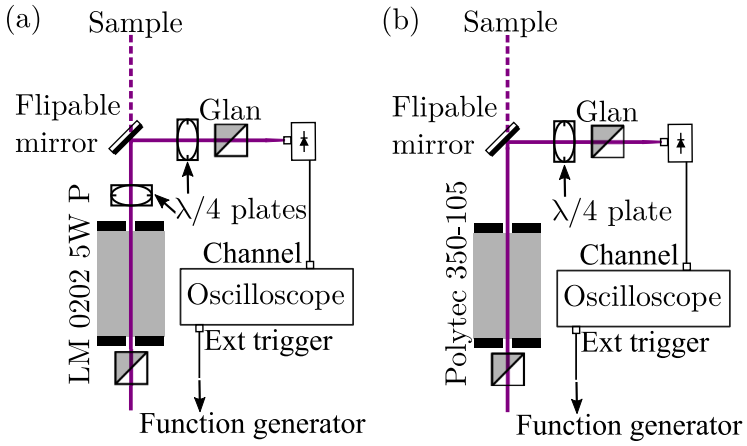

Figure 3.3 Scheme to test the polarization achieved with the EOMs. The optical elements were placed in the path of the pump beam shortly before the cryostat. Only one focusing lens followed after the flipable mirror. The purple lines denote the pump beam. After passing through a Glan-Taylor prism, which ensures a clean linear polarization, and the (a): `LINOS LM 0202 5W P` and a $\lambda/4$ plate or the (b): `Polytec 350-105 Laser Modulator` its polarization is analyzed using a $\lambda/4$ plate, a Glan and a fast photodiode (`Thorlabs DET10A/M`), connected to an oscilloscope. The diode was terminated with a 50 Ω load to achieve fast operation.

Figure 3.3 illustrates the schemes to allow for a helicity modulation of the pump beam (purple line) using either the `LINOS LM 0202 5W P` (cf. Fig. 3.3(a)) or the `Polytec 350-105 Laser Modulator` (cf. Fig. 3.3(b)) and to test the achieved degree of circular polarization. To this end a flipable mirror was put in the path of the pump beam so that its polarization could be analyzed using quarter-wave plate and a Glan. A fast photodiode (`Thorlabs DET10A/M`) connected to an oscilloscope allowed us to determine the polarization for a "0" or "1" TTL signal and check the degree of circular polarization. Here, it is important to note that a 50 Ω resistor (termination) was required to achieve the fast rise time of the diode of about 1 ns.

3.1.4 Mode-locked Lasers

Compared to continuous-wave (CW) light sources mode-locked lasers are more suitable to perform time-resolved measurements and can measure coherent spin dynamics directly. Instead of a standing wave in the resonator, a light pulse travels around the resonator, and at certain times short, but intense light pulses are emitted from the laser system. The concept of a mode-locked laser was described by Lamb [Lam64] in 1964 and realized experimentally the same year by Hargrove *et al.* [Har64].

The laser system, used for the experiments in this work, was a `Coherent Mira 900-D` titan:sapphire laser or alternatively its high power variant `Coherent Mira 900-D HP`. Except for the tuning range of 700 nm to 1000 nm (HP: 700 nm to 980 nm) and the average output power $P \approx 1\,\mathrm{W}$ (HP: $P > 2.8\,\mathrm{W}$) the specifications of both lasers are identical: They emit pulses of width of about 2 ps at a repetition frequency of $f_\mathrm{R} = 75.75\,\mathrm{MHz}$, which corresponds to a repetition period of $T_\mathrm{R} = 13.2\,\mathrm{ns}$. Both lasers are pumped by a frequency-doubled, diode-pumped Nd:YVO_4 solid state laser (`Coherent VERDI V-18`, maximum power $P = 18\,\mathrm{W}$).

3.1.5 Second Harmonic Generation

To obtain the necessary energies to study the spin coherence in the ZnSe epilayers, we need to double the frequency ω of the Ti:sapphire laser (cf. Section 3.1.4) using a beta barium borate (BBO) crystal [Fra61]. Thus, instead of being restricted to the titan:sapphire energy range from about 1.25 eV to 1.7 eV, we could also work at photon energies from 2.5 eV to 3.4 eV [Hei15a], which was necessary to study the electron spin coherence in the ZnSe epilayers.

In the experiments, presented in this thesis, the crystal was located in a dedicated device (`Photop TP-2000B`), which contained a half-wave plate to adjust the polarization and focusing optics. Furthermore, it allowed us to adjust the angle of the crystal with respect to the $\boldsymbol{k}$ vector of the fundamental laser beam with the frequency ω. Thereby, we achieved the phase matching condition and increased the efficiency of the conversion of two photons with the frequency ω to one photon with the frequency 2ω.

3.2 Experimental Techniques

3.2.1 Photoluminescence Spectroscopy

A photoluminescence spectrum allows us to obtain information on the electron states of the sample. A light source (here a CW laser) provides photons whose energy E_exc must exceed the band gap E_g of the semiconductor or the band gap of the barrier material for heterostructures, e. g., quantum wells (QWs) or quantum dots (QDs). Upon absorption by the material, a photon excites an electron from the valence band (VB) into the conduction band (CB), while a vacancy in the valence band, called hole, remains (cf. Section 2.1.2).

Due to the condition $E_\mathrm{exc} > E_\mathrm{g}$ the excited electrons have an energy, which exceeds the minimum energy of the CB. Thus, an electron can either relax non-radiatively to an energetically lower state up to the minimum of the CB and then recombine with a hole under emission of a photon or immediately recombine radiatively with a hole. In any case, the energy of the emitted photon is equal to the energy difference between the hole and the electron state due to the conservation of energy. As a result, a PL spectrum consists of a series of peaks whose relative amplitude is proportional to the relative oscillator strength of the underlying transitions and the occupation of the corresponding electron states (cf. actual PL spectra of the studied samples in Section 3.3). Figure 3.4 shows the scheme used for the PL measurements. A CW diode laser (`Coherent Cube, Part No. 1069413`) provided an excitation of the sample with a photon energy $E_\mathrm{exc} = 3.05\,\mathrm{eV}$. A cut mirror

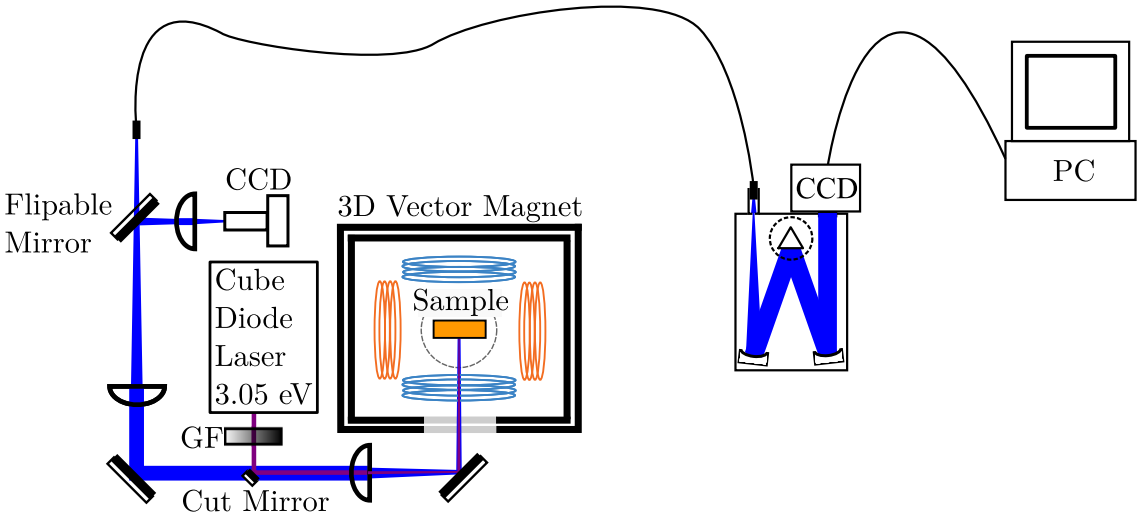

Figure 3.4 Scheme used for PL measurements. The continuous-wave (CW) diode laser provided the optical excitation of the studied samples, which were mounted in the optical cryostat, described before. The laser beam was redirected by a cut mirror, a further mirror and then focused onto the sample surface. A system of lenses and mirrors collected the resulting PL and coupled it into an optical fiber. This fiber, in turn, was connected to the entrance slit of the imaging spectrometer. The flippable mirror in front of the fiber entrance allowed us to either image the sample surface on the auxiliary charge-coupled device (CCD) camera or measure the PL spectrum with the spectrometer.

coupled its beam into the optical path, used for the collection of the PL and for imaging the sample on the auxiliary CCD camera [Boy70]. The same lens, which collected the PL, focused the laser beam onto the sample surface. This optical excitation resulted in the emission of PL from the sample provided it fulfilled the condition $E_{\mathrm{exc}} > E_{\mathrm{g}}$.

This PL was collected and coupled into the fiber by the assembly of mirrors and lenses adjusted for this purpose. The output of the fiber was connected to the entrance slit of the imaging spectrometer. The spectrometer, an `Acton SpectraPro 2500`, was an imaging Czerny-Turner monochromator [Cze30] with a focal length of 0.5 m and three different diffraction gratings (1. 600 gr/mm blazed at 500 nm, 2. 1200 gr/mm and 3. 2400 gr/mm holographic-visible).

In a Czerny-Turner monochromator, the light from the entrance slit falls upon the first of two aspherical mirrors so that a collimated beam is reflected onto the diffraction grating mounted on a motorized turret. This turret allows us to adjust the center wavelength and switch between the different gratings on the turret. The grating diffracts the light from the first mirror onto the second aspherical mirror (cf. schematic in Fig. 3.4), which collimates it and reflects it onto the CCD chip.

The `Princeton Instruments PIXIS: 256F-OE CCD` featured a 1024×256 pixels UV-enhanced silicon, Peltier cooled photodiode matrix (26.6 mm $\times$ 6.7 mm) that was read-out by an integrated controller.

3.2.2 Time-resolved Kerr Rotation Technique

Mode-locked lasers providing ultra-short laser pulses offer the advantage of time-resolved measurements. One of the most common time-resolved spectroscopy techniques is the pump-probe technique. The basic principle of this technique is to excite or to prepare the system under study in a specific state with the pump pulse and then observe the response or evolution of the system with the probe pulse.

The time-resolved Kerr rotation (TRKR) technique represents a realization of this technique, which is especially suitable to study the electron spin dynamics and based on the magneto-optical Kerr effect (cf. Section 2.4.4). Figure 3.5 shows a schematic of the employed TRKR setup. The frequency of the laser pulses, emitted by the mode-locked titan:sapphire laser, was doubled by the SHG box and then they were divided into a pump and a probe beam by a beam splitter (BS). The probe beam was directed to the sample on a fixed optical path, while the pump beam was passed through a mechanical delay line, which allowed us to vary the temporal distance between the arrival of the pump and probe pulses at the sample.

The circularly polarized pump pulses create a macroscopic spin polarization of the ensemble of donor-bound electron spins. The helicity of the pump was modulated by an EOM with the modulation frequency f_m. The pump helicity modulation frequency f_m was varied from 10 kHz to 1000 kHz. The macroscopic spin polarization, in turn, leads to a rotation of the polarization plane (see Section 2.4.4) of the reflected, initially linearly polarized probe pulses, which was measured with a balanced photodetector (`New Focus NFI-2107-FS-M`, bandwidth 10 MHz) in combination with a half-wave plate and a Wollaston prism. This detector was connected to either the `Stanford Research Systems SR 844` or the `Signal Recovery 7265` lock-in amplifier, depending on the modulation frequency: The `Stanford Research Systems SR 844` can be used for modulation frequencies from 25 kHz to 200 MHz, while the `Signal Recovery 7265` works at modulation frequencies from 0.1 Hz to 250 kHz. Please note that the data obtained from measurements with different lock-in amplifiers were normalized to each other by performing a measurement at the same conditions at a modulation frequency, which fell in the range of both lock-ins, e. g., 200 kHz or 250 kHz, for two times using first one and then the other lock-in. This approach was used for the measurements presented in Chapter 4.

For the measurements, presented in Chapters 5 and 6, a different lock-in amplifier was used: The `Zurich Instruments HF2LI` can be used at modulation frequencies f_m from DC to 50 MHz so that it was not necessary to switch the lock-in to change f_m. However, please note that frequencies exceeding 2 MHz can only be demodulated, if the internal reference of the lock-in amplifier is used for the modulation.

The high repetition frequency $f_\mathrm{R} = 75.75\,\mathrm{MHz}$ of the mode-locked lasers, used in this thesis, in combination with lock-in amplifiers greatly improved the signal-to-noise ratio, since we averaged over a few hundred laser pulses in one helicity modulation cycle. The signal from one helicity modulation cycle, in turn, was averaged again several thousand times by the lock-in amplifier, e. g., 5000 times at a helicity modulation frequency of $f_\mathrm{m} = 50\,\mathrm{kHz}$ and a time constant (TC) of 100 ms.

Figure 3.6 shows a TRKR measurement for sample #1 at a modulation frequency $f_\mathrm{m} = 100\,\mathrm{kHz}$ at zero magnetic field. The peak at $\Delta t = 0$ results from the simultaneous

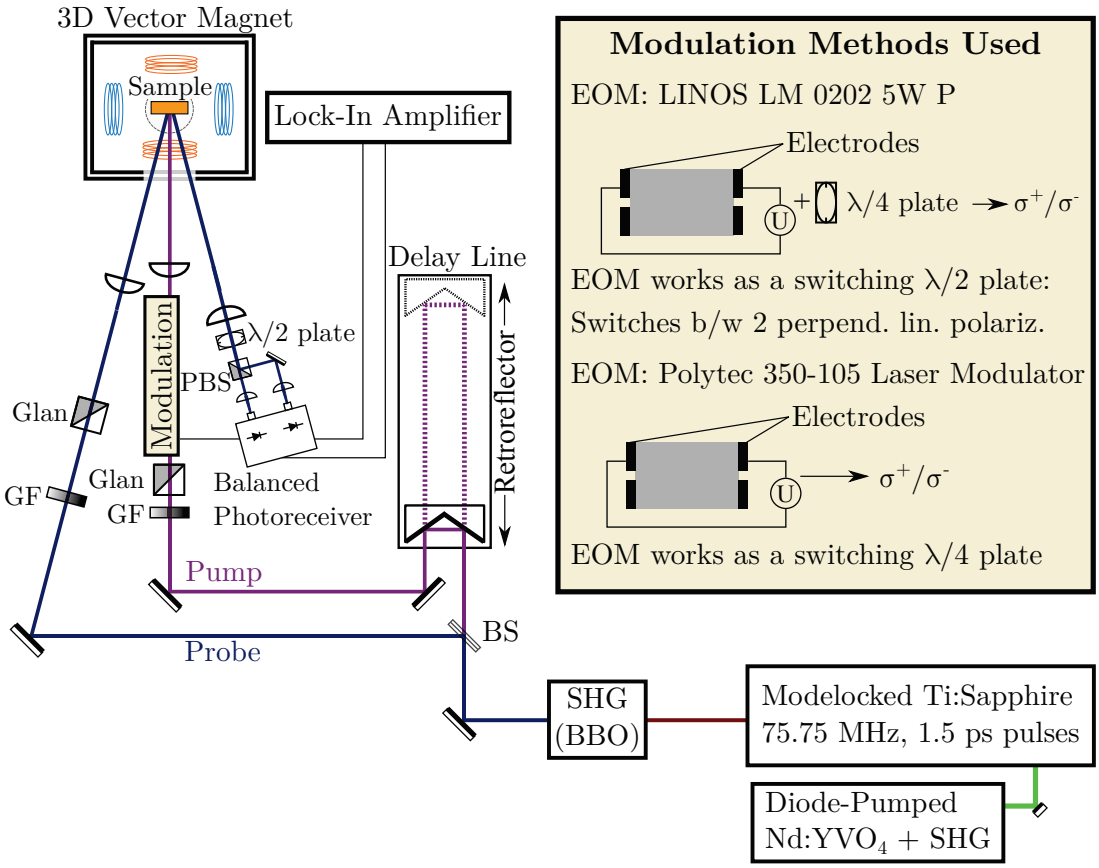

Figure 3.5 Schematic of the TRKR setup. A degenerate pump-probe configuration is used for most of the experiments, nevertheless, the pump (dark violet) and the probe (blue) are drawn in different colors to enable good differentiation between both beams. The optical components are partly denoted by the following abbreviations: "BBO" (beta barium borate), "BS" (beam splitter), "GF" (neutral gray filter, neutral density filter), "Glan" (Glan-Taylor prism), "$\lambda/2$ plate" (half-wave plate), "PBS" (polarizing beam splitter, drawn schematically, a Wollaston prism with a beam separation of 20° is used), "$\lambda/4$ plate" (quarter-wave plate), "SHG" (second harmonic generation). The accumulation of ellipses in the cryostat schematically show the arrangement of the split coils, where the series of blue ellipses illustrate the split coil for the magnetic field in Voigt geometry (B_V) and the orange ellipses the split coil for the magnetic field in Faraday geometry (B_F).

arrival of the pump and the probe pulse. Then the KR signal decays, as the spin polarization decreases. However, the nonzero KR signal at negative time delay indicates that the spin polarization induced by the pump pulses decays on a timescale that exceeded the laser repetition period $T_\mathrm{R} = 13.2\,\mathrm{ns}$. This allowed us to measure the spin polarization shortly before the arrival of the next pump pulse, as it was used for the PR and RSA measurements. The orange arrow in Fig. 3.6 shows the exact probe pulse position at $\Delta t = -20\,\mathrm{ps}$ used for these measurements.

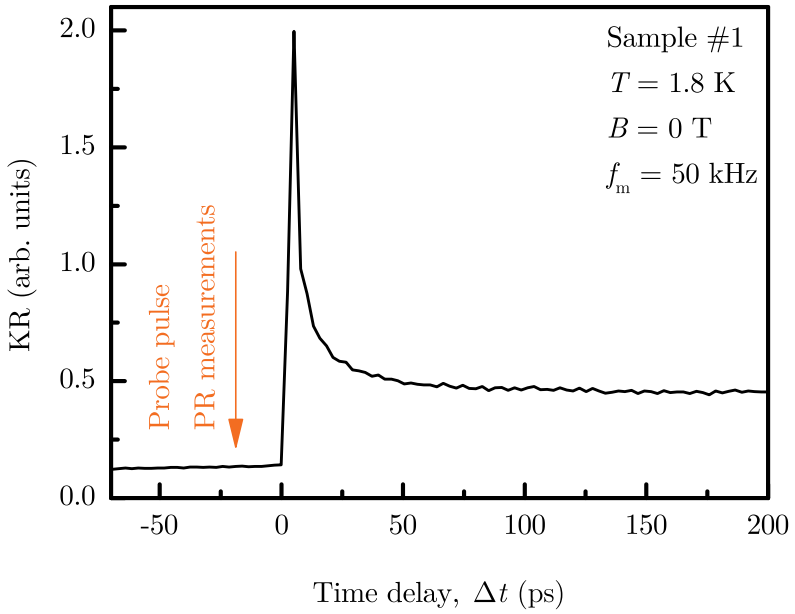

Figure 3.6 TRKR measurement at $B = 0\,\mathrm{T}$, performed at a pump power of $P_{\mathrm{Pu}} = 1.5\,\mathrm{mW}$ and a probe power of $P_{\mathrm{Pr}} = 0.7\,\mathrm{mW}$.

3.3 Investigated Samples

The samples under study were homogeneously fluorine-doped ZnSe:F epilayers, grown by molecular-beam epitaxy on a (001)-oriented GaAs substrate (see layer structure of the samples illustrated in Fig. 3.7). The epilayer was separated from the substrate by a 20-nm-thick $Zn_{0.85}Mg_{0.15}Se$ barrier layer to prevent carrier diffusion into the substrate. This

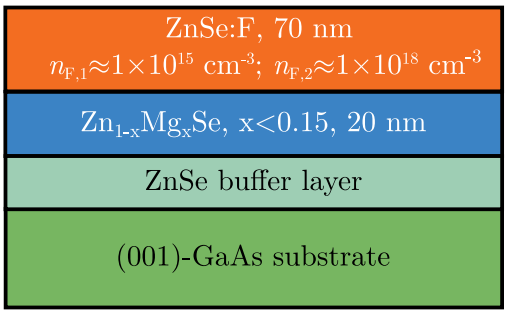

Figure 3.7 Layer structure of the studied samples. A thin buffer layer of ZnSe, grown on (001)-oriented GaAs substrate, is followed by a higher band gap ZnMgSe barrier. The top layer is formed by a fluorine-doped ZnSe epilayer. The structure of Samples #1 and #2 is identical except for the fluorine concentration n_{F} in the top layer.

barrier, in turn, was grown on top of a thin ZnSe buffer layer to reduce the defect density at the III-V/II-VI heterointerface. Two samples with different fluorine concentrations

were investigated in this thesis. Here, the fluorine concentration n_F depended on the applied fluorine flux during growth [Gre12] and was estimated from capacitance-voltage measurements using Schottky contacts [Gre12]. Sample #1 had a fluorine concentration of $n_F \approx 1 \times 10^{15}\,\mathrm{cm}^{-3}$, while sample #2 had a fluorine concentration $n_F \approx 1 \times 10^{18}\,\mathrm{cm}^{-3}$ that was three orders of magnitude higher than for sample #1 and close to the metal-insulator transition (Mott Transition) [Mot67]. Combining the estimated Bohr radius of $a_B = 4.825\,\mathrm{nm}$ of the donor-bound electron (see Ref. [Gre12]) with the Mott criterion [Gru16c]

$$2a_B = \frac{3}{2\pi} n_{F,c}^{1/3} \tag{3.2}$$

$$\Rightarrow a_B n_{F,c}^{-1/3} \approx 0.24, \tag{3.3}$$

we can estimate the critical fluorine concentration, at which the metal-insulator transition should occur

$$\Rightarrow n_{F,c} \approx \frac{0.014}{a_B^3},$$

$$\Rightarrow n_{F,c} \approx 1.2 \times 10^{17}\,\mathrm{cm}^3.$$

Thus, sample #2 had a fluorine concentration that was already above the estimated

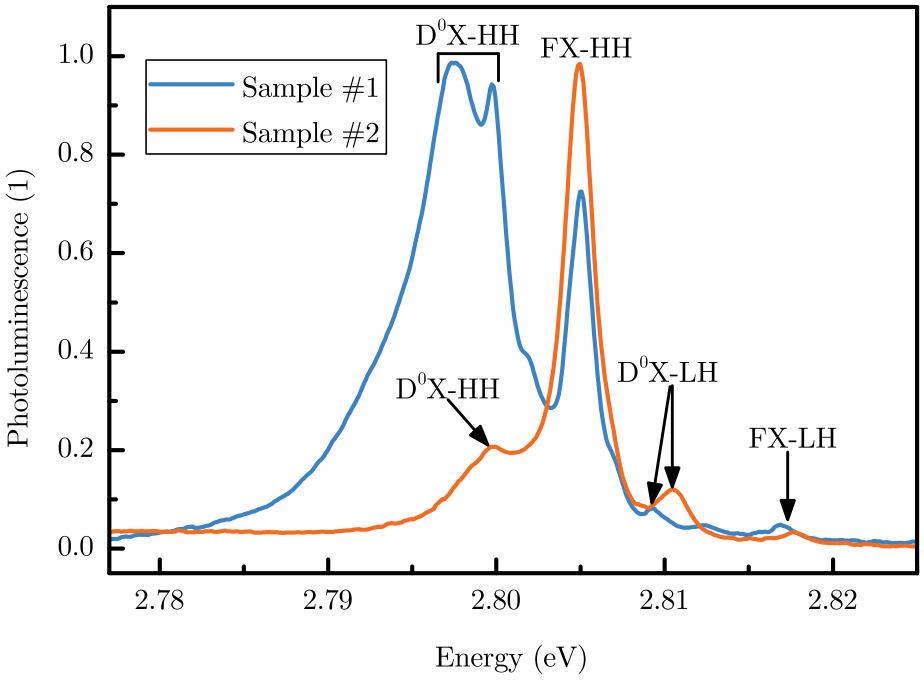

Figure 3.8 PL spectra of samples #1 and #2, measured at $B = 0$ and $T = 1.8\,\mathrm{K}$. A CW laser ($E_{exc} = 4.05\,\mathrm{eV}$) provided the necessary above barrier excitation.

critical concentration for the Mott transition. However, we can still observe PL from the sample (see Fig. 3.8).

Figure 3.8 shows the photoluminescence spectra of samples #1 and #2. We can assign their peaks to the optical transitions corresponding to different exciton complexes (cf. Ref. [Paw06; Gre12]), marked by the following abbreviations: FX denotes the free exciton lines, containing light hole (LH) and heavy hole (HH, cf. Section 2.1.2), while D^0X denotes the respective lines of the donor-bound excitons (trions, cf. Section 2.2).

3.4 Experimental Configurations

3.4.1 Resonant Spin Amplification Configuration

The resonant spin amplification (RSA) configuration of the TRKR technique represents a very sensitive tool to measure the effective magnetic field felt by the electron spins, i. e., to determine the electron Larmor precession frequency very precisely (cf. Ref. [Kik98]). In contrast to the "standard" configuration of the TRKR technique the time delay was not varied in the RSA configuration. It was fixed at small negative time delay $\Delta t = -20\,\mathrm{ps}$ of the probe pulse relative to the pump pulse (cf. orange arrow in Fig. 3.6), while the magnetic field in Voigt geometry ($\boldsymbol{B}_\mathrm{V} \perp \boldsymbol{k}$) was scanned to vary the Larmor precession frequency of the electron spins.

One can imagine the precessing electron spins as a very fast clock intrinsic to the system. The experimenter then lets this clock interact with a fast external clock, provided by the mode-locked titan:sapphire laser. At certain magnetic fields B_V, the frequencies of these two clocks synchronize, and each following pump pulse increases the spin polarization. These B_V can be calculated using the phase synchronization condition (PSC) [Yug12]

$$\omega_\mathrm{L} = N\omega_\mathrm{R}, N \in \mathbb{N} \tag{3.4}$$

$$\Leftrightarrow \frac{\mu_\mathrm{B} g_\mathrm{e} B_\mathrm{V}}{\hbar} = N\omega_\mathrm{R}, \tag{3.5}$$

$$\Leftrightarrow B_\mathrm{V} = \frac{N\hbar\omega_\mathrm{R}}{\mu_\mathrm{B} g_\mathrm{e}}. \tag{3.6}$$

Figure 3.9 schematically illustrates how the spin-polarized electron ensembles created by succeeding pump pulses superimpose either with destructive phase (blue line, upper curve) or constructive phase (red line, lower curve). Here, the blue line shows the "worst-case," a superposition with opposite phase that leads to a significant reduction of the spin polarization after the arrival of the 2nd pump pulse. Note that in this simplified schematic only spins polarized by three consecutive pump pulses were considered and superimposed according to Eq. (3.7), while at the experimental conditions the number of pulses to consider should be infinitely large (cf. Refs.[Yug12; Bel16]).

This results in the phenomenon called resonant spin amplification (RSA) at these particular magnetic fields [Kik98], which reveals itself as a series of period peaks in the Kerr rotation signal in dependence on the magnetic field. By summing up the contributions of each pump pulse to the macroscopic spin polarization along the z axis for a fixed time delay Δt (in analogy to Ref. [Yug12])

$$S_z(\omega_\mathrm{L}, \Delta t) = \sum_{j=0}^{\infty} S_0 \exp\left(-\frac{\Delta t + jT_\mathrm{R}}{T_2^*}\right) \cos\left(\omega_\mathrm{L}(\Delta t + jT_\mathrm{R})\right), \tag{3.7}$$

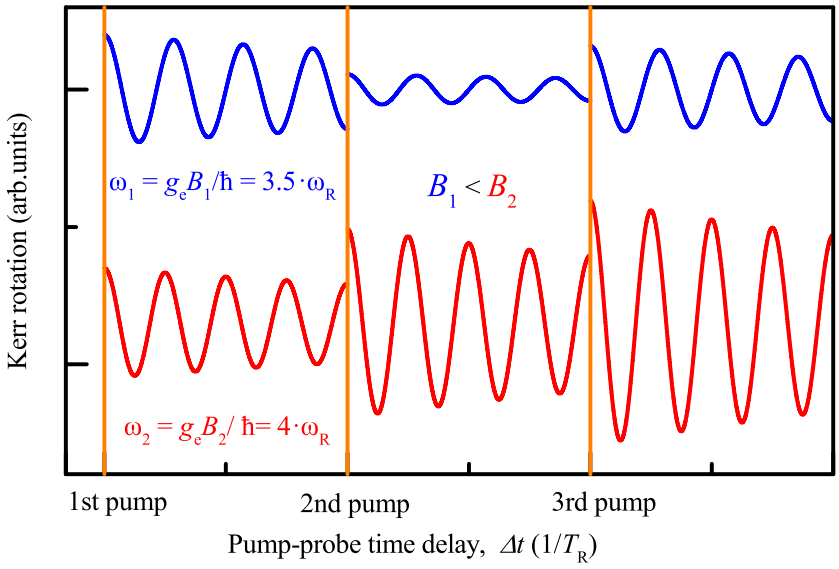

Figure 3.9 Schematic to illustrate the effect of Larmor precession of resident electrons polarized from different pump pulses. The electron spins oriented by different pumps have either a constructive phase (red line, lower curve) or a destructive phase (blue line, upper curve) with respect to each other.

we obtain

$$S_z(\omega_\mathrm{L}, \Delta t) = S_0 \exp\left(-\frac{\Delta t + T_\mathrm{R}}{T_2^*}\right) \frac{\cos(\omega_\mathrm{L}\Delta t) - \exp\left(-\frac{T_\mathrm{R}}{T_2^*}\right)\cos(\omega_\mathrm{L}(\Delta t + T_\mathrm{R}))}{\cos(\omega_\mathrm{L}\Delta t) - \cosh\left(\frac{T_\mathrm{R}}{T_2^*}\right)}. \tag{3.8}$$

This expression depends on the magnetic field B_V via the electron Larmor precession frequency ω_L (cf. Eq. (2.15)) and allows one to determine the inhomogeneous spin dephasing time from a nonlinear fit to an RSA spectrum, see, e. g., Ref. [Gre12]. Furthermore, we can measure the effective magnetic field, felt by the ensemble of electron spins, very precisely, if the g factor is known, e. g., from a TRKR measurement.

3.4.2 Polarization Recovery Configuration

The polarization recovery measurements also employed the pump-probe scheme. As in the RSA configuration, the time delay Δt of the probe pulse with respect to the arrival of the pump pulse was not varied in the polarization recovery configuration, but fixed at a small negative value $\Delta t \approx -20\,\mathrm{ps}$ (cf. orange arrow in Fig. 3.6). Measuring the KR signal at this temporal position simplifies the interpretation of the results, since these can only arise from long-living spins, whose polarization decays on a timescale exceeding the laser repetition period T_R [Hei15b]. For example, the exciton recombination time in fluorine-doped ZnSe is about $(210 \pm 40)\,\mathrm{ps}$ ($\mathrm{D^0X}$-HH, cf. Ref. [Gre12]) so that the KR signal at negative time delays Δt should originate only from the resident electrons in the epilayer that are bound to the fluorine donors at low temperatures.

The circularly polarized pump pulses create a macroscopic spin polarization of the ensemble of donor-bound electrons by optically pumping one of the two eigenstates $|\uparrow\rangle$ and $|\downarrow\rangle$ of the spin of the donor-bound electron, where the eigenstates are defined by the external magnetic field applied in the Faraday geometry. The macroscopic spin polarization of the donor-bound electrons hereby occurs due to the replacement of these initially non-polarized electrons with spin-polarized electrons (see Sec. 2.4 and Refs. [Hei15b; Dya84]).

The helicity of the pump pulses was modulated by the EOM with the modulation frequency f_m. The pump helicity modulation leads to a spin polarization that alternates between the $|\uparrow\rangle$ and the $|\downarrow\rangle$ state. The pump helicity modulation frequency f_m was varied from 10 kHz to 700 kHz, which was the key for the spin inertia measurements. Note that we observed a change of the pump polarization upon altering f_m (only `LINOS LM 0202 5W P` EOM) so that we waited a few minutes each time f_m was changed and used the scheme, illustrated in Fig. 3.3(a), to check and readjust the pump polarization.

3.4.3 Measurement of the Nuclear Spin Relaxation Time

To estimate the nuclear spin relaxation time at the conditions of the TRKR experiment we had to quickly switch between to different helicity modulation frequencies $f_{\mathrm{m},1}$ and $f_{\mathrm{m},2}$. To that end, we employed two AFGs, connected to a TTL multiplexer. The multiplexer was based on a `Texas Instruments SN74LS257AN` integrated circuit (high-performance multiplexer with an average propagation delay of 12 ns). Taking into account the rise time of 8 ns of the EOM (`Polytec 350-105 Laser Modulator`), we conclude that the switching of the modulation frequency occurs on a timescale that is much shorter than the measured nuclear spin relaxation time on the order of a few milliseconds.

The KR signal was continuously demodulated at both modulation frequencies ($f_{\mathrm{m},1}$ and $f_{\mathrm{m},2}$) by two lock-in amplifiers to allow for the recording of the transients upon switching f_m. The time constants (TCs) of the lock-ins were set to a few tens of microseconds to allow for a time resolution of a few hundred microseconds. We obtained a time-resolved signal by recording the output signals of the lock-ins with a `National Instruments NI USB-6251` fast analog-digital converter (ADC). The ADC was triggered using the same signal (f_aux) as the TTL multiplexer. Note that the short TCs of the lock-ins led to a signal to noise ratio (SNR) that was much worse than for the TRKR measurements, where the much longer TC of 100 ms resulted in an averaging of the KR signal. Here, we improved the SNR by averaging over about 100 switching cycles, triggered at a rate determined by the frequency f_aux, with a `LabVIEW` program. Note that the ADC actually had a time resolution of 50 ns so that the limiting factor for these measurements were the TCs of the lock-ins. See Section 6.1 for details and results.

Figure 3.10 shows a schematic of the connections of these electronic devices. Note that the different blocks do not necessarily represent separate devices, but are drawn separately to simplify the scheme. For example, the `Tektronix AFG 3022` featured two channels, and the `Zurich Instruments HF2LI` contained two demodulators. Note that the scheme, shown in Fig. 3.10, was extended by an optical shutter (`Thorlabs SH05 shutter head` and `Thorlabs SC10 controller`) to simultaneously block the pump and the probe beam and estimate the nuclear spin relaxation time in the dark. The shutter had a close activation time of 4.08 ms. It was also triggered with the frequency f_aux. However, we used

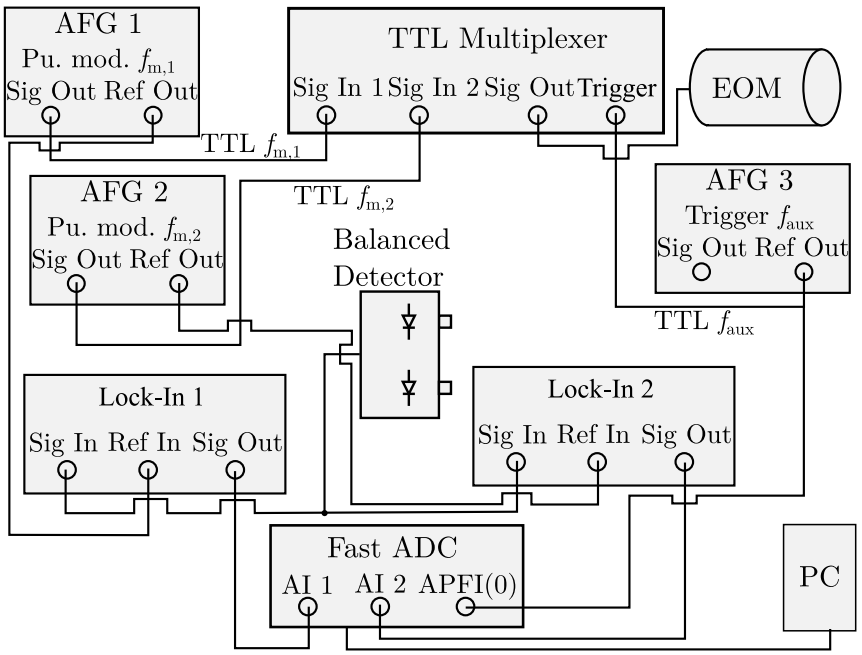

Figure 3.10 Schematic to illustrate the electronic devices used for the measurement of the nuclear spin relaxation time and their connections to each other. The black lines denote connections, made with Bayonet Neill Concelman (BNC) cables.

a separate channel of the AFG to set a relative phase compared to the trigger of the ADC and the TTL multiplexer and thereby triggered the shutter shortly after switching f_m (cf. Section 6.1 for details.).

3.4.4 Optically Detected Nuclear Magnetic Resonance

The goal of an optically detected nuclear magnetic resonance (ODNMR) measurement is to determine the nuclear magnetic resonance (NMR) frequency f_{NMR} in the external magnetic field. Thus, we measured the KR signal at a fixed time delay (RSA configuration, $\Delta t = -20\,\text{ps}$) and a fixed, transverse magnetic field B_V in dependence on the frequency f_{RF} of a CW radio frequency (RF) excitation, where the RF amplitude A_{RF} was kept constant. Preferably, we selected a magnetic field B_V, where the KR signal was particular sensitive to a change of the nuclear spin polarization/the Overhauser field B_N (cf. Section 2.3.8 and Chapters 5 and 6 for details).

Figure 3.11 shows a schematic of the electronic devices used and how they were connected. To increase the signal-to-noise ratio an additional amplitude modulation (frequency: $f_{aux} = 18\,\text{Hz}$, modulation depth: 100 %) of the RF excitation was used (double modulation technique). The first lock-in amplifier (Lock-In 1) was connected to the balanced photodetector and demodulated the signal modulated with the pump helicity modulation frequency f_m, where the relation $f_m \gg f_{aux}$ held. Its output was connected to the input of the second lock-in amplifier (Lock-In 2), which thereby determined the difference of the KR signal with and without RF excitation. The first function generator AFG 1 triggered

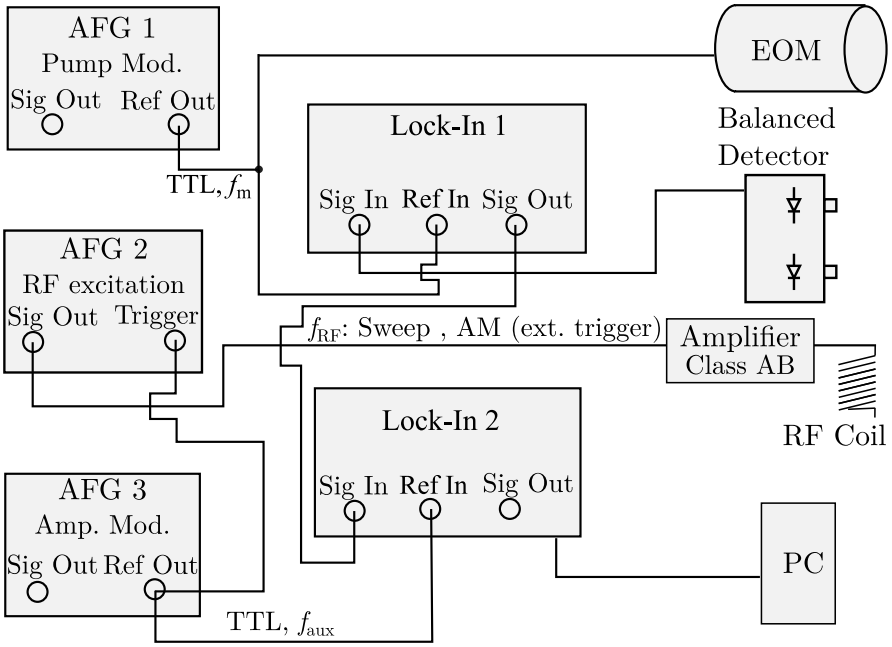

Figure 3.11 Schematic to illustrate the electronic devices used for an ODNMR measurement and their connections to each other. The black lines denote connections, made with BNC cables.

the helicity modulation with the EOM and provided the reference for Lock-In 1. The function generator AFG 2 was controlled by a Labview program that scanned f_{RF} in a specified range and recorded the KR signal as a function of f_{RF}. The AFG was set to produce a sine wave and its external trigger input, controlling the amplitude modulation, was connected to the reference output of AFG 3 that was set to the frequency f_{aux} and provided the reference for Lock-In 2.

3.4.5 Rabi Oscillations

The goal of the Rabi oscillations was to determine the proper RF pulse width τ_{p} for the measurements, based on coherent control of the nuclear spins (Ramsey fringes, Hahn echo; cf. the description in the following). The KR signal in dependence on τ_{p} was measured at fixed magnetic field B_{V} and at the corresponding resonance frequency ($f_{\mathrm{RF}} = f_{\mathrm{NMR}}(B_{\mathrm{V}})$), determined from a preliminary ODNMR measurement (cf. Section 3.4.4).

The electronic devices and their connection were the same as for the ODNMR measurements. However, for the Rabi oscillation measurements, AFG 2 was set to "n-burst mode", where n denotes the number of cycles at the frequency $f_{\mathrm{RF}} = f_{\mathrm{NMR}}$. Thus, the trigger from AFG 3 did not modulate the amplitude of its output signal, but triggered a burst with a length of n cycles so that Lock-In 2 measured the difference of the KR signal with and without this RF pulse with a width $\tau_{\mathrm{p}}(n) = n \cdot (2\pi/f_{\mathrm{NMR}})$. A Labview program varied the number of cycles n so that we obtained the KR signal in dependence on the pulse width τ_{p}. Please refer to Section 6.2.1 for a detailed explanation of the physics underlying the Rabi oscillation measurement.

3.4.6 Ramsey Fringes

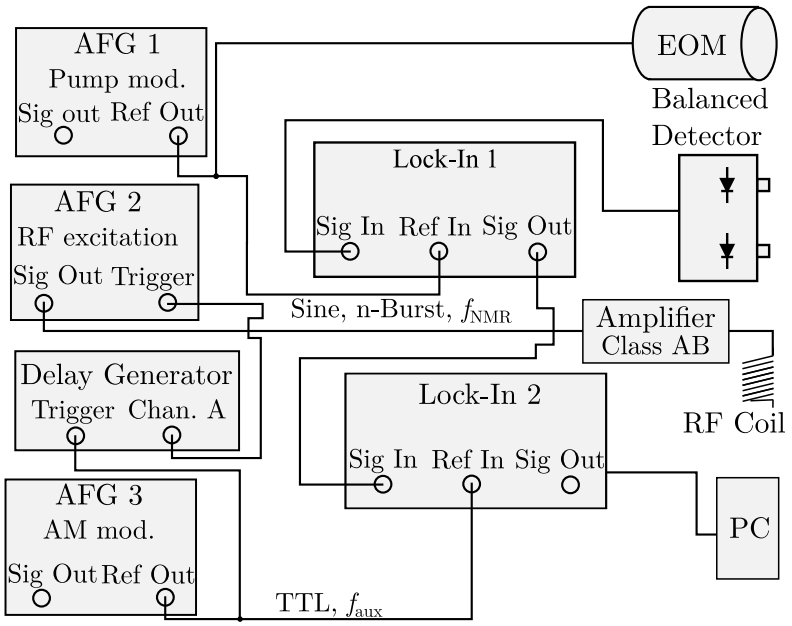

Figure 3.12 Schematic to illustrate the electronic devices used for a Ramsey fringes measurement and their connections to each other. The black lines denote connections, made with BNC cables.

The measurement of so-called *Ramsey fringes* required an additional device compared to the Rabi oscillation measurements: A computer-controlled delay generator (`Quantum Composers 9528 Digital Delay Pulse Generator`) allowed us to apply RF pulses with variable delay Δt (cf. schematic in Fig. 3.12). The measurements were performed at fixed magnetic field, where the resonance frequency $f_{\mathrm{RF}} = f_{\mathrm{NMR}}(B_{\mathrm{V}})$ was determined from a preliminary ODNMR measurement at the same B_{V}. From a preliminary Rabi oscillations measurement, following the ODNMR measurement, we obtained the pulse width τ_{p} of a $\pi/2$ pulse at constant RF amplitude A_{RF} (cf. Section 6.2.2 for a discussion of the underlying physics).

The delay generator, triggered with the rate f_{aux}, send a sequence of two short (μs) TTL pulses with a delay Δt between the pulses. Each pulse, in turn, triggered AFG 2 to send an RF pulse ("n-burst mode," $n = (\tau_{\mathrm{p}} \cdot f_{\mathrm{RF}})/2\pi$) of a pulse width τ_{p}. Here, the Channels A and B of the delay generator were both set to the "Channel A output." Channel A send a pulse immediately upon the external trigger, while the pulse from channel B was delayed with respect to the pulse from Channel A/the external trigger. A `LabVIEW` program varied this delay Δt between the Channels A and B of the delay generator so that we obtained the KR signal as a function of the time delay Δt between the $\pi/2$ pulses. Due to the finite pulse width τ_{p}, the delay Δt was defined as the temporal distance between the middle of the $\pi/2$ pulses. Note that the clock of the delay generator was set to "internal," while the trigger was set to "external."

3.4.7 Hahn Echo

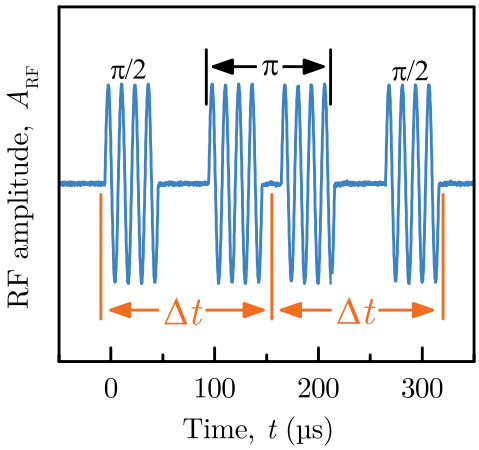

Figure 3.13 Pulse sequence used for the Hahn echo measurement, recorded with an oscilloscope. The orange lines and arrows show the definition of the time delay Δt. Taking into account the finite pulse width τ_p, the intervall $2\Delta t$ started at the beginning of the first $\pi/2$ pulse and ended after the action of the final $\pi/2$ pulse on the sample.

The Hahn echo sequence requires an additional π pulse in between the two $\pi/2$ pulses so that the scheme, shown in Fig. 3.12, could be used for the Hahn echo measurements, too. The only difference to the Ramsey fringes measurement was the configuration of the delay generator. We used the fact that a π pulse can be constructed of two consecutive $\pi/2$ pulses. The pulses from channels B, C and D were set to the "channel A output." All channels were set to 1 µs TTL pulses. Channel A triggered the first $\pi/2$ pulse, followed by a trigger pulse from channel B at $t = \Delta t - \tau_p$ (cf. Fig. 3.13) and a "consecutive" trigger pulse from channel C at $t \approx \Delta t$. Thus, the trigger pulses from Channels B and C triggered AFG 2 to send a π pulse. To finish the Hahn echo sequence (cf. Section 6.2.3 for the underlying physics) Channel D sent the trigger pulse at $t = 2\Delta t - \tau_p$ for the final $\pi/2$ pulse.

3.4.8 Relative Phase Between RF Excitation and Helicity Modulation

For the experiments on the orientation of the Knight field $\boldsymbol{B}_K$, presented in Section 5.3.3, we needed to set and measure the relative phase φ between the helicity modulation and the RF excitation with the coil. Figure 3.14 shows a schematic of the used devices and their connection to each other, where each line symbolizes a BNC cable. The phase between both can only be well-defined, if they are set to the same frequency ($f_{RF} = f_m$). We used two channels of the same AFG and configured it to operate Channel 2 at the frequency of Channel 1, while we could adjust the relative phase between the channels. Channel 2 was connected to a 5 Ω resistor in line with the RF coil. Connecting a BNC cable before and after the resistor to different channels of a digital oscilloscope, we could measure the voltage drop, which is directly proportional to the current through the resistor, as the difference of

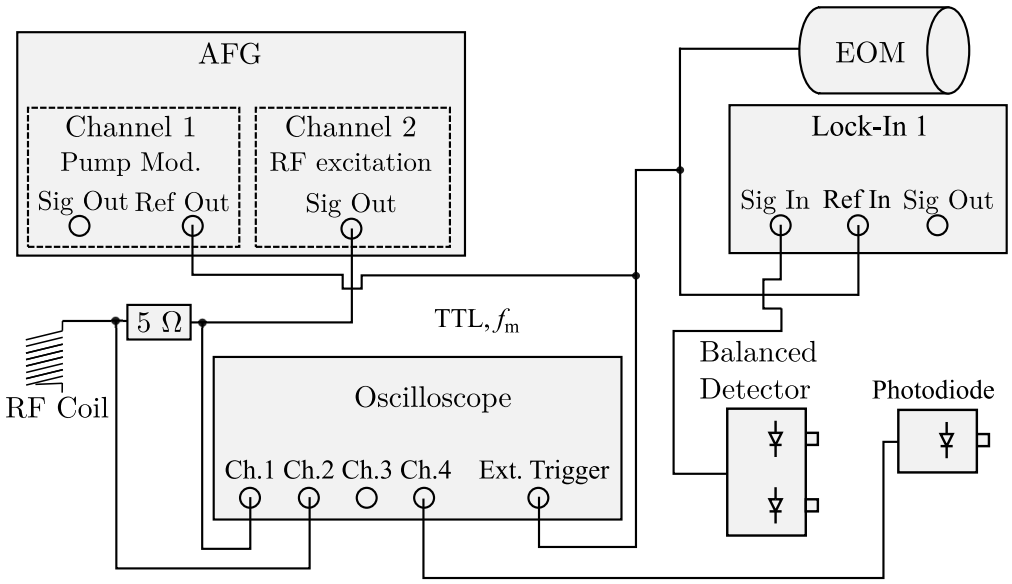

Figure 3.14 Schematic of the devices uses to test the phase between the helicity modulation and the RF excitation and their connections to each other. The black lines denote connections, made with BNC cables.

the signals of both channels. Due to the conservation of charge, the current through the resistor and the coil were the same. Furthermore, this oscilloscope was connected to the fast photodiode, used to check the pump polarization and the adjustment of the EOM (cf. Fig. 3.3).

The system of spins can be pushed on and pulled on with external magnetic fields, so one can do many tricks with resonances, with relaxation effects, with spin-echoes, and with other effects. It serves as a prototype of many complicated thermodynamics systems.

Richard Feynman [Fey13]

4 Electron Spin Dynamics - The Spin Inertia Effect

In this chapter the phenomenon, called "spin inertia effect" in Ref. [Hei15b], will be demonstrated on polarization recovery (PR) measurements for the nominally undoped sample #1 ($n_F \approx 1 \times 10^{15}\,cm^{-3}$) and the strongly doped sample #2 ($n_F \approx 1 \times 10^{18}\,cm^{-3}$, cf. also Section 3.3). Here, PR refers to the suppression of the effect of the fluctuating nuclear fields on the electron spin polarization in an external magnetic field. An external field applied in any direction with respect to the sample surface and the electron spin polarization reduces the effect of the average hyperfine field of the fluctuating nuclear spins on the electron spin polarization [Mer02]. Here, we applied the magnetic field in the Faraday geometry (parallel to the pump $\boldsymbol{k}$-vector) to simplify the interpretation of the results and to allow us to measure the longitudinal spin relaxation time T_1 in a broad range of external magnetic fields.

4.1 Polarization Recovery in a Longitudinal Magnetic Field

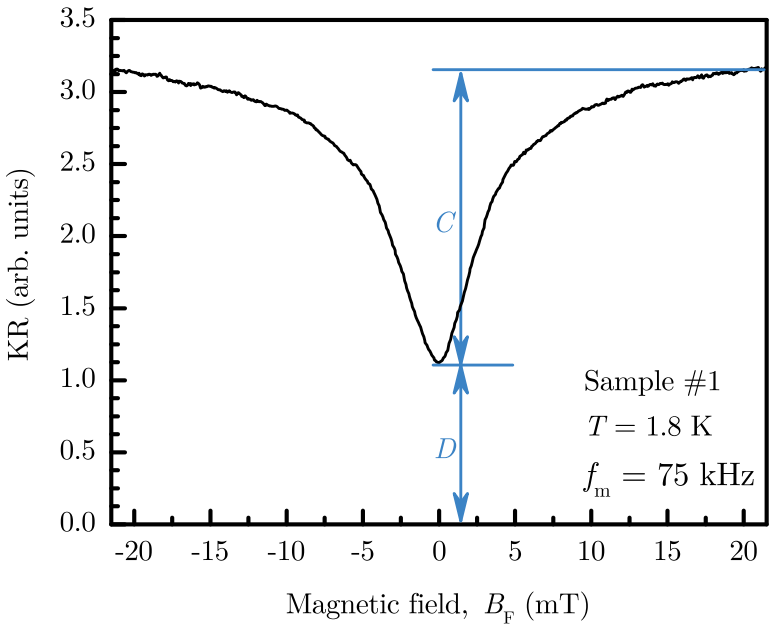

Figure 4.1 Kerr rotation (KR) signal as a function of the magnetic field B_F. The PR measurement was performed at $P_{Pu} = 1.5\,mW$ and $P_{Pr} = 0.5\,mW$. We find $C = 2.05$ arb. units and $D = 1.12$ arb. units, so the relation $C : D$ is about $1.83 : 1$ (cf. discussion in the text).

The true gain of a measurement at a fixed, negative time delay Δt (here: $\Delta t \approx -20\,\mathrm{ps}$) is to measure the Kerr rotation (KR) signal in dependence on the magnetic field. Here, the dependence of the KR signal on the magnetic field in Faraday geometry B_F was investigated by performing a PR measurement (cf. Ref. [Hei15b] and Section 3.4.2). Figure 4.1 shows such a PR measurement. The magnetic field B_F was varied from $-18\,\mathrm{mT}$ to $18\,\mathrm{mT}$, while all other parameters were kept constant. The KR signal is symmetrical around its minimum at $B_\mathrm{F} = 0\,\mathrm{T}$ and shows a saturation behavior for increasing B_F. We speak of the phenomenon of "polarization recovery": The spin polarization along the direction of observation is decreased at zero or small magnetic fields, while this depolarization of the spins is decreasing with increasing magnetic field in Faraday geometry B_F. The KR signal only measures the projection of $\boldsymbol{S}$ on the direction of observation and the electron spin system is not isolated from the rest of the semiconductor, but also interacts with the nuclear spins via the hyperfine interaction (cf. Sec. 2.3.6 and note that there are further interactions, e. g., with phonons, not taken into account here). At external magnetic fields that are weaker or comparable to the randomly oriented hyperfine fields resulting from the nuclear spin fluctuations, the Larmor precession of the electron spins in these hyperfine fields leads to a decrease of the electron spin polarization [Mer02; Hei15b]. Due to their random orientation, these fields can be described as an isotropic field, whose components along the x, y and z axes have equal strength or probability $p = 1/3$ [Pet08]. The z axis is oriented along the external magnetic field and the optical axis so that this component of the average hyperfine field does not alter the spin polarization. However, the x and y components lead to a Larmor precession of the electrons spins, initially oriented along the z axis, and thereby each component decreases the projection of the spin polarization on the direction of observation ($\parallel z$) by 1/3. This behavior and the resulting dependence of the PR amplitude A_PR on B_F are described by the following equation [Pet08; Gre12]

$$A_\mathrm{PR}(B_\mathrm{F}) = A_0 \left[1 - \frac{2/3}{1 + (B_\mathrm{F}/B_\mathrm{N})^2}\right]. \tag{4.1}$$

Here, B_N is the magnitude of the fluctuating hyperfine fields, and A_0 is the PR or KR amplitude at magnetic fields $B_\mathrm{F} \gg B_\mathrm{N}$, where the influence of the fluctuating hyperfine fields is suppressed by the stronger external field. The blue arrows in Fig. 4.1 illustrate the depth of the PR dip C and the remaining PR amplitude D at $B_\mathrm{F} = 0$. According to the considerations above their ratio should be $2 : 1$. We find $C = 2.05\,\mathrm{arb.\ units}$ and $D = 1.12\,\mathrm{arb.\ units}$, so their ratio is about $1.83 : 1$. This deviation can be caused by an offset of the measured signal, which might occur due to scattered pump light, since no double modulation (no modulation of the probe) was used. The theoretical model (Eq. (4.1)) allows us to estimate the average hyperfine field B_N. To account for small deviations of the zero position of the hall sensor (cf. also Section 3.1.1) and for other imperfections of the experimental setup (offset (see discussion before, etc.)) two additional fitting parameters are added to Eq. (4.1)

$$A_\mathrm{PR}(B_\mathrm{F}) = A_0 \left[1 - \frac{2/3}{1 + ((B_\mathrm{F} - B_0)/B_\mathrm{N})^2}\right] + A_\mathrm{off}. \tag{4.2}$$

Here, B_0 is the shift of the zero magnetic field position, and A_off is the offset.

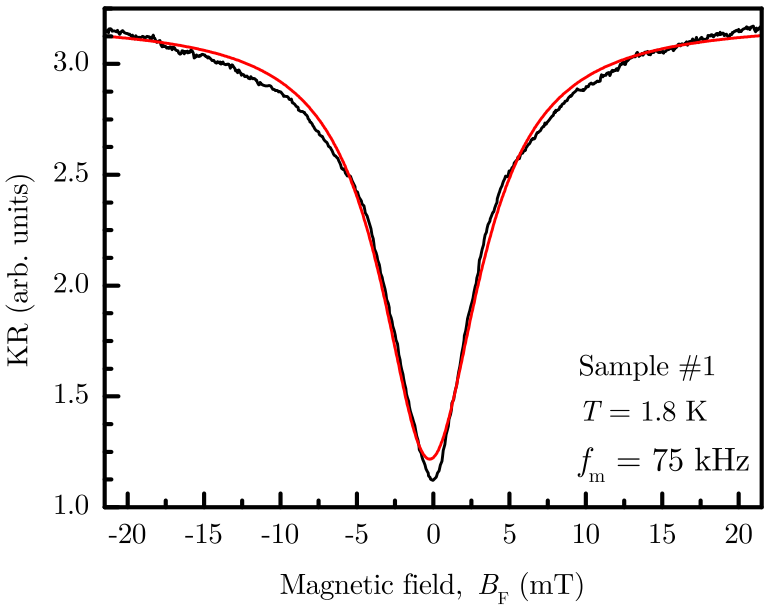

Figure 4.2 PR measurement, performed at $P_{Pu} = 1.5\,\mathrm{mW}$ and $P_{Pr} = 0.5\,\mathrm{mW}$. The red line shows the best fit to the data based on Eq. (4.2).

Figure 4.2 shows a fit to the data using Eq. (4.2). All parameters of the best fit are shown in Tab. 4.1. The fit yields an average hyperfine field $B_N = (3.89 \pm 0.02)\,\mathrm{mT}$. This is two times larger than the result of Greilich *et al.* [Gre12] who found a half-width at half maximum (HWHM) $B_N = 1.65\,\mathrm{mT}$ for a ZnSe epilayer with a higher fluorine concentration ($n_F \approx 6 \times 10^{17}\,\mathrm{cm}^3$) than sample #1 ($n_F \approx 1 \times 10^{15}\,\mathrm{cm}^3$). The difference of the HWHM of

Table 4.1 Parameters of the best fit to the PR data shown in Fig. 4.2. The errors are obtained from the fit.

A_0	2.96 ± 0.01	arb. units
B_N	3.89 ± 0.02	mT
A_{off}	0.23 ± 0.01	arb. units
B_0	-0.22 ± 0.01	mT

the PR dip for sample #1 and the one reported in Ref. [Gre12] cannot be solely explained by the fluctuating hyperfine fields that should be identical for both samples. This becomes clear when estimating the inhomogeneous dephasing time T_2^* from this result with the following equation [Gre12]

$$T_2^* = \frac{2\sqrt{3}\hbar}{\mu_B g_e B_N} = (9.21 \pm 0.05)\,\mathrm{ns}. \tag{4.3}$$

This time is considerably smaller than the result from a fit to the zero RSA peak of $T_2^* = 33\,\mathrm{ns}$, determined for sample #1 in Ref. [Gre12]. Thus, we suggest that the difference

of the width of the PR dip and the Hanle peak (zero RSA peak, cf. also Section 2.4.3), which is not predicted by the theory of Merkulov *et al.* [Mer02], might originate from some sample specific anisotropy or novel effect, whose investigation is out of the scope of this thesis.

4.2 The Spin Inertia Effect

4.2.1 Observation of the Spin Inertia Effect

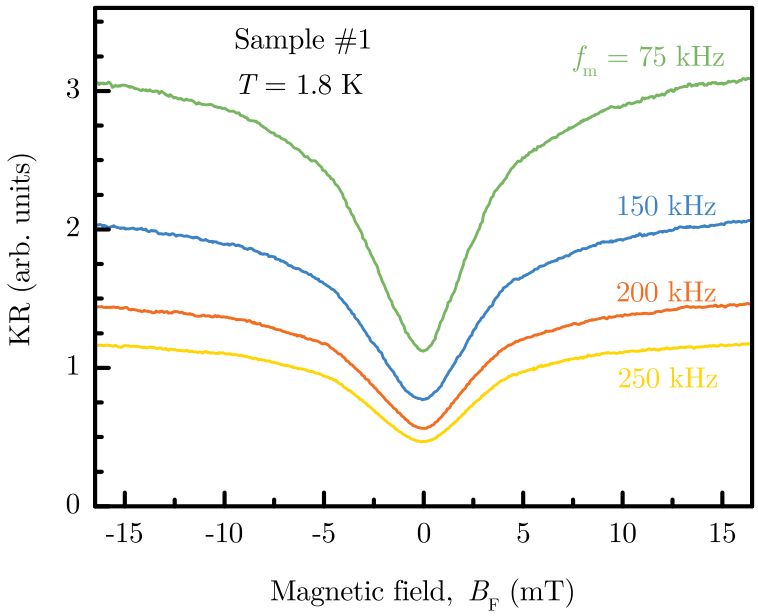

Figure 4.3 Polarization recovery curves, measured at f_m =75 kHz, 150 kHz, 200 kHz, and 250 kHz. All measurements for sample #1 at $P_{Pu} = 1.5$ mW and $P_{Pr} = 0.5$ mW.

Figure 4.3 shows the dependence of the PR signal on the pump helicity modulation frequency. We observe a decrease of the magnitude of the PR signal with increasing pump helicity modulation frequency f_m, while its dependence on B_F or the shape of the PR with a dip around $B_F = 0$ with a full-width at half maximum (FWHM) of about 7.8 mT remains the same [Hei15b]. The strong decrease of the magnitude of the PR signal in a frequency range from 75 kHz to 250 kHz suggests that the electron spin relaxation time τ_S (cf. Section 2.4.2) is on the order of a few µs [Hei15b].

In what follows this phenomenon, tentatively called "spin inertia effect" in Ref. [Hei15b], shall be investigated quantitatively.

4.2.2 Theoretical Model to Extract the Electron Spin Relaxation Time

Starting from the concepts of optical orientation, presented in Ref. [Mei84], we develop a model that describes the observed dependence of the PR signal on f_m and allows us to determine the electron spin relaxation time [Hei15b]. Both samples, even the nominally

undoped sample #1, are n-type semiconductors. Thus, the epilayer contains resident electrons. The resident electrons are bound to the fluorine donors at low temperatures. Exciting the D^0X-HH transition with circularly polarized light results in a replacement of these initially unpolarized electrons with photogenerated, spin-oriented electrons [Hei15b; Dya84]. As a result, the macroscopic spin polarization of the donor-bound electrons increases. However, this process competes with the electron spin relaxation with the time τ_S and the possible recombination of the spin-oriented electrons with photogenerated holes. The corresponding time constant $\tau = \frac{n_0}{G}$ for the latter depends on the electron-hole generation rate $G \propto P_{\mathrm{Pu}}$ and the concentration of resident electrons n_0. Combined τ_S and τ yield the spin lifetime T_S (cf. Eq. (2.29) in Section 2.4.1)

$$\begin{aligned} & \frac{1}{T_S} = \frac{1}{\tau_S} + \frac{1}{\tau}, \\ \Leftrightarrow\ & \frac{1}{T_S} = \frac{1}{\tau_S} + \frac{G}{n_0}, \\ \Rightarrow\ & \frac{1}{T_S} = m \cdot P_{\mathrm{Pu}} + b, \end{aligned} \tag{4.4}$$

where the last line contains parameters which are accessible in the experiment and can be used for a linear fit. The parameter $m \propto 1/n_0$ is the slope of this fit. We calculate the spin relaxation time τ_S from the y-intersection $b = 1/\tau_S$.

Figure 4.4 qualitatively illustrates the effect of a finite spin lifetime T_S on the spin polarization under helicity-modulated excitation with the modulation frequency f_{m} (see also Section 3.4.2). T_S is the time it takes to reach a steady-state spin polarization S_0. The steady-state polarization S_0, in turn, depends on the experimental conditions ($1/\tau \propto G \propto P_{\mathrm{Pu}}$), the spin relaxation time and optical selection rules. The sign of the macroscopic spin polarization depends on the helicity (σ^+- or σ^--polarized) of the exciting light. Thus, a switching of the helicity changes the sign of the macroscopic spin polarization with the time T_S. It depends on the speed or frequency f_{m} of the helicity modulation of the pump whether or not the steady-state spin polarization for a constant circular polarization S_0 can be reached before the helicity of the pump is inverted again.

In the following, the employed pulsed excitation (cf. Sections 3.1.4 and 3.2.2) shall be treated as a continuous-wave (CW) excitation. The observations in Fig. 4.3 hint at a spin lifetime T_S in the microsecond range. Thus, the modulation periods of high frequencies, e. g., $f_{\mathrm{m}} = 250\,\mathrm{kHz}$, were also in the microsecond range. Comparing a modulation frequency of $f_{\mathrm{m}} = 250\,\mathrm{kHz}$ to the laser repetition frequency $f_{\mathrm{R}} = 75.75\,\mathrm{MHz}$ yields the following relation

$$\frac{1}{f_{\mathrm{m}}} = 4\,\mu\mathrm{s} \gg \frac{1}{f_{\mathrm{R}}}. \tag{4.5}$$

At these conditions, the sample is exposed to a train of about 150 pump pulses of the same circular polarization (σ^+ or σ^-) before the pump helicity is inverted again. The high number of pulses justifies the approximation of the pulsed excitation by a CW excitation with the same average power. Employing this approximation, a quantitative model is developed.

The following kinetic equation describes the time dependence of the macroscopic spin polarization along the direction of observation S_z in the absence of static magnetic

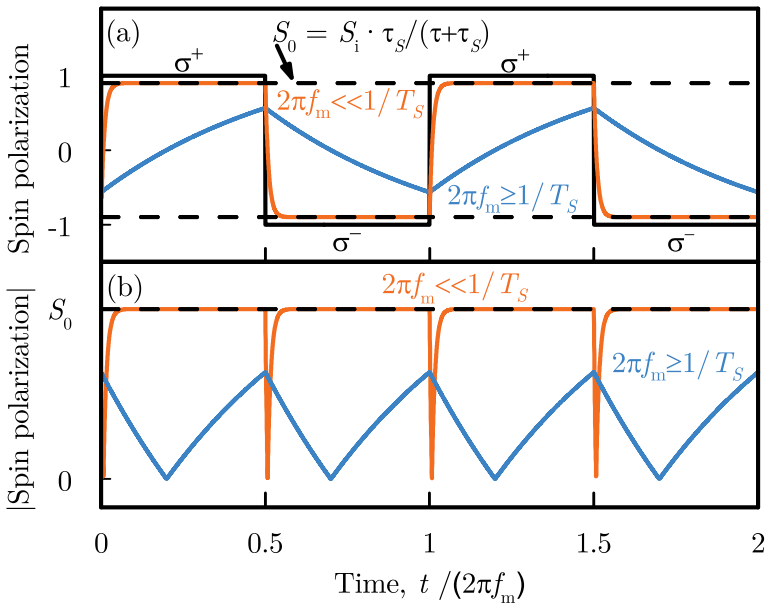

Figure 4.4 Spin polarization (model calculations, see Eqs. (4.10) and (4.11)) under helicity modulated excitation with the frequency f_m in the limiting cases $2\pi f_\mathrm{m} \ll 1/T_S$ (orange lines) and $2\pi f_\mathrm{m} \geq 1/T_S$ (blue lines) [Hei15b]. (a) Spin polarization along the direction of observation (S_z): The orange line illustrates the case when the modulation with f_m is slow compared to the time scale given by the spin lifetime T_S. Thus, the steady-state spin polarization $\pm S_0$ is reached before the helicity of the pump is inverted again. It seems to follow the helicity of the exciting light without "inertia." In contrast to this, the spin polarization cannot reach $\pm S_0$ if the helicity is switched fast compared to the time scale given by T_S (blue line). (b) Modulus of the spin polarization along the direction of observation $|S_z|$ for both limiting cases. Here, the influence of a fast modulation (blue line, $2\pi f_\mathrm{m} \geq 1/T_S$) becomes even more obvious: While for a slow modulation (orange line, $2\pi f_\mathrm{m} \ll 1/T_S$) $|S_z|$ is equal or close to the steady-state value $|S_0|$ for the almost whole modulation period, $|S_z|$ is strongly decreased in the opposite case (blue line, $2\pi f_\mathrm{m} \geq 1/T_S$) and the relation $|S_z| < S_0$ holds for the whole modulation period.

fields [Dya84; Hei15b]

$$\frac{\mathrm{d}S_z(t)}{\mathrm{d}t} = \frac{S_\mathrm{i} - S_z(t)}{\tau} - \frac{S_z(t)}{\tau_S}. \tag{4.6}$$

Here, S_i is the initially injected spin polarization whose sign depends on the laser polarization and optical selection rules. The first term on the right side S_i/τ describes the increase of the spin polarization due to the optically generated electron spins with the time τ. However, the possible recombination of already spin-polarized electrons with photogenerated holes leads to a decrease of the spin polarization. This is described by the term $-S_z(t)/\tau$. All other processes leading to a decrease of the spin polarization are represented by the term $-S_z(t)/\tau_S$.

For a constant circular polarization of the pump, S_z does not change (steady-state)

$$\frac{\mathrm{d}S_z(t)}{\mathrm{d}t} = 0,$$

and we obtain the stationary solution S_0

$$S_0 = S_\mathrm{i}\frac{\tau_S}{\tau_S+\tau} = S_\mathrm{i}\frac{G\tau_S}{G\tau_S+n_0}. \tag{4.7}$$

However, in this experiment, the injected spin polarization changes its sign with the helicity modulation frequency f_m so that we have to modify Eq. (4.6) and solve the following equation

$$\frac{\mathrm{d}S_z(t)}{\mathrm{d}t} = \frac{S_0(t)-S_z(t)}{\tau} - \frac{S_z(t)}{\tau_S}, \tag{4.8}$$

where $S_0(t) = S_\mathrm{i}(t)\frac{\tau_S}{\tau_S+\tau}$ is a square-wave signal with the frequency f_m, a constant amplitude $|S_0|$ and a duty cycle of 50% [Hei15b].

The lock-in amplifier averages the KR signal, which is proportional to the concentration of resident electrons n_0 and their average spin polarization along the z direction $S_z = S_z(t)$, over the modulation period $T_\mathrm{m} = 1/(2\pi f_\mathrm{m})$ and records the modulus of the following correlator

$$\begin{aligned} L(f_\mathrm{m}) &= \langle n_0 S_z \exp(i2\pi t/T_\mathrm{m})\rangle|_{T_\mathrm{m}}, \\ &= \int_0^{T_\mathrm{m}} \frac{n_0 S_z \exp(i2\pi t/T_\mathrm{m})}{T_\mathrm{m}}\mathrm{d}t. \end{aligned} \tag{4.9}$$

To determine $|L(f_\mathrm{m})|$ we first need to solve Eq. (4.8), where we treat both half cycles separately. Without loss of generality $S_0(t)$ shall be equal to $+|S_0|$ in the first half cycle from $t = 0$ to $t = T_\mathrm{m}/2$ and the solution is given by

$$S_z(t) = |S_0|\left(1 - \frac{2\mathrm{e}^{-\frac{t}{T_S}}}{1+\mathrm{e}^{-\frac{T_\mathrm{m}}{2T_S}}}\right), \tag{4.10}$$

while in the second half cycle from with $S_0(t) = -|S_0|$ from $t = T_\mathrm{m}/2$ to $t = T_\mathrm{m}$ S_z can be determined to

$$S_z(t) = |S_0|\left\{-1 + 2\left(\mathrm{e}^{\frac{T_\mathrm{m}}{2T_S}} - \frac{1}{1+e^{\frac{-T_\mathrm{m}}{2T_S}}}\right)\mathrm{e}^{-\frac{1}{T_S}}\right\}. \tag{4.11}$$

Combining Eqs. (4.9) to (4.11), we determine the following correlator

$$L(f_\mathrm{m}) = -\frac{2n_0|S_0|}{\pi(i+2\pi f_\mathrm{m}T_\mathrm{m})} \tag{4.12}$$

and its modulus

$$|L(f_\mathrm{m})| = \frac{L_0}{\sqrt{1+(2\pi f_\mathrm{m}T_S)^2}},\ L_0 = \frac{2n_0|S_0|}{\pi}, \tag{4.13}$$

which is the actual quantity measured by the lock-in amplifier. Here, Eq. (4.13) allows us to extract the spin lifetime T_S by measuring the KR amplitude at the same conditions, e. g., temperature T, magnetic field B_F and pump power P_Pu, for different helicity modulation frequencies f_m and determine T_S from a fit to the KR amplitude in dependence on f_m.

However, the spin lifetime T_S depends on the pump power ($G \propto P_{\mathrm{Pu}}$, cf. Eq. (4.4)). Therefore, it is no suitable quantity to characterize the electrons spin dynamics. To obtain the spin relaxation time τ_S, which is independent of the pump power and equal to the T_1 time in a magnetic field, we have to determine T_S for several different P_{Pu}, plot the inverse spin lifetime $1/T_S$ against P_{Pu} and extrapolate to zero pump power (cf. Eq. (4.4))

$$\lim_{G\to 0} \frac{1}{T_S}(G) \to \frac{1}{\tau_S}. \tag{4.14}$$

In the following section, this procedure is used to determine the spin relaxation time of the donor-bound electron spins in sample #1 and sample #2.

4.2.3 Measurement of the Spin Relaxation Time

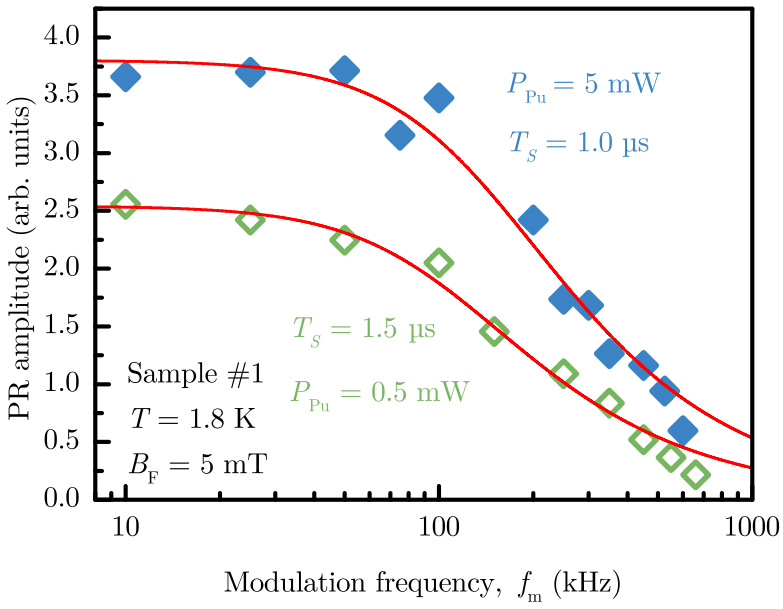

Figure 4.5 Measurements of PR amplitudes at constant magnetic field $B_{\mathrm{F}} = 5\,\mathrm{mT}$ in dependence on f_{m} for sample #1 at two different pump powers ($P_{\mathrm{Pu}} = 0.5\,\mathrm{mW}$ and $5\,\mathrm{mW}$). The red lines are nonlinear fits to the corresponding data using Eq. (4.13).

Figure 4.5 shows measurements of PR amplitudes in dependence on f_{m}, performed at two different pump powers $P_{\mathrm{Pu}} = 0.5\,\mathrm{mW}$ and $5\,\mathrm{mW}$. The amplitude was determined at $B_{\mathrm{F}} = 5\,\mathrm{mT}$ from PR measurements, as shown in Figs. 4.1 and 4.3. At both pump powers, the PR amplitudes remain nearly constant at low modulation frequencies on the order of a few $10\,\mathrm{kHz}$, while the amplitudes exhibit a strong decrease above $100\,\mathrm{kHz}$ ("cutoff frequency"). The red lines show best fits to the data using Eq. (4.13) with the amplitude of the correlator L_0 and the spin lifetime T_S as the fitting parameters. Table 4.2 shows these parameters. Note that the errors stated are obtained from the fit, and possible systematic errors might exceed these errors by far. While at the higher pump power $P_{\mathrm{Pu}} = 5\,\mathrm{mW}$ we obtain $T_S = 1.0\,\mu\mathrm{s}$, the spin lifetime increases to $1.5\,\mu\mathrm{s}$ at $P_{\mathrm{Pu}} = 0.5\,\mathrm{mW}$. This indicates

Table 4.2 Parameters of the best fits to the PR amplitude in dependence on f_{m} for $P_{\mathrm{Pu}} = 0.5\,\mathrm{mW}$ and 5 mW, shown in Fig. 4.5. The errors are obtained from the fit.

P_{Pu}			
5 mW	L_0	3.8 ± 0.1	arb. units
	T_S	1.0 ± 0.1	µs
0.5 mW	L_0	2.5 ± 0.1	arb. units
	T_S	1.5 ± 0.1	µs

that a stronger optical excitation indeed speeds up the electron spin relaxation. To investigate this further and to check the validity of Eq. (4.4), we performed additional measurements at $P_{\mathrm{Pu}} = 1.7\,\mathrm{mW}$, 2.3 mW, and 3.3 mW.

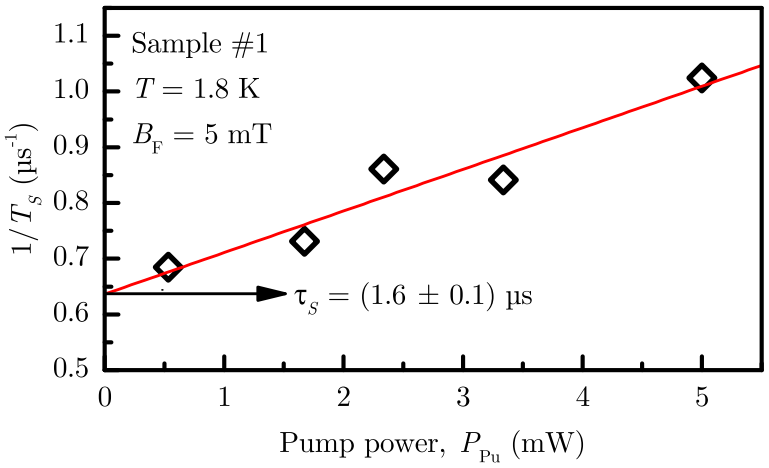

Figure 4.6 Inverse spin lifetime $1/T_S$ in dependence on the pump power. The red line is a linear fit to the data using the following equation: $1/T_S = m \cdot P_{\mathrm{Pu}} + b$ (see Eq. (4.4))

Figure 4.6 shows the inverse spin lifetime $1/T_S$ in dependence on the pump powerP_{Pu}, where the T_S are obtained from nonlinear best fits to the PR amplitude as a function of the modulation frequency with Eq. (4.13). The red line is a linear fit to the data using Eq. (4.4). Table 4.3 shows the parameters of this fit. We calculated τ_S from the fitting

Table 4.3 Parameters of the linear fit shown in Fig. 4.6. The errors are obtained from the fit.

m	0.07 ± 0.01	$\mu\mathrm{s}^{-1}\mathrm{mW}^{-1}$
b	0.64 ± 0.04	$\mu\mathrm{s}^{-1}$

parameter b (y-intersection)

$$\tau_S = \frac{1}{b}. \tag{4.15}$$

According to Gaussian error propagation, the relative error of the spin relaxation time η_{τ_S}

is equal to the relative error of the y-intersection η_b. It can be calculated as follows

$$\eta_b = \frac{\sigma_b}{b}, \qquad (4.16)$$
$$\eta_b = 6.03\,\%.$$

Here, the absolute error of the y-intersection $\sigma_b = 0.04\,\mu s^{-1}mW^{-1}$ is used. Using Eq. (4.15) and $\eta_{\tau_S} = \eta_b$, we obtain a spin relaxation time

$$\tau_S = (1.6 \pm 0.1)\,\mu s.$$

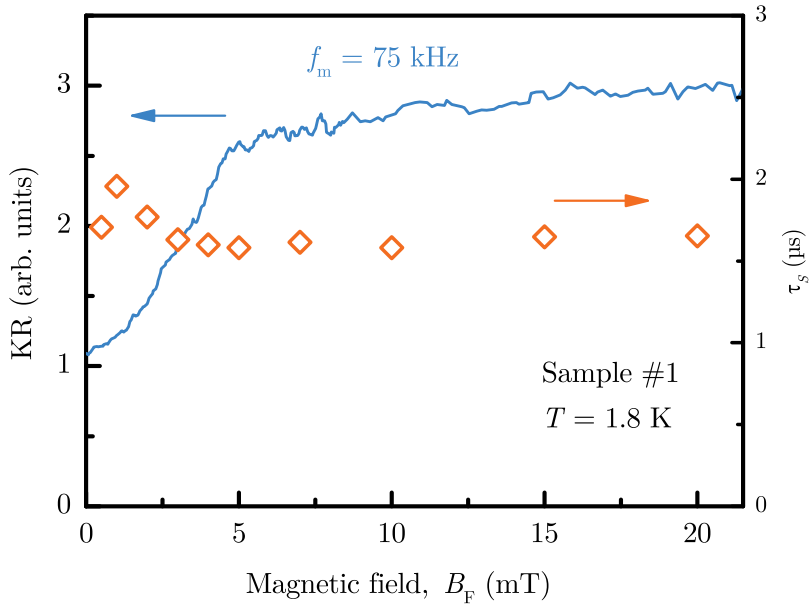

Figure 4.7 The blue line is a "typical" PR measurement for sample #1, performed at a pump power of $P_{Pu} = 5\,mW$. The orange diamonds show spin relaxation times τ_S for sample #1 in dependence on B_F (right scale), calculated from PR measurements. The PR amplitude in dependence on f_m at fixed B_F and P_{Pu} yields the spin lifetime T_S (cf. Fig. 4.5). The spin relaxation τ_S is extrapolated from $1/T_S$ as a function of P_{Pu}.

Figures 4.5 and 4.6 show data determined at fixed magnetic field $B_F = 5\,mT$. However, these data were obtained from "full" PR measurements, which cover a range from about $-20\,mT$ to $20\,mT$, so we can use these measurements to investigate the magnetic field dependence of τ_S in this range. The orange diamonds in Fig. 4.7 show spin relaxation times in dependence on B_F, calculated from the PR amplitude in dependence on f_m at fixed magnetic field. τ_S remains nearly constant in the studied magnetic field range, and the range of the data set is of the same order of magnitude as the error of the fit $\sigma_{\tau_S} \approx 0.1\,\mu s$. The blue line in Fig. 4.7 shows a PR measurement for the same magnetic field range as the τ_S data.

While the spin relaxation time τ_S remains nearly constant in the displayed magnetic field range, the KR signal increases from its minimum at $B_F = 0$ to its saturation value

at about 20 mT (cf. Section 4.1). This is in good agreement with the behavior shown in Fig. 4.3, where the spin inertia effect occurs as a decrease in the overall amplitude of the PR curves (cf. A_0 in Eq. (4.2)) with increasing modulation frequency f_m, but does not seem to alter the shape of the PR curves. However, we still might observe a dependence of

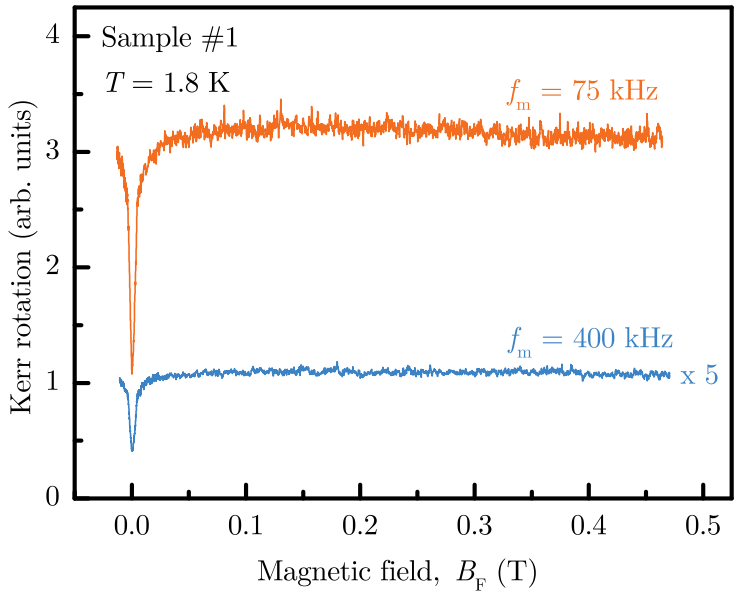

Figure 4.8 Two PR measurements over an extended magnetic field range at $P_{Pu} = 7\,\text{mW}$. The orange line shows a measurement at $f_m = 75\,\text{kHz}$. The data, obtained at at $f_m = 400\,\text{kHz}$, (blue line) are multiplied by a factor of 5, so that we can compare the shape of the curves more easily.

the spin relaxation time on B_F at stronger fields exceeding the range of a PR measurement. Figure 4.8 shows two PR measurements performed over an extended magnetic field range from about $-0.01\,\text{T}$ to $0.47\,\text{T}$. The pump power is $P_{Pu} = 7\,\text{mW}$ for both measurements. The PR curve measured at $f_m = 75\,\text{kHz}$ (blue line) exhibits a dip at $B_F = 0$, increases to its saturation value at about $0.02\,\text{T}$ and then remains constant. The same behavior can be observed for the PR curve, measured at $f_m = 400\,\text{kHz}$. Here, the data are multiplied by a factor of 5 to simplify the comparison of both curves. These observations suggest that τ_S does not depend on B_F in the investigated range. Figure 4.9 shows the result of additional measurements at different B_F of even larger magnitude. The diamond symbols show the PR amplitude in dependence on f_m at $B_F = 0.5\,\text{T}$, $1.0\,\text{T}$, $1.5\,\text{T}$, $2.0\,\text{T}$, and $2.5\,\text{T}$ for sample #1. The PR amplitudes do not exhibit any dependence on the magnetic field, and the whole data set fits well to the best fit to the data at $B_F = 0.5\,\text{T}$ (red line) using Eq. (4.13).

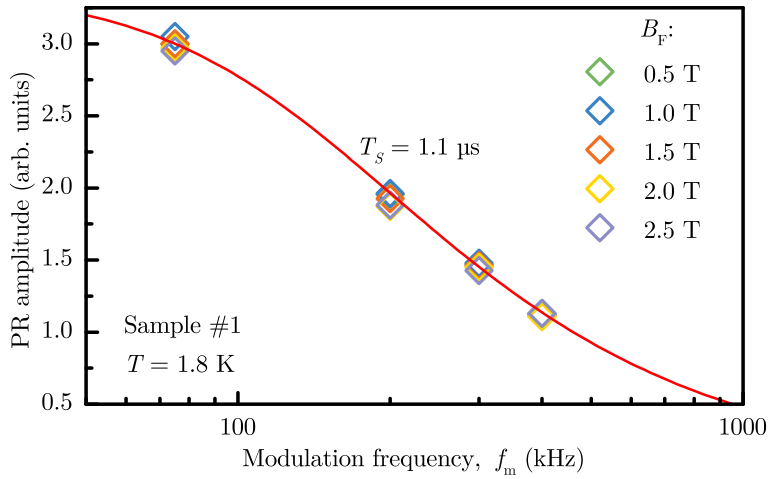

Figure 4.9 PR amplitude in dependence on f_m measured at $B_F = 0.5\,T$, $1.0\,T$, $1.5\,T$, $2.0\,T$, and $2.5\,T$. The red line is a fit to the data at $B_F = 0.5\,T$ using Eq. (4.13), but also fits well to the data at other B_F. The pump power is at $P_{Pu} = 7\,mW$ for all measurements.

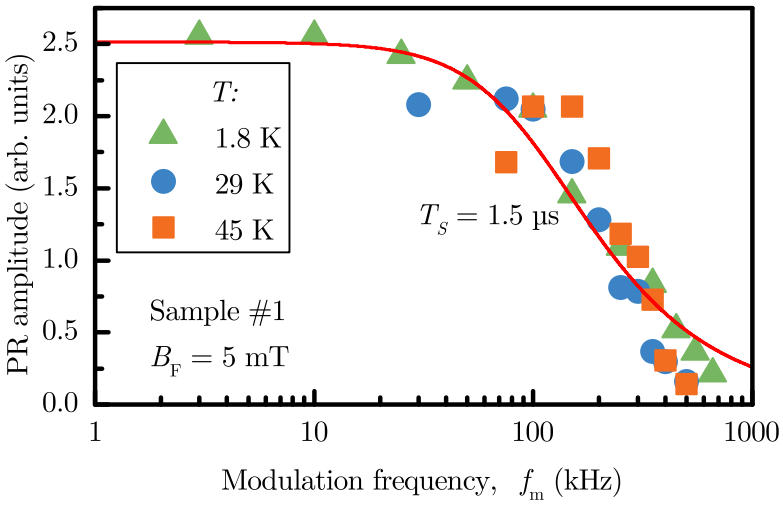

Figure 4.10 PR amplitude in dependence on f_m measured at $B_F = 5\,mT$ at the following temperatures $T = 1.8\,K$, $29\,K$, and $45\,K$. The red line is a fit to the data at $T = 1.8\,K$ using Eq. (4.13). The pump power is at $P_{Pu} = 1.2\,mW$ for all measurements.

To gain further inside into the spin dynamics of the donor-bound electrons, we investigate a possible temperature dependence of the spin relaxation time τ_S. Figure 4.10 shows the PR amplitude in dependence on f_m measured at $T = 1.8\,K$, $29\,K$, and $45\,K$. The pump power is at $P_{Pu} = 1.2\,mW$ and the amplitudes are determined from the measured PR curves at the magnetic field position $B_F = 5\,mT$. The PR amplitude decreases at elevated

temperatures and the data at $T = 29\,\mathrm{K}$ are normalized to the measurement at $T = 1.8\,\mathrm{K}$ and $f_\mathrm{m} = 100\,\mathrm{kHz}$. The red line is a best fit to the data at $T = 1.8\,\mathrm{K}$ yielding $T_S = 1.5\,\mu\mathrm{s}$. The shape of the PR amplitude in dependence on f_m remains nearly the same at the higher temperatures, and the data are consistent with the fit. Thus, we conclude that the spin lifetime T_S and as a consequence also the spin relaxation time τ_S (see Eq. (4.4)) do not exhibit any dependence on the temperature T in the range from 1.8 K to 45 K.

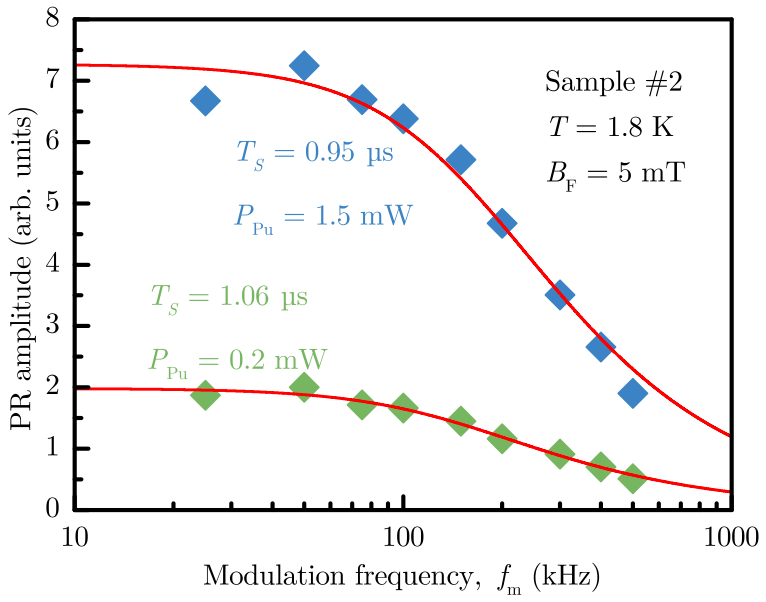

Figure 4.11 Measurements of PR amplitudes at constant magnetic field $B_\mathrm{F} = 5\,\mathrm{mT}$ in dependence on f_m for sample #2 at two different pump powers ($P_\mathrm{Pu} = 0.2\,\mathrm{mW}$ and 1.5 mW). The red lines are nonlinear fits to the corresponding data using Eq. (4.13).

As a first test of the influence of the donor concentration, we determine the spin relaxation time τ_S of the donor-bound electrons in sample #2 ($n_\mathrm{F} \approx 1 \times 10^{18}\,/\mathrm{cm}^3$), whose donor concentration is three orders of magnitude higher than for sample #1 ($n_\mathrm{F} \approx 1 \times 10^{15}\,/\mathrm{cm}^3$. Figure 4.11 shows the corresponding measurements to determine the spin lifetime T_S at different pump powers for this sample. Here, the amplitude at $B_\mathrm{F} = 5\,\mathrm{mT}$ in dependence on the modulation frequency is obtained from PR measurements. Note that the procedure and even more important the conditions were the same as those used for sample #1 (see Figs. 4.5 and 4.6), while the wavelength of the laser is adjusted to ensure resonant D^0X-HH excitation.

In addition to the shown dependencies at $P_\mathrm{Pu} = 0.2\,\mathrm{mW}$ and 1.5 mW, the spin lifetime was also determined from measurements at $P_\mathrm{Pu} = 0.5\,\mathrm{mW}$ and 0.75 mW. Figure 4.12 shows the resulting inverse spin lifetime as a function of P_Pu and a linear fit to the data. The extrapolated spin relaxation time is $\tau_S = (1.09 \pm 0.03)\,\mu\mathrm{s}$ (see Eqs. (4.15)). Here, the error is given by Gaussian error propagation of the error of the intersection b of the fit (cf. Eq. (4.16)).

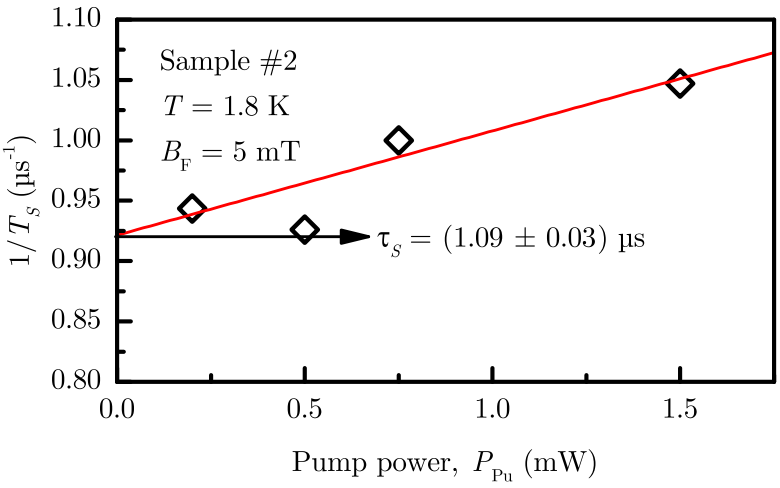

Figure 4.12 Inverse spin lifetime $1/T_S$ in dependence on the pump power P_{Pu} for sample #2. The red line is a linear fit to the data using the following equation $1/T_S = m \cdot P_{\mathrm{Pu}} + b$ (see Eq. (4.4)).

4.3 Discussion

The measured spin relaxation times $\tau_S = (1.6 \pm 0.1)$ µs for sample #1 ($n_{\mathrm{F}} \approx 1 \times 10^{15}$ /cm^3) and $\tau_S = (1.09 \pm 0.03)$ µs for sample #2 ($n_{\mathrm{F}} \approx 1 \times 10^{18}$ /cm^3) are not among the longest determined in experiment. For example, Jarmola *et. al.* demonstrated a T_1 time of about 200 s at $T = 10$ K for electron spins bound to nitrogen-vacancies (NVs) in synthetic diamond with a low NV center concentration (cf. also discussion of different material systems in Chap. 1). Akimov *et al.* [Aki06; Aki09] determined spin-flip times of about 10 µs for an electron spin in a single CdSe/ZnSe quantum dot.

However, the spin relaxation times τ_S determined for fluorine-doped ZnSe are long enough to hint on a certain potential of this material system as a quantum bit. From a purely scientific point of view not the determined spin relaxation time for sample #1 itself, but its independence of the temperature T in the studied range from 1.8 K to 45 K and of the longitudinal magnetic field B_{F} from 0 T to 2.5 T is a surprising result. One commonly observes a dependence of the spin relaxation time on the magnetic field, e. g., $T_1 \propto B_{\mathrm{F}}^{-\nu}$, $3 \lesssim \nu \lesssim 4$ for electrons bound to donor impurities [Fu06; Lin16].

While Colton *et al.* [Col04] measured a T_1 of up to 1.4 µs in an n-doped GaAs/AlGaAs heterostructure (1 μm GaAs epilayer) with a donor concentration of $n_{\mathrm{D}} = 3 \times 10^{15}$ /cm^3, Fu *et. al* [Fu06] demonstrated a T_1 time of a few µs in an n-doped high purity GaAs sample, but here the donor concentration ($n_{\mathrm{D}} \approx 5 \times 10^{13}$ cm^{-3}) was two orders of magnitude smaller. Thereby, the huge discrepancy between the results for the same material was assigned to the increased spin-spin interaction in the higher doped sample by the authors of the latter publication. Thus, the spin relaxation time in weaker doped ZnSe layers might be increased as well.

For the discussion of possible spin relaxation mechanisms in the studied samples in particular, but also from a more general point of view, it is useful to describe the spin

relaxation as the effect of temporally fluctuating magnetic fields on the electron spin [Hei15b]. If these fields fluctuate on timescales, which are very short compared to the spin relaxation time ($\tau_S \gg \tau_c$, τ_c: correlation time of the fluctuating magnetic fields), they are averaged dynamically, and the spin relaxation can be described by the relatively simple Eq. (4.6). The spin relaxation time does not change for magnetic fields B_F from 0 T to 2.5 T, and we can conclude that the fluctuating fields can overcome the Zeeman splitting of the electron spins even at 2.5 T. This implies that the field, which describes the dominating relaxation mechanism must have a wide frequency range and, thus, a correlation time τ_c, which is limited by (energy-time uncertainty principle) [Hei15b]

$$\tau_c < \frac{\hbar}{\mu_B g_e B_F} \approx 4.0\,\text{ps}.$$

As a consequence, the following discussion of possible relaxation mechanisms focuses on processes which could occur on very short timescales [Hei15b]:

1. Spin-flip scatterings by phonons (Elliott-Yafet mechanism) [Ell54; Ake15].

2. Spin relaxation due to spin-orbit coupling and its modulation by lattice vibrations (phonons) [Pin57].

3. Jumps of electrons between different donor: The exchange interaction between electrons on neighboring donors and jumps of electrons to unoccupied donor sites can lead to electron spin flip-flop transitions [Kav08].

4. Scattering between free and donor-bound electrons, which leads to electron spin flips due to the exchange interaction.

5. Charge fluctuations in the environment of the donors, which, e. g., could occur during the pulsed optical excitation with a pulse width of about 1.5 ps [Hei15b].

We can discard the 1. process, since we do not observe a dependence of the spin relaxation time τ_S on the temperature T in the range from 1.8 K to 45 K and a spin relaxation rate due to phonon scattering should exhibit a temperature dependence.

The 2. process can be excluded as an explanation for the spin relaxation in the studied magnetic field range, because according to Eq. (12) in Ref. [Pin57] the inverse relaxation time $(1/T_1)_{SO}$ resulting from this mechanism is proportional to the fourth power of the Zeeman splitting between the $|\downarrow\rangle$- and the $|\uparrow\rangle$-state - in other words to the fourth power of the Larmor frequency $\omega_L = (E_\uparrow - E_\downarrow)/\hbar = (g_e \mu_B B_F)/\hbar$. Thus, τ_S and the T_1 time respectively should exhibit a B_F^{-4} dependence. However, Fu *et al.* [Fu06] measured a T_1 time of several milliseconds of the donor-bound electrons in n-doped GaAs (see also Ref. [Lin16]) and found that this particular mechanism occurred only at sufficiently high magnetic fields ($B_F > 5$ T). Here, the magnitude of the field at which the mechanism became dominant could be approximated with the following inequality

$$g_e \mu_B B_F > k_B T. \tag{4.17}$$

For the parameters of the samples $g_e = 1.1 \pm 0.1$ [Gre12], the experiment $T = 1.8\,\mathrm{K}$ and the values of the constants [Moh15] $\mu_B = 5.7884 \times 10^{-5}\,\mathrm{eV\,T^{-1}}$ and $k_B = 8.6173 \times 10^{-5}\,\mathrm{eV\,K^{-1}}$ we obtain

$$B_F > (2.4 \pm 0.2)\,\mathrm{T},$$

which is close to the maximum of the investigated field range. Thus, it might be interesting to investigate the magnetic field dependence at even lower temperatures or at higher magnetic fields using a different cryostat with only a single split-coil.

The spin relaxation due to jumps of electrons between donor-sites (3. process) was described theoretically by Kavokin [Kav08]. Calculations by Korenev (see Ref. [Hei15b]) with the parameters of the material system studied here yielded a jump time, which by far exceeds the estimated 4 ps.

The 4. process is implausible, because the binding of the electrons to the fluorine donors should depend on the temperature in the range from 30 K to 45 K [Hei15b]. Furthermore, the laser was tuned into resonance with the donor-bound heavy hole exciton, so there should not be any photo-excited electrons with excess energy relaxing to this state, which, in turn, could be scattered by the donor-bound electrons.

Thus, the only mechanism remaining is the 5. process - charge fluctuations in the vicinity of the donors, which could be caused by the pulsed laser excitation. However, we tested the influence of a pulsed pump on the spin relaxation time τ_S by performing measurements with a CW pump, while the probe beam remained a train of picosecond pulses. The change of τ_S was negligible and neither its dependence on the magnetic field ($\tau_S = \tau_S(B_F)$) nor its dependence on the temperature exhibited any changes compared to the measurements with the pulsed pump beam. Nevertheless, this mechanism is the most likely explanation apart from new and unknown mechanisms. Here, it is important to note that these observations only allow us to exclude a direct influence of the pulsed pump beam. Even a CW excitation can induce charge fluctuations due to the fast carrier recombination within hundreds of picoseconds [Gre12; Hei15b].

4.4 Conclusion

The spin inertia method is neither the first nor the only method to measure the longitudinal spin relaxation time of electrons in semiconductors. However, it represents a novel approach to study the longitudinal spin dynamics and offers some advantages, especially in comparison to the "common" measurement of the Hanle curve [Han24; Hap72; Ale73; Bud02].

The method based on the Hanle effect employs the Larmor precession of the electron spins in a magnetic field applied in the Voigt geometry as a "clock" intrinsic to the system. However, to calculate the spin lifetime T_S from the half-width at half maximum $B_{1/2}$ of the Hanle curve an independent measurement of the electron g factor g_e is required. The method does not allow one to determine the spin relaxation time τ_S as a function of the magnetic field, while the spin inertia method, which uses an external "clock," can be used to determine τ_S in the whole range of longitudinal magnetic field limited only by the specifications of the magnet. Furthermore, the measurement of the Hanle curve only yields the spin lifetime T_S (the spin relaxation time τ_S in the limit of zero excitation density), if the relaxation time approximation is valid [Hei15b], i. e., the relaxation is caused by

processes with short correlation times (Markovian processes [Mar90; How12]). Then one can assume a dynamic averaging of the magnetic fields of different origin, which cause the relaxation of the electron spin. If, however, the electrons spins are strongly localized as it is the case in the material system under study or, e. g., in QDs, this approximation is not valid, because here the dwell time of an electron at the fluorine donor or in the QD is long compared to the precession period in the hyperfine fields of the nuclei with nonzero nuclear spin. As a result, the width of the Hanle curve is then determined by the inhomogeneous spin dephasing time T_2^* in these fields [Eps01; Dzh02; Mer02; Kuz13] and not by the spin lifetime T_S or the spin relaxation time τ_S and longitudinal spin relaxation time T_1, respectively, in the limit of zero excitation density.

In contrast to this, the spin inertia method can and has been used to study material systems with strongly localized electron spins - here the electron spins bound to the fluorine donors in ZnSe - where there is no dynamic averaging of the magnetic fields of different origin, i. e., the measurement of the Hanle curve does not allow one to determine the T_1 time. It can be used to measure the T_1 time in the whole range of longitudinal magnetic field starting from zero field. However, two requirements have to be fulfilled to employ this method [Hei15b]:

1. It must be possible to optically create a detectable spin polarization (at least a few percent).

2. The spin relaxation time or the lifetime of the polarized carriers should be neither too long (line filter of the lock-in amplifier) nor too short (maximum frequency of the EOM, the lock-in amplifier or the balanced photoreceiver; increased risk of a frequency dependent response of the equipment or cables). For the setup employed here the author recommends to study samples with estimated τ_S from about 100 ns to 5 ms.

These two rather technical requirements are the only limitations of the spin inertia method, but one should characterize the frequency dependence of all equipment before the measurements to ensure an accurate result.

Below a comparison to other methods, which did not involve a measurement of the Hanle curve, is presented. The comparison is made in chronological order.

Colton *et al.* determined the T_1 time of electron spins in n-doped GaAs from time-resolved measurements of the degree of circular polarization of the PL of free excitons [Col04]. Here, nanosecond pulses (pump: 256 ns, probe: 16 ns) were cut from a CW laser using an acousto-optical modulator (AOM). Both pulses were circularly polarized and their time delay was varied. A photoelastic modulator (PEM, retardance: $\lambda/4$ plate) in combination with a linear polarizer in the detection path analyzed the PL excited by the probe pulses. A disadvantage of this pioneering scheme compared to the spin inertia method is that the probe pulses also alter the spin polarization, since they are circularly polarized. Furthermore, the time resolution is limited by the minimum pulse width of about 15 ns compared to mode-locked lasers with pulses in the femtosecond range and the detection relies on the fast spin exchange of photoexcited and resident electrons [Vek76; Pag81; Pag82; Col04].

Akimov *et al.* used another method, which is very similar to the spin inertia method, to study the electron spin dynamics in a CdSe/ZnSe Stranski-Krastanov quantum dot

(QD) [Aki06; Aki09]. While the helicity was also modulated, here the detection relied on a time-resolved measurement of the polarization degree of the emission from the trion ground state singlet, but the transients upon switching the helicity were recorded directly. The method presented in this thesis is a very similar approach adapted to the pump-probe regime. However, it is important to note that this modification of the method with the pulsed excitation has an advantage, when it is employed to study samples with resident carriers: The measurement of the KR signal at a small negative time-delay prior to the arrival of the next pump pulse simplifies the interpretation of the origin of the signal. Usually, the exciton recombination time τ_X is much shorter than the laser repetition period T_R (here: $\tau_\mathrm{X} = 210\,\mathrm{ps} \ll T_\mathrm{R}$ [Gre12]) so that the signal before the next pump pulse should originate from spin-polarized resident electrons only. In contrast to this, the trion lifetime had to be taken into account for the analysis of the transients in Refs. [Aki06; Aki09].

Fu *et al.* used a technique, which was based on optical pumping to the $|\uparrow\rangle$-state and a consecutive PL excitation measurement of the repopulation of the $|\downarrow\rangle$-state, to measure the magnetic field dependence of the T_1 time of the donor-bound electrons in high purity n-doped GaAs. In contrast to the spin inertia method and the work of Colton *et al.* [Col04], the magnetic field was applied in the Voigt geometry. However, the spectral filtering, employed for the detection of the spin polarization, only worked for magnetic fields $B_\mathrm{V} > 4\,\mathrm{T}$. Thus, this method can only yield a lower limit of the T_1 time at $B_\mathrm{V} < 4\,\mathrm{T}$, which is a disadvantage compared to the spin inertia method.

Heiss *et al.* determined the hole spin relaxation time T_1^h directly from the degree of circular polarization of the electroluminescence of an ensemble of singly charged InGaAs/GaAs QDs [Hei07]. To that end, single QD layers were located in the intrinsic region of a $n-i-$metal photodiode. The charge of the dots and the spin polarization were prepared optically, stored and subsequently read out by a forward bias pulse at the photodiode after a variable time delay Δt. Using this scheme the hole spin relaxation time in dependence on the temperature and the magnetic field was investigated, where the maximal time $T_1^h = (270 \pm 180)\,\mu\mathrm{s}$ was measured at $T = 8\,\mathrm{K}$ and $B = 1.5\,\mathrm{T}$. While allowing for a direct measurement of the spin relaxation time, this technique is limited to sample structures (diodes, gated QDs) that allow one to apply a voltage to induce electroluminescence. Moreover, it is more perturbative than the spin inertia method, since the system is strongly disturbed by the current injection.

Another direct approach was based on measurements of the photoinduced circular dichroism (PCD) using the optical pump-probe technique [Fra11], where the range of possible delays between the pump and the probe was extended by increasing the interval between the pump pulses with a pulse picker and by modulating the probe beam at $f_\mathrm{m} = 470\,\mathrm{kHz}$. This way the hole spin relaxation time $T_1^\mathrm{h} = (650 \pm 100)\,\mathrm{ns}$ in InAs/GaAs QDs was measured, but according to the authors the signal-to-noise ratio decreased for increased intervals between the pump pulses and the decrease of the average pump power with increasing interval required a complex model rather than a simple mono-exponential decay. In addition to this modification of the "conventional" pump-probe scheme, a second method, called dark-bright time-scanning spectroscopy (DTS), was used to verify this result and a similar hole spin relaxation time of $T_1^\mathrm{h} = (900 \pm 100)\,\mathrm{ns}$ was measured. The DTS was based on a differential absorption measurement (PCD measurement), where the intensity of the pump beam was modulated using an acousto-optical modulator (AOM),

which allowed one to set bright and dark intervals of variable duration. Thus, this method is similar to the spin inertia method and according to the authors of Ref. [Fra11] can be used for a similar range of relaxation times from 50 ns to 1 ms.

In Ref. [Col12] a direct measurement of the electron spin relaxation time T_1 in an n-doped 14 nm GaAs quantum well (QW), based on a two-color pump-probe scheme, was demonstrated. Removing the influence of the nuclear polarization with an additional radio frequency excitation a T_1 time of about 1 µs was measured at $T = 1.5\,\mathrm{K}$ and $B_\mathrm{F} = 1.5\,\mathrm{T}$. While the spin polarization was determined from the KR of the linearly polarized probe beam as in the "traditional" TRKR technique, the time-delay between pump and probe was controlled by electronic gating, which allowed for much longer delays than a commonly used mechanical delay line. The probe pulses were cut from a CW laser with an AOM (pulse width about 10 ns) and the pump pulses provided by fast diode laser so that the time resolution of this scheme was limited.

Belykh *et al.* extended the "traditional" pump-probe Faraday rotation technique with tailored trains of pump pulses down to single pulses, cut out from the pulse train of a mode-locked laser with a repetition rate of 76 MHz with an EOM, and by increasing the interval between probe pulses with a pulse picker [Bel16]. This scheme provided access to a very long time range compared to a mechanical delay, but in contrast to Ref. [Col12] still offered a picosecond time resolution. Thereby, the submicrosecond electron spin dynamics in n-type bulk GaAs was measured, where a spin relaxation time T_1 of up to 270 ns was observed. Compared to the spin inertia method the so-called extended pump-probe Faraday rotation spectroscopy offers many advantages, e. g., resolving nontrivial spin dynamics and access to electron or hole spin synchronization under periodic laser excitation [Bel16], but is more demanding in terms of the necessary equipment and suffers from a decreased signal-to-noise ratio due to the decreased average pump and probe power. Thus, the spin inertia method can be an alternative to this more universal and sophisticated method, if the signal-to-noise ratio is already low in "traditional" pump-probe Faraday spectroscopy or the necessary equipment is not available.

There is nothing that nuclear spins will not do for you, as long as you treat them as human beings.

Erwin Hahn [Lia99]

5 Inhomogeneous Nuclear Spin Polarization

Zhukov *et al.* [Zhu14] demonstrated that despite contrary claims in the literature [Ast08a; Fli10; Gre12; Col12] a helicity modulated excitation does not necessarily suppress the build-up of a dynamic nuclear polarization (DNP). Moreover, the authors even developed an all-optical nuclear magnetic resonance (NMR) technique. It was based on the time-resolved Kerr rotation (TRKR) in the resonant spin amplification (RSA) configuration and relied on a helicity modulated pump beam to address the NMR. In this chapter, the nature of the observed NMR in fluorine-doped zinc selenide will be investigated.

5.1 Observation of Nuclear Polarization under Helicity-modulated Excitation

Despite the claims in the literature we observe signatures, indicating nuclear effects, in the RSA spectra (cf. Section 3.4.1) for samples #1 and #2, which were measured using a helicity modulated pump beam. Figure 5.1(a) shows several RSA spectra of sample #2, measured at different pump powers P_{Pu} ranging from 0.1 mW to 8 mW. The measurements were performed at a temperature of $T = 1.8\,\mathrm{K}$, a helicity modulation frequency of $f_{\mathrm{m}} = 185\,\mathrm{kHz}$, and a probe power of $P_{\mathrm{Pr}} = 0.5\,\mathrm{mW}$. The spectra are normalized and translated vertically relative to each other in order to stress the key observation: The positions of the peaks in the range from 15 mT to 40 mT change in dependence on the pump power P_{Pu} compared to their position at $P_{\mathrm{Pu}} = 0.1\,\mathrm{mW}$. This behavior shall be denoted "shift" from here on. The left inset is a magnified illustration of the peak at $B_{\mathrm{V}} = 28.5\,\mathrm{mT}$ that shows how the shift compared to the peak position at $P_{\mathrm{Pr}} = 0.1\,\mathrm{mW}$ increased when increasing the pump power. The shift as a function of the pump power (right inset) exhibits a saturation behavior.

We calculated the difference between the peak positions at $P_{\mathrm{Pu}} = 8\,\mathrm{mW}$ compared to the positions at $P_{\mathrm{Pu}} = 0.1\,\mathrm{mW}$ as a function of the peak position (magnetic field B_{V}) at $P_{\mathrm{Pu}} = 0.1\,\mathrm{mW}$ (see black solid circles in Fig. 5.1(b), the black lines are shown as a guide to the eye). Figure 5.2 shows how the peak positions, needed for the calculation of this shift, were obtained: To reproducibly determine the peak positions, the `Peak Analyzer` of `Origin Pro 9.0` was used to fit Lorentz curves (Lorentzians) to the peaks

$$\theta_{\mathrm{KR}}(B_{\mathrm{V}}) = A_{\mathrm{off}} + \sum_i \frac{2A_i}{\pi} \frac{B_{\mathrm{FWHM},i}}{4(B_{\mathrm{V}} - B_{\mathrm{c},i})^2 + B_{\mathrm{FWHM},i}^2}. \tag{5.1}$$

Here, A_{off} is the offset of the KR signal; A_i are the amplitudes of the Lorentzians and $B_{\mathrm{FWHM},i}$ their full-width at half maximum (FWHM). Most important are the location

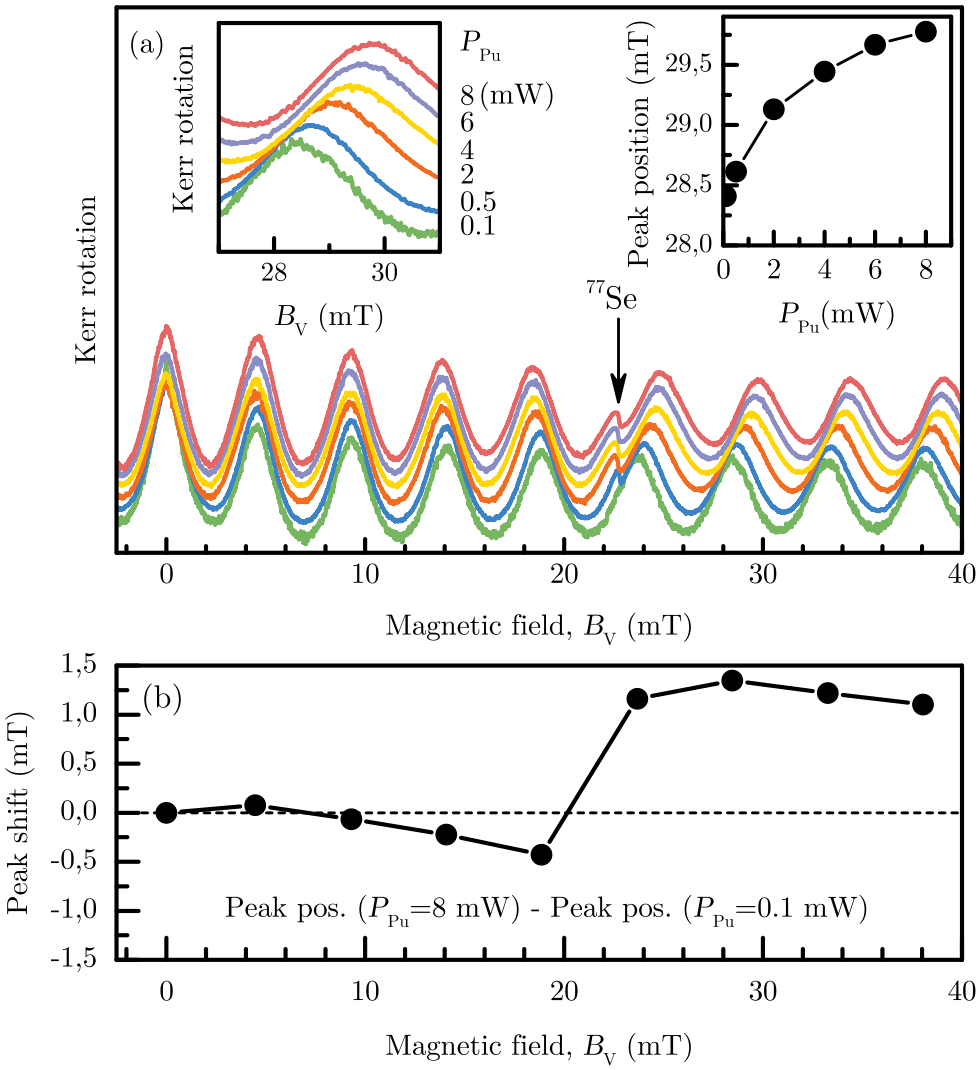

Figure 5.1 (a) Normalized RSA spectra, measured at different pump powers. The left inset illustrates the changes of a single peak with increasing pump power P_{Pu}, while the right inset shows the dependence of the peak position on P_{Pu}. (b) Pump power induced change of the peak position (peak shift) as a function of the peak position (magnetic field B_V) at $P_{Pu} = 0.1\,\mathrm{mW}$.

parameters $B_{c,i}$ of the Lorentzians, yielding the RSA peak positions. The resulting dependence exhibits a dispersive profile with the resonance at $B_V \approx 23\,\mathrm{mT}$, i.e., the peaks at smaller B_V than the resonance are shifted in the direction of smaller magnetic field, while the peaks at higher magnetic field are shifted towards higher magnetic fields.

However, the peak at $B_V = 23.85\,\mathrm{mT}$ ($P_{Pu} = 0.1\,\mathrm{mW}$), i.e., the peak at the resonance position, deviates from a single Lorentzian and exhibits a small additional peak at the left flank at $P_{Pu} \geq 0.5\,\mathrm{mW}$. The magnitude of this additional peak increases with increasing pump power, while its position remains unchanged at $B_V = 22.6\,\mathrm{mT}$. Explanations of these

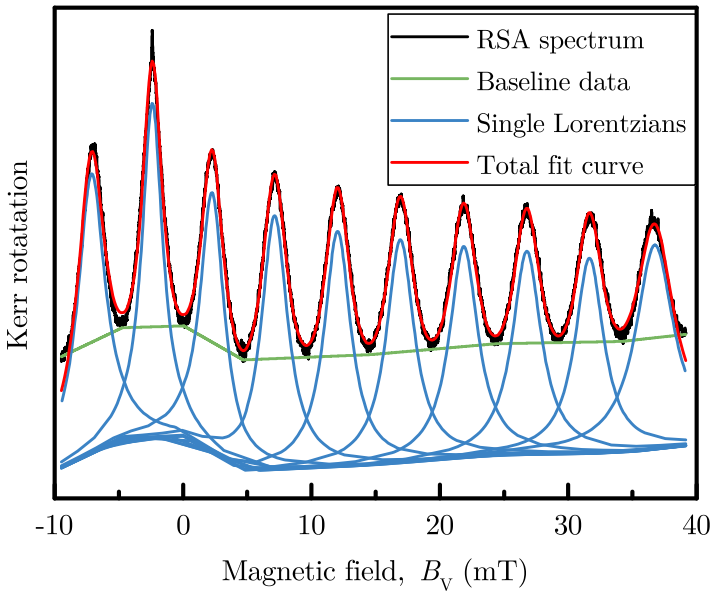

Figure 5.2 Example of the determination of the RSA peak position. Here the RSA spectrum at $P_{\mathrm{Pu}} = 0.1\,\mathrm{mW}$, also depicted in Fig. 5.1, was fitted with Lorentzians (blue lines) using the `Peak Analyzer of Origin Pro 9.0`. The green line is the baseline data used for the fit, and the red line represents the superposition of all Lorentzians.

phenomena will be given in Section 5.4. For now the dispersive profile shall be referred to as *broad signature* and the small additional peak as *narrow signature*.

Considering the theory of RSA, the spacing of the RSA peaks should be given by the phase synchronization condition (cf. Section 3.4.1 and Ref. [Yug12])

$$\omega_{\mathrm{L}} = N\frac{2\pi}{T_{\mathrm{R}}},\ N \in \mathbb{N}, \tag{5.2}$$

$$\frac{\mu_{\mathrm{B}} g_{\mathrm{e}} B}{\hbar} = N\frac{2\pi}{T_{\mathrm{R}}}. \tag{5.3}$$

RSA is a very sensitive method to measure the Larmor precession frequency of the electron spins. However, the magnitude of the magnetic field B, which determines the Larmor frequency ω_{L}, is not necessarily solely determined by the external magnetic field B_{V}. It can be a superposition of the external field and additional fields within the sample, which change the effective magnetic field leading to the Larmor precession.

Thus, a shift of the RSA peaks reflects a change of the Larmor precession frequency ω_{L} and we conclude that this change is caused by an additional magnetic field. It was demonstrated that nuclear magnetic resonances (NMRs) could be provided all-optically by helicity-modulated excitation in the RSA regime [Zhu14]. We calculated the magnetic field of NMR of the ^{77}Se isotope at a resonance frequency $f_{\mathrm{NMR}} = f_{\mathrm{m}} = 185\,\mathrm{kHz}$ and obtained

$$B_{\mathrm{NMR}} = \frac{2\pi f_{\mathrm{m}}}{\gamma_{\mathrm{Se}}} B_{\mathrm{NMR}} \approx 22.68\,\mathrm{mT}, \tag{5.4}$$

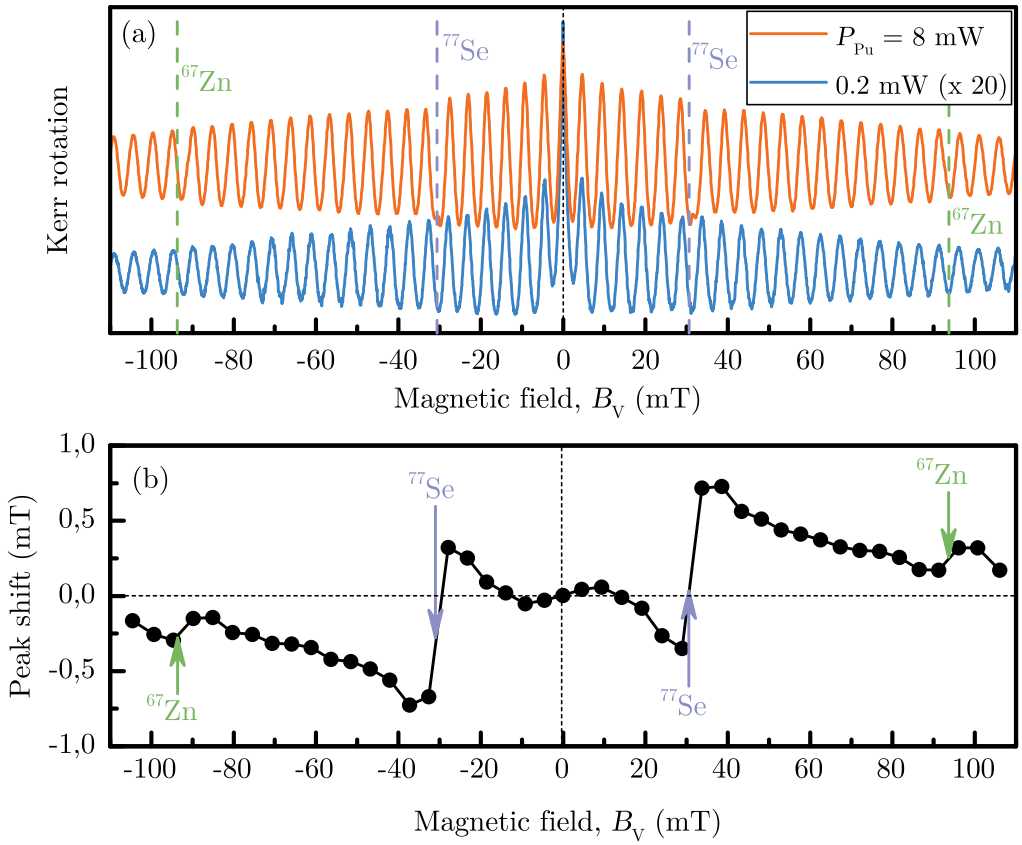

Figure 5.3 (a) RSA spectra (sample #2), measured at a broad, symmetric range of magnetic field at $f_m = 250\,\text{kHz}$ and $T = 1.8\,\text{K}$ for two pump powers. The spectrum at $P_{Pu} = 0.2\,\text{mW}$ (blue) is multiplied by a factor of 20 and translated vertically to allow for an easier comparison of the peak positions. (b) Pump power induced peak shift, determined as described before, as a function of the peak position (magnetic field B_V) at $P_{Pu} = 0.2\,\text{mW}$.

where $\gamma_{Se} = 5.125\,387 \times 10^7\,\text{rad}\,\text{s}^{-1}\,\text{T}$ (see Ref. [Har02]) was the gyromagnetic ratio of the selenium nuclei. The field B_{NMR} is at the resonance of the observed dispersive profile of the shift, supporting the hypothesis that the shift originates from a polarization of the nuclear spins of this isotope. We further suggest that this polarization is induced by the helicity-modulated optical excitation at a frequency $f_m = 185\,\text{kHz}$, since the resonance at B_{NMR}, revealing itself in the form of the dispersive profile of the shift and in the form of the small additional peak in the RSA spectra, corresponds to an NMR frequency $f_{NMR} = 185\,\text{kHz} = f_m$. Thus, we conclude that both the *narrow signature* and *broad signature* are caused by the nuclear spin polarization of the ^{77}Se nuclei and shall be referred to simply as *resonance* in the following.

To further support this and to check for possible effects of other isotopes with nonzero nuclear spin, e. g. the ^{67}Zn isotope (See also Table 2.1 in Section 2.1), we performed an RSA measurement at a bigger, symmetric range of magnetic field B_V. Figure 5.3(a) shows

the corresponding RSA spectra, measured at $T = 1.8\,\mathrm{K}$, $f_\mathrm{m} = 250\,\mathrm{kHz}$ and pump powers of $P_\mathrm{Pu} = 8\,\mathrm{mW}$ (orange, top spectrum) and $P_\mathrm{Pu} = 0.2\,\mathrm{mW}$ (blue, bottom spectrum). The spectrum at $P_\mathrm{Pu} = 0.2\,\mathrm{mW}$ is multiplied by a factor of 20 and translated vertically for an easier comparison of both spectra. The dashed lines mark the calculated positions of NMR (B_NMR, cf. Eq. (5.4)) at $f_\mathrm{m} = 250\,\mathrm{kHz}$ for the ^{77}Se (dashed, purple lines) and the ^{67}Zn (dashed, green lines) isotopes, where the gyromagnetic ratio $\gamma_\mathrm{Zn} = 1.676\,688 \times 10^7\,\mathrm{rad\,s^{-1}\,T}$ (cf. Ref. [Har02]) was used.

Both spectra exhibit a decreasing amplitude when increasing B_V. The spectrum at $P_\mathrm{Pu} = 8\,\mathrm{mW}$ exhibits two small additional peaks that are both located between two RSA peaks and are quite close to the calculated values $B_\mathrm{NMR} = \pm 30.65\,\mathrm{mT}$. However, we do not observe such peaks for zinc (see dashed, light red lines at $B_\mathrm{NMR} = \pm 93.68\,\mathrm{mT}$).

The power induced shift as a function of the peak position/magnetic field B_V, shown in Fig. 5.3(b), reveals resonances of both the ^{77}Se and the ^{67}Zn isotope (cf. Table 2.1). The magnitude of the peak shift A_shift, defined by the difference between the maximum shift towards stronger magnetic field and the maximum shift towards weaker magnetic field, is much weaker in the case of zinc. While for the selenium isotope we find $A_\mathrm{shift} \approx 0.99\,\mathrm{mT}$ at $B_\mathrm{V} < 0$ and $A_\mathrm{shift} \approx 1.07\,\mathrm{mT}$ at $B_\mathrm{V} > 0$, the magnitude of the shift is almost 10 times smaller for the zinc isotope - $A_\mathrm{shift} \approx 0.15\,\mathrm{mT}$ at $B_\mathrm{V} < 0$ and $B_\mathrm{V} > 0$.

This discrepancy of the shift for both isotopes is probably caused by the different natural abundances χ of the isotopes ($\chi_\mathrm{Se} = 7.58\,\%$ and $\chi_\mathrm{Zn} = 4.11\,\%$, cf. Ref. [Gre12] and Table 2.1) and their different hyperfine constants ($A_\mathrm{Se} = 33.6\,\mu\mathrm{eV}$ and $A_\mathrm{Zn} = 3.7\,\mu\mathrm{eV}$, cf. Ref. [Gre12]). The ^{67}Zn isotope has a nuclear spin of $I = \frac{5}{2}$, and the nuclear Zeeman levels are split six-fold ($2I + 1$), while selenium with $I = \frac{1}{2}$ does not exhibit a quadrupole moment and the nuclear Zeeman levels represent a two-level system. Thus, the nuclear spin transitions of ^{67}Zn are not limited to a single transition, i. e., the central (first order) transition from $I_z = -\frac{1}{2}$ to $I_z = \frac{1}{2}$ determining the gyromagnetic ratio γ_Zn, but the resonance exhibits additional, weaker transitions between the other levels. We assume that this makes the processes, leading to a nuclear spin polarization (cf. discussions in this chapter), less efficient for zinc - another reason for the difference of A_shift between zinc and selenium.

Nevertheless, the RSA measurements are sensitive enough to observe at least the central transition of the ^{67}Zn isotope, which demonstrates the high sensitivity of optical methods for studying nuclear effects (cf. also Ref. [San06]). In the following, we will focus on the effects related to the ^{77}Se isotope. Indeed those effects are much stronger, and this isotope dominates when it comes to electron-nuclear interaction in this material system.

5.2 Experimental Investigations of the Shift of the RSA Peaks

To learn more about the nature of the shift of the RSA peaks, caused by the nuclear spins of the ^{77}Se isotope, and to obtain hints at underlying mechanisms of nuclear spin polarization, we investigate its dependence on the magnetic field, the temperature, and the electron spin polarization. Figure 5.4 shows the shift of the RSA peaks around the NMR of ^{77}Se at different magnetic field ranges and modulation frequencies f_m. Here, the

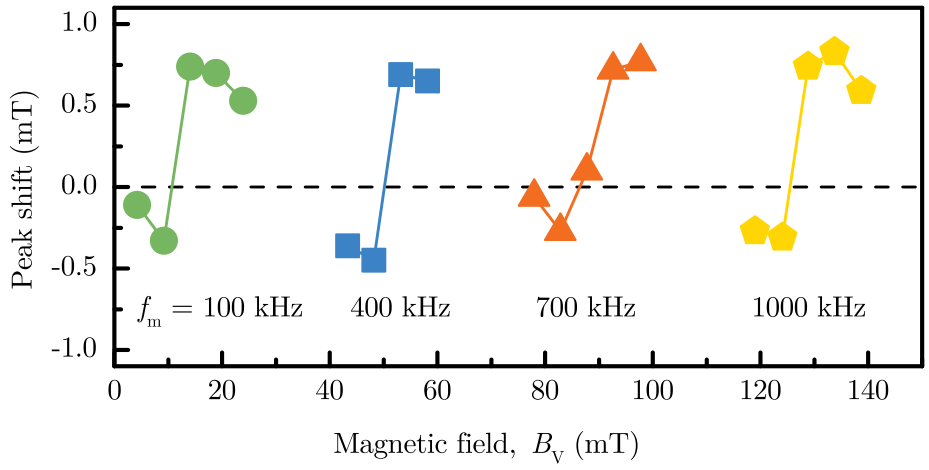

Figure 5.4 Shift of RSA peaks (sample #2) at different modulation frequencies f_m=100 kHz, 400 kHz, 700 kHz, and 1000 kHz and magnetic field ranges, respectively. The shift was calculated from the difference of the peak positions of RSA spectra at $P_{Pu} = 10$ mW and at $P_{Pu} = 0.2$ mW. $T = 1.8$ K.

resonance shifts when changing f_m. This observation supports the hypothesis that the nuclear polarization is induced by the helicity-modulated excitation with the modulation frequency f_m. Using Eq. (5.4) we calculated B_{NMR} for the ^{77}Se isotope and performed RSA measurements in a small range of magnetic field B_V around the resonance, where two RSA spectra, one at $P_{Pu} = 0.2$ mW and one at $P_{Pu} = 10$ mW, were recorded. The shift was then calculated from these spectra as described before.

Although the shift and its dispersive profile were studied at a magnetic field range from 0 mT to 140 mT and at modulation frequencies f_m from 100 kHz to 1000 kHz, the shape of the dispersive profile and the magnitude of the shift A_{shift} remain nearly the same.

Figure 5.5 illustrates the shift of the RSA peaks (sample #1) at different temperatures T=1.8 K, 18 K, and 26 K. We observe a reduction of the shift of the RSA peaks with increasing temperature. This behavior is in contrast to the electron spin dynamics: The longitudinal spin relaxation time of the donor-bound electrons is independent of the temperature in the range from 1.8 K to 45 K (cf. Chapter 4) and Greilich *et al.* (see Ref. [Gre12]) reported that the inhomogeneous spin dephasing time T_2^* was stable up to temperatures of $T = 40$ K. Thus, the observation of a temperature dependence of the shift of the RSA peaks might be caused by a decrease in the efficiency of the processes, which lead to this shift, or by an increase in the nuclear spin temperature (cf. Section 2.3.9) due to the increased lattice temperature.

The magnetic field dependence and the temperature dependence support the two hypotheses about the origin of the shift:

1. The shift of the RSA peaks is caused by the nuclear spins of the ^{77}Se isotope.

2. The shift is induced by the helicity-modulated excitation of the donor-bound electron

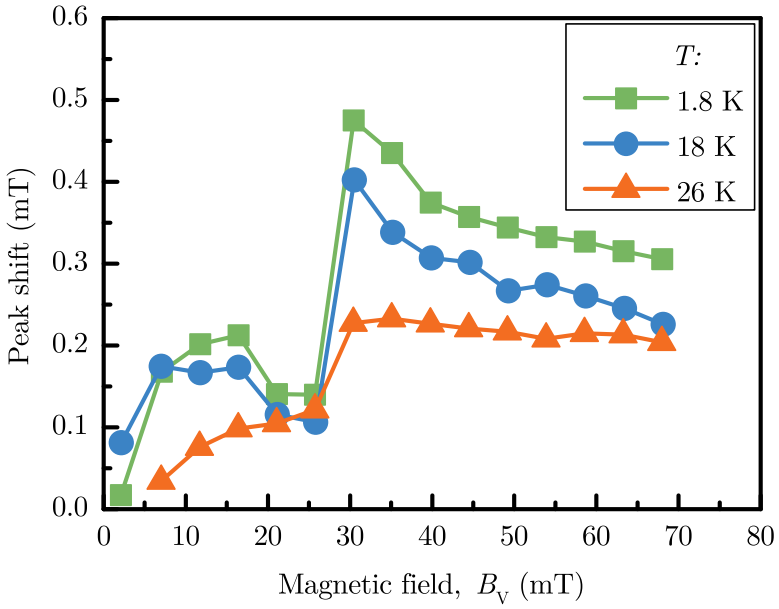

Figure 5.5 Shift at of RSA peaks (sample #1) at different temperatures T=1.8 K, 18 K, and 26 K. The shift was calculated from the difference of the peak positions of RSA spectra at $P_{Pu} = 10\,mW$ and at $P_{Pu} = 0.2\,mW$. The modulation frequency was set to $f_m = 200\,kHz$ for all measurements.

spins.

The latter hypothesis leads to the assumption that the nuclear spins are influenced by the electron spin polarization, induced by the circularly polarized pump pulses and, thus, alternating with the modulation frequency f_m. We examine the influence of the degree of the circular polarization of the pump beam and thereby the degree of the electron spin polarization on the shift of the RSA peaks (cf. Section 2.2). To that end, we altered the adjustment of the EOM so that it modulated the pump beam between two elliptical polarizations (cf. Section 3.1.3). Note that the conditions for these measurements were chosen to reflect those of the measurements of the RSA spectra in dependence on the pump power P_{Pu} (see Fig. 5.1(a) and (b)), so that we can easily compare the behavior as a function of these two parameters.

Figure 5.6(a) shows several RSA spectra measured at different degree of circular polarization ρ_c of the pump beam ranging from 15 % to 100 %. Note that due to the nature of the Kerr rotation effect the magnitude of the RSA signals is proportional to the degree of electron spin polarization and thereby also proportional to the circular polarization degree, so the spectra are normalized and translated vertically with respect to each other for a better comparison of the peak positions. The positions of the RSA peaks change with increasing ρ_c and the magnitude of the small additional peak increases when increasing ρ_c, similar to the behavior observed for the pump power dependence of the RSA spectra, illustrated in Fig. 5.1(a).

In analogy to the analysis of the power dependence of the shift (cf. right inset of

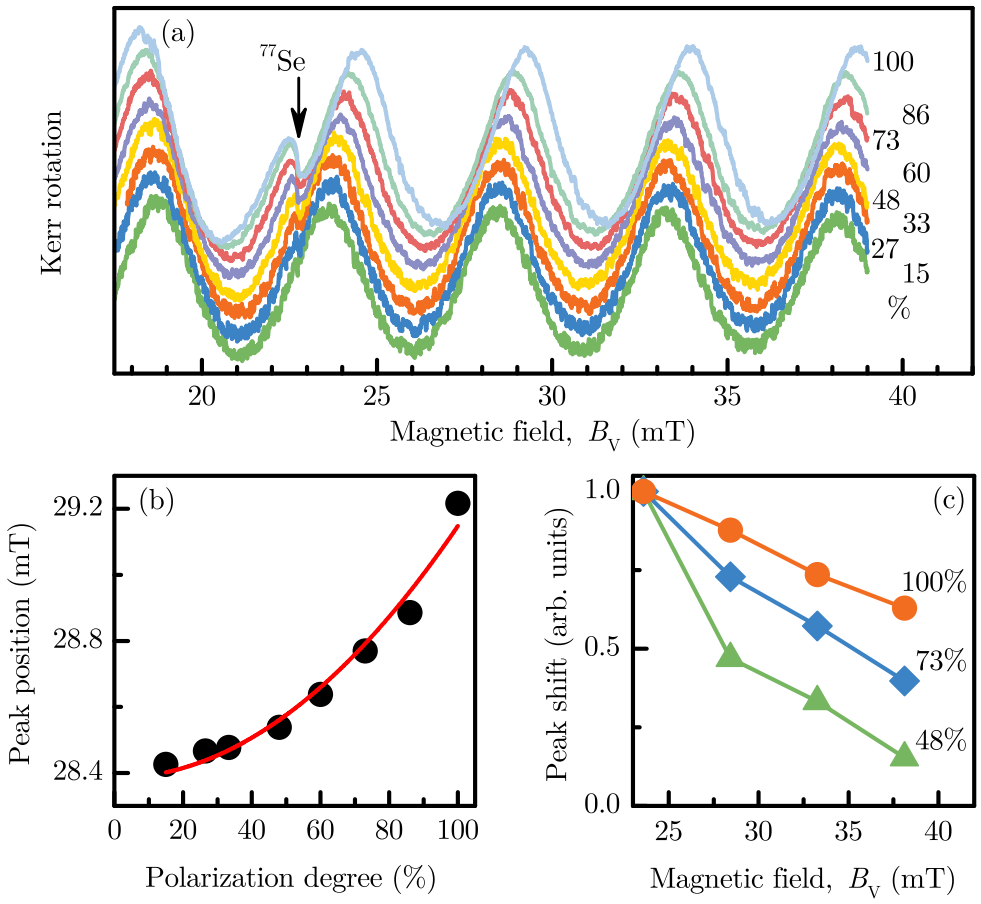

Figure 5.6 (a) RSA spectra (sample #2) at different degrees of circular polarization ρ_c of the pump beam. (b) Position of the RSA peak at $B_V \approx 28.4\,\mathrm{mT}$ ($\rho_c = 15\,\%$) as a function of the degree of circular polarization ρ_c. (c) Relative peak shifts for different circular polarization degrees in dependence on B_V. The data are normalized to the shift of the peak at $B_V = 24\,\mathrm{mT}$. The shift was calculated as the difference of the peak positions at the given ρ_c and at $\rho_c = 15\,\%$. The modulation frequency was set to $f_m = 185\,\mathrm{kHz}$, the pump power was at $P_{Pu} = 10\,\mathrm{mW}$, and the temperature was kept at $T = 1.8\,\mathrm{K}$ for all measurements.

Fig. 5.1(a)) Fig. 5.6(b) shows the position of the RSA peak at $B_V \approx 28.4\,\mathrm{mT}$ as a function of the degree of circular polarization ρ_c of the pump beam. The peak position shifts towards higher magnetic field with increasing ρ_c as it is the case for increasing P_{Pu}, but quantitatively the behavior differs: While the dependence of the position of this peak on P_{Pu} exhibits a saturation behavior, here we can fit the peak position as a function of ρ_c by a quadratic function

$$A_{shift}(\rho_c) = c_2 \cdot \rho_c^2 + c_0. \tag{5.5}$$

The nonlinear fit of Eq. (5.5) to the data yields $c_2 = 7.64 \times 10^{-5}\,\mathrm{mT}/\%^2$ and $c_0 = 28.38\,\mathrm{mT}$. The fit is shown by the red line in Fig. 5.6(b).

Figure 5.6(c) shows the dependence of the normalized shift (normalized to the shift of the

peak at $B_V \approx 24\,\mathrm{mT}$) on the peak position (magnetic field B_V) measured at $\rho_c = 15\,\%$. The decay of the shift with increasing B_V is accelerated at lower degrees of circular polarization ρ_c.

These results stress the importance of the electron spin polarization for the observed shift of the RSA peaks. The position of the resonance at the field of NMR of the ^{77}Se isotope indicates that the shift is related to the nuclear spins of this isotope. However, comparing the Larmor precession frequencies of the electrons ω_L and the nuclei ω_N we find that the Larmor precession frequency of the electron spins is several orders of magnitude larger. Their ratio was calculated using the following equation

$$\frac{\omega_L}{\omega_N} = \frac{g_e \mu_B B_V/\hbar}{\gamma_{Se} B_V} \approx 1940. \tag{5.6}$$

Thus, the nuclei should only be able to interact with the time-averaged electron spin polarization, which is constant for each half-cycle of the helicity modulation (cf. discussion in Section 4.2.2). The question remains, how the electron spins, precessing in the yz plane, can induce a nuclear spin polarization along the x axis ($\parallel B_V$). Thus, we performed a complete tomography of the average electron spin.

5.3 Tomography of the Electron Spin

5.3.1 S_z Component: Time-resolved Kerr Rotation Measurements

Although RSA is a very sensitive method to determine the Larmor precession frequency ω_L and thereby the effective magnetic field acting on the electron spins, it has the restriction that this very precise measurement can be performed only at certain external magnetic fields B_V at the position of the RSA peaks. Between these peaks, the KR signal is minimal, since the spin polarization from different pumps destructively interferes. The distance between the RSA peaks, in turn, is determined by the laser repetition frequency ω_R and the electron g factor g_e (cf. Eq. (3.6) in Section 3.4.1). Only the former, ω_R can be altered without altering parameters, which are relevant for the studied physics, e.g., the excitation wavelength. However, this requires the use of a pulse picker and can only reduce the described problem to a certain extend due to the finite width of the RSA peaks, determined by the inhomogeneous spin dephasing time T_2^*.

There is another, technically less demanding possibility to determine the Larmor precession frequency ω_L of the electron spins and thereby the nuclear fields, leading to the shift of the RSA peaks, in very fine steps. We fixed the magnetic field and performed a time-resolved Kerr rotation measurement using (almost) the full range of the delay line. Here, an additional retroreflector was used to double the range of the accessible delay. We performed a sequence of measurements at different magnetic fields B_V, increased in steps of 1 mT.

Figure 5.7 shows a single TRKR spectrum at $B_V = 25.3\,\mathrm{mT}$. We observe oscillations, indicating a Larmor precession of the spins of the donor-bound electrons about the superposition of the external magnetic field B_V and possible nuclear fields B_N. The red line is a fit to the data using the following equation

$$\theta_{KR}(t) = A_0 \cos(\omega_L t + \varphi) \exp(-(t/T_2^*)) + A_{off}. \tag{5.7}$$

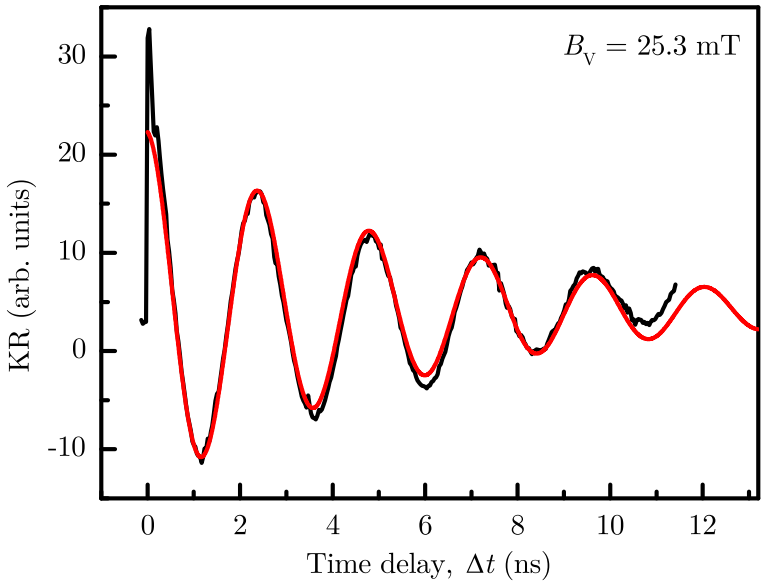

Figure 5.7 Single TRKR spectrum (sample #2) measured at $B_V = 25.3\,\mathrm{mT}$, $f_m = 185\,\mathrm{kHz}$, $P_{Pu} = 8\,\mathrm{mW}$, and $T = 1.8\,\mathrm{K}$. The delay line was scanned at constant B_V at steps of 2.5 mm, which corresponded to time steps of about 33.4 ps. The red line is the best fit to the data according to Eq. (5.7).

This allows us to determine the electron Larmor frequency ω_L and other quantities, such as the inhomogeneous spin dephasing time T_2^*. Note, however, that the focus here is on the precise determination of ω_L and that large $T_2^* \approx T_R$ on the order of the laser repetition period can only be precisely determined from RSA measurements. Table 5.1 shows the parameters of the best fit to the data. Figure 5.8 shows a contour plot interpolated from 33

Table 5.1 Parameters of the best fit to the TRKR data at $B_V = 22.3\,\mathrm{mT}$ shown in Fig. 5.7. The errors are obtained from the fit.

A_0	18.2 ± 0.3	arb. units
ω_L	2.600 ± 0.003	GHz
φ	0.06 ± 0.01	1
T_2^*	5.9 ± 0.1	ns
A_{off}	4.14 ± 0.05	arb. units

TRKR spectra, measured at B_V ranging from 7 mT to 38 mT. The increase of the number of minima and maxima when increasing the field B_V indicates that the Larmor precession frequency ω_L increases with increasing B_V. This is expected due to the nature of the Zeeman energy (cf. Eq. (2.15)). However, the spectra exhibit deviations from a strictly monotonic increase: Around the field of NMR $B_{NMR} = 22.68\,\mathrm{mT}$ we observe a small kink, marked by the dashed black circle. This indicates that the nuclear fields alter the electron Larmor frequency ω_L. By performing these series of measurements at two different pump

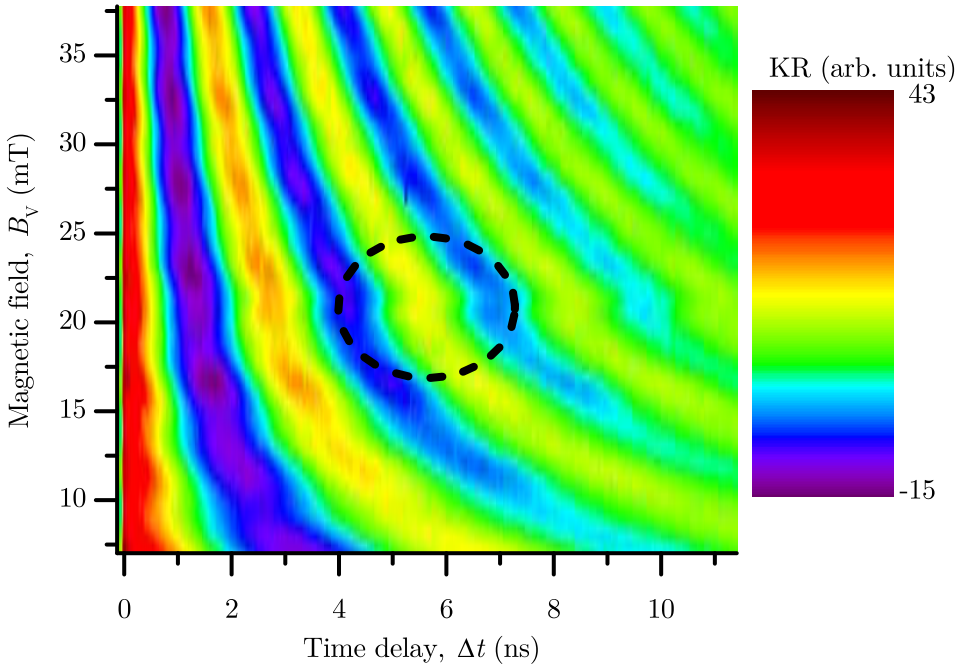

Figure 5.8 Contour plot interpolated from the TRKR spectra at different B_V. The measurements were performed at $f_m = 185\,\text{kHz}$, $P_{Pu} = 8\,\text{mW}$ and $T = 1.8\,\text{K}$. B_V was varied using incremental steps of 1 mT. The time step is about 33.4 ps. The black dashed circle marks the kink in the monotonic dependence of the oscillations on the magnetic field B_V.

powers $P_{Pu} = 8\,\text{mW}$ and $P_{Pu} = 0.12\,\text{mW}$, we calculated the shift ΔB from the difference of the Larmor frequencies, obtained from the fits to the data using the following relation

$$\Delta B = \frac{\hbar\,(\omega_L(P_{Pu} = 8\,\text{mW}) - \omega_L(P_{Pu} = 0.12\,\text{mW}))}{\mu_B g_e} \tag{5.8}$$

and the electron g factor $g_e = 1.1$ [Gre12].

This allows us to determine the dispersive profile at a finer resolution of the magnetic field B_V. Furthermore, we calculated the spin polarization along the z direction $S_z(t)$ for the whole laser repetition period T_R using Eq. (5.7) and the parameters of the fits to the measured data, where the offset parameter A_{off} was set to zero. Integrating S_z over T_R we obtained the average spin polarization S_z as a function of the magnetic field B_V, depicted in Fig. 5.9(a). The averaging of the S_z component is expected to result in a finite value at low magnetic fields B_V at which the Larmor precession period T_L and the inhomogeneous spin dephasing time T_2^* fulfill the following relation [Hei15a]:

$$T_L = \frac{2\pi}{\omega_L} \gtrsim T_2^* \tag{5.9}$$

Combining this relation with Eq. (2.15), we estimate the magnetic field range with finite spin polarization

$$B_V \lesssim \frac{2\pi\hbar}{g_e \mu_B T_2^*} = 7.9\,\text{mT}. \tag{5.10}$$

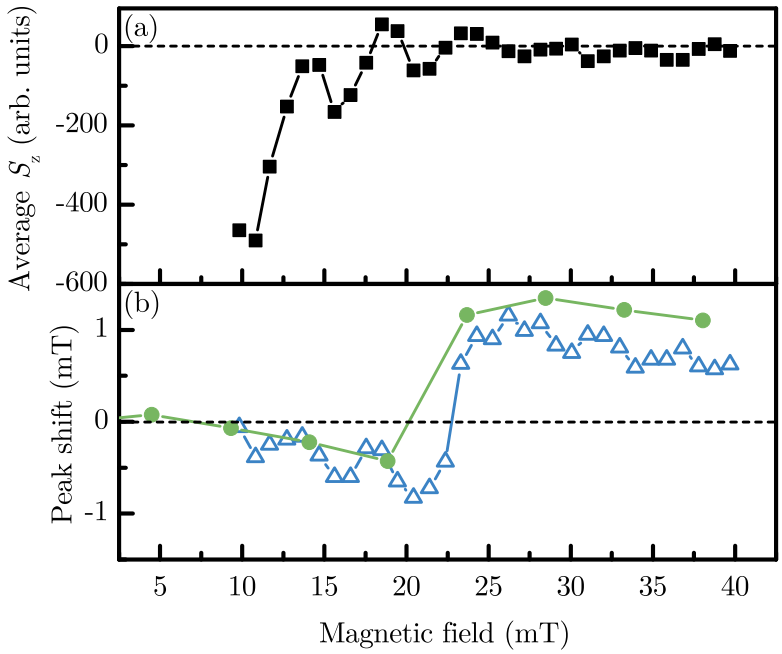

Figure 5.9 (a) Average spin polarization along the z direction S_z as a function of B_V calculated using the nonlinear fits with Eq. (5.7) to the data depicted in Fig. 5.8. (b) Peak shift determined from TRKR measurements, depicted in Fig. 5.8 and from RSA measurements (cf. Fig. 5.1). In analogy to Ref. [Hei15a].

Following these considerations, we do not expect a significant spin polarization along the z axis S_z at magnetic fields B_V up to 140 mT, where the shift of the RSA peaks is still observed. The dependence of S_z on B_V calculated from the experimental data, shown in Fig. 5.9(a) allows us to test this hypothesis.

We observe a quickly decaying, finite polarization S_z in the range of B_V from 10 mT to 15 mT, while it remains at $S_z \approx 0$ at fields $B_V > 15$ mT. We interpret the decay occurring from 10 mT to 15 mT as the tail of the Hanle curve (cf. Section 2.4.3 and Refs. [Han24; Hei15a; Dya84]), which resembles a Lorentzian centered at $B_V = 0$, whose half-width at half maximum (HWHM) is given by Eq. (5.10).

The maximum of the shift occurs at the resonance $B_{NMR} = 22.68$ mT (^{77}Se, cf. Eq. (5.4)) at this modulation frequency $f_m = 185$ kHz, where the tail of the Hanle curve already decreases to zero. Keeping in mind that the magnitude of the shift A_{shift} and the shape of its dispersive profile remain constant at magnetic fields B_V ranging from 0 mT to 140 mT (cf. Fig. 5.4), in stark contrast to the observed dependence of the spin polarization along the z axis S_z, we conclude that the high nuclear fields, corresponding to strong shifts of the RSA peaks, are probably induced by a spin polarization along the x or the y axis.

5.3.2 S_x Component: Possible Shift of the NMR Frequency

The results so far indicate that the shift of the RSA peaks results from a magnetic field B_N of nuclear origin, which should have at least a certain component along the x direction ($\| \boldsymbol{B}_\mathrm{V}$) to cause the observed shift of the RSA peaks. Thus, the nuclear spin polarization of the ^{77}Se isotope might result from a finite average electron polarization along the x direction S_x.

However, such a spin polarization should result in an effective magnetic field acting on the nuclear spins, the so-called Knight field (cf. Ref. [Kni49]). It will be denoted B_K in the following. This field, in turn, would alter the nuclear Larmor precession frequency ω_N. It would not only be determined by the external field B_V, but by the superposition of B_V and B_K. Thus, the idea of the measurements, presented in the following, is to check for a deviation of the nuclear Larmor frequency or NMR frequency as a function of B_V from that described by Eq. (2.16) in Chapter 2. Especially, a significant offset at $B_\mathrm{V} = 0\,\mathrm{T}$ would indicate a Knight field B_K along the x direction.

Experimentally, we tested this by optically detected nuclear magnetic resonance (ODNMR, cf. Section 3.4.4) measurements. A small radio frequency (RF) coil (cf. Section 3.1.2) near the sample surface resonantly heated the nuclear spin system, if the resonance condition $f_\mathrm{RF} = f_\mathrm{NMR}$ was met. A double modulation technique was used to increase the signal-to-noise ratio, where an amplitude modulation with 100 % modulation depth was applied to the RF excitation (cf. Section 3.4.4 for the experimental details) in addition to the helicity modulation of the pump beam with the frequency f_m.

Figure 5.10(a) depicts an RSA spectrum at $f_\mathrm{m} = 50\,\mathrm{kHz}$ to illustrate the magnetic field position B_V (orange dashed line) at which the RF measurement, shown in Fig. 5.10(b), was performed. We chose the position $B_\mathrm{V} = 5.1\,\mathrm{mT}$ on the right flank of the RSA peak left of the *small resonance*, since this position is expected to be most sensitive to a resonant heating of the nuclear spins. This heating reduces the shift of this peak and thereby leads to an increase of the KR signal at fixed $B_\mathrm{V} = 5.1\,\mathrm{mT}$.

The KR signal as a function of the RF frequency f_RF is depicted in Fig. 5.10(b). At $f_\mathrm{RF} \approx 40\,\mathrm{kHz}$ the KR signal shows a peak with a width of about 2.3 kHz (full-width at half maximum (FWHM), cf. fit using Eq. (5.11)). Note that the RF amplitude $A_\mathrm{RF} = 0.05\,\mathrm{V_{pp}}$ ($\mathrm{V_{pp}}$="Volt peak to peak") was chosen as low as possible to avoid a broadening of the NMR [Hei15a]. The exact NMR frequency can be determined by a fit of a Lorentzian to the data

$$\theta_\mathrm{KR}(f_\mathrm{RF}) = \frac{2A_0}{\pi}\frac{\Gamma}{4\cdot(f_\mathrm{RF}-f_\mathrm{NMR})^2+\Gamma^2} + A_\mathrm{off}. \tag{5.11}$$

This fit, illustrated by the red line in Fig. 5.10(b), yields a resonance frequency of $f_\mathrm{NMR} = (39.27 \pm 0.02)\,\mathrm{kHz}$. Table 5.2 is a summary of all parameters of the fit and their errors. Here, A_0 is the amplitude, Γ the FWHM, and A_off the offset.

By performing measurements at different B_V in the range from 4 mT to 20 mT and the corresponding fits with Eq. (5.11) we determine the NMR frequency f_NMR as a function of the magnetic field B_V, shown in Fig. 5.10(c). The red line is a linear fit to the data using the following equation

$$f_\mathrm{NMR}(B_\mathrm{V}) = B_\mathrm{V}\cdot m + b. \tag{5.12}$$

The data are weighted using the errors from the fits of the Lorentzians (cf. Eq. (5.11)).

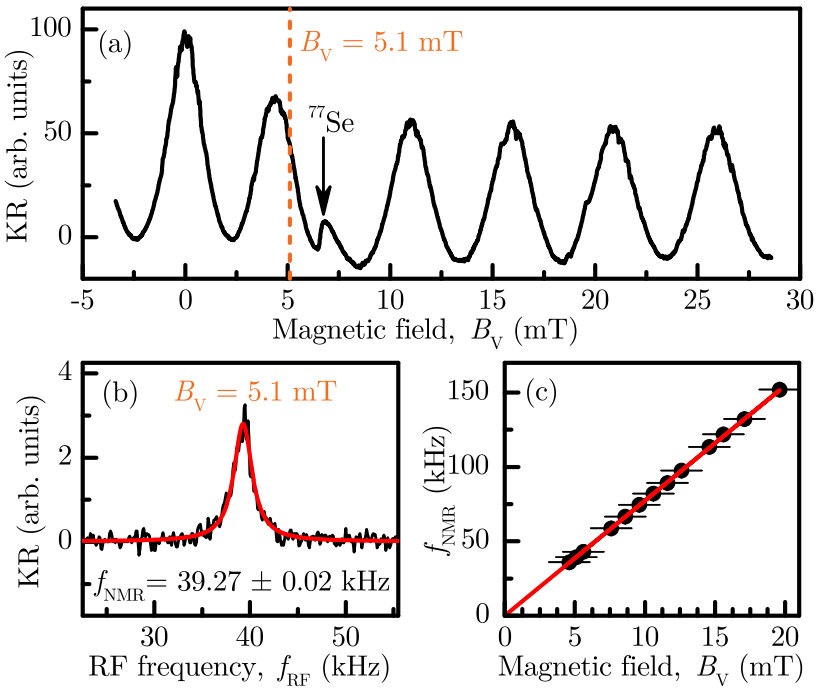

Figure 5.10 (a) RSA spectrum measured at $f_m = 50\,\text{kHz}$. The orange dashed line is the magnetic field position B_V at which the RF measurement, shown in panel (b), was performed. (b) Kerr rotation at fixed $B_V = 5.1\,\text{mT}$ in dependence on the applied RF frequency f_{RF}. The red line is a nonlinear fit using Eq. (5.11). (c) Dependence of f_{NMR} on B_V. Red line is a linear fit to the data. All measurements at $T = 1.8\,\text{K}$ and $P_{Pu} = 8\,\text{mW}$. In analogy to Ref. [Hei15a].

We find a slope of $m = (7.78 \pm 0.03)\,\text{kHz}\,\text{mT}^{-1}$, which is about 4.5 % lower than the value from the literature (cf. Ref. [Har02]) $\gamma_{Se}/(2\pi) \approx 8.157\,\text{kHz}\,\text{mT}^{-1}$. From the y-intersection $b = (-0.4 \pm 0.2)\,\text{kHz}$ we estimate the magnitude of a possible Knight field B_K along the x direction

$$B_K = \frac{2\pi b}{\gamma_{Se}} = (49 \pm 25)\,\mu\text{T}, \tag{5.13}$$

where the relative error of the Knight field B_K is equal to the relative error of the y-intersection $\eta_b = \sigma_b/b$ according to Gaussian error propagation. These findings indicate that the Knight field, resulting from a possible average spin polarization along the x direction S_x, is on the order of a few tens of µT.

Table 5.2 Parameters of the best fit to the KR signal at $B_V = 5.1\,\text{mT}$ in dependence on f_{RF} shown in Fig. 5.10(b). The errors are obtained from the fit.

A_0	18.2 ± 0.3	arb. units
f_{NMR}	39.27 ± 0.02	kHz
Γ	2.31 ± 0.05	kHz
A_{off}	0.009 ± 0.009	arb. units

5.3.3 S_y: Compensation of the Knight Field with RF Fields

As discussed before (cf. Eq. (5.6) and its discussion in Section 5.2), the electron Larmor frequency ω_L is much bigger than the nuclear Larmor frequency ω_N so that any interaction between the electron spin system and the nuclear spin system should originate from an average electron spin polarization, which is temporally constant or constant on the time-scale given by the nuclear Larmor precession period $T_N = 2\pi/\omega_N$. To test for the latter possibility, we used the same arbitrary function generator (AFG) to trigger the EOM and provide the RF voltage, where both channels were set to the same frequency: $f_m = f_{RF}$. This ensures that the Knight field, following the helicity-modulation, and the oscillating magnetic field, originating from the RF coil, had defined a phase with respect to each other. This phase φ was controlled with the AFG and was determined from the voltage drop at an additional resistor connected in line with the RF coil (cf. Section 3.4.8).

The advantages and peculiarities of this approach can be best explained in the frame of the rotating wave approximation, where we change to a coordinate system rotating with the frequency $2\pi f_m$ about the x axis in the direction of the nuclear precession (rotating frame system(RFS)). In the RFS, the nuclear spin, the parts of the average electron spin polarization $\boldsymbol{S}$ following the helicity modulation and the corresponding Knight field $\boldsymbol{B}_K$, as well as the magnetic field of the RF coil $\boldsymbol{B}_{RF}$, do not exhibit any precession, but are fixed.

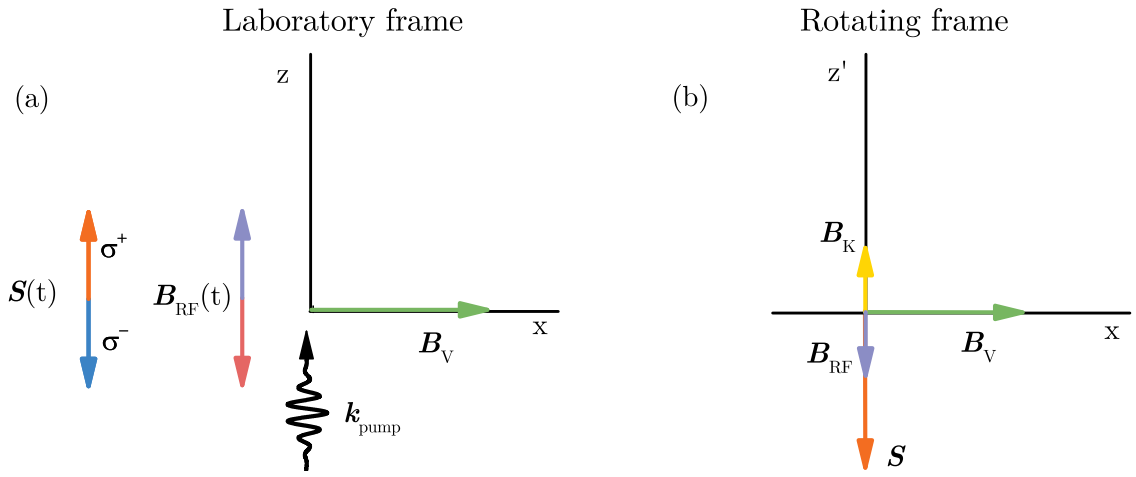

Figure 5.11 (a) Illustration of the xz plane in the laboratory frame. The pump beam $\boldsymbol{k}_{pump}$, the part of the average spin polarization following the helicity modulation $\boldsymbol{S}$ and the RF field $\boldsymbol{B}_{RF}$ are oriented along the z direction, where the z components of $\boldsymbol{S}$ and $\boldsymbol{B}_{RF}$ alternate sign with f_m, denoted by the double arrows. The external magnetic field $\boldsymbol{B}_V$ is oriented along the x direction. (b) Illustration of the xz' plane in a frame rotating about the x axis with $2\pi f_m$. Here $\boldsymbol{k}_{pump}$ cannot be shown, but the rotating frame is more suitable to illustrate the Knight field $\boldsymbol{B}_K$ (yellow arrow), which results from the average electron spin polarization $\boldsymbol{S}$ (orange arrow).

Figure 5.11 illustrates this transition and the concept of these measurements by depicting these vectors in both the xz plane of the laboratory frame (a) and in the xz' plane of the rotating frame (b). For simplicity the nuclear spin is not shown yet. In Fig. 5.11(a) (laboratory frame) $\boldsymbol{S}$ and $\boldsymbol{B}_{RF}$ are shown as a blue-orange and a purple-red double arrow

to emphasize that they alternate sign with f_m. Due to the transformation to the frame rotating about the x axis (cf. Fig. 5.11(b)), they become fixed vectors, but their relative orientation/angle with respect to each other depends on the relative phase φ between the helicity modulation and the RF voltage.

Here, they are shown in parallel configuration to illustrate the main idea of the measurements presented in the following: The goal is to determine suitable parameters for the RF excitation to compensate or at least to decrease the effect of the Knight field $\boldsymbol{B}_\mathrm{K}$ on the nuclei. While both the RF amplitude A_RF and the phase φ should influence the shift of the RSA peaks, its dependence on the phase is of special importance, because it allows us to conclude which component of the average spin polarization $\boldsymbol{S}$ induces the nuclear spin polarization through its corresponding Knight field $\boldsymbol{B}_\mathrm{K}$.

To that end, we performed a series of measurements: We varied the parameters of the RF excitation and recorded the KR signal. The KR signal is recorded for an interval of 20 s for each pair of parameters (A_RF,φ), where the first and last 5 s of the interval the KR signal was measured without RF excitation and a consecutive interval of 10 s in the middle was measured with RF excitation. The measurements were performed in this way (i) to ensure that there is enough time to repolarize the nuclei in between the RF excitations and (ii) to average over laser power fluctuations and other noise to improve the signal to noise ratio. Figure 5.12 shows an example of such a measurement.

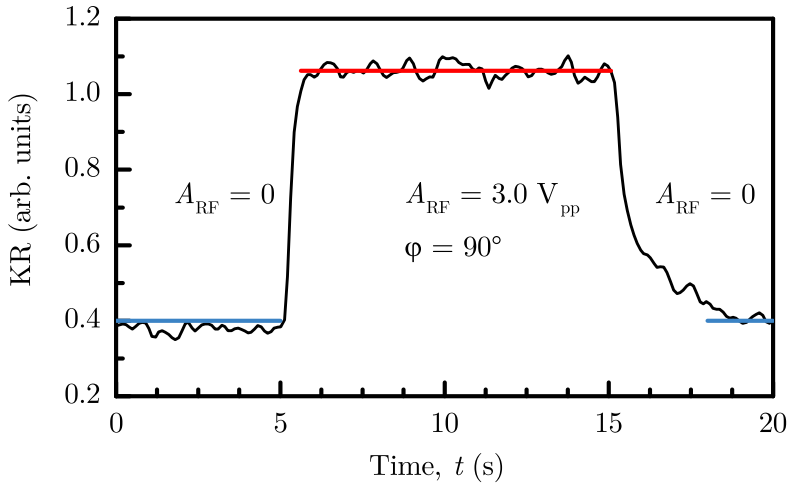

Figure 5.12 KR signal in dependence on the time at $B_\mathrm{V} = 26.0\,\mathrm{mT}$, $P_\mathrm{Pu} = 10\,\mathrm{mW}$, and $T = 1.8\,\mathrm{K}$. From $t = 5\,\mathrm{s}$ to $t = 15\,\mathrm{s}$ an RF excitation with $A_\mathrm{RF} = 3.0\,\mathrm{V_{pp}}$ and $\varphi = 90°$ was applied to the sample (sample #2), while no RF excitation was applied during the rest of the time.

To determine the change induced by the RF excitation, we averaged both the KR signal without RF excitation and the signal with RF excitation and calculated their difference. Here, specific intervals ("RF off"(blue lines): 0 s to 5 s and 18 s to 20 s; "RF on"(orange line): 5.6 s to 15 s) were selected for the averaging to exclude to a good extend the transients connected with the switching of the RF excitation. Here, a common average for both "RF off"-intervals was calculated.

Figure 5.13 shows the difference of KR signals with and without RF excitation, calculated as described before, at fixed magnetic field (Fig. 5.13(a) $B_V = 26.0\,\mathrm{mT}$ and Fig. 5.13(b) $B_V = 27.8\,\mathrm{mT}$) in dependence on A_{RF} and φ. The magnetic field position $B_V = 26.0\,\mathrm{mT}$

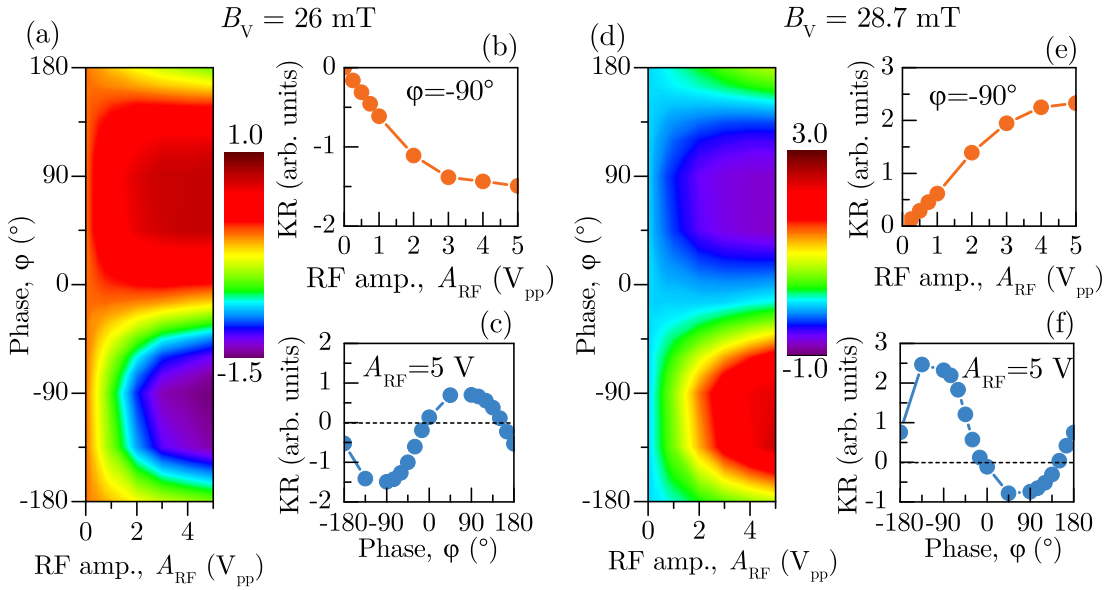

Figure 5.13 (a) Contour plot: KR signal difference at fixed $B_V = 26.0\,\mathrm{mT}$ and $f_m = f_{RF} = 185\,\mathrm{kHz}$ in dependence on the RF amplitude A_{RF} (x axis) and the phase φ between the RF excitation and the helicity modulation. The graphs to the right of the contour plot show cuts through this plot at fixed phase $\varphi = -90°$ (b) and RF amplitude $A_{RF} = 5\,V_{pp}$ (c), respectively. (d) Same as in (a), but at $B_V = 28.7\,\mathrm{mT}$. All measurements at $T = 1.8\,\mathrm{K}$ and $P_{Pu} = 8\,\mathrm{mW}$. In analogy to Ref. [Hei15a].

(Fig. 5.13(a)) corresponds to the right flank of the first RSA peak following the resonance at $B_{NMR} = 22.68\,\mathrm{mT}$. Thus, a reduction of the shift of this peak, caused by the RF excitation, should lead to a decrease of the KR signal (denoted by blue color), while an increase of the shift should lead to an increase of the KR signal (denoted by red color). We observe that the higher is the RF amplitude A_{RF}, the stronger is the change of the KR signal, but the efficiency of this change and its sign strongly depend on the phase φ between the helicity modulation of the pump and the RF excitation. It exhibits a maximum (red region in the contour plot) around $\varphi = 90°$ and a minimum (blue region in the contour plot) around $\varphi = -90°$. The cut through the contour plot at $A_{RF} = 5\,V_{pp}$, shown in Fig. 5.13(c), confirms this observation.

We interpret the maximum of the KR signal difference occurring at RF excitation with $\varphi = 90°$ as an amplification of the nuclear spin polarization by the RF field. The minimum of the KR signal difference at $\varphi = -90°$ suggests that here the nuclear spin polarization is reduced by this field.

The phase that compensates the shift of the RSA peak most efficiently is $\varphi = -90°$. This hints at the orientation of the Knight field $\boldsymbol{B}_K$, which induced the nuclear spin polarization. This phase difference between the helicity modulation and the RF field means that the

Knight field, oscillating with the helicity modulation frequency f_m, is oriented along the y axis in the laboratory system at the beginning of a modulation cycle, rotates about the external field B_V, and, thus, becomes oriented parallel to the z axis ($+z$ direction). Since this rotation takes a finite time, a quarter of the modulation period $\frac{T_\mathrm{m}}{4}$, it equals a phase difference of 90° in the RFS. Thus, the Knight field is best compensated, when the RF field is applied directly along the $-z$ direction ($\varphi = -90°$). The reduction of the Knight field, in turn, decreases the nuclear spin polarization and, thereby, compensates the shift of this RSA peak (see also Figs. 5.11 and 5.14).

The occurrence of the maximum KR signal at a phase of $\varphi = 90°$ supports this interpretation. This phase φ corresponds to an RF field applied along the $+z$ direction, which should enhance the effect of the Knight field oriented in the same direction and therefore increase the shift of the RSA peak. The observed increase of the signal most likely results from an increased shift of the RSA peak, so this observation confirms the considerations on the orientation of the Knight field described before.

The dependence of the difference of the KR signals ("RF on" - "RF off") on the RF amplitude A_RF is shown by the cut through the contour plot at $\varphi = -90°$ (Fig. 5.13(b)). It decreases with increasing A_RF, and this decrease saturates at $A_\mathrm{RF} = 5\,\mathrm{V_{pp}}$. Performing Rabi oscillation measurements (cf. Section 3.4.5), we estimate the strength of the effective field at the saturated RF amplitude level $A_\mathrm{RF} = 5\,\mathrm{V_{pp}}$ to $B_\mathrm{RF} \approx 170\,\mu\mathrm{T}$ (cf. Section 3.4.5, Eq. (6.4), and Chapter 6). However, it is important to note that this saturation amplitude is determined at fixed magnetic field $B_\mathrm{V} = 26.0\,\mathrm{mT}$ and thus a possible dependence of the saturation effect on the distance from the field of NMR B_NMR is not tested here.

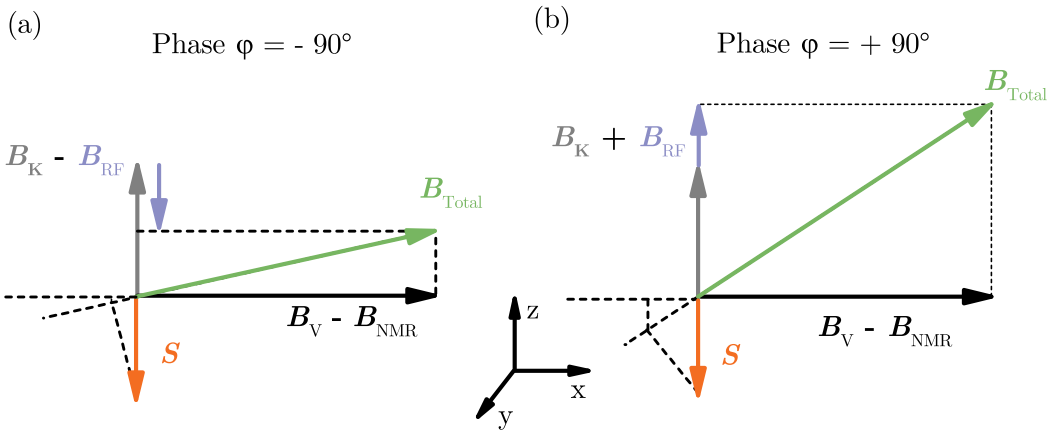

Figure 5.14 Illustration of the Knight field $\boldsymbol{B}_\mathrm{K}$ and the RF field $\boldsymbol{B}_\mathrm{RF}$ in the rotating frame systems (RFSs) at $B_\mathrm{V} - B_\mathrm{NMR} > 0$ and a phase of $\varphi = -90°$ (a) and $\varphi = 90°$ (b), respectively. In analogy to Ref. [Hei15a].

The previous observations (cf. Fig. 5.4) already suggest that the shift of the RSA peaks and therefore the underlying mechanism, e.g., the Knight field component inducing the nuclear spin polarization, should not depend on B_V in the range from 0 mT to 140 mT. To further confirm this hypothesis, we performed the same measurements at $B_\mathrm{V} = 28.7\,\mathrm{mT}$.

This magnetic field corresponds to the left flank of the second peak following the RSA peak, which exhibits the small additional peak at $B_V = B_{NMR}$. Since the KR signal was measured on the left flank instead of on the right flank as in Fig. 5.13(a), the interpretation of an increase or a decrease of the KR signal difference ("RF on" - "RF off") is reversed. Thus, blue color denotes an increase of the shift of the RSA peak, while red color means that the shift was reduced by the RF excitation.

Except for a reversed dependence of the KR signal difference on the RF excitation the overall behavior is very similar to that at $B_V = 26.0\,\mathrm{mT}$ (cf. Fig. 5.13(a)). The shift and thus the nuclear spin polarization is reduced at $\varphi = -90°$ and increases at $\varphi = 90°$, which indicates that the Knight field component inducing the nuclear spin polarization has a constant phase relative to the RF excitation and is oriented along the y axis at the beginning of the modulation cycle. Note that the asymmetry of the change of the KR signal difference probably results from the specific position on the flank of the RSA peak, e. g., the slopes for a shift towards higher and lower magnetic fields differ.

As in Fig. 5.13(b) the effect of the RF excitation at $\varphi = -90°$ saturates at $A_{RF} = 5\,V_{pp}$. However, the magnitude of the induced change differs, which probably is a result of a different position on the flank compared to Fig. 5.13(a).

The effect of an RF excitation with $f_{RF} = f_m$ was investigated further by recording RSA spectra, while the sample was exposed to the RF field. Figure 5.15(a) shows several RSA spectra, measured for sample #2 at a pump power of $P_{Pu} = 10\,\mathrm{mW}$, a helicity modulation/RF frequency of $f_m = f_{RF} = 185\,\mathrm{kHz}$, a phase of $\varphi = -90°$ and RF amplitudes A_{RF} in the range from $1.2\,V_{pp}$ to $2.4\,V_{pp}$. In addition, two spectra measured without RF excitation are shown: The spectrum at the bottom of the waterfall plot (black line) is measured at low power ($P_{Pu} = 0.2\,\mathrm{mW}$) and serves as a reference (cf. also vertical dashed black lines referring to their positions) to calculate the shift of the RSA peaks of all other spectra, while the top spectrum (light orange line) is recorded at high power ($P_{Pu} = 10\,\mathrm{mW}$) and serves as a reference for the shift of the peaks without the influence of the RF excitation.

Starting from the second spectrum from the top of the waterfall plot (blue line, $A_{RF} = 1.2\,V_{pp}$) the measurements are performed with increasing RF amplitude A_{RF} (increment: $0.2\,V_{pp}$). The data are arranged in this way to illustrate how the increasing RF amplitude let the peaks approach the positions at $P_{Pu} = 0.2\,\mathrm{mW}$ (bottom spectrum (black line) and cf. vertical dashed black lines denoting its peak positions). Here, the peaks close to the resonance even exhibit a shift in the opposite direction compared to the reference spectrum (black line, $P_{Pu} = 0.2\,\mathrm{mW}$) without RF excitation.

In addition to the shift of the peak positions we observe another deviation from the high power RSA spectrum without RF excitation (top spectrum, light orange line, $P_{Pu} = 10\,\mathrm{mW}$): While the shift of the peaks around B_{NMR} in the opposite direction only becomes pronounced at "higher" RF amplitudes $A_{RF} \geq 1.8\,V_{pp}$, the small, additional peak almost completely disappeared already at $A_{RF} = 1.2\,V_{pp}$. The corresponding RSA spectrum (second spectrum from the top, blue line) only exhibits a slight kink at its former position. This kink was even inverted at higher RF amplitudes A_{RF}.

Figure 5.15(b) shows the shift of the RSA peak positions under RF excitation compared to the reference spectrum at $P_{Pu} = 0.2\,\mathrm{mW}$ without RF excitation. Similar to the measurements at fixed magnetic field (cf. Fig. 5.13), we observe a decrease of the shift of

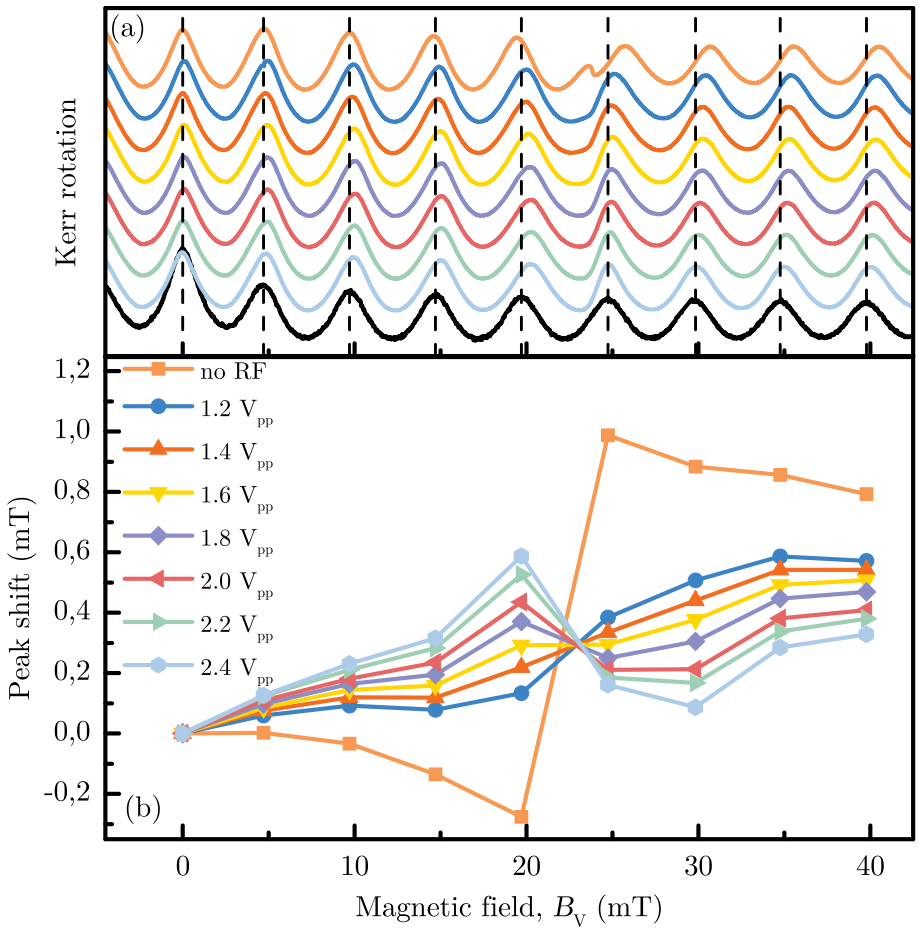

Figure 5.15 (a) RSA spectra (sample #2) under RF excitation at $\varphi = -90°$, $P_{\mathrm{Pu}} = 10\,\mathrm{mW}$, $T = 1.8\,\mathrm{K}$, $f_{\mathrm{m}} = f_{\mathrm{RF}} = 185\,\mathrm{kHz}$, and different RF amplitudes A_{RF} (cf. legend in (b)). The RSA spectrum at the bottom of the waterfall plot (black line, $P_{\mathrm{Pu}} = 0.2\,\mathrm{mW}$) and the spectrum at the top (light orange line), $P_{\mathrm{Pu}} = 10\,\mathrm{mW}$) are measured without additional RF excitation and serve as a reference to calculate the shift. The vertical dashed black lines mark the peak positions of the bottom spectrum. (b) Shift of the RSA peaks in relation to their position at $P_{\mathrm{Pu}} = 0.2\,\mathrm{mW}$ without RF excitation as a function of the magnetic field (their positio)n at low power without RF excitation.

the RSA peaks at $\varphi = -90°$ under RF excitation for all A_{RF}. As the shift itself depends strongly on the distance $B_{\mathrm{V}} - B_{\mathrm{NMR}}$ from the resonance, we expect that the influence of the RF excitation will also depend on it.

Indeed the data support this hypothesis: While an RF amplitude of $A_{\mathrm{RF}} = 1.2\,\mathrm{V_{pp}}$ is sufficient to decrease the shift of the peaks on the left side and the right side of B_{NMR} to a large extent, the effect on the shift of the peaks at the tails of the dispersive profile is significantly weaker. The spectra at higher A_{RF} add further support to these considerations: Although the first peaks on both sides of the resonance already shifted in the opposite direction with increasing A_{RF}, so that the dispersive profile was inverted close to B_{NMR},

the peaks at the tails exhibited only a weak shift in the opposite direction. Note that the shift of all spectra exhibits a significant, positive offset, which is subject of further studies and is out of the scope of this work.

5.4 Theoretical Model of the Shift of the RSA Peaks

All-optical NMR, as it occurs in the form of the resonances of the ^{77}Se and the ^{67}Zn isotopes in the RSA spectra, can be the result of two different processes [Zhu14]: resonant heating or resonant cooling of the nuclear spin system (NSS). The former occurs when the exciting light has a constant helicity, but is intensity modulated with a frequency $f_\mathrm{m} \approx f_\mathrm{NMR}$. The optical pumping (cf. Ref. [Coh66]) with variable intensity results in fluctuations in the number of photoexcited electrons and thus the optically induced spin polarization $\boldsymbol{S}$. Hence the Knight field $\boldsymbol{B}_\mathrm{K}$, which is directly proportional to $\boldsymbol{S}$, oscillates with f_m. This field efficiently heats up the NSS at $f_\mathrm{m} \approx f_\mathrm{NMR}$ and thereby decreases the polarization of the nuclear spins [Zhu14]. The process of resonant heating is observed in Fig. 5.10(a), where the KR signal in dependence on the RF frequency f_RF at fixed B_V was measured. The only difference is that here the nuclei are not heated by the oscillating Knight field $\boldsymbol{B}_\mathrm{K}$, but by the RF field $\boldsymbol{B}_\mathrm{RF}$. In both cases, the nuclear spin heating occurs as an absorption-like signal (cf. Fig. 5.10(a)).

The main observation - the shift of the RSA peaks - can be explained by resonant cooling of the NSS, which can occur under helicity modulated optical excitation. A helicity modulation is usually considered to reduce or even suppress dynamic nuclear polarization (DNP) [Ast08a; Fli10; Gre12; Col12]. However, it is important to note that this is not always the case and it depends on the exact experimental conditions and the properties of the sample under study. If the helicity modulation period T_m is longer than the transverse relaxation time of the nuclear spins T_2^N (cf. [Hei16] and Chapter 6) [Mei84; Zhu14] or the helicity modulation frequency f_m is tuned into resonance with the nuclear Larmor frequency or NMR frequency f_NMR, a significant DNP can be observed [Zhu14]. In the latter case, the DNP is the result of resonant nuclear spin cooling in the oscillating Knight field $\boldsymbol{B}_\mathrm{K}$, which in contrast to resonant heating exhibits a dispersive profile [Zhu14], as it is observed for the shift of the RSA peaks in dependence on the magnetic field B_V.

5.4.1 Classical Nuclear Spin Cooling in the Rotating Frame System

To describe this process in relation to the experimental results, we should recall the experimental configuration and its peculiarities. Figure 5.16(a) shows the orientation of the pump beam $\boldsymbol{k}$ vector $\boldsymbol{k}_\mathrm{pump}$, the resulting average electron spin $\boldsymbol{S}$, oscillating with f_m and the external field $\boldsymbol{B}_\mathrm{V}$ in the laboratory frame system (LFS). Since the strongest shift and most pronounced additional, small RSA peaks are observed for the ^{77}Se nuclei, only the nuclear spins of this isotope shall be considered in the theoretical model. According to Ref. [Fle84], dynamic nuclear polarization is the result of nuclear spin flips in the Knight field $\boldsymbol{B}_\mathrm{K}$ of the electron spins, which is given by the following equation

$$\boldsymbol{B}_\mathrm{K} = b_\mathrm{e}\boldsymbol{S}. \tag{5.14}$$

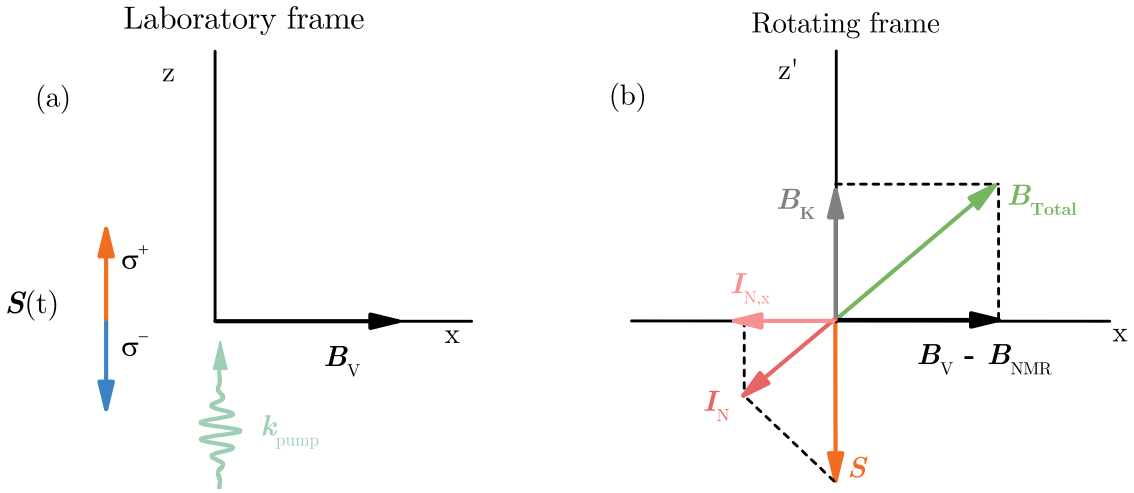

Figure 5.16 (a) Illustration of the spin orientation and the external magnetic field in the xz plane of the laboratory frame system (LFS). The orange and blue arrows denote the average spin $\boldsymbol{S}$ for a σ^+- and σ^--polarized pump, respectively. Since the pump helicity is modulated with f_m, the spin oscillates between an orientation along the z and the $-z$ direction: $\boldsymbol{S} = \boldsymbol{S}(t)$ The turquoise arrow denotes the orientation of the pump beam $\boldsymbol{k}$ vector $\boldsymbol{k}_\mathrm{pump}$ (along the z direction), while the external magnetic field $\boldsymbol{B}_\mathrm{V}$ is oriented along the x direction and perpendicular to $\boldsymbol{S}$ and $\boldsymbol{k}_\mathrm{pump}$. (b) Scheme of internal and external magnetic fields in the rotating frame system (RFS). $\boldsymbol{B}_\mathrm{K}$ (gray arrow) and $\boldsymbol{S}$ are the average Knight field and spin, respectively. The superposition of the field $\boldsymbol{B}_\mathrm{K}$ resulting from the average spin and the external field $\boldsymbol{B}_\mathrm{V}$ leads to a total magnetic field $\boldsymbol{B}_\mathrm{total}$ (green arrow), which deviates from the x direction. The red and light red arrows denote the induced nuclear spin polarization of ^{77}Se and its projection on the x axis, respectively. In analogy to Ref. [Hei15a].

Here b_e denotes the maximal Knight field amplitude at the center of the donor and is given by

$$b_\mathrm{e} = -\frac{A_\mathrm{Se} v_0}{\gamma_\mathrm{Se} \hbar \pi a_\mathrm{loc}^3}, \tag{5.15}$$

where a_loc is the localization radius of the electron at the donor and v_0 is the primitive cell volume with a two-atom basis [Fle84; Hei15a]. It is given by $v_0 = a_0^3/4$. Here $a_0 = 0.566\,\mathrm{nm}$ denotes the lattice constant of ZnSe [Paw11].

Near the resonance ($B_\mathrm{V} \approx B_\mathrm{NMR}$), the Knight field $\boldsymbol{B}_\mathrm{K}$ precesses synchronously with the nuclear spins (cf. Fig. 5.16(b)) and provides a temporally constant energy flow into the NSS. This energy flow, in turn, results in the build-up of a nuclear spin polarization $\boldsymbol{I}$. If the external field B_V is close to the field of NMR B_NMR, the projection of the nuclear spin polarization on the x axis is given by

$$I_x = \frac{(\boldsymbol{S} \cdot \boldsymbol{B}_\mathrm{K})(B_\mathrm{V} - B_\mathrm{NMR})}{(B_\mathrm{V} - B_\mathrm{NMR})^2 + B_\mathrm{K}^2 + B_\mathrm{L}^2}. \tag{5.16}$$

Here, B_L denotes the root mean square local field resulting from the nuclear dipole-dipole interactions [Fle84; Zhu14; Hei15a]. The build-up of the nuclear spin polarization can be interpreted as nuclear spin cooling in the RFS. The Knight field, oscillating at a frequency

of $2\pi f_\mathrm{m}$, is described by a superposition of two components rotating about the x axis (magnetic field) in opposite directions. At $B_\mathrm{V} \approx B_\mathrm{NMR}$ the component, which rotates in the same direction as the nuclear spin, is the important one, while the other one can be neglected. Since the selenium spins have $\gamma_\mathrm{Se} > 0$, the nuclear spins rotate counterclockwise in the yz' plane. The Knight field component rotating in the same direction as the nuclear spins is constant. Therefore, the nuclear spin polarization is projected onto the direction of the external magnetic field $\boldsymbol{B}_\mathrm{V}$ (x direction) by the superposition of the constant Knight field $\boldsymbol{B}_\mathrm{K}$ and the external magnetic field $\boldsymbol{B}_\mathrm{V}$, which results in a total magnetic field $\boldsymbol{B}_\mathrm{total} = (\boldsymbol{B}_\mathrm{V} - \boldsymbol{B}_\mathrm{NMR}) + \boldsymbol{B}_\mathrm{K}$ deviating from the x direction. The projected component of the nuclear spin I_x alters the electron Larmor precession frequency and thereby causes the shift of the RSA peaks, which will be explained in more detail in the following. Note that according to Eq. (5.16) I_x vanishes at the resonance $B_\mathrm{V} = B_\mathrm{NMR}$ in agreement with the dispersive profile of the shift of the RSA peaks.

The shift is caused by a nuclear field $\boldsymbol{B}_\mathrm{N}$ acting back on the electron spins, the so-called Overhauser field [Ove53]. In analogy to the Knight field $\boldsymbol{B}_\mathrm{K}$, the Overhauser field $\boldsymbol{B}_\mathrm{N}$ results from the collective magnetic moments of a polarized spin ensemble - here the nuclear spins. Thus, its projection on the x axis $B_{\mathrm{N},x}$ is directly proportional to I_x:

$$B_{\mathrm{N},x} = \frac{A_\mathrm{Se}\chi_\mathrm{Se} I_x}{\mu_\mathrm{B} g_\mathrm{e}} \tag{5.17}$$

Here, $A_\mathrm{Se} = 33.6\,\mu\mathrm{eV}$ is the hyperfine constant of selenium, taken for a primitive cell with two nuclei [Syp11b; Syp11a], and $\chi_\mathrm{Se} = 0.0758$ is the natural abundance of the ^{77}Se isotope.

Combining Eq. (5.16) and Eq. (5.17) we can begin to explain the observed shift of the RSA peaks: The projection of the nuclear spin polarization on the x axis as a function of the magnetic field B_V has a dispersive profile, where its sign is determined by the detuning $B_\mathrm{V} - B_\mathrm{NMR}$ from the NMR. The superposition of the external field and the Overhauser field leads to an effective field $B_\mathrm{eff} = B_\mathrm{V} + B_{\mathrm{N},x}$, determining the Larmor precession frequency $\omega_\mathrm{L} = \frac{\mu_\mathrm{B} g_\mathrm{e}}{\hbar}(B_\mathrm{V} + B_{\mathrm{N},x})$ of the electron spins so that it deviates from the expected strictly linear dependence on B_V. These equations can explain the observed shift, but we should keep into account the sign of the observed shift, determined by the signs of all quantities in Eqs. (5.15) to (5.17). The gyromagnetic ratio $\gamma_\mathrm{Se} > 0$ and the hyperfine constant $A_\mathrm{Se} > 0$ have a positive sign, so that Eq. (5.15) yields $b_\mathrm{e} < 0$. Thus, for $g_\mathrm{e} > 0$, as it is the case in this material, Eqs. (5.16) and (5.17) reproduce the sign of the induced shifts, illustrated in Figs. 5.1(b), 5.3(b), 5.4, 5.5 and 5.9(b). According to Eq. (5.17), the Overhauser field component $B_{\mathrm{N},x}$ is positive at $B_\mathrm{V} < B_\mathrm{NMR}$ and thus leads to a shift of the RSA peaks towards smaller B_V, while it is zero at $B_\mathrm{V} = B_\mathrm{NMR}$ and becomes negative at $B_\mathrm{V} > B_\mathrm{NMR}$ so that the RSA peaks shift towards higher magnetic field.

Combining Eq. (5.14) and Eq. (5.16) yields

$$I_x = \frac{b_\mathrm{e} S^2 (B_\mathrm{V} - B_\mathrm{NMR})}{(B_\mathrm{V} - B_\mathrm{NMR})^2 + b_\mathrm{e}^2 S^2 + B_\mathrm{L}^2}. \tag{5.18}$$

The induced nuclear spin polarization and the resulting shift of the RSA peaks should exhibit an S^2 dependence, which is in very good agreement with the experimentally observed dependence (cf. Fig. 5.6(b)). In addition, it also fits to the fast decrease of the

shift with increasing detuning from the resonance illustrated by the data in Fig. 5.6(c), because there also is an S^2 term in the denominator of Eq. (5.18).

5.4.2 Nuclear Spin Polarization and Nuclear Spin Diffusion

To test if the model can describe the observe shift also quantitatively, we search proper parameters to simulate the data calculated from fits to the TRKR spectra, which are shown by the blue triangles in Fig. 5.9(b). The simulation was performed on the basis of the following equation, obtained by combining Eq. (5.17) and Eq. (5.18)

$$B_{\mathrm{N},x}(B_{\mathrm{V}}) = \frac{A_{\mathrm{Se}}\chi_{\mathrm{Se}}}{\mu_{\mathrm{B}} g_{\mathrm{e}}} \frac{b_{\mathrm{e}} S^2 (B_{\mathrm{V}} - B_{\mathrm{NMR}})}{(B_{\mathrm{V}} - B_{\mathrm{NMR}})^2 + b_{\mathrm{e}}^2 S^2 + B_{\mathrm{L}}^2}. \tag{5.19}$$

This equation contains only two free parameters: the spin polarization S and the maximal Knight field amplitude b_{e}. Here, we find that the spin polarization should be fixed at $S = 0.07$ (cf. the following discussions) and the only remaining parameter is b_{e}.

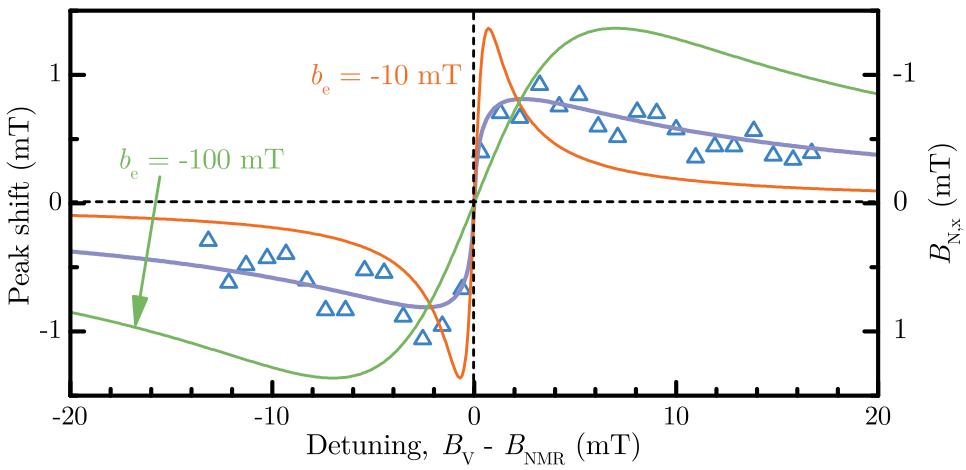

Figure 5.17 Peak shifts calculated from TRKR spectra (blue triangles, left axis, shifted downwards to compensate for the offset) and the nuclear field component $B_{\mathrm{N},x}$ according to the theoretical model represented by Eq. (5.19) for two different maximal Knight field amplitudes $b_{\mathrm{e}} = -10\,\mathrm{mT}$ (orange line) and $b_{\mathrm{e}} = -100\,\mathrm{mT}$ (green line). The purple line represents $B_{\mathrm{N},x}$, obtained from a nonlinear best fit to a model, which takes into account that the magnitude of the Knight field depends on the distance from the donor (cf. Eq. (5.27).

Figure 5.17 shows two attempts to determine the proper maximal Knight amplitude b_{e} to fit the model to the experimentally determined shift (blue triangles): While a value of $b_{\mathrm{e}} = -10\,\mathrm{mT}$ results in a very steep, fast decaying dispersive profile around $B_{\mathrm{V}} \approx B_{\mathrm{NMR}}$, whose maximum exceeds the experimentally determined value, a higher value of $b_{\mathrm{e}} = -100\,\mathrm{mT}$ leads to a broader, slowly decaying dispersive profile, which mirrors the long tails of the experimental data, but not the steep change around the resonance. We already assume that a superposition of profiles with different b_{e} might be able to model the observed profile, but how do we motivate or explain this superposition?

The flaw of the model given by Eq. (5.19) is that it assumes a homogeneous Knight field over the whole localization volume of the donor-bound electron [Hei15a], while the probability density of the electron

$$\Psi^2(r) = \frac{1}{\pi a_{\mathrm{loc}}^3} \exp\left(-2r/a_{\mathrm{loc}}\right) \tag{5.20}$$

and therefore also the magnitude of its Knight field

$$B_{\mathrm{K}}(r) = b_{\mathrm{e}} S \exp\left(-2r/a_{\mathrm{loc}}\right) \tag{5.21}$$

depend on the distance from the donor r.

The approximation by a homogeneous Knight field B_{K} is only valid, if nuclear spin diffusion due to flip-flop processes between neighboring nuclei leads to a uniform nuclear spin polarization (cf. Refs. [Blo54; Dya08]). This approximation was successfully used to explain the occurrence of the small additional peak in RSA spectra, measured for a fluorine-doped ZnSe epilayer (sample #1 in this thesis) and other kinds of material systems (CdTe/CdMgTe QW heterostructure, a single ZnSe/ZnMgSe QW and a GaAs epilayer) [Zhu14].

It is important to note that nuclear spin flips are only allowed, if they obey the law of conservation of energy. Thus, the energy difference due to the nuclear spin flip-flops must not exceed the energy $\hbar\gamma_{\mathrm{Se}} B_{\mathrm{L}}$, which can be compensated by the nuclear dipole-dipole reservoir. To estimate if the spin diffusion is possible in this material we first need to calculate the average distance between neighboring nuclei with non-zero nuclear spin (^{77}Se). It is determined by the lattice constant $a_0 = 0.566\,\mathrm{nm}$ and the natural abundance of ^{77}Se $\chi_{\mathrm{Se}} = 0.0758$

$$R = \frac{a_0}{\chi_{\mathrm{Se}}^{1/3}} \approx 1.34\,\mathrm{nm}. \tag{5.22}$$

This allows us to obtain the difference of the Knight field at two neighboring ^{77}Se nuclei in dependence on the distance r from a donor, and compare it to the local nuclear field $B_{\mathrm{L}} \approx 0.006\,\mathrm{mT}$ [Zhu14]

$$b_{\mathrm{e}} S \exp\left(-2r/a_{\mathrm{loc}}\right)\left[1 - \exp\left(-2R/a_{\mathrm{loc}}\right)\right] \leq B_{\mathrm{L}}. \tag{5.23}$$

From this equation, we obtain an estimation of the distance r from the donor at which nuclear spin diffusion becomes possible.

We also need to determine the maximal Knight field amplitude b_{e}. The localization radius of the donor-bound electron can be calculated from its donor binding energy or activation energy $E_{\mathrm{a}} \approx 27\,\mathrm{meV}$ [Gre12] (see also Ref. [Mer72]) and its effective mass $m_{\mathrm{e}}^* = 0.145 m_{\mathrm{e}}$ [Gre12] via the following equation [Hei15a]

$$a_{\mathrm{loc}} = \frac{\hbar}{\sqrt{2 m_{\mathrm{e}}^* E_{\mathrm{a}}}} \approx 3.4\,\mathrm{nm}, \tag{5.24}$$

where $m_{\mathrm{e}} = 0.511\,\mathrm{MeV}$ is the electron rest mass [Moh15]. Evaluating Eq. (5.15) with $a_{\mathrm{loc}} = 3.4\,\mathrm{nm}$ yields a significant Knight field of

$$b_{\mathrm{e}} \approx -370\,\mathrm{mT}$$

at the donor center, which can be explained by the strong localization of the electron at the donor. As stated before (cf. also Ref. [Hei15a]), the average spin polarization has a value of $S = 0.07$ and together with the Knight field amplitude $b_\mathrm{e} = -370\,\mathrm{mT}$ allows us to estimate the area around a donor, where the nuclear spin diffusion would violate the principle of conservation of energy. Using Eqs. (5.22) and (5.23), we find that the nuclear spin polarization should be spatially inhomogeneous in a radius of about $3.9a_\mathrm{loc}$ around a donor.

At the doping level $n_\mathrm{F} \approx 1 \times 10^{18}\,\mathrm{cm}^{-3}$ of sample #2 the average distance $\bar{d}$ between them can be calculated as

$$\bar{d} = \left(\frac{3}{4\pi n_\mathrm{F}}\right)^{1/3} \approx 6.2\,\mathrm{nm} \approx 1.8a_\mathrm{loc}. \tag{5.25}$$

As a result, nuclear spin diffusion should be completely hindered in sample #2, since the distance from a donor at which nuclear spin diffusion would become possible is not reached at this dopant concentration.

For sample #1 with a donor concentration of $n_\mathrm{F} \approx 1 \times 10^{15}\,\mathrm{cm}^{-3}$ we find

$$\bar{d} \approx 62\,\mathrm{nm} \approx 18a_\mathrm{loc}$$

so that here the nuclear spin diffusion is possible at least in the volume between the donors. However, the spin diffusion should still be hindered at distances $r < 3.9a_\mathrm{loc}$ and the nuclear spin polarization is very small outside this volume (cf. discussion of Fig. 5.18). Thus, the main contribution to the shift should stem from inhomogeneously polarized nuclei, as it is the case for sample #2. These considerations are supported by the observed shifts of the RSA peaks and the corresponding dispersive profiles for sample #1, which are very similar to those for sample #2.

Following these considerations, we improve the model by taking into account the spatial inhomogeneity of the nuclear spin polarization. Due to the spherical symmetry of the Knight field of the donor-bound electrons, the induced nuclear spin polarization is still isotropic, but depends on the distance from the donor. It is given by

$$I_x(r) = \frac{b_\mathrm{e} S^2 \left(B_\mathrm{V} - B_\mathrm{NMR}\right) \exp\left(-2r/a_\mathrm{loc}\right)}{\left(B_\mathrm{V} - B_\mathrm{NMR}\right)^2 + b_\mathrm{e}^2 S^2 \exp\left(-4r/a_\mathrm{loc}\right)}, \tag{5.26}$$

where the small local nuclear field B_L is neglected. To determine the projection of the Overhauser field on the x direction, we integrate over the $I_x(r)$ at different distances from the donor and weigh them with the probability density of the donor-bound electron

$$B_{\mathrm{N},x} = \frac{A_\mathrm{Se}\chi_\mathrm{Se}}{\mu_\mathrm{B} g_\mathrm{e}} \int I_x(r) \Psi^2(r) 4\pi r^2 dr. \tag{5.27}$$

The best fit (purple line) to the data (blue triangles), using Eq. (5.27) and shown in Fig. 5.17, yields $b_\mathrm{e} = -370\,\mathrm{mT}$ and $S = 0.07$.

Now that we know the parameters for the model it is instructive to illustrate the characteristic quantities (B_K, B_L, I_x) as a function of their distance from the donor. Figure 5.18 shows on a logarithmic scale how the magnitude of the Knight field B_K (gray

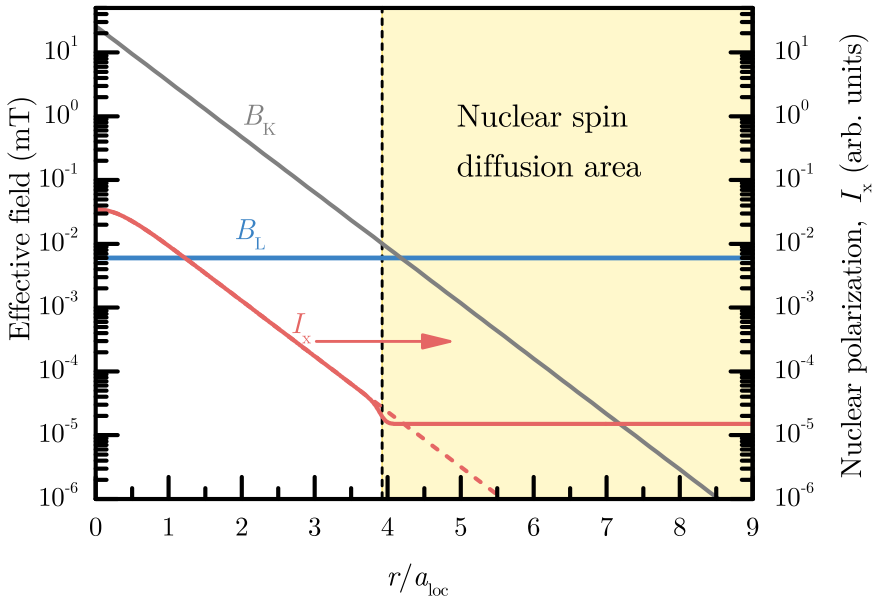

Figure 5.18 Illustration of the Knight field B_K (gray line, left axis), the local nuclear field B_L (blue line, left axis), and the projection of the nuclear spin polarization on the x axis I_x as a function of the distance from the donor as a function of the localization radius of the donor-bound electron a_{loc}. The data were calculated using Eqs. (5.21) and (5.26) with following parameters: $b_e = 370\,\mathrm{mT}$, $S = 0.07$, and $a_{loc} = 3.4\,\mathrm{nm}$, resulting in a maximal Knight field amplitude $B_K(0) = b_e S = 25.9\,\mathrm{mT}$. The yellow filling marks the nuclear spin diffusion area, beginning at $r > 3.9a_{loc}$. In analogy to Ref. [Hei15a].

line, left axis) intersects with the local nuclear field B_L (blue line, left axis) at a distance of about $3.9a_{loc}$. At this distance (dashed line, border to the yellow-filled nuclear spin diffusion area) the projection of the nuclear spin polarization on the x axis I_x already decreases by three orders of magnitude (factor 1200) compared to its maximal value directly at the donor center. Thus, the nuclear spin polarization in the nuclear spin diffusion area is homogeneous, yet very small compared to the polarization in the spatial inhomogeneous area ($r < 3.9a_{loc}$). Moreover, evaluating the integral

$$\int_0^{3.9a_{loc}} \Psi^2(r) 4\pi r^2 dr \tag{5.28}$$

we find that the donor-bound electron is to 98% confined to the area with a spatial inhomogeneous nuclear polarization [Hei15a]. Thus, even at the dopant level of sample #1, where should be a large volume of homogeneously polarized nuclei in between the donor centers, the main contribution to the Overhauser field component $B_{N,x}$ should originate from the inhomogeneously polarized nuclei in the vicinity of the donors.

5.4.3 Estimations of the S_y Spin Polarization

We do not find a significant spin polarization along the z axis S_z at magnetic fields $B_\mathrm{V} > 15\,\mathrm{mT}$, which is in good agreement with the dependence $S_z = S_z(B_\mathrm{V})$ predicted by the Hanle curve (cf. Section 2.4.3). The half-width of the Hanle curve is given by (cf. Eq. (2.34))

$$B_{1/2} = \frac{\hbar}{g_\mathrm{e}\mu_\mathrm{B}T_2^*} \approx 1.26\,\mathrm{mT}. \tag{5.29}$$

Here the natural constants [Moh15] $\hbar = 6.5821 \times 10^{-16}\,\mathrm{eV\,s}$, $\mu_\mathrm{B} = 5.7884 \times 10^{-5}\,\mathrm{eV\,T^{-1}}$, the electron g factor $g_\mathrm{e} = 1.1 \pm 0.1$ [Gre12], and the inhomogeneous spin dephasing time $T_2^* \approx 8\,\mathrm{ns}$ (sample #2, cf. Ref. [Gre12]) were used. Thus, according to the Hanle curve, the average spin polarization should be reduced by a factor

$$\left(B_\mathrm{V}/B_{1/2}\right)^2 \approx \left(\frac{20\,\mathrm{mT}}{1.29\,\mathrm{mT}}\right)^2 \approx 240. \tag{5.30}$$

However, the nonlinear fit using Eq. (5.27) to the dispersive profile of the experimentally determined shift (see the purple line in Fig. 5.17) yields a constant, average spin polarization of $S = 0.07$ and the dispersive profile of the shift itself does not exhibit any changes for increasing external field B_V even up to 140 mT. This observation allows us to assume that, in contrast to the considerations regarding the Hanle curve of the electron spins, a significant average spin polarization is present at a wide range of magnetic fields B_V. The experiments using additional RF fields with $f_\mathrm{m} = f_\mathrm{RF}$ hint at an average spin polarization along the y direction S_y. Thus, we estimate the average spin polarization components S_y and S_z based on the theory by I.A. Yugova, presented in Ref. [Zhu14]. Figure 5.19(a) shows both components as a function of the magnetic field B_V. The data were calculated using Eq. (13) from Ref. [Zhu14], where the averaging was done over one laser repetition period T_R. Realistic parameters $T_2^* \approx 10\,\mathrm{ns}$ and $T_\mathrm{R} = 13.2\,\mathrm{ns}$ were chosen for the calculations [Hei15a], where we assumed an optical pulse area [Zhu14]

$$\Theta = \int 2\langle d\rangle E(t)dt/\hbar = 0.5. \tag{5.31}$$

Here, $\langle d\rangle$ is the dipole transition matrix element, and $E(t)$ is the electric field of the laser pulse. A pulse area of $\Theta = \pi$ results in a 100% generation of the donor-bound excitons ($\mathrm{D^0X}$-HH).

For these realistic parameters the S_z component exhibits a significant polarization only around $B_\mathrm{V} = 0$ and decays to nearly zero for $B_\mathrm{V} > 10\,\mathrm{mT}$ in good agreement with the experimental data (cf. Fig. 5.9(a)), while the S_y component decays much slower with increasing B_V. The inset emphasizes their difference at higher fields. According to Ref. [Zhu14] the vector sum of the components decreases with increasing magnetic field as $1/B_\mathrm{V}$. Note that both components exhibit small oscillations in dependence on the magnetic field B_V.

Figure 5.19(b) illustrates the relative phase between the two spin polarization components in dependence on the magnetic field B_V. Except for a narrow region around $B_\mathrm{V} = 0$, we find a nearly constant phase difference of 0.5π or 1.5π of S_y relative to S_z for $B_\mathrm{V} > 5\,\mathrm{mT}$, which is in good agreement with the experimental results presented in Fig. 5.13. As said

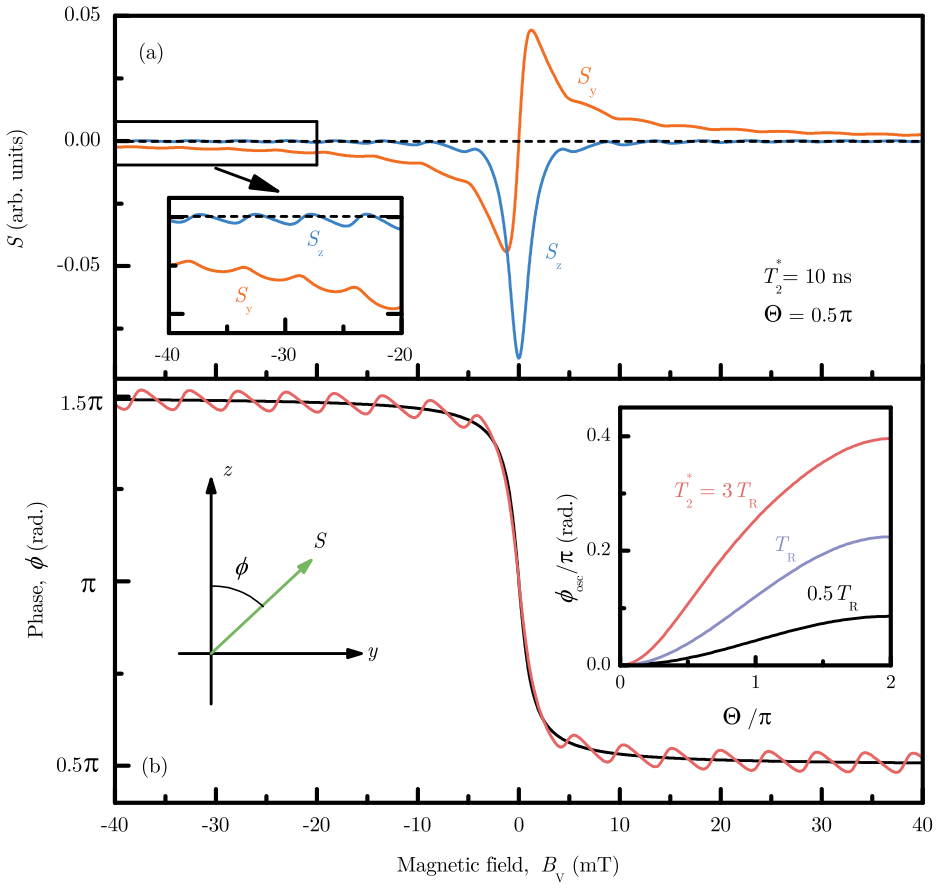

Figure 5.19 (a) Average spin components (orange line: S_y, blue line: S_z) in dependence on the magnetic field B_V. The inset emphasizes the difference of the magnitudes of the S_y and the S_z component at elevated magnetic fields B_V from 30 mT to 40 mT. (b) Phase ϕ between the spin components S_y and S_z simulated at two different spin dephasing times $T_2^* = 3T_R$ (red line) and $T_2^* = 0.5T_R$ (black line). Note that the colors correspond to the curves, shown in the inset. This inset illustrates the phase oscillation amplitude ϕ_{osc} in dependence on the optical pulse area Θ for three different spin dephasing times. The longer the spin dephasing takes in relation to the repetition period T_R, the larger the theoretically predicted phase oscillation amplitude ϕ_{osc}. In analogy to Ref. [Hei15a].

before, the phase between S_y and S_z is only nearly constant: It exhibits small oscillations. The inset of Fig. 5.19(b) shows these oscillations as a function of the optical pulse area Θ and for three different inhomogeneous spin dephasing times T_2^* in units of the laser repetition period T_R. The longer the spin dephasing time is in relation to the repetition period T_R, the larger the theoretically predicted phase oscillation amplitude ϕ_{osc}, which explains the small oscillations of both components in Fig. 5.19(a).

Following these considerations and the experimental results, only the spin polarization component S_y could explain the occurrence of the shift, resulting from a polarization of the nuclei, even at higher magnetic fields B_V. Nevertheless, the total average spin polarization

S should decay with the inverse external magnetic field $\propto \frac{1}{B_\mathrm{V}}$ according to the theory presented in Ref. [Zhu14]. The nuclear spin polarization, in turn, is proportional to S^2 (cf. Eq. (5.26) and the experimental results, shown in Fig. 5.6) and thus in contrast to the experimental results, presented in Fig. 5.4, should decay as B_V^{-2}. These experimental results (Fig. 5.4) hint at the existence of a significant average spin polarization component even at elevated external magnetic field up to $B_\mathrm{V} = 140\,\mathrm{mT}$.

This assumption is further supported by the experiments on the compensation of the Knight field B_K with an additional RF field B_RF(cf. Fig. 5.13), which demonstrate that there is a significant average spin polarization component S_y in the range of the investigated fields B_V from 20 mT to 40 mT. Taking into account these two experimental observations, we conclude that a strong average spin polarization component S_y exists and does not change in the studied magnetic field range from 0 mT to 140 mT, which contradicts the theoretical simulation, presented in Fig. 5.19. The spin polarization component S_y causes the nuclear spin polarization, which, in turn, leads to a shift of the RSA peaks at higher excitation densities.

5.5 Conclusion

We present a detailed study of the electron-nuclear interaction at the conditions of a time-resolved Kerr rotation (TRKR) experiment. Despite the low natural abundance of isotopes with nonzero nuclear spin in the studied material system ZnSe (cf. Table 2.1), we observe significant effects resulting from the nuclear spins. Since the low natural abundance is emphasized as an advantage of this material system [Gre12], these effects might seem surprising at first. Comparing the maximum Overhauser field B_N in InGaAs QDs reported by Auer *et al.* [Aue09]

$$B_\mathrm{N}^\mathrm{max} = 6.9\,\mathrm{T}$$

with estimations for our material system according to Eq. (5) from Ref. [Tes08]

$$B_\mathrm{N}^\mathrm{max} = \frac{I_\mathrm{Se}\chi_\mathrm{Se}A_\mathrm{Se} + I_\mathrm{Zn}\chi_\mathrm{Zn}A_\mathrm{Zn}}{g_\mathrm{e}\mu_\mathrm{B}} \approx 25.3\,\mathrm{mT}, \tag{5.32}$$

the strong effects resulting from the nuclear spin polarization are even more surprising.

However, adapting the considerations of Akimov *et al.* [Aki06], who studied CdSe/ZnSe quantum dots (QDs), for donor-bound electrons in ZnSe, we can explain the strong nuclear signatures in the resonant spin amplification (RSA) signals: The strength of the electron-nuclear hyperfine interaction is not only characterized by the isotope abundances χ and the hyperfine constants A, but also by the number of nuclei N_L effectively seen by the electron [Aki06].

Due to the low natural abundance and the strong localization of the electron spin at the fluorine donor the number of nuclei interacting with a single electron spin is very small. About 790 ^{77}Se and 430 ^{67}Zn nuclei interact with a donor-bound electron confined to its localization volume with radius a_loc [Gre12], so the total number of nuclei with nonzero spin in this volume is about $N_\mathrm{L} = 1220$. This is in stark contrast to the situation in typical III-V QDs, where N_L is in the range from 1×10^5 to 1×10^6 [Aki06]. Taking into account

that the effect of the Knight field B_K on a single nucleus scales like A/N_L, we can explain the significant electron-nuclear interaction in the studied material system.

We use the TRKR in RSA configuration and obtain a deep insight into the electron-nuclear spin dynamics. The optical orientation of the electron spins by the pump beam results in a dynamic nuclear polarization (DNP) at high pump power and reveals itself as a shift of the RSA peak positions. Zhukov *et al.* already demonstrated that the TRKR technique in RSA configuration allows one to all-optically measure the nuclear magnetic resonance (NMR) frequency, where the NMR in the external field B_V (Voigt geometry) was addressed by the helicity modulation frequency of the pump beam. While in that study the pump was modulated using different photoelastic modulators (PEMs), which allowed only for a modulation at certain, fixed frequencies, in this work an electro-optical modulator (EOM) modulated the pump beam and allowed us to vary the helicity modulation frequency f_m in a broad range. Furthermore, we focus on the detailed study of a single material system and the nature of the inhomogeneous nuclear spin polarization, revealing itself not only in the form of the small additional peak in the RSA spectra, but also in the form of the shift of the RSA peaks.

To obtain an even better understanding, we performed TRKR measurements in the same magnetic field range as the RSA spectra, where B_V was increased in incremental steps of 1 mT. This allows us to determine the induced nuclear fields not only at the positions of RSA peak but also in between the peaks. The increased magnetic field resolution reveals the sharp transition at $B_V = B_{NMR}$.

The experimental findings allow us to develop and test a quantitative model, describing the observed shifts of the RSA peaks at high pump power with all their peculiarities. The model is based on classical nuclear spin cooling in the rotating frame system, which results in a DNP. This conclusion is supported by the position of the small additional peak in the RSA spectra and its dependence on the helicity modulation frequency f_m. The shape and the width of the dispersive profile of the shift of the RSA peaks indicate that the DNP is driven by the inhomogeneous Knight field $\boldsymbol{B}_K$ of the donor-bound electrons. Measurements using an additional RF field indicate that the field $\boldsymbol{B}_K$ is pointing along the y direction and does not depend on the external magnetic field B_V in the studied range from 20 mT to 40 mT. Furthermore, the dispersive profile of the peak shift, measured at increased modulation frequencies f_m to shift it to higher B_V, exhibits no changes in the studied B_V range from 0 mT to 140 mT. The model equation for the nuclear polarization along the x direction allows us to estimate the value of the Knight field $\boldsymbol{B}_K$. This value, in turn, leads to the conclusion that the nuclear spin diffusion is hindered within a radius of about $3.9a_{loc}$ around a fluorine donor center. Taking into account the average distance between donors for sample #2 of $\bar{d} \approx 1.8a_{loc}$, we conclude that no nuclear spin diffusion can take place in this sample so that the DNP results in an inhomogeneous nuclear spin polarization explaining the occurrence of the broad dispersive profile of the shift of the RSA peaks. While the average distance between donors is much larger for sample #1 ($\bar{d} \approx 18a_{loc}$) and thus nuclear spin diffusion is possible in the area between the donors, the magnitude of the Knight field B_K at distances exceeding $3.9a_{loc}$ is very small, and so the main contribution to the Overhauser field B_N should originate from the inhomogeneous nuclear spin polarization within $r < 3.9a_{loc}$.

While the presented model accurately describes the observed dispersive profile of the

shift of the RSA peaks, except for the offset of the dispersive profiles, which is out of the scope of this thesis and is subject of further studies, the significant, constant spin polarization component S_y providing the DNP contradicts the theoretical model presented in Ref. [Zhu14]. According to this model the modulus of the average spin polarization should decay as B_{V}^{-1} and, in turn, should lead to a reduction of the shift of the RSA peaks. However, this is not observed in experiment and this suggests that there is a relatively strong spin polarization component S_y that does not depend on the magnetic field B_{V} in the studied range. This component S_y could result from certain intrinsic anisotropies of fluorine-doped ZnSe. The fluorine donor, placed in the lattice at a selenium site, could cause such an anisotropy. A further possible explanation is an anisotropy of the electron spin generation, resulting from strain in the crystal lattice.

However, a DNP mechanism, which does not rely on a relatively strong, constant spin polarization component S_y, was considered and investigated experimentally. At sufficiently high pump power the DNP could be provided via the optical Stark effect, which denotes the interaction of the absorption resonance with the circularly polarized light. Korenev [Kor11] described that in the case of pulsed excitation the laser pulses can induce an electron spin polarization component S_x along the external field B_{V}, if the electron spins precess in phase with multiples of the laser repetition frequency (cf. phase synchronization condition for RSA peaks (Eq. (3.6))). Due to the interaction with the absorption resonance, the sign of the induced spin polarization should depend on the energy difference between absorption and excitation. Thus, we determined the shift of the RSA peaks at excitation energies below and above the D^0X-HH resonance. We observe no sign changes of the induced shift and conclude that the DNP is not provided via the optical Stark effect.

It is for low fields,[...], that a theoretical examination making use of thermodynamic principles yields new quantitative predictions. In particular, a spin temperature is analytically defined, and its identity with thermodynamic temperature is experimentally established.

A. Abragam and W. G. Proctor [Abr58]

6 Dynamics of the Nuclear Spin Polarization

In Chapter 5, the induced spatially inhomogeneous nuclear spin polarization is explained using a model based on the concept of classical nuclear spin cooling (see also Ref. [Hei15a]). However, this concept implies that the nuclear spin system (NSS) can be described using the spin temperature approach (cf. Section 2.3.9). Thus, the spin relaxation time T_1^{N} and the spin coherence time T_2^{N} of the ensemble of nuclear spins must fulfill the following relation (cf. Eq. (2.27))

$$T_1^{\mathrm{N}} \gg T_2^{\mathrm{N}}, \tag{6.1}$$

where both characteristic times of the NSS will be measured at the conditions of the pump-probe experiment in this chapter.

6.1 Measurement of the Nuclear Spin Relaxation Time T_1^{N}

To determine the first of these two times, we develop an all-optical approach. It is based on a fast switching between two different pump helicity modulation frequencies $f_{\mathrm{m},1}$ and $f_{\mathrm{m},2}$ (cf. Section 3.4.3 for a description of the employed electronic components). Note that all measurements presented in this chapter were performed for sample #2 ($n_{\mathrm{F}} \approx 1 \times 10^{18}\,\mathrm{cm}^{-3}$, cf. Section 3.3) at the following conditions (unless specified otherwise): $P_{\mathrm{Pu}} = 8\,\mathrm{mW}$, $P_{\mathrm{Pr}} = 0.5\,\mathrm{mW}$ and $T = 1.8\,\mathrm{K}$. The first modulation frequency $f_{\mathrm{m},1}$ (example measurement in Fig. 6.1: $f_{\mathrm{m},1} = 100\,\mathrm{kHz}$) was selected to ensure that the magnetic field of the optically addressed nuclear magnetic resonance (example: $B_{\mathrm{NMR}} = 12.3\,\mathrm{mT}$) is close to the external field (example: $B_{\mathrm{V}} = 15.7\,\mathrm{mT}$) so that the KR signal is maximally influenced by the nuclear polarization, corresponding to the shift of the RSA peak near the resonance. We chose the second modulation frequency $f_{\mathrm{m},2} = 1050\,\mathrm{kHz}$ so that the distance between the field of NMR $B_{\mathrm{NMR}} = 128.7\,\mathrm{mT}$ (cf. Eq. (5.4)) and the external field (example: $B_{\mathrm{V}} = 15.7\,\mathrm{mT}$) was very large. This ensures that the nuclear polarization becomes very small upon switching to $f_{\mathrm{m},2}$ despite the extended tails of the dispersive profile of the shift of the RSA peaks, described in Section 5.1. As a result, the change of the KR signal due to the change of f_{m} will be maximal, if the external field B_{V} is set to the right flank of the RSA peak following the resonance (cf. Fig. 6.1(a)). This is the case for the example measurement, where the magnetic field position B_{V} is illustrated by the arrow in Fig. 6.1(a). Note the relatively large KR signal difference between $f_{\mathrm{m},1}$ and $f_{\mathrm{m},2}$ at this field, which improves the signal-to-noise ratio of the KR transient recorded upon switching the helicity modulation frequency.

Figure 6.1(a) shows a comparison of two RSA spectra: The spectrum at $f_{\mathrm{m},1} = 100\,\mathrm{kHz}$ is illustrated by the blue line and the one at $f_{\mathrm{m},2} = 1050\,\mathrm{kHz}$ by the green line. All

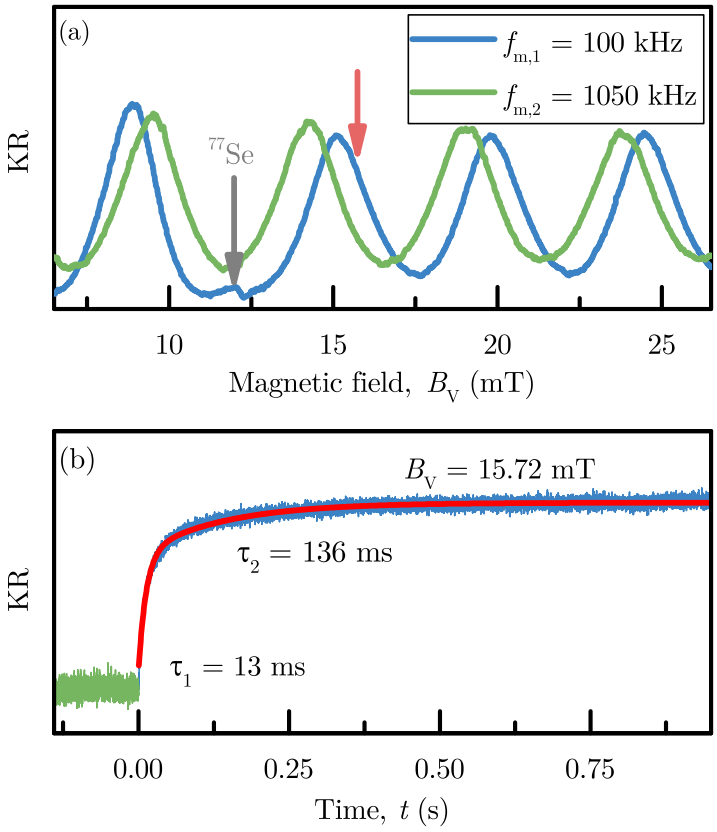

Figure 6.1 (a) RSA spectra (sample #2), measured at $f_{m,1} = 100\,\text{kHz}$ (blue line) and $f_{m,2} = 1050\,\text{kHz}$ (green line). The optically induced NMR of the ^{77}Se isotope at $f_{m,1} = 100\,\text{kHz}$ is shown by the gray arrow, and the red arrow marks the magnetic field position ($B_V = 15.72\,\text{mT}$) for the measurement shown in Fig. 6.1(b). (b) KR signal transients at fixed B_V, induced by switching from $f_{m,2}$ (green line) to $f_{m,1}$ (blue line). The red line shows a double exponential fit to the data. Its parameters are given in Table 6.1. In analogy to [Hei16].

peak positions slightly differ for the two modulation frequencies, where the peak at $f_{m,1}$ following the NMR of the ^{77}Se (see gray arrow) exhibits the largest shift with respect to the corresponding peak at $f_{m,2}$.

Figure 6.1(b) illustrates the transient upon switching the modulation frequency from $f_{m,2}$ to $f_{m,1}$ averaged over many switching cycles. The measurement at fixed B_V allows us to detect the change of the KR signal due to the shift of the RSA peak, which, in turn, results from a change of the spin polarization of the ^{77}Se nuclei. Upon switching from $f_{m,2}$ to $f_{m,1}$ at $t = 0$ the KR signal increases and saturates in less than a second. The transient from 0 s to 0.9 s is fitted with a double exponential function, given by the following equation

$$\theta_{KR}(t) = A_{off} - A_1 \exp\left(-\frac{t}{\tau_1}\right) - A_2 \exp\left(-\frac{t}{\tau_2}\right). \tag{6.2}$$

Here, A_1 and A_2 are the amplitudes of the exponential functions, τ_1 and τ_2 their rise times

and A_{off} is the offset of the KR signal. Table 6.1 shows the parameters of the best fit to the data. Since the transient is the result of a repolarization of the nuclear spins, a

Table 6.1 Parameters of the best fit to the transient shown in Fig. 6.1(b). The errors are obtained from the fit.

A_1	0.0425 ± 0.0001	arb. units
A_2	0.0189 ± 0.0001	arb. units
τ_1	13 ± 1	ms
τ_2	136 ± 1	ms
A_{off}	$0.066\,03 \pm 0.000\,01$	arb. units

possible explanation of this double exponential behavior might be the inhomogeneity of the Knight field B_K and the nuclear spin polarization, discussed in the previous chapter (cf. Chapter 5). Then the minimal repolarization time τ_1 should stem from the strongly polarized nuclei near the donor centers, which, in turn, interact with the strongest Knight field B_K and thus are most sensitive to a change of the helicity modulation frequency. We suggest that the maximal repolarization time τ_2 corresponds to a repolarization of the weaker polarized nuclei at the edge of the localization volume of the donor-bound electrons, where a much weaker Knight field B_K leads to a slower repolarization process. Figure 6.2

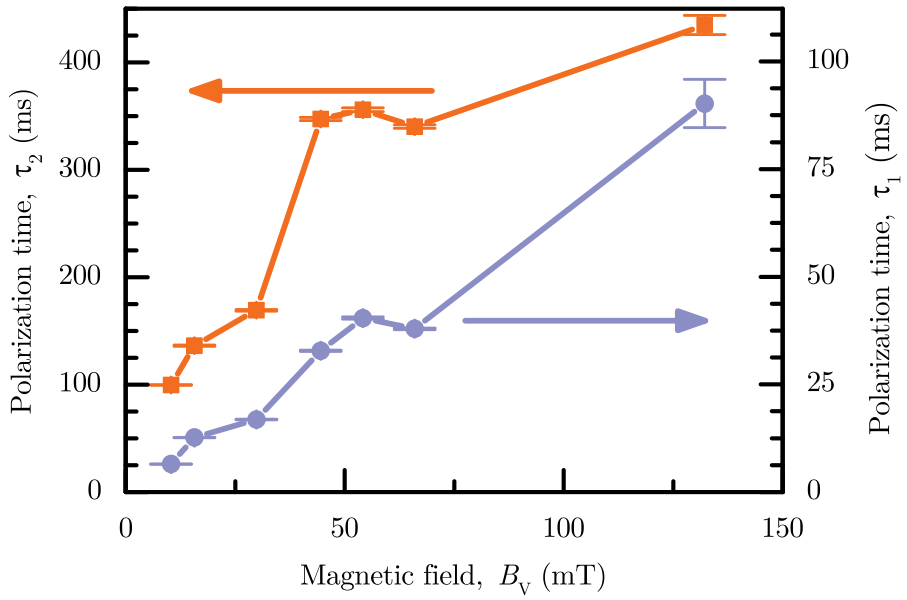

Figure 6.2 Maximal τ_2 (left y axis, orange squares) and minimal τ_1 (right axis, violet circles) polarization time as a function of the magnetic field B_V. The corresponding lines are shown as a guide to the eye. The off-resonant (nuclei) frequency $f_{m,2}$ was kept at 1050 kHz for all measurements, while $f_{m,1}$ was varied together with B_V and set to the following values 50 kHz, 100 kHz, 200 kHz, 300 kHz, 400 kHz, and 500 kHz. $P_{Pu} = 8$ mW, $P_{Pr} = 0.5$ mW, and $T = 1.8$ K. In analogy to [Hei16].

summarizes the results of several measurements, which are similar to the one depicted

in Fig. 6.1(a) and (b). We performed the measurements at different magnetic fields B_V, where the first modulation frequency $f_{m,1}$ was adapted to ensure that we achieved a high degree of nuclear spin polarization and thus a maximal change of the KR signal upon switching to $f_{m,2}$. We determine an estimation of the maximal τ_2 (left y axis, orange squares) and minimal τ_1 (right axis, purple circles) polarization time as a function of B_V. The corresponding orange and purple lines are shown as a guide to the eye. We observe an increase of both polarization times τ_1 and τ_2 with increasing magnetic field B_V. A possible explanation of this behavior is the increasing difference between the electron (cf. Eq. (2.15)) and nuclear (cf. Eq. (2.16)) Zeeman splitting. In summary, the nuclear polarization time, which corresponds to the nuclear spin relaxation time T_1^N at the conditions of the TRKR experiment, is between about 10 ms (minimal polarization time τ_1 at $B_V = 10.3$ mT) and about 400 ms (maximal polarization time τ_2 at $B_V = 132.2$ mT).

However, we expect a much longer time T_1^N in the dark due to the lack of spin-polarized electrons, whose Knight field B_K leads to nuclear spin flips. To check this hypothesis, we performed an additional measurement, where the repolarization process due to the switching of f_m was interrupted with an optical shutter (`Thorlabs SH05 shutter head` and `Thorlabs SC10 controller`, cf. also Section 3.4.3). Figure 6.3 depicts the results of

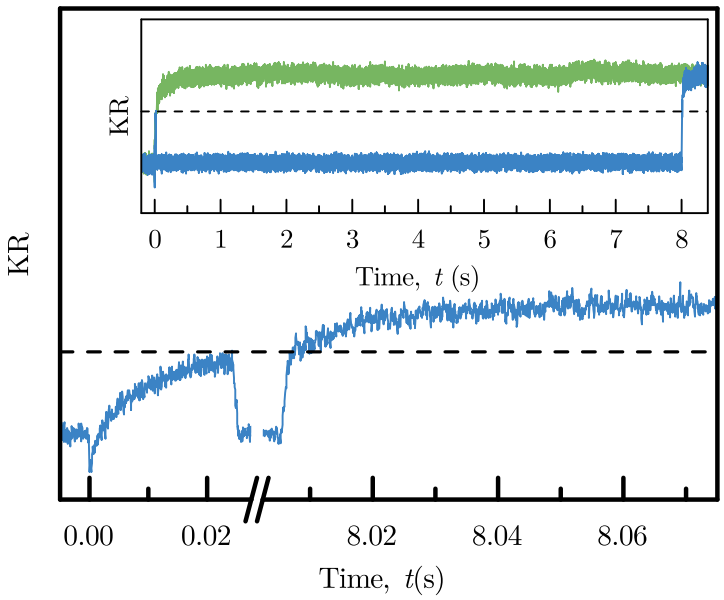

Figure 6.3 KR transient (blue line) upon switching from $f_{m,1} = 50$ kHz to $f_{m,2} = 1050$ kHz, where the depolarization of the nuclear spins was started and then interrupted for 8 s by the mechanical shutter. Note that the time axis (x axis) exhibits a break from 0.0275 s to 8.0025 s to allow for a better comparison of the signal before closing the shutter and after reopening it. The dashed line at the KR signal level upon closing the shutter is shown as a guide to the eye. The inset illustrates the whole interrupted depolarization process (blue line) and shows the same transient without an interruption by a shutter (green line) for comparison. The dashed line in the inset is also a guide to the eye. In analogy to Ref. [Hei16].

this measurement. The modulation frequency was switched from $f_{\mathrm{m},1}$ to $f_{\mathrm{m},2}$ at $t = 0$ and shortly afterward the shutter was closed ($t \approx 24\,\mathrm{ms}$). As a result, the depolarization process is started, but is interrupted for 8 s. Nevertheless, the KR signal level (see dashed line) before closing and after reopening the shutter are nearly identical. Thus, we conclude that blocking the illumination of the sample slows down the depolarization or repolarization process by preventing electron-nuclear spin flip-flops with spin-polarized electrons. The fact that no nuclear spin relaxation occurs during the dark time allows us to conclude that the nuclear spin relaxation time in the dark $T_1^{\mathrm{N,dark}}$ should exceed several tens of seconds. Please note that the measurement presented here only provides a lower limit for $T_1^{\mathrm{N,dark}}$.

In summary, an all-optical technique allows us to determine the order of magnitude of the nuclear spin relaxation time T_1^{N} at the conditions of the TRKR experiments, presented in the previous chapters (cf. Chapter 4 and Chapter 5), and also to obtain a lower limit of this time in the dark $T_1^{\mathrm{N,dark}}$. However, to obtain the nuclear spin coherence time T_2^{N}, we have to achieve coherent control of the nuclear spins and thus have to leave the all-optical regime.

6.2 Coherent Control of the Nuclear Spins

The coherent control of the ^{77}Se nuclei in sample #2 was achieved by an additional radio frequency (RF) excitation with a small coil near the surface of the sample, which was similar but not identical to the one used in Sections 5.3.2 and 5.3.3. We performed all measurements using a double modulation technique (cf. Sections 3.4.4 to 3.4.7 for details).

6.2.1 Preliminary Measurements

Resonant RF pulses are most effective to manipulate the nuclear spins. Thus, we first determine the NMR frequency at fixed external magnetic field B_{V} by an optically detected nuclear magnetic resonance (ODNMR) measurement. Figure 6.4 shows an RSA spectrum (blue line), measured at a helicity modulation frequency of $f_{\mathrm{m}} = 50\,\mathrm{kHz}$. The orange arrow marks the magnetic field position $B_{\mathrm{V}} = 7.5\,\mathrm{mT}$, where the ODNMR measurement (cf. Section 3.4.4 for the technical details) was performed. The inset depicts the result of the actual ODNMR measurement with continuous-wave (CW) RF excitation: the KR signal (blue line) at $f_{\mathrm{m}} = 50\,\mathrm{kHz}$ as a function of the RF frequency f_{RF} at fixed RF amplitude $A_{\mathrm{RF}} = 0.5\,\mathrm{V_{pp}}$ ($\mathrm{V_{pp}}$="Volt peak to peak"). Here, f_{RF} was varied from 56.5 kHz to 65.5 kHz. The KR signal exhibits a dip at about 61 kHz, which we interpret as the result of a decrease of the nuclear spin polarization along the external magnetic field B_{V} due to resonant heating of the nuclear spin system (NSS). The red line is a fit of a Lorentzian (cf. Eq. (5.11)) to the data. Table 6.2 shows the parameters of this fit, where the NMR frequency $f_{\mathrm{NMR}} = (60.93 \pm 0.01)\,\mathrm{kHz}$ is the most important parameter. Performing measurements, based on the same approach, we determined the NMR frequency f_{NMR} for each magnetic field position B_{V} before proceeding with the further measurements, presented in the following. To achieve coherent control of the nuclear spin ensemble, we had to switch from a CW RF excitation to a pulsed RF excitation, where the variation of the pulse width τ_{p} allowed us to control the effect on the nuclear spins. The measurement, depicted in Fig. 6.5, shows the KR signal (blue line) at $f_{\mathrm{m}} = 50\,\mathrm{kHz}$ as a function of the RF

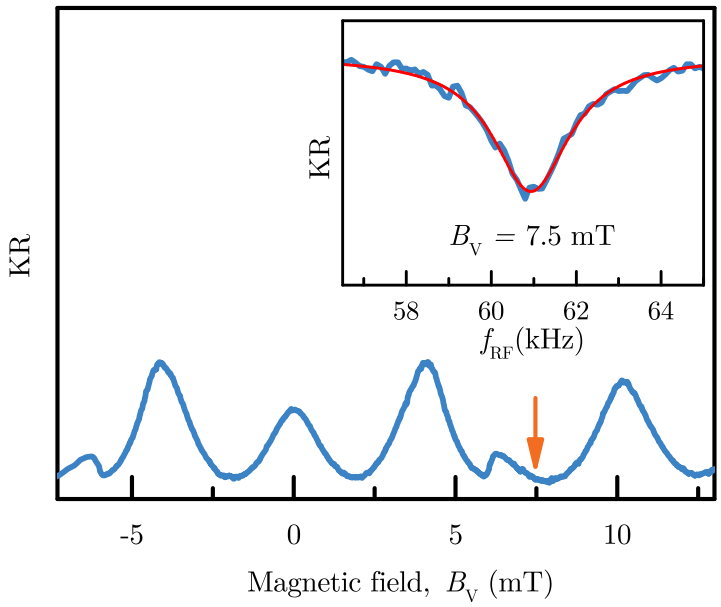

Figure 6.4 Kerr rotation signal (blue line) in dependence on the magnetic field B_V (RSA spectrum). The orange arrow marks the magnetic field $B_V = 7.5\,\mathrm{mT}$ for the measurement, shown in the inset. The inset depicts the KR signal in dependence on f_{RF}, where the red line is a nonlinear fit using Eq. (5.11). The values of the fitting parameters are given in Table 6.2. In analogy to Ref. [Hei16].

Table 6.2 Parameters of the best fit to the KR signal in dependence on f_{RF}, shown in Fig. 6.4. See also Eq. (5.11). The errors are obtained from the fit.

Amplitude	A_0	-950 ± 25	arb. units
NMR frequency	f_{NMR}	60.93 ± 0.01	kHz
FWHM	Γ	2.19 ± 0.06	kHz
Offset	A_{off}	-8 ± 2	arb. units

pulse width at a fixed RF amplitude $A_{RF} = 4\,V_{pp}$. It exhibits oscillations, which we can explain by the rotation of the nuclear spins about the effective magnetic field B_{eff} produced by the RF coil. These oscillations are known as so-called Rabi oscillations [Rab37; Rab38; Rab39]. The red line in Fig. 6.5 shows a fit to the data, using the following equation (exponentially damped oscillation):

$$\theta_{KR}(\tau_p) = A_0 \exp\left(-\frac{\tau_p}{\tau_0}\right) \sin\left(2\pi f_{Rabi}\tau_p + \varphi\right) + A_{off} \tag{6.3}$$

Table 6.3 shows the values of the parameters of the best fit to the data. Here, the Rabi frequency f_{Rabi} is the most important parameter, since it allows us to estimate the effective magnetic field B_{eff} of the RF coil [Hei16]

$$B_{eff} = \frac{2\pi f_{Rabi}}{\gamma_{Se}}. \tag{6.4}$$

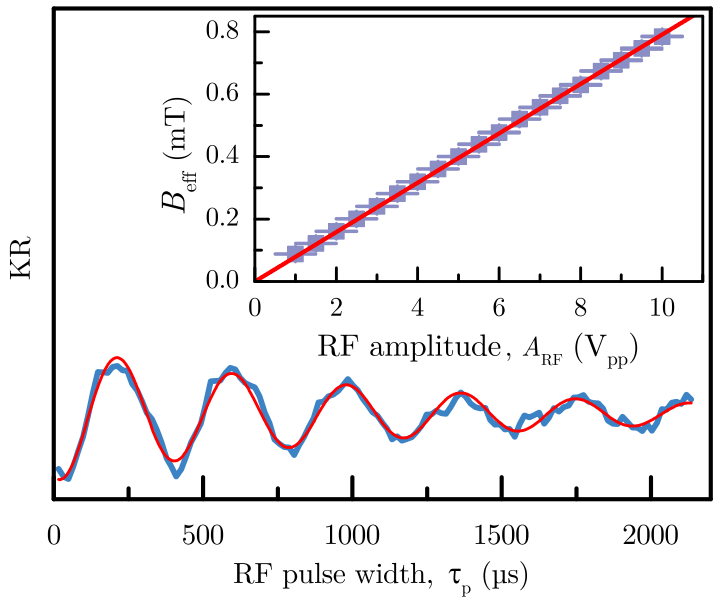

Figure 6.5 Kerr rotation (blue line) in dependence on the RF pulse width τ_{p} at $B_{\mathrm{V}} = 7.5\,\mathrm{mT}$, $A_{\mathrm{RF}} = 4\,V_{\mathrm{pp}}$ and $f_{\mathrm{RF}} = 60.9\,\mathrm{kHz} \approx f_{\mathrm{NMR}}$. The red line is a nonlinear fit to the data (cf. Eq. (6.3) and Table 6.3. The inset illustrates the effective magnetic field B_{eff} of the RF coil (violet squares with error bars) as a function the applied RF amplitude A_{RF} (cf. Eq. (6.4) and discussion in the text). The red line is a weighted linear fit to the data using Eq. (6.5). In analogy to Ref. [Hei16].

Combining the Rabi frequency $f_{\mathrm{Rabi}} \approx (2.61 \pm 0.01)\,\mathrm{kHz}$, determined from the fit to the

Table 6.3 Parameters of the best fit to the data shown in Fig. 6.5. The errors are obtained from the fit.

Amplitude	A_0	114 ± 4	arb. units
Rabi frequency	f_{Rabi}	2.61 ± 0.01	kHz
Phase	φ	1.0 ± 0.1	1
Decay constant	τ_0	70 ± 4	µs
Offset	A_{off}	165 ± 1	arb. units

data in Fig. 6.5, with the gyromagnetic ratio of ^{77}Se $\gamma_{\mathrm{Se}} = 5.125\,387 \times 10^7\,\mathrm{rad\,s^{-1}\,T}$ (see Ref. [Har02]) we obtain an effective field of

$$B_{\mathrm{eff}} \approx (320 \pm 1)\,\mu\mathrm{T},$$

where the relative errors of f_{Rabi} and B_{eff} are identical according to Gaussian error propagation.

The inset shows the effective magnetic field of the coil as a function of the applied RF amplitude A_{RF} and thereby summarizes the results of several of such measurements (violet squares with error bars). The red line is a weighted linear fit to the data according to the

following equation:

$$B_{\text{eff}}(A_{\text{RF}}) = m \cdot A_{\text{RF}} \tag{6.5}$$

The fit yields a slope of

$$m = (79.1 \pm 0.2)\,\mu\text{T}\,\text{V}_{\text{pp}}^{-1}.$$

It is important to note that the frequency dependence of the effective field produced by the coil is not studied here. However, this rather technical detail is not important for the validity of the results on the nuclear spin dynamics, presented in the following. The NMR frequency and Rabi oscillation measurements were performed prior to the following measurements for each magnetic field position B_{V} to determine the proper parameters for the Ramsey and Hahn echo measurements.

6.2.2 Measurement of the Inhomogeneous Nuclear Spin Dephasing Time

Using the methods (ODNMR and Rabi oscillation measurements) described in the previous chapter, we determined the parameters for the actual measurements, relying on a coherent control of the nuclear spins. Using these parameters we performed different experiments. The Ramsey method [Ram49; Ram50; Ram95] employs a sequence of two $\pi/2$ pulses with a variable delay Δt between the pulses (cf. Section 3.4.6 for the details of the experimental setup). The inset of Fig. 6.6 illustrates how we determined the width τ_{p} of a $\pi/2$ pulse from a Rabi oscillation measurement (KR signal (blue line) in dependence on the pulse width τ_{p}). The orange arrow marks the length of a $\pi/2$ pulse. The measurement using the Ramsey method (cf. Fig. 6.6) was performed at the same conditions as the Rabi oscillation measurement. The blue line illustrates the KR signal at $f_{\text{m}} = 50\,\text{kHz}$ as a function of the time delay Δt. Here, Δt was the distance between the middle of the pulses (width $\tau_{\text{p}} \approx 65\,\mu\text{s}$) and the distance of 65 µs was subtracted. The KR signal exhibits oscillations with a period of $(2.3301 \pm 0.0001)\,\mu\text{s}$, determined from the fit with an exponentially damped oscillation shown by its envelope (red lines). Please refer to Eq. (6.3) for the fitting function (Rabi frequency f_{Rabi} replaced with "Ramsey frequency" f_{Ramsey}) and to Table 6.4 for the values of the parameters of the best fit. We can explain the oscillations in Fig. 6.6 using

Table 6.4 Parameters of the best fit to the data shown in Fig. 6.6. The errors are obtained from the fit.

Amplitude	A_0	133 ± 2	arb. units
Ramsey frequency	f_{Ramsey}	429.16 ± 0.02	kHz
Phase	φ	5.99 ± 0.01	1
Decay constant	τ_0	160 ± 5	µs
Offset	A_{off}	647.1 ± 0.4	arb. units

the "graphical" representation of a quantum mechanical two-level system, developed by Felix Bloch [Blo46], the so-called Bloch sphere. The north pole of the sphere represents the ground state $|0\rangle$, while the south pole corresponds to the excited state $|1\rangle$; both are defined with respect to the external magnetic field B_{V}. The equator represents the superposition state of $|0\rangle$ and $|1\rangle$ with equal probability of both states, where each point on the equator

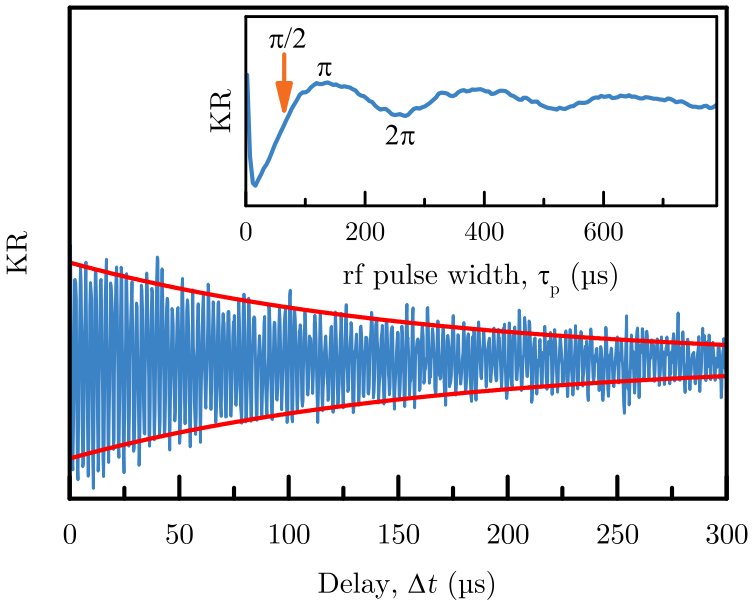

Figure 6.6 Kerr rotation signal (blue line) in dependence on the time delay Δt. $B_V = 52.7\,\mathrm{mT}$, $f_{RF} = 429.5\,\mathrm{kHz}$, $A_{RF} = 10\,V_{pp}$ and $\tau_p \approx 65\,\mu s$. The red lines show the envelope of the best fit of a damped oscillation to the data. The inset shows the Kerr signal (blue line) as a function of the pulse width τ_p. The orange arrow marks the width of the $\pi/2$ pulse used for the measurement of the Ramsey fringes. In analogy to Ref. [Hei16].

corresponds to a different relative phase between these two eigenstates. The actual state of the system is denoted by the Bloch vector

$$|\Psi\rangle = \cos\left(\frac{\Theta}{2}\right)|0\rangle + \exp(i\phi)\sin\left(\frac{\Theta}{2}\right)|1\rangle\,. \tag{6.6}$$

This graphical representation is illustrated in Fig. 6.7. It is important to note that this representation can be used for single spins as well as the collective magnetization or average spin polarization of an ensemble. There it can be useful to draw more than one Bloch vector to illustrate, e.g., dephasing processes.

The first $\pi/2$ pulse applied during the Ramsey method rotates the Bloch vector of the ensemble of the nuclear spins from the north pole ($|\Psi\rangle = |0\rangle$, $\Theta = 0$) to the equator ($\Theta = \pi/2$) of the Bloch sphere. The system is in a superposition state, and the spins precess in the equatorial plane with the nuclear Larmor frequency, which is determined by the Zeeman splitting of the nuclear spins. The relative phase ϕ changes due to the precession and the subsequent $\pi/2$ pulse rotates the Bloch vector either back to the north pole ($|0\rangle$) or to the south pole ($|1\rangle$) depending on the time delay Δt between the pulses, which determines the change of ϕ. This explains the oscillations of the KR signal in dependence on Δt, so-called Ramsey fringes. We should also note that the frequency of these oscillations corresponds to the nuclear Larmor frequency in the external magnetic field B_V: $f_{Ramsey} = \frac{\omega_N}{2\pi} = f_{NMR}$.

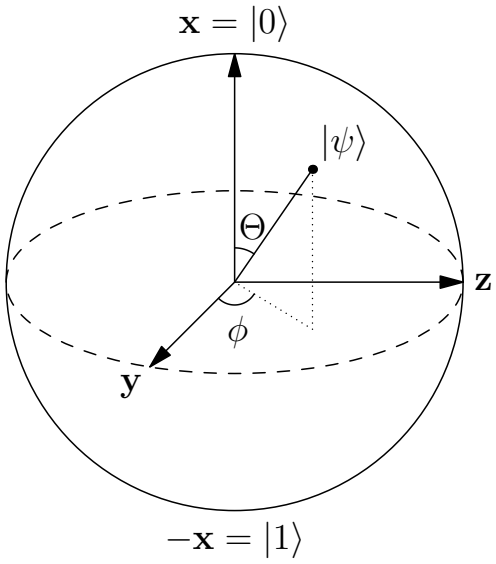

Figure 6.7 Schematic of a Bloch sphere [Blo46]. Each point on the surface of the sphere (Bloch vector) denotes a specific superposition state of the eigenstates $|0\rangle$ and $|1\rangle$ or an average polarization of an ensemble of spins. Rendered with `Asymptote` with code in analogy to Ref. [Glo12].

We can explain the exponential decay of the signal in Fig. 6.6 by the following considerations: Due to inhomogeneities in the sample, different ^{77}Se spins of the ensemble may have slightly different nuclear Larmor frequencies ω_N. Thus, the average polarization decreases during the precession on the equator of the Bloch sphere, which, in turn, results in a smaller KR signal upon rotation to the $|0\rangle$ or $|1\rangle$ state by the second $\pi/2$ pulse. It is important to note that this is not the only effect decreasing the average polarization. Nevertheless, the decay constant τ_0 of the fit (envelope is shown by red lines in Fig. 6.6) represents the inhomogeneous nuclear spin dephasing time $T_2^{*,\mathrm{N}}$, which describes the dephasing due to ensemble inhomogeneities as well as other mechanisms, e.g., spin flips. At the experimental conditions ($B_\mathrm{V} = 52.7\,\mathrm{mT}$), the initially coherently precessing nuclei run out of phase during the time

$$T_2^{*,\mathrm{N}} = \tau_0 = (160 \pm 5)\,\mu\mathrm{s}.$$

6.2.3 Measurement of the Nuclear Spin Coherence Time

To determine the nuclear spin coherence time T_2^N, we have two options:

1. Measure Ramsey fringes of a single spin, which is not feasible for nuclear spins.
2. Eliminate the dephasing due to ensemble inhomogeneities. Here, it is important that the inhomogeneous dephasing is a reversible effect.

We realize the second option by applying a π pulse, while the spins precess about the equator of the Bloch sphere. The π pulse then inverts the orientation of the spins. Modifying the Ramsey method with an additional π pulse in between the two $\pi/2$ pulses we obtain the Hahn echo sequence [Hah50]. The first $\pi/2$ pulse rotates the spins to the equator of the

Bloch sphere, where they precess with the nuclear Larmor frequency ω_N. As a result, the spin ensemble dephases during the interval Δt before the arrival of the π pulse, which inverts the orientation of all spins of the ensemble. The spins, in turn, rephase during the next interval Δt, so that the dephasing due to ensemble inhomogeneities during the first interval Δt is reversed. After a time $2\Delta t$ a subsequent $\pi/2$ pulse rotates the average spin of the ensemble to the south pole ($|1\rangle$) of the Bloch sphere, which leads to a Hahn echo (nuclear spin echo) [Hei16; Hah50]. Since it was experimentally very difficult to measure the amplitude exactly at the occurrence of the nuclear spin echo and to time the arrival of the second $\pi/2$ pulse properly, we only set the first interval exactly to Δt, but varied the arrival time of the final $\pi/2$ pulse and measured the KR as a function of the time after the arrival of this pulse.

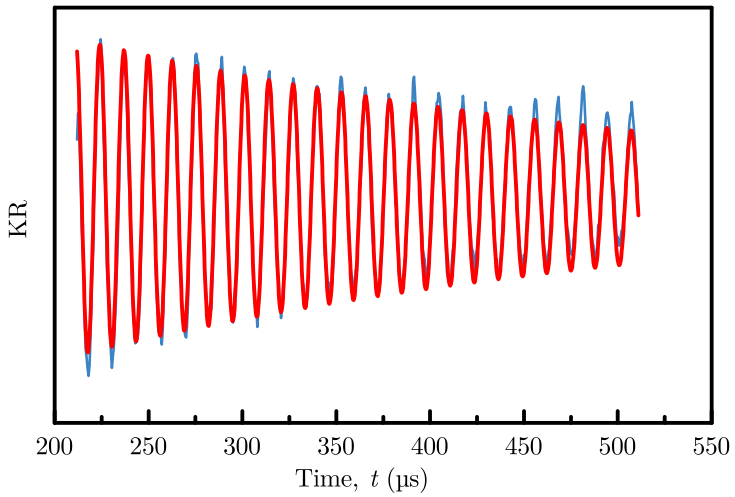

Figure 6.8 KR signal (blue line) as a function of the time t of the arrival of the second $\pi/2$ pulse. $f_m = 50\,\text{kHz}$, $f_{RF} = 77.9\,\mu\text{s}$, $B_V = 52.7\,\text{mT}$. The time delay, determining only the interval between first $\pi/2$ pulse and the π pulse, was at $\Delta t = 100\,\mu\text{s}$.

Figure 6.8 shows an example of such a measurement. The KR signal exhibits oscillations that we interpret as a signature similar to the Ramsey fringes, shown in Fig. 6.6. We suggest that the absence of a pronounced nuclear spin echo peak results from the weak inhomogeneity of the nuclear spin ensemble, addressed by our rather long RF pulses (cf. also Section 6.3). However, we calculated the echo amplitude at $t = 2\Delta t$ using the result of a fit of an exponentially damped oscillation to the KR signal as a function of time. The echo amplitude, determined from these fits and shown in Fig. 6.9, decays exponentially with the nuclear spin coherence time T_2^N. The inset in Fig. 6.9 illustrates the RF pulse sequence used for the Hahn echo measurement at $B_V = 9.6\,\text{mT}$, $f_{RF} = 77.9\,\text{kHz}$, and $A_{RF} = 10\,V_{pp}$. We determined the width of a $\pi/2$ pulse $\tau_p \approx 50\,\mu\text{s}$ (four cycles at 77.9 kHz) from a Rabi oscillation measurement and the π pulse, in turn, was constructed of two successive $\pi/2$ pulses. The orange lines and arrows in the inset depict how the time delay Δt was defined. Figure 6.9 illustrates the actual result of the Hahn echo measurement - the nuclear spin echo amplitude (blue squares with error bars) as a function of the time $2\Delta t$ between the

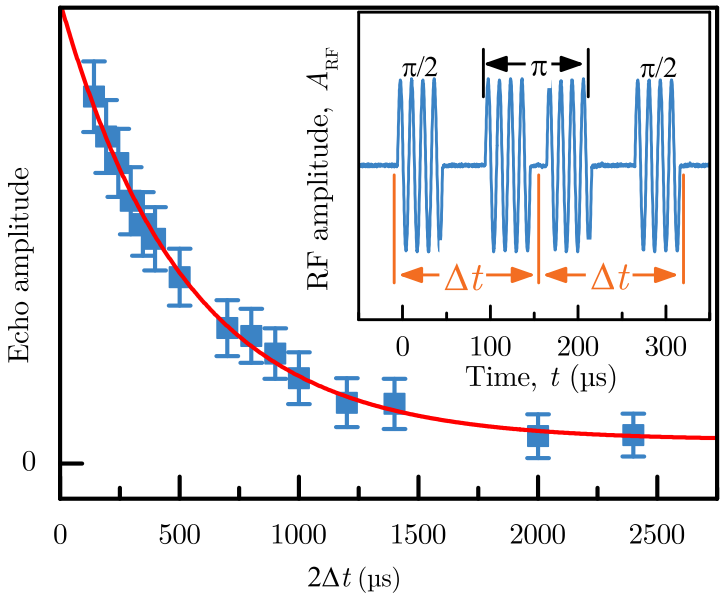

Figure 6.9 Nuclear spin echo amplitude as a function of the total time $2\Delta t$ between the arrival of the first $\pi/2$ pulse and after the arrival of the second $\pi/2$ pulse. The red line is the best fit to the data using Eq. (6.7) (cf. Table 6.5 for the values of the fitting parameters). The inset shows the RF pulse sequence used for the measurements. The orange lines illustrate how the interval Δt was determined. In analogy to Ref. [Hei16].

$\pi/2$ pulses. The red line is a fit to the data using the following equation:

$$A_{\text{echo}}(2\Delta t) = A_0 \exp\left(-\left(\frac{2\Delta t}{T_2^{\text{N}}}\right)\right) + A_{\text{off}} \tag{6.7}$$

Table 6.5 shows the values of the parameters of the best fit to the data. We obtain a

Table 6.5 Parameters of the best fit to the data shown in Fig. 6.6. The errors are obtained from the fit.

Amplitude	A_0	125 ± 3	arb. units
Nuclear spin coherence time	T_2^{N}	520 ± 25	µs
Offset	A_{off}	7 ± 1	arb. units

nuclear spin coherence time of

$$T_2^{\text{N}} = (520 \pm 25)\,\mu\text{s}.$$

6.3 Discussion

Note that ideally all employed pulses should be instantaneous compared to all characteristic timescales of the system under study, i.e., the nuclear Larmor precession period $2\pi/\omega_{\text{N}}$,

the inhomogeneous nuclear spin dephasing time $T_2^{*,\mathrm{N}}$ and the nuclear spin coherence time T_2^{N}. This consideration also holds for the measurement of the Ramsey fringes described before. However, we should note that the same physics applies in the case, where the pulse width τ_p is longer than the Larmor precession period $2\pi/\omega_\mathrm{N}$ of the nuclear spins, but is still shorter than the inhomogeneous spin dephasing time $T_2^{*,\mathrm{N}}$ [All12]. A longer pulse duration results in the selection of a spectral subensemble of the inhomogeneously broadened spin ensemble. This, in turn, leads to a reduction of the amplitude of the signal, but should not alter the measured T_2^{N} time (Hahn echo measurement). However, it might lead to a slightly longer inhomogeneous nuclear spin dephasing time $T_2^{*,\mathrm{N}}$ (Ramsey fringes measurement), since the subensemble exhibits less inhomogeneity than the whole inhomogeneously broadened spin ensemble. Our considerations are supported by the fact that the nuclear spin coherence time $T_2^{\mathrm{N}} \approx 520\,\mu\mathrm{s} \approx 3T_2^{*,\mathrm{N}}$ is not much longer than the nuclear inhomogeneous spin dephasing time $T_2^{*,\mathrm{N}}$ despite the strongly inhomogeneous Knight field B_K and the inhomogeneous nuclear spin polarization in the studied sample (sample #2, cf. Chapter 5).

Nevertheless, the results presented in this chapter allow us to conclude that the nuclear spin temperature approach is valid in the fluorine-doped ZnSe material system at the conditions of the time-resolved Kerr rotation (TRKR) experiments, presented in Chapters 4 and 5, since the following relation holds

$$T_1^{\mathrm{N}} \approx 10\,\mathrm{ms} \gg T_2^{\mathrm{N}} \approx 520\,\mu\mathrm{s}.$$

Thus, we can explain the inhomogeneous nuclear spin polarization, studied in Chapter 5, using the classical model of nuclear spin cooling.

Comparing the results presented here with the data from the literature we find that they are in reasonable agreement: Sanada *et al.* measured a nuclear spin dephasing time of $T_2^{*,\mathrm{N}} = 90\,\mu\mathrm{s}$ and a nuclear spin coherence time of $T_2^{\mathrm{N}} = 270\,\mu\mathrm{s}$ for GaAs/(Al,Ga)As quantum wells (QWs). Similar times ($T_2^{*,\mathrm{N}} = 16\,\mu\mathrm{s}$ and $T_2^{\mathrm{N}} = 310\,\mu\mathrm{s}$) were determined for a single GaAs/(Al,Ga)As quantum dot (QD) [Mak11]. Thus, the times for systems with weaker localized electrons in QWs as well as for systems with strongly localized electrons (QDs) are on the same order of magnitude as those reported in this thesis. However, we should note that there is an import difference between the GaAs and the ZnSe material system: In GaAs/(Al,Ga)As all nuclei have a nonzero spin and all these spins interact not only via dipole-dipole interaction, but also via quadrupole interaction, since $I > \frac{1}{2}$ for all nuclei. This interaction plays an import role in the GaAs material system [Che14].

6.4 Conclusion

We perform a complete study of the nuclear spin dynamics at the conditions of the TRKR experiments. Known advantages of optical detection are exploited: Despite the low natural abundance of the nuclear spins in the ZnSe epilayer, we observe clear signatures of the nuclear spin polarization, which is an example of the high sensitivity of the optical detection [San06]. Furthermore, the optical detection allows us to selectively study the nuclear spins in the epilayer in the vicinity of the fluorine donors. This high selectivity is a further advantage compared to methods solely based on RF excitation and detection [San06].

The detection of the nuclear spin polarization by means of coherently precessing electron spins (cf. also the pioneering work in Ref. [Zhu14], the results in Chapter 5, and Ref. [Hei15a]) instead of the circular polarization degree of the photoluminescence, as it is commonly used to detect nuclear fields by measurements of the Hanle curve (cf. for example Refs. [Che09; Fli10; Che11]), offers an additional advantage [Zhu14]: The width of the Hanle curve and thereby the magnetic field range (B_V range) for the measurements are determined by the electron spin relaxation time τ_S or inhomogeneous spin dephasing time T_2^*. This is an especially severe limitation for systems with very long τ_S or T_2^*, where the Hanle curve is as narrow as a few tenth of mT [Zhu14]. As a result, one cannot resolve the contributions of different isotopes to the Overhauser field B_N on the magnetic field axis.

In contrast to this, the detection of the nuclear fields by coherently precessing electron spins allows us to address and resolve a single isotope by working at higher magnetic fields B_V, where the nuclear Zeeman splitting of the isotopes becomes so large that the NMR frequencies of different isotopes, addressed by the pump helicity modulation frequency f_m, split up on the magnetic field scale B_V [Zhu14; Hei16].

A further advantage of the detection by coherently precessing electron spins is the possibility to determine the nuclear Overhauser field B_N [Ove53] even for an ensemble of electron spins, where one cannot resolve the Zeeman splitting in the field B_N spectrally as it is the case for single dot spectroscopy [Hei16; Mak11; Che13b; Che13a].

> [...] nature isn't classical, dammit, and if you want to make a simulation of nature, you'd better make it quantum mechanical, and by golly it's a wonderful problem, because it doesn't look so easy.
>
> Richard Feynman [Fey82; Tra12]

7 Summary

In this thesis, a comprehensive study of the spin dynamics in the fluorine-doped ZnSe material system is presented. Here, the dynamics of the ensemble of the donor-bound electron spins is investigated via the time-resolved pump-probe Kerr rotation technique. Modifying the "standard" scheme with helicity modulation of the pump beam with variable frequency, we develop the spin inertia method (cf. Chapter 4 and [Hei15b]). Studying the coherently precessing donor-bound electron spins in the resonant spin amplification (RSA) configuration at different modulation frequencies allows us to characterize the inhomogeneous nuclear spin polarization of the constituent isotopes with nonzero nuclear spin ($I \neq 0$, cf. Chapter 5 and Ref. [Hei15a]). This polarization is the result of dynamic nuclear polarization (DNP) in the inhomogeneous Knight field B_K of the precessing electrons. We employ a novel approach, using additional radio frequency (RF) excitation during RSA measurements and at fixed magnetic fields in RSA configuration. This approach allows for a deeper understanding of the underlying mechanism. The RF excitation also provides coherent control of the nuclear spins of the ^{77}Se isotope, demonstrated in Chapter 6 and Ref. [Hei16]. The coherent control allows us to measure the inhomogeneous nuclear spin dephasing time $T_2^{*,\mathrm{N}} = (160 \pm 5)\,\mu\mathrm{s}$ and the nuclear spin coherence time $T_2^\mathrm{N} = (520 \pm 25)\,\mu\mathrm{s}$ of the ^{77}Se nuclei under the conditions of the pump-probe experiment, presented in Chapter 5. Moreover, the longitudinal nuclear spin relaxation time T_1^N is determined under these conditions. Here, we use a novel approach based on the fast switching between two different modulation frequencies (cf. Section 3.4.3), where a fast analog-digital converter (ADC) recorded the corresponding KR signal transients.

In Chapter 4, the spin inertia method is explained and used to measure the longitudinal spin relaxation time T_1 of the ensemble of donor-bound electrons in a wide range of magnetic fields B_F, temperatures, and pump powers. The T_1 time of about 1.6 µs of the donor-bound electron spins in the weakly doped sample #1 ($n_\mathrm{F} \approx 1 \times 10^{15}\,\mathrm{cm}^{-3}$) remains nearly constant at external magnetic fields B_F (Faraday geometry) varied from zero up to 2.5 T and in a temperature range 1.8 K to 45 K. These observations impose strong restrictions on possible spin relaxation mechanisms: We rule out scattering between free and donor-bound electrons, jumping of electrons between different donor centers, scattering between phonons and donor-bound electrons, and with less certainty charge fluctuations in the environment of the donors caused by the 2 ps pulsed laser excitation, while charge fluctuations still could result from the fast recombination (≈ 210 ps [Gre12]) of the $\mathrm{D^0X}$-HH complex. Measurements of the strongly doped sample #2 ($n_\mathrm{F} \approx 1 \times 10^{18}\,\mathrm{cm}^{-3}$) yield a slightly shorter longitudinal spin relaxation time $T_1 \approx 1.1\,\mu\mathrm{s}$, where the difference to the weaker doped sample #1 might be caused by increased interaction between spins at neighboring donor centers. These longitudinal spin relaxation times hint at a potential electron spin coherence time T_2 in the microsecond range, especially of donor-bound electron spins isolated in nanostructures, e. g., Refs. [San09; De 10; Kim12; Sle13]. This underlines

the potential of the ZnSe:F material system for quantum information applications (cf. also discussion in Chapter 1).

We find that an excitation with helicity-modulated laser pulses results in a transverse nuclear spin polarization that we detect as a change of the Larmor precession frequency of the donor-bound electron spins in a magnetic field applied in the Voigt geometry (cf. Chapter 5). The frequency shift in dependence on the magnetic field B_V shows a pronounced dispersion-like shape with resonances at the fields of nuclear magnetic resonance B_NMR of the constituent zinc and selenium isotopes that are addressed by the helicity modulation frequency f_m of the pump beam. We study the frequency shift as a function of the external magnetic field B_V, the temperature and under the influence of additional RF excitation. The width of the resonance and its shape hint at a strong spatial inhomogeneity of the nuclear spin polarization in the vicinity of a fluorine donor. Considering the results of a complete tomography of the average electron spin, we suggest a mechanism of the optically induced nuclear spin polarization that is based on the concept of resonant nuclear spin cooling driven by the inhomogeneous Knight field B_K of the donor-bound electrons. This explanation relies on the validity of the spin temperature approach that we, in turn, verify by the measurements presented in Chapter 6.

Using the all-optical induction and detection of the nuclear spin polarization by coherently precessing electron spins we measure the longitudinal nuclear spin relaxation time T_1^N of the ^{77}Se isotope in a magnetic field range from 10 to 130 mT under illumination (cf. Chapter 6). We extend the optical TRKR spectroscopy with RF methods to measure the inhomogeneous nuclear spin dephasing time $T_2^{*,\mathrm{N}} = (160 \pm 5)\,\mu\mathrm{s}$ and the nuclear spin coherence time $T_2^\mathrm{N} = (520 \pm 25)\,\mu\mathrm{s}$ of this isotope. This way, we maintain the advantages of the optical detection, such as high selectivity and sensitivity [San06], while the RF methods provide coherent control of the nuclear spins. The T_1^N time is on the order of several milliseconds, while the T_2^N time is several hundred microseconds. The experimentally determined condition $T_1^\mathrm{N} \gg T_2^\mathrm{N}$ verifies the validity of the classical model of nuclear spin cooling that describes the optically induced nuclear spin polarization in Chapters 5 and 6.

The strong nuclear effects, presented in Chapters 5 and 6 of this thesis, support the considerations of Greilich *et al.* [Gre12] that despite the low natural abundance of isotopes with nonzero nuclear spin in the ZnSe host crystal, the spin coherence of the donor-bound electrons is still limited by the fluctuating hyperfine fields. Taking into account the longitudinal electron spin relaxation time T_1, measured in Chapter 4, this indicates that structures, grown from isotopically purified, nuclear spin free ZnSe, could exhibit increased electron spin coherence times T_2 of several microseconds. Still, a possible influence of the nuclear spin of the fluorine donor on the electron spin coherence needs to be clarified.

List of Publications

- F. Heisterkamp, E. A. Zhukov, A. Greilich, D. R. Yakovlev, V. L. Korenev, A. Pawlis, and M. Bayer. "Longitudinal and transverse spin dynamics of donor-bound electrons in fluorine-doped ZnSe: Spin inertia versus Hanle effect". *Phys. Rev. B* 91 (23 June 2015), p. 235432
- F. Heisterkamp, A. Greilich, E. A. Zhukov, E. Kirstein, T. Kazimierczuk, V. L. Korenev, I. A. Yugova, D. R. Yakovlev, A. Pawlis, and M. Bayer. "Inhomogeneous nuclear spin polarization induced by helicity-modulated optical excitation of fluorine-bound electron spins in ZnSe". *Phys. Rev. B* 92 (24 Dec. 2015), p. 245441
- F. Heisterkamp, E. Kirstein, A. Greilich, E. A. Zhukov, T. Kazimierczuk, D. R. Yakovlev, A. Pawlis, and M. Bayer. "Dynamics of nuclear spin polarization induced and detected by coherently precessing electron spins in fluorine-doped ZnSe". *Phys. Rev. B* 93 (8 Feb. 2016), p. 081409
- E. A. Zhukov, E. Kirstein, N. Kopteva, F. Heisterkamp, D. R. Yakovlev, V. L. Korenev, I. A. Yugova, A. Pawlis, M. Bayer, and A. Greilich. "Quantization of electron spin precession and reduction of spin dephasing through coupling to nuclear bath in ZnSe:F". *In preparation for submission to Phys. Rev. Lett.* (2017)

Bibliography

[Abr58] A. Abragam and W. G. Proctor. “Spin Temperature”. *Phys. Rev.* 109 (5 Mar. 1958), pp. 1441–1458.

[Ake15] Hiroshi Akera, Hidekatsu Suzuura, and Yoshiyuki Egami. “Spin relaxation in a quantum well by phonon scatterings”. *Phys. Rev. B* 92 (20 Nov. 2015), p. 205311.

[Aki06] I. A. Akimov, D. H. Feng, and F. Henneberger. “Electron Spin Dynamics in a Self-Assembled Semiconductor Quantum Dot: The Limit of Low Magnetic Fields”. *Phys. Rev. Lett.* 97 (5 Aug. 2006), p. 056602.

[Aki09] I.A. Akimov, D.H. Feng, and F. Henneberger. “Nonequilibrium Optical Spin Cooling in Charged Quantum Dots”. In: *Semiconductor Quantum Bits*. Pan Stanford Publishing, 2009.

[Ale73] E. B. Aleksandrov. “OPTICAL MANIFESTATIONS OF THE INTERFERENCE OF NONDEGENERATE ATOMIC STATES”. *Soviet Physics Uspekhi* 15.4 (1973), p. 436.

[All12] L. Allen and J.H. Eberly. *Optical Resonance and Two-Level Atoms*. Dover Books on Physics. Dover Publications, 2012.

[All38] J. F. Allen and A. D. Misener. “Flow of liquid helium II”. *Nature* 141.3558 (1938), p. 75.

[Ast02] G. V. Astakhov, D. R. Yakovlev, V. P. Kochereshko, W. Ossau, W. Faschinger, J. Puls, F. Henneberger, S. A. Crooker, Q. McCulloch, D. Wolverson, N. A. Gippius, and A. Waag. “Binding energy of charged excitons in ZnSe-based quantum wells”. *Phys. Rev. B* 65 (16 Apr. 2002), p. 165335.

[Ast08a] G. V. Astakhov, R. I. Dzhioev, K. V. Kavokin, V. L. Korenev, M. V. Lazarev, M. N. Tkachuk, Yu. G. Kusrayev, T. Kiessling, W. Ossau, and L. W. Molenkamp. “Suppression of Electron Spin Relaxation in Mn-Doped GaAs”. *Phys. Rev. Lett.* 101 (7 Aug. 2008), p. 076602.

[Ast08b] G. V. Astakhov, M. M. Glazov, D. R. Yakovlev, E. A. Zhukov, W. Ossau, L. W. Molenkamp, and M. Bayer. “Time-resolved and continuous-wave optical spin pumping of semiconductor quantum wells”. *Semiconductor Science and Technology* 23.11 (2008), p. 114001.

[Aue09] T. Auer, R. Oulton, A. Bauschulte, D. R. Yakovlev, M. Bayer, S. Yu. Verbin, R. V. Cherbunin, D. Reuter, and A. D. Wieck. “Measurement of the Knight field and local nuclear dipole-dipole field in an InGaAs/GaAs quantum dot ensemble”. *Phys. Rev. B* 80 (20 Nov. 2009), p. 205303.

[Bar13] N. Bar-Gill, L. M. Pham, A. Jarmola, D. Budker, and R. L. Walsworth. "Solid-state electronic spin coherence time approaching one second". *NATURE COMMUNICATIONS* 4 (Apr. 2013).

[Bel16] V. V. Belykh, E. Evers, D. R. Yakovlev, F. Fobbe, A. Greilich, and M. Bayer. "Extended pump-probe Faraday rotation spectroscopy of the submicrosecond electron spin dynamics in n-type GaAs". *Phys. Rev. B* 94 (24 Dec. 2016), p. 241202.

[Ber78] V. L. Berkovits, C. Hermann, G. Lampel, A. Nakamura, and V. I. Safarov. "Giant Overhauser shift of conduction-electron spin resonance due to optical polarization of nuclei in semiconductors". *Phys. Rev. B* 18 (4 Aug. 1978), pp. 1767–1779.

[Bil49] Bruce H. Billings. "The Electro-Optic Effect in Uniaxial Crystals of the Type X H2PO4. I. Theoretical". *J. Opt. Soc. Am.* 39.10 (Oct. 1949), pp. 797–801.

[Blo29] Felix Bloch. "Über die Quantenmechanik der Elektronen in Kristallgittern". *Zeitschrift für Physik* 52.7-8 (1929), pp. 555–600.

[Blo46] F. Bloch. "Nuclear Induction". *Phys. Rev.* 70 (7-8 Oct. 1946), pp. 460–474.

[Blo54] N. Bloembergen. "Nuclear magnetic relaxation in semiconductors". *Physica* 20.7-12 (1954), pp. 1130–1133.

[Bol84] Ludwig Boltzmann. "Ableitung des Stefan'schen Gesetzes, betreffend die Abhängigkeit der Wärmestrahlung von der Temperatur aus der electromagnetischen Lichttheorie". *Annalen der Physik* 258.6 (1884), pp. 291–294.

[Bos24] S. N. Bose. "Plancks Gesetz und Lichtquantenhypothese". *Zeitschrift für Physik* 26.1 (1924), pp. 178–181.

[Boy70] W. S. Boyle and G. E. Smith. "Charge coupled semiconductor devices". *Bell System Technical Journal* 49.4 (1970), pp. 587–593.

[Bud02] D. Budker, W. Gawlik, D. F. Kimball, S. M. Rochester, V. V. Yashchuk, and A. Weis. "Resonant nonlinear magneto-optical effects in atoms". *Rev. Mod. Phys.* 74 (4 Nov. 2002), pp. 1153–1201.

[Bul09] Iulia Buluta and Franco Nori. "Quantum Simulators". *Science* 326.5949 (2009), pp. 108–111. eprint: `http://science.sciencemag.org/content/326/5949/108.full.pdf`.

[Cal17] Tommaso Calarco. *QUantum TEchnologies Flagship QUTE-F*. 2017. eprint: `http://cordis.europa.eu/fp7/ict/fet-proactive/docs/flagship-ie-jan10-18_en.pdf`. URL: `http://cordis.europa.eu/fp7/ict/fet-proactive/docs/flagship-ie-jan10-18_en.pdf`.

[Che09] Roman V. Cherbunin, Sergey Yu. Verbin, Thomas Auer, Dmitri R. Yakovlev, Dirk Reuter, Andreas D. Wieck, Ilya Ya. Gerlovin, Ivan V. Ignatiev, Dmitry V. Vishnevsky, and Manfred Bayer. "Dynamics of the nuclear spin polarization by optically oriented electrons in a (In,Ga)As/GaAs quantum dot ensemble". *Phys. Rev. B* 80 (3 July 2009), p. 035326.

[Che11] R. V. Cherbunin, K. Flisinski, I. Ya. Gerlovin, I. V. Ignatiev, M. S. Kuznetsova, M. Yu. Petrov, D. R. Yakovlev, D. Reuter, A. D. Wieck, and M. Bayer. "Resonant nuclear spin pumping in (In,Ga)As quantum dots". *Phys. Rev. B* 84 (4 July 2011), p. 041304.

[Che13a] E. A. Chekhovich, M. M. Glazov, A. B. Krysa, M. Hopkinson, P. Senellart, A. Lemaitre, M. S. Skolnick, and A. I. Tartakovskii. "Element-sensitive measurement of the hole-nuclear spin interaction in quantum dots". *Nat. Phys.* 9.2 (Feb. 2013), pp. 74–78.

[Che13b] E. A. Chekhovich, M. N. Makhonin, A. I. Tartakovskii, A. Yacoby, H. Bluhm, K. C. Nowack, and L. M. K. Vandersypen. "Nuclear spin effects in semiconductor quantum dots." *Nature materials* 12.6 (2013), pp. 494–504.

[Che14] E. A. Chekhovich, M. Hopkinson, M. S. Skolnick, and A. I. Tartakovskii. "Quadrupolar induced suppression of nuclear spin bath fluctuations in self-assembled quantum dots". *Nat. Commun.* 6 (2014), pp. 1–7.

[Chr15] David J. Christle, Abram L. Falk, Paolo Andrich, Paul V. Klimov, Jawad Ul Hassan, Nguyen T. Son, Erik Janzen, Takeshi Ohshima, and David D. Awschalom. "Isolated electron spins in silicon carbide with millisecond coherence times". *NATURE MATERIALS* 14.2 (Feb. 2015), pp. 160–163.

[Cir12] J. Ignacio Cirac and Peter Zoller. "Goals and opportunities in quantum simulation". *NATURE PHYSICS* 8.4 (Apr. 2012), pp. 264–266.

[Cla09] Susan M. Clark, Kai-Mei C. Fu, Qiang Zhang, Thaddeus D. Ladd, Colin Stanley, and Yoshihisa Yamamoto. "Ultrafast Optical Spin Echo for Electron Spins in Semiconductors". *Phys. Rev. Lett.* 102 (24 June 2009), p. 247601.

[Coh66] C. Cohen-Tannoudji and A. Kastler. "Optical Pumping". In: *Progress in Optics*. Ed. by E. Wolf. Vol. 5. North-Holland, Amsterdam, 1966. Chap. I, pp. 3–78.

[Col04] J. S. Colton, T. A. Kennedy, A. S. Bracker, and D. Gammon. "Microsecond spin-flip times in $n-$GaAs measured by time-resolved polarization of photoluminescence". *Phys. Rev. B* 69 (12 Mar. 2004), p. 121307.

[Col12] J. S. Colton, D. Meyer, K. Clark, D. Craft, J. Cutler, T. Park, and P. White. "Long-lived electron spins in a modulation doped (100) GaAs quantum well". *Journal of Applied Physics* 112.8, 084307 (2012).

[Cze30] M. Czerny and A.F. Turner. "Über den Astigmatismus bei Spiegelspektrometern". German. *Zeitschrift für Physik* 61.11-12 (1930), pp. 792–797.

[Dam71] Raymond Damadian. "Tumor Detection by Nuclear Magnetic Resonance". *Science* 171.3976 (1971), pp. 1151–1153. eprint: `http://science.sciencemag.org/content/171/3976/1151.full.pdf`.

[Dam77] R Damadian, M Goldsmith, and L Minkoff. "NMR in cancer: XVI. FONAR image of the live human body". *Physiological chemistry and physics* 9.1 (1977), pp. 97–100, 108.

[De 10] K. De Greve, S. M. Clark, D. Sleiter, K. Sanaka, T. D. Ladd, M. Panfilova, A. Pawlis, K. Lischka, and Y. Yamamoto. "Photon antibunching and magnetospectroscopy of a single fluorine donor in ZnSe". *Applied Physics Letters* 97.24 (2010).

[Dem11] W. Demtröder. *Laserspektroskopie 1: Grundlagen*. Springer Berlin Heidelberg, 2011.

[Dir26] P. A. M. Dirac. "On the Theory of Quantum Mechanics". *Proceedings of the Royal Society of London A: Mathematical, Physical and Engineering Sciences* 112.762 (1926), pp. 661–677.

[DiV00] David P. DiVincenzo. "The Physical Implementation of Quantum Computation". *Fortschritte der Physik* 48.9-11 (2000), pp. 771–783.

[Dya08] Mikhail I. Dyakonov. "Basics of Semiconductor and Spin Physics". In: *Spin Physics in Semiconductors*. Ed. by Mikhail I. Dyakonov. Berlin: Springer-Verlag, 2008. Chap. 1.

[Dya84] Mikhail I. Dyakonov and Vladimir I. Perel. "Theory of Optical Spin Orientation of Electrons and Nuclei in Semiconductors". In: *Optical Orientation*. Ed. by F. Meier and B.P. Zakharchenya. Modern Problems in Condensed Matter Sciences. Amsterdam: North-Holland, 1984. Chap. 2, p. 15.

[Dzh02] R. I. Dzhioev, V. L. Korenev, I. A. Merkulov, B. P. Zakharchenya, D. Gammon, Al. L. Efros, and D. S. Katzer. "Manipulation of the Spin Memory of Electrons in n-GaAs". *Phys. Rev. Lett.* 88 (25 June 2002), p. 256801.

[Ell54] R. J. Elliott. "Theory of the Effect of Spin-Orbit Coupling on Magnetic Resonance in Some Semiconductors". *Phys. Rev.* 96 (2 Oct. 1954), pp. 266–279.

[Eps01] R. J. Epstein, D. T. Fuchs, W. V. Schoenfeld, P. M. Petroff, and D. D. Awschalom. "Hanle effect measurements of spin lifetimes in InAs self-assembled quantum dots". *Applied Physics Letters* 78.6 (2001), pp. 733–735.

[Fer26] E. Fermi. "Zur Quantelung des idealen einatomigen Gases". *Zeitschrift für Physik* 36.11-12 (1926), pp. 902–912.

[Fey13] R.P. Feynman, Feynman Richard P Sands Matthew L Leighton Robert B, R.B. Leighton, and M. Sands. "The Feynman Lectures on Physics, Desktop Edition Volume II: The New Millennium Edition". In: Feynman Lectures on Physics. Basic Books, 2013. Chap. 37, p. 13.

[Fey82] Richard P Feynman. "Simulating physics with computers". *International journal of theoretical physics* 21.6 (1982), pp. 467–488.

[Fie39] Markus Fierz. "Über die relativistische Theorie kräftefreier Teilchen mit beliebigem Spin". *Helvetica Physica Acta* 12 (1939).

[Fle84] V. G. Fleisher and I.A. Merkulov. "Optical orientation of the Coupled Electron-Nuclear Spin System of a Semiconductor". In: *Optical Orientation*. Ed. by F. Meier and B.P. Zakharchenya. Modern Problems in Condensed Matter Sciences. Amsterdam: North-Holland, 1984. Chap. 5.

[Fli10] K. Flisinski, I. Ya. Gerlovin, I. V. Ignatiev, M. Yu. Petrov, S. Yu. Verbin, D. R. Yakovlev, D. Reuter, A. D. Wieck, and M. Bayer. "Optically detected magnetic resonance at the quadrupole-split nuclear states in (In,Ga)As/GaAs quantum dots". *Phys. Rev. B* 82 (8 Aug. 2010), p. 081308.

[Fra11] F. Fras, B. Eble, P. Desfonds, F. Bernardot, C. Testelin, M. Chamarro, A. Miard, and A. Lemaître. "Hole-spin initialization and relaxation times in InAs/GaAs quantum dots". *Phys. Rev. B* 84 (12 Sept. 2011), p. 125431.

[Fra61] P. A. Franken, A. E. Hill, C. W. Peters, and G. Weinreich. "Generation of Optical Harmonics". *Phys. Rev. Lett.* 7 (4 Aug. 1961), pp. 118–119.

[FRS97] J. Larmor D.Sc. F.R.S. "LXIII. On the theory of the magnetic influence on spectra; and on the radiation from moving ions". *Philosophical Magazine Series 5* 44.271 (1897), pp. 503–512. eprint: `http://dx.doi.org/10.1080/14786449708621095`.

[Fu06] Kai-Mei C. Fu, Wenzheng Yeo, Susan Clark, Charles Santori, Colin Stanley, M. C. Holland, and Yoshihisa Yamamoto. "Millisecond spin-flip times of donor-bound electrons in GaAs". *Phys. Rev. B* 74 (12 Sept. 2006), p. 121304.

[Gab07] G. Gabrielse, D. Hanneke, T. Kinoshita, M. Nio, and B. Odom. "Erratum: New Determination of the Fine Structure Constant from the Electron g Value and QED [Phys. Rev. Lett. **97** , 030802 (2006)]". *Phys. Rev. Lett.* 99 (3 July 2007), p. 039902.

[Ger10] C. Gerthsen and D. Meschede. *Gerthsen Physik*. Springer-Lehrbuch. Springer Berlin Heidelberg, 2010.

[Ger22a] Walther Gerlach and Otto Stern. "Das magnetische Moment des Silberatoms". *Zeitschrift für Physik* 9.1 (1922), pp. 353–355.

[Ger22b] Walther Gerlach and Otto Stern. "Der experimentelle Nachweis der Richtungsquantelung im Magnetfeld". *Zeitschrift für Physik* 9.1 (1922), pp. 349–352.

[Glo12] Glosser.ca. *Bloch sphere; a geometrical representation of a two-level quantum system. Rendered with Asymptote.* Dec. 19, 2012. URL: `https://commons.wikimedia.org/wiki/File:Bloch_Sphere.svg` (visited on 12/02/2016).

[Gre06a] A. Greilich, R. Oulton, E. A. Zhukov, I. A. Yugova, D. R. Yakovlev, M. Bayer, A. Shabaev, Al. L. Efros, I. A. Merkulov, V. Stavarache, D. Reuter, and A. Wieck. "Optical Control of Spin Coherence in Singly Charged (In, Ga)As/GaAs Quantum Dots". *Phys. Rev. Lett.* 96 (22 June 2006), p. 227401.

[Gre06b] A. Greilich, D. R. Yakovlev, A. Shabaev, Al. L. Efros, I. A. Yugova, R. Oulton, V. Stavarache, D. Reuter, A. Wieck, and M. Bayer. "Mode Locking of Electron Spin Coherences in Singly Charged Quantum Dots". *Science* 313.5785 (2006), pp. 341–345. eprint: `http://science.sciencemag.org/content/313/5785/341.full.pdf`.

[Gre12] A. Greilich, A. Pawlis, F. Liu, O. A. Yugov, D. R. Yakovlev, K. Lischka, Y. Yamamoto, and M. Bayer. “Spin dephasing of fluorine-bound electrons in ZnSe”. *Phys. Rev. B* 85 (12 Mar. 2012), p. 121303.

[Gri12] D.J. Griffiths. In: *Quantenmechanik*. Always learning. Pearson, 2012. Chap. 4.

[Grn77] E. I. Grncharova and V. I. Perel. “Relaxation of Nulear Spins Interacting With Holes in Semiconductors”. *Soviet Physics-Semiconductors* 11.9 (1977), pp. 997–1000.

[Gru16a] M. Grundmann. *The Physics of Semiconductors: An Introduction Including Nanophysics and Applications*. Graduate Texts in Physics. Springer International Publishing, 2016.

[Gru16b] Marius Grundmann. “Crystals”. In: *The Physics of Semiconductors: An Introduction Including Nanophysics and Applications*. Cham: Springer International Publishing, 2016, pp. 41–80.

[Gru16c] Marius Grundmann. “Electronic Defect States”. In: *The Physics of Semiconductors: An Introduction Including Nanophysics and Applications*. Cham: Springer International Publishing, 2016, pp. 203–253.

[Gru16d] Marius Grundmann. “Heterostructures”. In: *The Physics of Semiconductors: An Introduction Including Nanophysics and Applications*. Cham: Springer International Publishing, 2016. Chap. 12, pp. 399–435.

[Gru16e] Marius Grundmann. “Optical Properties”. In: *The Physics of Semiconductors: An Introduction Including Nanophysics and Applications*. Cham: Springer International Publishing, 2016. Chap. 9, pp. 291–341.

[Hah50] E. L. Hahn. “Spin Echoes”. *Phys. Rev.* 80 (4 Nov. 1950), pp. 580–594.

[Han07] R. Hanson, L. P. Kouwenhoven, J. R. Petta, S. Tarucha, and L. M. K. Vandersypen. “Spins in few-electron quantum dots”. *Rev. Mod. Phys.* 79 (4 Oct. 2007), pp. 1217–1265.

[Han24] Wilhelm Hanle. “Über magnetische Beeinflussung der Polarisation der Resonanzfluoreszenz”. German. *Zeitschrift für Physik* 30.1 (1924), pp. 93–105.

[Hap72] William Happer. “Optical Pumping”. *Rev. Mod. Phys.* 44 (2 Apr. 1972), pp. 169–249.

[Har02] Robin K. Harris, Edwin D. Becker, Sonia M. Cabral De Menezes, Robin Goodfellow, and Pierre Granger. “NMR nomenclature: Nuclear spin properties and conventions for chemical shifts (IUPAC recommendations 2001)”. *Concept. Magnetic Res.* 14.5 (2002), pp. 326–346.

[Har64] L. E. Hargrove, R. L. Fork, and M. A. Pollack. “LOCKING OF He–Ne LASER MODES INDUCED BY SYNCHRONOUS INTRACAVITY MODULATION”. *Applied Physics Letters* 5.1 (1964), pp. 4–5.

[Hei07] D. Heiss, S. Schaeck, H. Huebl, M. Bichler, G. Abstreiter, J. Finley, D. Bulaev, and Daniel Loss. “Observation of extremely slow hole spin relaxation in self-assembled quantum dots”. *Phys. Rev. B* 76 (24 Dec. 2007), p. 241306.

[Hei15a] F. Heisterkamp, A. Greilich, E. A. Zhukov, E. Kirstein, T. Kazimierczuk, V. L. Korenev, I. A. Yugova, D. R. Yakovlev, A. Pawlis, and M. Bayer. "Inhomogeneous nuclear spin polarization induced by helicity-modulated optical excitation of fluorine-bound electron spins in ZnSe". *Phys. Rev. B* 92 (24 Dec. 2015), p. 245441.

[Hei15b] F. Heisterkamp, E. A. Zhukov, A. Greilich, D. R. Yakovlev, V. L. Korenev, A. Pawlis, and M. Bayer. "Longitudinal and transverse spin dynamics of donor-bound electrons in fluorine-doped ZnSe: Spin inertia versus Hanle effect". *Phys. Rev. B* 91 (23 June 2015), p. 235432.

[Hei16] F. Heisterkamp, E. Kirstein, A. Greilich, E. A. Zhukov, T. Kazimierczuk, D. R. Yakovlev, A. Pawlis, and M. Bayer. "Dynamics of nuclear spin polarization induced and detected by coherently precessing electron spins in fluorine-doped ZnSe". *Phys. Rev. B* 93 (8 Feb. 2016), p. 081409.

[How12] R.A. Howard. "Dynamic Probabilistic Systems: Markov Models". In: Dover Books on Mathematics. Dover Publications, 2012, pp. 551–576.

[Jah00] J. Jahns. *Photonik: Grundlagen, Komponenten und Systeme*. De Gruyter, 2000.

[Kal08] V.K. Kalevich, K.V. Kavokin, and I.A. Merkulov. "Dynamic Nuclear Polarization and Nuclear Fields". In: *Spin Physics in Semiconductors*. Ed. by Mikhail I. Dyakonov. Berlin: Springer-Verlag, 2008. Chap. 11.

[Kap38] P. Kapitza. "Viscosity of Liquid Helium below the λ-Point". *Nature* 141 (1938), pp. 74–74.

[Kav08] K. V. Kavokin. "Spin relaxation of localized electrons in n-type semiconductors". *Semiconductor Science and Technology* 23.11 (2008), p. 114009.

[Kel15] J. Kelly, R. Barends, A. G. Fowler, A. Megrant, E. Jeffrey, T. C. White, D. Sank, J. Y. Mutus, B. Campbell, Yu Chen, Z. Chen, B. Chiaro, A. Dunsworth, I. -C. Hoi, C. Neill, P. J. J. O'Malley, C. Quintana, P. Roushan, A. Vainsencher, J. Wenner, A. N. Cleland, and John M. Martinis. "State preservation by repetitive error detection in a superconducting quantum circuit". *NATURE* 519.7541 (Mar. 2015), pp. 66–69.

[Ken06] T. A. Kennedy, A. Shabaev, M. Scheibner, Al. L. Efros, A. S. Bracker, and D. Gammon. "Optical initialization and dynamics of spin in a remotely doped quantum well". *Phys. Rev. B* 73 (4 Jan. 2006), p. 045307.

[Kik98] J. M. Kikkawa and D. D. Awschalom. "Resonant Spin Amplification in n-Type GaAs". *Phys. Rev. Lett.* 80 (19 May 1998), pp. 4313–4316.

[Kim12] Y. M. Kim, D. Sleiter, K. Sanaka, Y. Yamamoto, J. Meijer, K. Lischka, and A. Pawlis. "Semiconductor qubits based on fluorine implanted ZnMgSe/ZnSe quantum-well nanostructures". *Phys. Rev. B* 85 (8 Feb. 2012), p. 085302.

[Kni01] E Knill, R Laflamme, and GJ Milburn. "A scheme for efficient quantum computation with linear optics". *NATURE* 409.6816 (Jan. 2001), pp. 46–52.

[Kni49] W. D. Knight. "Nuclear Magnetic Resonance Shift in Metals". *Phys. Rev.* 76 (8 Oct. 1949), pp. 1259–1260.

[Koo03] Bert Koopmans. “Laser-Induced Magnetization Dynamics”. In: *Spin Dynamics in Confined Magnetic Structures II*. Ed. by Burkard Hillebrands and Kamel Ounadjela. Berlin, Heidelberg: Springer Berlin Heidelberg, 2003, pp. 256–323.

[Koo07] Bert Koopmans. “Time-resolved Kerr-effect and Spin Dynamics in Itinerant Ferromagnets”. In: *Handbook of Magnetism and Advanced Magnetic Materials*. John Wiley & Sons, Ltd, 2007.

[Kor11] V. L. Korenev. “Multiple stable states of a periodically driven electron spin in a quantum dot using circularly polarized light”. *Phys. Rev. B* 83 (23 June 2011), p. 235429.

[Kuz13] M. S. Kuznetsova, K. Flisinski, I. Ya. Gerlovin, I. V. Ignatiev, K. V. Kavokin, S. Yu. Verbin, D. R. Yakovlev, D. Reuter, A. D. Wieck, and M. Bayer. “Hanle effect in (In,Ga)As quantum dots: Role of nuclear spin fluctuations”. *Phys. Rev. B* 87 (23 June 2013), p. 235320.

[Lad10] T. D. Ladd, F. Jelezko, R. Laflamme, Y. Nakamura, C. Monroe, and J. L. O’Brien. “Quantum computers”. *NATURE* 464.7285 (Mar. 2010), pp. 45–53.

[Lam64] Willis E. Lamb. “Theory of an Optical Maser”. *Phys. Rev.* 134 (6A June 1964), A1429–A1450.

[Lei03] D. Leibfried, R. Blatt, C. Monroe, and D. Wineland. “Quantum dynamics of single trapped ions”. *Rev. Mod. Phys.* 75 (1 Mar. 2003), pp. 281–324.

[Lev01] M.H. Levitt. *Spin Dynamics: Basics of Nuclear Magnetic Resonance*. Wiley, 2001.

[Lia99] Z.P. Liang and P.C. Lauterbur. *Principles of Magnetic Resonance Imaging: A Signal Processing Perspective*. IEEE Press Series on Biomedical Engineering. Wiley, 1999, p. 291.

[Lin16] Xiayu Linpeng, Todd Karin, M. V. Durnev, Russell Barbour, M. M. Glazov, E. Ya. Sherman, S. P. Watkins, Satoru Seto, and Kai-Mei C. Fu. “Longitudinal spin relaxation of donor-bound electrons in direct band-gap semiconductors”. *Phys. Rev. B* 94 (12 Sept. 2016), p. 125401.

[Llo96] Seth Lloyd. “Universal Quantum Simulators”. *Science* 273.5278 (1996), pp. 1073–1078. eprint: `http://science.sciencemag.org/content/273/5278/1073.full.pdf`.

[Mak11] M. N. Makhonin, K. V. Kavokin, P. Senellart, A. Lemaître, A. J. Ramsay, M. S. Skolnick, and A. I. Tartakovskii. “Fast control of nuclear spin polarization in an optically pumped single quantum dot”. *Nat. Mater.* 10.11 (2011), pp. 844–848.

[Mar90] Andrei Andreyevich Markov. “Ob odnom voproce DI Mendeleeva”. *Zapiski Imperatorskoi Akademii Nauk SP6* 62 (1890), pp. 1–24.

[Mau12] P. C. Maurer, G. Kucsko, C. Latta, L. Jiang, N. Y. Yao, S. D. Bennett, F. Pastawski, D. Hunger, N. Chisholm, M. Markham, D. J. Twitchen, J. I. Cirac, and M. D. Lukin. “Room-Temperature Quantum Bit Memory Exceeding One Second”. *Science* 336.6086 (2012), pp. 1283–1286. eprint: `http://science.sciencemag.org/content/336/6086/1283.full.pdf`.

[McR07] D.W. McRobbie, E.A. Moore, M.J. Graves, and M.R. Prince. *MRI from Picture to Proton*. Cambridge University Press, 2007.

[Mei84] F. Meier and B.P. Zakharchenya. *Optical orientation*. Modern problems in condensed matter sciences. North-Holland, 1984.

[Mer02] I. A. Merkulov, Al. L. Efros, and M. Rosen. "Electron spin relaxation by nuclei in semiconductor quantum dots". *Phys. Rev. B* 65 (20 Apr. 2002), p. 205309.

[Mer72] J. L. Merz, H. Kukimoto, K. Nassau, and J. W. Shiever. "Optical Properties of Substitutional Donors in ZnSe". *Phys. Rev. B* 6 (2 July 1972), pp. 545–556.

[Moh15] P. J. Mohr, B. N. Taylor, and D. B. Newell. *The 2014 CODATA Recommended Values of the Fundamental Physical Constants (Web Version 7.1)*. Website. Feb. 2015.

[Mom11] Koichi Momma and Fujio Izumi. "*VESTA3* for three-dimensional visualization of crystal, volumetric and morphology data". *Journal of Applied Crystallography* 44.6 (Dec. 2011), pp. 1272–1276.

[Mon11] Thomas Monz, Philipp Schindler, Julio T. Barreiro, Michael Chwalla, Daniel Nigg, William A. Coish, Maximilian Harlander, Wolfgang Hänsel, Markus Hennrich, and Rainer Blatt. "14-Qubit Entanglement: Creation and Coherence". *Phys. Rev. Lett.* 106 (13 Mar. 2011), p. 130506.

[Moo75] G. E. Moore. "Progress in digital integrated electronics". *IEDM Tech. Digest* (1975), pp. 11–13.

[Moo98] GE Moore. "Cramming more components onto integrated circuits (Reprinted from Electronics, pg 114-117, April 19, 1965)". *PROCEEDINGS OF THE IEEE* 86.1 (Jan. 1998), pp. 82–85.

[Mot67] NF Mott. "Electrons in disordered structures". *Advances in Physics* 16.61 (1967), pp. 49–144.

[Muh14] Juha T. Muhonen, Juan P. Dehollain, Arne Laucht, Fay E. Hudson, Rachpon Kalra, Takeharu Sekiguchi, Kohei M. Itoh, David N. Jamieson, Jeffrey C. McCallum, Andrew S. Dzurak, and Andrea Morello. "Storing quantum information for 30 seconds in a nanoelectronic device". *NATURE NANOTECHNOLOGY* 9.12 (Dec. 2014), pp. 986–991.

[Mur11] Frank Murmann. *Deutsch: Das Bild beschreibt die Drehung der Polarisationsachse um den Winkel Theta, sowie die daraus resultierende Elliptizität*. Ed. by Frank Murmann. Sept. 23, 2011. URL: `https://commons.wikimedia.org/wiki/File:Kerrwinkel.svg` (visited on 01/03/2017).

[Neg06] C. Negrevergne, T. S. Mahesh, C. A. Ryan, M. Ditty, F. Cyr-Racine, W. Power, N. Boulant, T. Havel, D. G. Cory, and R. Laflamme. "Benchmarking Quantum Control Methods on a 12-Qubit System". *Phys. Rev. Lett.* 96 (17 May 2006), p. 170501.

[Odo06] B. Odom, D. Hanneke, B. D'Urso, and G. Gabrielse. "New Measurement of the Electron Magnetic Moment Using a One-Electron Quantum Cyclotron". *Phys. Rev. Lett.* 97 (3 July 2006), p. 030801.

[Ove53] Albert W. Overhauser. “Polarization of Nuclei in Metals”. *Phys. Rev.* 92 (2 Oct. 1953), pp. 411–415.

[Pag81] Daniel Paget. “Optical detection of NMR in high-purity GaAs under optical pumping: Efficient spin-exchange averaging between electronic states”. *Phys. Rev. B* 24 (7 Oct. 1981), pp. 3776–3793.

[Pag82] Daniel Paget. “Optical detection of NMR in high-purity GaAs: Direct study of the relaxation of nuclei close to shallow donors”. *Phys. Rev. B* 25 (7 Apr. 1982), pp. 4444–4451.

[Pan12] Jian-Wei Pan, Zeng-Bing Chen, Chao-Yang Lu, Harald Weinfurter, Anton Zeilinger, and Marek Żukowski. “Multiphoton entanglement and interferometry”. *Rev. Mod. Phys.* 84 (2 May 2012), pp. 777–838.

[Pas17] Rüdiger Paschotta. *Electro-optic Modulators*. Jan. 4, 2017. URL: `https://www.rp-photonics.com/electro_optic_modulators.html` (visited on 01/04/2017).

[Pau25] W. Pauli. “Über den Zusammenhang des Abschlusses der Elektronengruppen im Atom mit der Komplexstruktur der Spektren”. *Zeitschrift für Physik* 31.1 (1925), pp. 765–783.

[Pau40] W. Pauli. “The Connection Between Spin and Statistics”. *Phys. Rev.* 58 (8 Oct. 1940), pp. 716–722.

[Paw06] A. Pawlis, K. Sanaka, S. Götzinger, Y. Yamamoto, and K. Lischka. “Investigation of excitons bound to fluorine donors in ZnSe”. *Semiconductor Science and Technology* 21.10 (2006), p. 1412.

[Paw08] A. Pawlis, M. Panfilova, D. J. As, K. Lischka, K. Sanaka, T. D. Ladd, and Y. Yamamoto. “Lasing of donor-bound excitons in ZnSe microdisks”. *Phys. Rev. B* 77 (15 Apr. 2008), p. 153304.

[Paw09] A. Pawlis, M. Panfilova, K. Sanaka, T.D. Ladd, D.J. As, K. Lischka, and Y. Yamamoto. “Low-threshold ZnSe microdisk laser based on fluorine impurity bound-exciton transitions”. *Microelectronics Journal* 40.2 (2009). Wide Band Gap Semiconductor Nanostructures for Optoelectronic Applications, pp. 256–258.

[Paw11] A. Pawlis, T. Berstermann, C. Brüggemann, M. Bombeck, D. Dunker, D. R. Yakovlev, N. A. Gippius, K. Lischka, and M. Bayer. “Exciton states in shallow ZnSe/(Zn,Mg)Se quantum wells: Interaction of confined and continuum electron and hole states”. *Phys. Rev. B* 83 (11 Mar. 2011), p. 115302.

[Pet08] M. Yu. Petrov, I. V. Ignatiev, S. V. Poltavtsev, A. Greilich, A. Bauschulte, D. R. Yakovlev, and M. Bayer. “Effect of thermal annealing on the hyperfine interaction in InAs/GaAs quantum dots”. *Phys. Rev. B* 78 (4 July 2008), p. 045315.

[Pin57] David Pines, John Bardeen, and Charles P. Slichter. “Nuclear Polarization and Impurity-State Spin Relaxation Processes in Silicon”. *Phys. Rev.* 106 (3 May 1957), pp. 489–498.

[Pla13] Jarryd J. Pla, Kuan Y. Tan, Juan P. Dehollain, Wee H. Lim, John J. L. Morton, Floris A. Zwanenburg, David N. Jamieson, Andrew S. Dzurak, and Andrea Morello. "High-fidelity readout and control of a nuclear spin qubit in silicon". *NATURE* 496.7445 (Apr. 2013), pp. 334–338.

[Poc94] F. Pockels. "Ueber den Einfluss des elektrostatischen Feldes auf das optische Verhalten piezoelektrischer Krystalle. Mit 14 Textfiguren". *Abhandlungen der Gesellschaft der Wissenschaften in Göttingen, Mathematisch-Physikalische Klasse* 39 (1894), pp. 1–204.

[Pol09] Alberto Politi, Jonathan C. F. Matthews, and Jeremy L. O'Brien. "Shor's Quantum Factoring Algorithm on a Photonic Chip". *Science* 325.5945 (2009), pp. 1221–1221. eprint: `http://science.sciencemag.org/content/325/5945/1221.full.pdf`.

[Pou51] R. V. Pound. "Nuclear Spin Relaxation Times in Single Crystals of LiF". *Phys. Rev.* 81 (1 Jan. 1951), pp. 156–156.

[Pur46] E. M. Purcell, H. C. Torrey, and R. V. Pound. "Resonance Absorption by Nuclear Magnetic Moments in a Solid". *Phys. Rev.* 69 (1-2 Jan. 1946), pp. 37–38.

[Rab37] I. I. Rabi. "Space Quantization in a Gyrating Magnetic Field". *Phys. Rev.* 51 (8 Apr. 1937), pp. 652–654.

[Rab38] I. I. Rabi, J. R. Zacharias, S. Millman, and P. Kusch. "A New Method of Measuring Nuclear Magnetic Moment". *Phys. Rev.* 53 (4 Feb. 1938), pp. 318–318.

[Rab39] I. I. Rabi, S. Millman, P. Kusch, and J. R. Zacharias. "The Molecular Beam Resonance Method for Measuring Nuclear Magnetic Moments. The Magnetic Moments of $_3\mathrm{Li}^6$, $_3\mathrm{Li}^7$ and $_9\mathrm{F}^{19}$". *Phys. Rev.* 55 (6 Mar. 1939), pp. 526–535.

[Ram49] Norman F. Ramsey. "A New Molecular Beam Resonance Method". *Phys. Rev.* 76 (7 Oct. 1949), pp. 996–996.

[Ram50] Norman F. Ramsey. "A Molecular Beam Resonance Method with Separated Oscillating Fields". *Phys. Rev.* 78 (6 June 1950), pp. 695–699.

[Ram95] N.F. Ramsey. "Successive oscillatory fields at radio to optical frequencies". English. *Appl. Phys. B* 60.2-3 (1995), pp. 85–88.

[Sae13] Kamyar Saeedi, Stephanie Simmons, Jeff Z. Salvail, Phillip Dluhy, Helge Riemann, Nikolai V. Abrosimov, Peter Becker, Hans-Joachim Pohl, John J. L. Morton, and Mike L. W. Thewalt. "Room-Temperature Quantum Bit Storage Exceeding 39 Minutes Using Ionized Donors in Silicon-28". *Science* 342.6160 (2013), pp. 830–833. eprint: `http://science.sciencemag.org/content/342/6160/830.full.pdf`.

[San06] H. Sanada, Y. Kondo, S. Matsuzaka, K. Morita, C. Y. Hu, Y. Ohno, and H. Ohno. "Optical Pump-Probe Measurements of Local Nuclear Spin Coherence in Semiconductor Quantum Wells". *Phys. Rev. Lett.* 96 (6 Feb. 2006), p. 067602.

[San09] Kaoru Sanaka, Alexander Pawlis, Thaddeus D. Ladd, Klaus Lischka, and Yoshihisa Yamamoto. “Indistinguishable Photons from Independent Semiconductor Nanostructures”. *Phys. Rev. Lett.* 103 (5 July 2009), p. 053601.

[San12] Kaoru Sanaka, Alexander Pawlis, Thaddeus D. Ladd, Darin J. Sleiter, Klaus Lischka, and Yoshihisa Yamamoto. “Entangling Single Photons from Independently Tuned Semiconductor Nanoemitters”. *Nano Lett.* 12.9 (2012), pp. 4611–4616.

[Sch11] A. Schwan, B.-M. Meiners, A. B. Henriques, A. D. B. Maia, A. A. Quivy, S. Spatzek, S. Varwig, D. R. Yakovlev, and M. Bayer. “Dispersion of electron g-factor with optical transition energy in (In,Ga)As/GaAs self-assembled quantum dots”. *Applied Physics Letters* 98.23 (2011), p. 233102. eprint: `http://dx.doi.org/10.1063/1.3588413`.

[Seo16] Hosung Seo, Abram L. Falk, Paul V. Klimov, Kevin C. Miao, Giulia Galli, and David D. Awschalom. “Quantum decoherence dynamics of divacancy spins in silicon carbide”. *NATURE COMMUNICATIONS* 7 (Sept. 2016).

[Sha03] A. Shabaev, Al. L. Efros, D. Gammon, and I. A. Merkulov. “Optical readout and initialization of an electron spin in a single quantum dot”. *Phys. Rev. B* 68 (20 Nov. 2003), p. 201305.

[Sho94] P. W. Shor. “Algorithms for quantum computation: discrete logarithms and factoring”. In: *Proceedings 35th Annual Symposium on Foundations of Computer Science*. Nov. 1994, pp. 124–134.

[Sle13] Darin J. Sleiter, Kaoru Sanaka, Y. M. Kim, Klaus Lischka, Alexander Pawlis, and Yoshihisa Yamamoto. “Optical Pumping of a Single Electron Spin Bound to a Fluorine Donor in a ZnSe Nanostructure”. *Nano Lett.* 13.1 (2013), pp. 116–120.

[Ste12] M. Steger, K. Saeedi, M. L. W. Thewalt, J. J. L. Morton, H. Riemann, N. V. Abrosimov, P. Becker, and H.-J. Pohl. “Quantum Information Storage for over 180 s Using Donor Spins in a 28Si “Semiconductor Vacuum””. *Science* 336.6086 (2012), pp. 1280–1283. eprint: `http://science.sciencemag.org/content/336/6086/1280.full.pdf`.

[Ste79] Jozef Stefan and Kaiserlich-Königlichen Hof und Staatsdruckerie. *Über die Beziehung zwischen der Wärmestrahlung und der Temperatur*. Aus der kk Hof- und Staatsdruckerei, 1879.

[Stö17] Thomas Stöhr. “Private communication”. 2017. unpublished.

[Syp11a] M. Syperek, D. R. Yakovlev, I. A. Yugova, J. Misiewicz, I. V. Sedova, S. V. Sorokin, A. A. Toropov, S. V. Ivanov, and M. Bayer. “Erratum: Long-lived electron spin coherence in CdSe/Zn(S,Se) self-assembled quantum dots [Phys. Rev. B **84** , 085304 (2011)]”. *Phys. Rev. B* 84 (15 Oct. 2011), p. 159903.

[Syp11b] M. Syperek, D. R. Yakovlev, I. A. Yugova, J. Misiewicz, I. V. Sedova, S. V. Sorokin, A. A. Toropov, S. V. Ivanov, and M. Bayer. “Long-lived electron spin coherence in CdSe/Zn(S,Se) self-assembled quantum dots”. *Phys. Rev. B* 84 (8 Aug. 2011), p. 085304.

[Tes08] C. Testelin, B. Eble, F. Bernardot, G. Karczewski, and M. Chamarro. “Signature of the Overhauser field on the coherent spin dynamics of donor-bound electrons in a single CdTe quantum well”. *Phys. Rev. B* 77 (23 June 2008). Useful article to calculate maximal Overhauser field, p. 235306.

[Tho95] R. J. Thomas, Benjamin Rockwell, H. R. Chandrasekhar, Meera Chandrasekhar, A. K. Ramdas, M. Kobayashi, and R. L. Gunshor. “Temperature dependence of strain in ZnSe(epilayer)/GaAs(epilayer)”. *Journal of Applied Physics* 78.11 (1995), pp. 6569–6573.

[Tra12] Andreas Trabesinger. “Quantum simulation”. *Nat. Phys.* 8 (2012), p. 263.

[Tra97] A. Trampert, O. Brandt, and K.H. Ploog. “Chapter 7 Crystal Structure of Group III Nitrides”. In: *Gallium Nitride (GaN) I*. Ed. by Jacques I. Pankove and Theodore D. Moustakas. Vol. 50. Semiconductors and Semimetals. Elsevier, 1997, pp. 167–192.

[Tyr03] A. M. Tyryshkin, S. A. Lyon, A. V. Astashkin, and A. M. Raitsimring. “Electron spin relaxation times of phosphorus donors in silicon”. *Phys. Rev. B* 68 (19 Nov. 2003), p. 193207.

[Van01] LMK Vandersypen, M Steffen, G Breyta, CS Yannoni, MH Sherwood, and IL Chuang. “Experimental realization of Shor’s quantum factoring algorithm using nuclear magnetic resonance”. *NATURE* 414.6866 (Dec. 2001), pp. 883–887.

[Vek76] VL Vekua, RI Dzhioev, BP Zakharchenya, and VG Fleisher. “Hanle effect in optical orientation of electrons in n-type semiconductors”. *Soviet Physics-Semiconductors* 10.2 (1976), pp. 210–212.

[Wal16] M. Mitchell Waldrop. “The chips are down for Moore’s law”. *Nature News* 530.7589 (2016), p. 144.

[Wes94] R.S. Westfall. *The Life of Isaac Newton*. Canto original series. Cambridge University Press, 1994, p. 106.

[Wid15] Matthias Widmann, Sang-Yun Lee, Torsten Rendler, Nguyen Tien Son, Helmut Fedder, Seoyoung Paik, Li-Ping Yang, Nan Zhao, Sen Yang, Ian Booker, Andrej Denisenko, Mohammad Jamali, S. Ali Momenzadeh, Ilja Gerhardt, Takeshi Ohshima, Adam Gali, Erik Janzen, and Joerg Wrachtrup. “Coherent control of single spins in silicon carbide at room temperature”. *NATURE MATERIALS* 14.2 (Feb. 2015), pp. 164–168.

[Woo24] R. W. Wood and A. Ellett. “Polarized Resonance Radiation in Weak Magnetic Fields”. *Phys. Rev.* 24 (3 Sept. 1924), pp. 243–254.

[Yak01] D.R. Yakovlev, G.V. Astakhov, W. Ossau, S.A. Crooker, N. Miura, A. Waag, N.A. Gippius, A.Yu. Sivachenko, and A.B. Dzyubenko. “Trions in ZnSe-Based Quantum Wells Probed by 50 T Magnetic Fields”. *physica status solidi (b)* 227.2 (2001), pp. 353–363.

[Yak08] D. R. Yakovlev and M. Bayer. “Coherent Spin Dynamics of Carriers”. In: *Spin Physics in Semiconductors*. Ed. by Mikhail I. Dyakonov. Berlin, Heidelberg: Springer Berlin Heidelberg, 2008, pp. 135–177.

[Yos83] S. Yoshida, S. Misawa, and S. Gonda. "Improvements on the electrical and luminescent properties of reactive molecular beam epitaxially grown GaN films by using AlN-coated sapphire substrates". *Applied Physics Letters* 42.5 (1983), pp. 427–429. eprint: `http://aip.scitation.org/doi/pdf/10.1063/1.93952`.

[Yu96] Peter Y. Yu and Manuel Cardona. "Electronic Band Structures". In: *Fundamentals of Semiconductors: Physics and Materials Properties*. Berlin, Heidelberg: Springer Berlin Heidelberg, 1996. Chap. 2, pp. 17–105.

[Yug12] I. A. Yugova, M. M. Glazov, D. R. Yakovlev, A. A. Sokolova, and M. Bayer. "Coherent spin dynamics of electrons and holes in semiconductor quantum wells and quantum dots under periodical optical excitation: Resonant spin amplification versus spin mode locking". *Phys. Rev. B* 85 (12 Mar. 2012), p. 125304.

[Zee97] Pieter Zeeman. "XXXII. On the influence of magnetism on the nature of the light emitted by a substance". *The London, Edinburgh, and Dublin Philosophical Magazine and Journal of Science* 43.262 (1897), pp. 226–239.

[Zhu14] E. A. Zhukov, A. Greilich, D. R. Yakovlev, K. V. Kavokin, I. A. Yugova, O. A. Yugov, D. Suter, G. Karczewski, T. Wojtowicz, J. Kossut, V. V. Petrov, Yu. K. Dolgikh, A. Pawlis, and M. Bayer. "All-optical NMR in semiconductors provided by resonant cooling of nuclear spins interacting with electrons in the resonant spin amplification regime". *Phys. Rev. B* 90 (8 Aug. 2014), p. 085311.

[Zhu17] E. A. Zhukov, E. Kirstein, N. Kopteva, F. Heisterkamp, D. R. Yakovlev, V. L. Korenev, I. A. Yugova, A. Pawlis, M. Bayer, and A. Greilich. "Quantization of electron spin precession and reduction of spin dephasing through coupling to nuclear bath in ZnSe:F". *In preparation for submission to Phys. Rev. Lett.* (2017).

[Zwi44] B Zwicker and P Scherrer. "Elektrooptische Eigenschaften der seignette-elektrischen Kristalle KH2PO4 und KD2PO4". *Helv. Phys. Acta* 17 (1944), p. 346.

List of Figures

Abbreviations

$\lambda/2$ plate	half-wave plate
$\lambda/4$ plate	quarter-wave plate
ADC	analog-digital converter
AFG	arbitrary function generator
AOM	acousto-optical modulator
BBO	beta barium borate
BNC	Bayonet Neill Concelman
BS	beam splitter
CB	conduction band
CCD	charge-coupled device
cf.	from Latin *confer*=“compare”
CW	continuous-wave
D^0X-HH	donor-bound exciton
DNP	dynamic nuclear polarization
DTS	dark-bright time-scanning spectroscopy
EOM	electro-optical modulator
fcc	face-centered cubic
FWHM	full-width at half maximum
FX	free exciton
GF	neutral gray filter
Glan	Glan-Taylor prism
HH	heavy hole
HWHM	half-width at half maximum
KLM	Knill-Laflamme-Milburn
KR	Kerr rotation
LFS	laboratory frame system
LH	light hole
MBE	molecular beam epitaxy
MRI	magnetic resonance imaging
NMR	nuclear magnetic resonance
NSS	nuclear spin system
ODNMR	optically detected nuclear magnetic resonance
PBS	polarizing beam splitter
PCD	photoinduced circular dichroism
PEM	photoelastic modulator
PL	photoluminescence
PR	polarization recovery
PSC	phase synchronization condition

QD	quantum dot
QW	quantum well
RF	radio frequency
RFS	rotating frame system
RSA	resonant spin amplification
SH	split-off hole
SHG	second harmonic generation
SNR	signal to noise ratio
T^-	trion
TC	time constant
TRKR	time-resolved Kerr rotation
TTL	transistor-transistor logic
VB	valence band
VESTA	visualization for electronic and structural analysis
VTI	variable temperature insert
X	exciton
ZnSe	zinc selenide

Symbols

A	Hyperfine constant or area.
A_0	Parameter for the amplitude in non-linear fits.
a_0	Lattice constant of the crystal (here usually ZnSe).
A_1	Parameter for the amplitude in non-linear fits.
A_2	Parameter for the amplitude in non-linear fits.
a_B	Bohr radius.
A_echo	Hahn echo (nuclear spin echo) amplitude.
a_epi	Lattice constant of the crystal, which shall be grown on the substrate.
a_sub	Lattice constant of the substrate, on which the crystal shall be grown.
A_n	Hyperfine constant of the nth nucleus.
A_i	Parameter for the amplitude of the i-th peak.
a_loc	Localization radius of the electron at the donor.
A_off	Offset parameter in non-linear fits.
A_PR	Polarization recovery amplitude.
A_RF	Amplitude of the signal applied to the RF coil.
A_Se	Hyperfine constant of the ^{77}Se isotope.
A_shift	Magnitude/Maximum of the RSA peak shift induced by a particular resonance.
A_Zn	Hyperfine constant of the ^{67}Zn isotope.
b	Fitting parameter for the y-intersection for a linear fit.
b_e	Maximal Knight field amplitude at the center of the donor.
$B_{1/2}$	Halfwidth of the Hanle curve.
$\boldsymbol{B}_\mathrm{N}$	Vector representation of the Overhauser field.
B_N	Overhauser field (absolute value) or strength of the average fluctuating hyperfine field.
$B_\mathrm{N}^\mathrm{max}$	Maximal Overhauser field.
$\boldsymbol{B}_\mathrm{N}$	Overhauser field vector or vector of the average fluctuating hyperfine field.
$B_{\mathrm{N},x}$	x-component of the Overhauser field.
B	Magnetic field (absolute value).
B_0	Deviation of zero on magnetic field scale (hall sensor) from actual zero position.
$B_{\mathrm{c},i}$	Center position of Lorenz peak (RSA peak).
B_eff	Effective magnetic field determining the electron Larmor precession frequency or effective magnetic field produced by the RF coil.
$B_{\mathrm{FWHM},i}$	Full-width half maximum of the i-th Lorenz peak (RSA peak).
B_F	Magnetic field (absolute value) in Faraday geometry.

B_L	Root mean square local field due to the nuclear dipole-dipole interactions.
B_NMR	Magnetic field at nuclear magnetic resonance.
B_RF	Magnetic field produced by the RF coil at the sample.
B_V	Magnetic field (absolute value) in Voigt geometry.
$\boldsymbol{B}$	Magnetic field vector.
$\boldsymbol{B}_\mathrm{NMR}$	Vector representation of the field of nuclear magnetic resonance
$\boldsymbol{B}_\mathrm{RF}$	Vector representation of the magnetic field produced by the RF coil at the sample.
$\boldsymbol{B}_\mathrm{total}$	Vector representation of the superposition of different magnetic fields.
$\boldsymbol{B}_\mathrm{V}$	Vector representation of the external magnetic field (Voigt geometry).
C	Depth of the PR dip at $B_\mathrm{F} = 0$.
c	Speed of light in vacuum: $299\,792\,458\,\mathrm{m\,s^{-1}}$ [Moh15].
c_0	Coefficient of the constant term in a polynomial.
c_2	Coefficient of the quadratic term of a polynomial.
χ	Natural abundance of an isotope.
χ_Se	Natural abundance of the ^{77}Se isotope with nonzero nuclear spin.
χ_Zn	Natural abundance of the ^{67}Zn isotope with nonzero nuclear spin.
D	Remaining PR amplitude at $B_\mathrm{F} = 0$.
$\bar{d}$	Average distance between donors.
ΔB	Shift of RSA peaks (usually compared to their position at low P_Pu.)
Δl	Difference of the azimuthmal quantum numbers l.
Δm_j	Difference of the projection of the total angular momentum m_j.
Δ_SO	Energy offset of the split-off hole band due to spin-orbit interaction.
Δt	Time delay between the pump and the probe pulses can be varied by moving the retroreflector on the delay line.
$\langle d \rangle$	Dipole transition matrix element.
E	Electric field of the laser beam/pulse.
e	Elementary charge.
E_a	Donor binding energy or activation energy
E_exc	Photon energy of the laser.
E_g	Energy difference between maximum energy in the valence band and minimal energy in the conduction band of a semiconductor or insulator.
ε	Lattice mismatch between two crystals.
E_n	Energy (eigenenergy) of the n-th electron eigenstate.
ε_KR	Kerr ellipticity.
$E_\downarrow$	Energy of the spin-down ($\lvert\downarrow\rangle$) state in a longitudinal magnetic field B_F.
$E_\uparrow$	Energy of the spin-down ($\lvert\downarrow\rangle$) state in a longitudinal magnetic field B_F.
$\boldsymbol{E}_\mathrm{stat}$	Static electric field, e.g. used in electro-optical modulators
η_b	Relative error of the y-intersection b in linear fits.
η_{τ_S}	Relative error of the spin relaxation time .
f_aux	Auxiliary reference frequency.
f_m	Pump helicity modulation frequency.
$f_\mathrm{m,1}$	First pump helicity modulation frequency.
$f_\mathrm{m,2}$	Second pump helicity modulation frequency.

f_{NMR}	Nuclear magnetic resonance frequency.
f_{Rabi}	Rabi frequency.
f_{Ramsey}	Ramsey frequency.
f_{RF}	Frequency of the radio frequency (RF) excitation.
$\tilde{F}$	Generalized Fresnel coefficient.
G	Electron-hole generation rate (photogeneration).
g	g-factor, dimensionless quantity, which measures the magnetic moment or gyromagnetic ratio of a particle or nuclei [Odo06; Gab07].
γ	Gyromagnetic ratio.
Γ	Full width half maximum (FWHM) of a Lorentzian or Γ point: Center of the Brillouin zone ($\boldsymbol{k} = 0$).
γ_{Se}	Gyromagnetic ratio of the ^{77}Se isotope.
γ_{Zn}	Gyromagnetic ratio of the ^{67}Zn isotope.
g_{e}	Electron g-factor
$g_{\mathrm{N},n}$	g-factor of the nth nucleus.
g_{N}	g-factor of nuclear spin.
$\hbar$	Reduced Planck constant.
H_{hf}	Hamilton operator of the electron-nuclear hyperfine interaction.
H_{so}	Hamilton operator of the spin-orbit interaction.
$H_{\mathrm{Ze,e}}$	Hamilton operator of the electronic Zeeman energy.
I	Nuclear spin.
I_{Se}	Nuclear spin of ^{77}Se.
I_{Zn}	Nuclear spin of ^{67}Zn.
$\boldsymbol{I}$	Nuclear spin vector. Can either refer to the vector representation of the components of the spin of a single nucleus or to the macroscopic spin polarization of an ensemble of nuclear spins.
I_x	x-component of the nuclear spin.
I_z	z-component of the nuclear spin.
j	Total angular momentum quantum number.
$\boldsymbol{J}$	Total angular momentum operator.
k_{B}	Boltzmann constant.
$\|0\rangle$	Ground state of quantum mechanical two-level system (eigenstate).
$\|1\rangle$	Excited state of quantum mechanical two-level system (eigenstate).
$\|\downarrow\rangle$	Electron spin in spin-down state.
$\|\uparrow\rangle$	Electron spin in spin-up state.
$\|\Psi\rangle$	State of a quantum mechanical system.
B_{K}	Magnitude of the Knight fieldF.
$\boldsymbol{B}_{\mathrm{K}}$	Vector representation of the Knight field.
k	Modulus of the wavevector of an electromagnetic wave or of a particle, e.g. electron.
$\boldsymbol{k}$	Wavevector of an electromagnetic wave or of a particle, e.g. electron.
$\boldsymbol{k}_{\mathrm{pump}}$	Wavevector of the pump beam, a pump pulse.
L	Correlator measured by the lock-in amplifier.
l	Azimuthal quantum number.

L_0	Value of the correlator measured
λ	Wavelength.
$\boldsymbol{L}$	Angular momentum vector.
m	Fitting parameter for the slope in linear fits. Here $m \propto 1/n_0$.
m_e	Free electron mass in vacuum (rest mass).
m_e^*	Effective electron mass.
m_HH^*	Effective heavy hole mass.
m_j	Projection of the total angular momentum.
m_LH^*	Effective light hole mass.
M	Modulus of the magnetization vector.
M_eq	Modulus of the equilibrium magnetization vector.
μ_B	Bohr magneton, a physical constant and a unit for the magnetic moment.
μ_N	Nuclear magneton.
$\boldsymbol{M}$	Magnetization vector.
m_z	Magnetic quantum number.
n_0	Resident electron concentration.
n_D	Concentration of donors in an n-doped semiconductor.
$n_\mathrm{F,c}$	Critical concentration of the fluorine dopant, at which the metal-insulator transition occurs.
n_F	Concentration of the fluorine dopant.
N_L	Number of nuclei in the localization of the donor.
ν	$\nu \in \mathbb{R}$, exponent of the magnetic field dependence of τ_S
f_R	Repetition frequency of the pulsed laser.
ω_R	Laser repetition frequency.
P	Power.
p	Probability, $p \in [0, 1]$.
Φ	Potential of the electric field.
φ	Parameter for the phase in non-linear fit of oscillations and relative phase of the RF excitation.
ϕ	Phase between the spin components S_y and S_z or azimuthal angle (phase) of the Bloch vector.
ϕ_osc	Amplitude of the oscillations of the phase between the spin components S_y and S_z.
P_Pr	Average power of the probe beam.
P_Pu	Average power of the pump beam.
Ψ	Envelope wave function of the electron.
$\boldsymbol{p}$	Momentum vector/momentum operator.
ρ_c	Degree of circular polarization.
R	Average distance between neighboring isotopes with non-zero nuclear spin.
r	Modulus of the electron position vector.
$\boldsymbol{r}$	Electron position vector.
S	Modulus of the electron spin vector. Can either refer to the vector representation of the components of the spin of a single electron or to the macroscopic spin polarization of an ensemble of electron spins.

S_0	Steady-state spin polarization, which is determined by $G \propto P_{\mathrm{Pu}}$, n_0, S_{i} and τ_S.
σ	Stefan-Boltzmann constant.
σ_{τ_S}	Absolute error of the spin relaxation time τ_S.
σ_b	Absolute error of the y-intersection b in linear fits.
$\boldsymbol{\sigma}$	Vector of the Pauli matrices.
σ_x	Pauli matrix for x-component of the spin.
σ_y	Pauli matrix for y-component of the spin.
σ_z	Pauli matrix for z-component of the spin.
S_{i}	z-component of the initially generated spin polarization, which depends on the pump helicity and optical selection rules.
σ^-	Left-circular polarization.
σ^+	Right-circular polarization.
$\boldsymbol{S}$	Electron spin vector. Can either refer to the vector representation of the components of the spin of a single electron or to the macroscopic spin polarization of an ensemble of electron spins.
S_x	x-component of the electron spin. Can either refer to the x-component of the spin of a single electron or to the macroscopic spin polarization of an ensemble of electron spins.
S_y	y-component of the electron spin. Can either refer to the z-component of the spin of a single electron or to the macroscopic spin polarization of an ensemble of electron spins.
S_z	z-component of the electron spin. Can either refer to the z-component of the spin of a single electron or to the macroscopic spin polarization of an ensemble of electron spins.
T	Absolute/thermodynamic temperature, here the Kelvin scale shall be used.
t	Time: Newtonian, absolute time, since relativistic corrections are not important for the phenomena studied in this thesis.
T_1	Longitudinal spin relaxation time of the electron spin.
T_1^{N}	Longitudinal spin relaxation time of the nuclear spin.
$T_1^{\mathrm{N,dark}}$	Longitudinal spin relaxation time of the nuclear spin without optical excitation.
T_2	Transverse spin relaxation time/coherence time of the electron spin.
T_2^{inh}	Inhomogeneous spin relaxation time (due to a dispersion of the precession frequencies) of the electron spins.
T_2^{N}	Transverse spin relaxation time/coherence time of the nuclear spin.
$T_2^{\mathrm{N,inh}}$	Inhomogeneous spin relaxation time (due to a dispersion of the precession frequencies) of the nuclear spins.
T_2^*	Inhomogeneous spin dephasing time of the electron spins.
$T_2^{*,\mathrm{N}}$	Inhomogeneous spin dephasing time of the nuclear spins.
τ	Recombination time of photogenerated carriers.
τ_0	Decay time of a mono exponentially damped function.
τ_1	1st rise time of double exponential fit.

τ_2	2nd rise time of double exponential fit.
τ_c	Correlation of the donor-bound electrons with the donor.
τ_p	Pulse width of RF or laser pulses.
τ_S	Electron spin relaxation time, equals the T_1 time in a magnetic field in Faraday geometry.
τ_X	Exciton recombination time.
Θ	Optical pulse area.
θ_KR	Kerr rotation angle or amplitude.
θ_nuc	Nuclear spin temperature.
$\tilde{\theta}$	Complex Kerr rotation.
T_L	Electron Larmor precession period.
T_m	Helicity modulation period.
T_N	Period of the nuclear Larmor precession.
T_R	Laser repetition period.
T_S	Electron spin lifetime.
$u_{n,\boldsymbol{k}}$	Periodic Bloch function.
v_0	Unit cell volume.
ω	Frequency of the electromagnetic wave (light).
ω_L	Larmor precession frequency of the electron spin.
ω_N	Larmor precession frequency of the nuclear spin.
x	Coordinate on the x axis of a cartesian coordinate system.
ξ	Dimensionless parameter.
y	Coordinate on the y axis of a cartesian coordinate system.
z	Coordinate on the z axis of a cartesian coordinate system.

Acknowledgments

Finally, I would like to thank all the people who have supported me during my PhD studies. I would like to thank my supervisor Prof. Dr. Manfred Bayer for the opportunity to do my PhD in his great group. Considering that I had already worked in theoretical physics and in the industry before I started my PhD, I am especially grateful to him for providing me this unique opportunity and believing in my abilities as a physicist. Last but not least, I would like to thank him for his support, encouragement, advice and patience during my time in his group.

I would like to thank my direct supervisors in the laboratory, Prof. Dr. Evgeny A. Zhukov and PD Dr. Alex Greilich for their advice and support, discussions, the great collaboration and the nice atmosphere in the lab. I have learned most from Evgeny Zhukov, who introduced me to the pump-probe setup in the Picolab. He taught me everything I need to know to work in the lab and has always been ready to give advice or help me in the lab. I also would like to thank him for his feedback on parts of this manuscript. Alex Greilich has always been ready to give advice and feedback on numerous talks and publications. I am especially grateful for his great ideas and feedback, regarding the experiments, his ability to explain almost any physical problem very understandably and his help in the lab. I also would like to thank him for reading the whole manuscript and his feedback on it.

I would like to thank Prof. Dr. Dmitri R. Yakovlev for the great collaboration in terms of our common publications and his great advice how to proceed to write this thesis. I am especially grateful for his patience during the review process of our first common publication. I also would like to thank him for reading the whole manuscript and his feedback on it. I would like to thank Dr. Tomasz Kazimierczuk for his support and efforts to automatize the setup and the great collaboration, regarding the nuclear dynamics experiments. I would like to thank Prof. Dr. Irina A. Yugova and Prof. Dr. Vladimir L. Korenev for the great collaboration. I would like to thank PD Dr. Alexander Pawlis for providing us with the great ZnSe samples, studied in this work. I would like to thank Dr. Vasilii V. Belykh for fruitful discussions and his feedback on the whole manuscript of this thesis. I would like to thank Dr. Jörg Debus for his advice on physical problems, the great collaboration as teaching assistant for Physics A2/B2 and his feedback on parts of this manuscript. I would like to thank Erik Kirstein for the great collaboration and his feedback on parts of this manuscript. He has been a great labmate with his drive to automatize the experiments and his excellent `Labview` skills. I would like to thank Dr. Damien Canneson, Henning Moldenhauer and Eiko Evers for their advice and feedback on parts of this manuscript.

I would like to thank Michaela Wäscher and Nina Colette for their great administrative support. They very patiently solve and explain all administrative issues and are always ready to help. I am especially grateful for Michaela's support and patience during numerous orders. I would like to thank Lars Wieschollek, Klaus Wiegers and Thomas Stöhr for their

excellent technical support. If it were not for Mr. Wiegers's excellent skills, operating the low-temperature facilities, we could not have used the `3D Vector Magnet` as often and intensively, as we did. I am very grateful to my father for his continuous support of and during my studies. Finally, I want to thank all other recent and former members of E2 for the great atmosphere. Thank you all very much!